UNIVERSIDADE DE LISBOA
INSTITUTO SUPERIOR TÉCNICO

Functionalization by ion implantation of Si: influence on wettability and tribomechanical properties at micro and nanoscales

Bruno Miguel Fernandes Nunes

Supervisor: Doctor Rogério Anacleto Cordeiro Colaço

Co-Supervisor: Doctor Eduardo Jorge da Costa Alves

Thesis approved in public session to obtain the PhD degree in Materials Engineering

Jury final classification: Pass with Distinction

Jury

Chairperson: Chairman of the IST Scientific Board

Members of the Committee:

Doctor Rogério Anacleto Cordeiro Colaço, Full Professor, Instituto Superior Técnico, Universidade de Lisboa

Doctor Eduardo Jorge da Costa Alves, Coordinator Researcher, Instituto de Plasmas e Fusão Nuclear, Instituto Superior Técnico, Universidade de Lisboa

Doctor Ana Paula Valagão Amadeu do Serro, Associate Professor, Instituto Superior de Ciências da Saúde Egas Moniz

Doctor Rui Manuel Coelho da Silva, Principal Investigator, Instituto de Plasmas e Fusão Nuclear, Instituto Superior Técnico, Universidade de Lisboa

Doctor Célio Gabriel Figueiredo Pina, Adjunct Professor, Escola Superior de Tecnologia de Setúbal, Instituto Politécnico de Setúbal

Doctor Sérgio de Almeida Graça, Principal Investigator, Rolex Switzerland

Funding Institutions: Fundação para a Ciência e a Tecnologia

2015

“*Nothing is so painful to the human*

mind as a great and sudden change.”

Mary Shelly

ABSTRACT

Commercialization of contact-based operation Si MEMS (Microelectromechanical systems) devices is still a distant reality. The small characteristic dimensions of the devices, ranging from 100 nm to 1 mm, lead to high surface adhesion phenomena making forces such as the capillarity or friction to become predominant over inertial or even operating ones, causing permanent failure either by stiction (permanent adhesion between contacting surfaces) or catastrophic failure by wear. In the present thesis, Si surfaces were single and co-implanted with different elements, namely Fe, C, Fe+C and Ti+C, with fluences ranging from $5x10^{15}$ cm^{-2} to $2x10^{17}$ cm^{-2}, in order to render Si hydrophobic and simultaneously improve Si wear resistance. The implanted samples were also annealed in vacuum for 30 min at different temperatures: 550 ºC, 800 ºC and 1000 ºC.

The first part of the thesis consisted in the structural characterization of the implanted and respective annealed samples using the following characterization techniques: FEG-SEM (field emission gun scanning electron microscopy), GIXRD (grazing incidence x-ray diffraction), RBS (Rutherford backscattering spectrometry) and XPS (X-ray photoelectron spectroscopy) in some samples. Afterwards, contact angle measurements were performed with water and diiodomethane, for surface energy determination and AFM (atomic force microscopy)-based nanowear experiments using a diamond tip. The results show that the dual ion-implantations globally performed better than the single ones. The highest contact angle was measured for the lower fluence of the dual Fe+C samples annealed at 800 ºC sample, with an angle 85º ± 8º, one of the highest angles ever reported using only ion-implantation. However, the sample that best fitted the initial requirements was the dual implanted Ti+C annealed at 800 ºC, which not only exhibited an almost hydrophobic behavior (contact angle of 82º ± 3º) but also presented the lowest measured specific wear coefficient, about ≈ 60 % smaller than the one presented by Si.

KEYWORDS

MEMS, Si, Ion-implantation, Dual ion-implantation, Nanowear, Wettability.

ACKNOWLEDGMENTS

Four years have passed since I started my Ph.D., a rollercoaster journey that allowed me to progress scientifically in my career and also, at the same time, to develop my character as a man. Now that the end is near and I am writing down my thesis last lines, I would like to take the time to express my gratitude to all of you that supported and helped me to accomplish this goal. For sure I will unintentionally forget someone, and if that is the case, my apologies in advance.

I would like to start to thank my supervisors, Professor Rogério Colaço and Doctor Eduardo Alves, for accepting me as their student and guidance during this journey. I would also like to thank Professor Benilde Saramago for letting me use the Q02.06 laboratory installations, Doctor Ana Paula Serro, for the support and friendly advises and Professor Ana Maria Rego for the XPS measurements.

To all my friends in IST that accompanied me and supported me during the phase, Liliana Cangueiro for all the new music and internet trivia updates, Gonçalo Monteiro for the photography advises and chess matches, Filipe Nascimento, Rodrigo Santos, Carole Loable also for all the book recommendations, my squash buddy Tomin Liu, Alexandre Cunha for the good mood, José Restolho for the erudite long talks on history, the little *bambina* Patrizia Paradiso, Diana Silva for the morning coffees company, Andreia Pimenta for her sense of humor, Raquel Galante for the Azorean lessons, Pedro Nolasco for the given Nanosurf support which allowed me to finish my thesis, Mário Vieira my last office colleague.

I would also like to thank to all the people in CTN, where also part of my work was developed, for the help and patience. A special word for Doctor Sérgio Magalhães for his friendship, Maria Fialho for the NDF support, Joana Lencastre and Catarina Ramos for the funniest lunch hours, Norberto Catarino for the technical support, Doctor Nuno Franco for the X-ray measurements, Jorge Rocha for all the ion-implantions and Filomena Baptista for all the help and warning emails concerning the apparatus reservations.

At last, I would like to thank to that special one, Ana, that accompanied me from day one to the end, and finally to my parents for constant support, one of the true universal constants.

INDEX

FIGURES INDEX

TABLES INDEX

ABREVIATION LIST

AFM, atomic force microscopy/e

ALD, atomic layer deposition

APTES ((3-aminopropyl)triethoxysilane)

a-Si, amorphous silicon

a-C, amorphous carbon

a-Si:H hydrogenated amorphous silicon

BE, binding energy

BioMEMS, biological microelectromechanical systems

BMIM-OctSO$_4$, 1-butyl-3-methylimidazolium octyl sulfate

BMIM-PF$_6$,1-butyl-3-methylimidazolium hexafluorophosphate

BSE, backscattered electrons

CMOS, complementary metol-on-oxide-semicondutor

CNT´s, carbon nanotubes

CVD, chemical vapor deposition

De, distilled

DeD, distilled and deionized

DLC, diamond-like carbon

DLP, digital light processor

DNA, Deoxyribonucleic acid

DMBI-PF6, 1,2-dimethyl–3-butyl imidazolium hexafluorophosphate

DMD, digital mirror device

DRIE, deep reactive ion etching

EBA, electron beam annealing

EDS, energy dispersive X-ray spectroscopy

ESCA, electron spectroscopy chemical analysis

FEG-SEM, field-emission gun scanning electron microscopy/e

GIRXD, grazing incidence X-ray diffraction

GW, Greenwood and Williamson

HRTEM, high resolution transmission electron microscopy

HV, Vickers hardness

IC´s, integrated circuits
IBAD, ion beam assisted deposition
IL´s, ionic liquids
LSS, by Lindhard, Sharff and Schiøt
MEMS, microelectromechanical systems
MINS, polyurethane acrylate
MOS, metal-oxide-semicondutor
NEMS, nanoelectromechanical systems
OTS, octadecyltrichlorosilane
PDMS, polydimethylsiloxane
PFPE,perflouropolyether
PKA, primary knock-on atom
PMMA, polymethylmethacrylate
PS, polystyrene
RCA, Radio Corporation America
RMS, root-mean-square
RBS, Rutherford backscattering spectrometry
RH, relative humidity
RF, radio frequency
RF MEMS, radio frequency micromechanical systems
RPM, revolutions per min minute
SAM´s, self-assembled monolayers
SE, secondary electrons
SPM, scanning probe microscope
SPEG, solid phase epitaxy growth
SRIM, stopping and range of ions into matter
SWNT, single wall nanotube
TRIM, transport of ions in matter
UNCD, ultrananocrystalline diamond

SYMBOLS LIST

a, cell parameter

a_C, contact radius

a_{TF}, screening Thomas-Fermi radius

a_0, Bhor radius

A, shared area of the two surfaces

A_n, nominal area

A_S, scanned area

A_R, real contact area

B, empirically determined parameter

C_t, compliance of a system

C_C, contact compliance

C_m, machine compliance

C_n, spring constant

C_1 to C_8, constants

d, interplanar distance

d_{ave}, average depth

D, total distance

(dE/dx), total energy-loss rate of an ion moving through a solid

$(dE/dx)_e$, energy-loss of a traveling ion due to electronic collisions

$(dE/dx)_n$, energy-loss of a traveling ion due to nuclear collisions

e, charge of the electron

E, energy

E_b, binding energy

E_d, displacement energy threshold

E_i, energy after collision

E_k, kinetic energy transferred

E_p, plane Young´s modulus

E_{photon}, photon energy

E_S, sphere Young´s modulus

$E_S(E)$, energy not lost to electronic excitation

E_R, reduced Young´s modulus

E_0, incoming energy

E_1, energy after collision

F, force

F_{vdw}, van der Waals forces

h, maximum displacement

h_c, contact depth

h_{max}, maximum depth

h_S, surface displacement

H, Hamaker constant

I, average excitation energy

k_{AB}, specific wear coefficient

K, proportionality constant between $S(E)_e$ and $\varepsilon^{1/2}$

K_{AB}, abrasive wear coefficient

K_i, kinematic factor

l, cube length

L, normal load

L_A, load supported by a single asperity

L_{ght}, length of the scan

L_d, lateral dimension of the wire frame

$\mathrm{L_g}$, sample profile length

m, empirically determined parameter

m_e, electron mass

m_L mean line

M_1, mass of the ion

M_2, mass of the solid

n_A, number of asperities elastically deformed

N, atomic density

N_A, total number of asperities

N_d, number of displaced atoms

$N_{dis}(x)$, spatial distribution of the implanted atoms

$P(z)$, probability density function of the asperities heights

r, radius of the sphere

r_r, roughness ratio

r_{asp}, radius of the multiple asperities

r_C, radius of the conical asperity

R, range

R_a, average roughness

R_{es}, resolution of the scan

R_p, projected range

R_q, root-mean-square (RMS)

R_t, maximum peak-to-valley distance

R_1 and R_2, curvature radius of the interfaces

S, stopping cross-section

S_t, total stiffness

S_C, contact stiffness

$[S]$, energy-loss factor or S factor

$S_e(E)$, electronic stopping power

$S_n(E)$, nuclear stopping power

S_Z, sensitivity of the photodetector

t, thickness

V, velocity

V_R, total removed volume

Q, wear rate

Q_i, total number of particles

H_i, indentation hardness

HV, Vickers hardness

$U_{(A+b)-(C+D)}$, vertical displacement in photodetector

W_{AA}, work of cohesion of A

W_{AB}, work of adhesion of two different surfaces A and B

W^*_{AB}, work of adhesion of two different surfaces in equilibrium with vapor

x, depth

z, separation distance between the two surfaces

Y, total number of particles detected

Z_1, atomic number of the incoming ion

Z_2, atomic number of the solid

GREEK SYMBOLS LIST

α, grazing angle

β, constant for the stiffness calculation

γ, surface tension

γ_A, surface energy of solid A

γ_{AV}, surface energy of solid A in equilibrium with the vapor

γ_B, surface energy of solid B

γ_{AB}, interfacial energy between the two phases

γ_{DD}, surface tension of diodomethane

γ_S, surface energy of a solid

γ_{SL}, interfacial surface free energy of a solid in equilibrium with liquid

γ_{SV}, interfacial surface free energy of a solid in equilibrium with vapor

γw, surface tension of water

$\gamma w/_{DD}$, interfacial tension between water and diodomethane

γ^{LV}, surface tension of the liquid in equilibrium with its vapor

γ^{SL}, the interfacial tension between the solid and the liquid

γ^{SV} surface free energy of the solid in equilibrium with the vapor

$\gamma_{LVDD}{}^d$, dispersive component of diiodomethane surface tension

γ_{LVDD}, diiodometane surface tension

$\gamma_{LVDD}{}^P$, polar component of diiodomethane surface tension

$\gamma_L{}^d$, dispersive component of the surface tension of the liquid

$\gamma_{LV}{}^d$, dispersive component of the surface tension in equilibrium with vapor

$\gamma_{LV}{}^p$, polar component of the surface tension in equilibrium with vapor

$\gamma_S{}^{ab}$, acid-base component of the surface free energy

$\gamma_S{}^d$, dispersive component of the surface free energy

$\gamma_S{}^H$, hydrogen bond component of the surface free energy

$\gamma_S{}^i$, induction component of the surface free energy

$\gamma_S{}^{nd}$, non-dispersive component of the surface free energy

$\gamma_S{}^P$, polar component of the surface free energy

$\gamma_{SV}{}^{d}$, dispersive component of the surface free energy of a solid in equilibrium with vapor

$\gamma_{SV}{}^{p}$, polar component of the surface free energy of a solid in equilibrium with vapor

$\gamma_{LVw}{}^{d}$, dispersive component of the water surface tension

$\gamma_{LVw}{}^{P}$, polar component of the water surface tension

$\gamma_{S}{}^{0}$, all remaining components of the surface energy

δEs, energy straggling

ΔP, pressure difference

ΔR_p, straggling

ε, dimensionless parameter used for the stopping power determination

$[\varepsilon]$, stopping cross section

ζ, a constant for the calculation of the number of displaced atoms

θ, contact angle of the smooth surface

θ_{DD}, diodomethane contact angle

θ_W, water contact angle

θ^d, diffraction angle

θ^W, attack angle of the conical asperity

θ^W, contact angle of the rough surface according Wenzel model

θ_1, incident angle

θ_2, exiting angle

λ, wavelength

μ, friction coefficient

υ, velocity

υ_0, Bhor velocity

υ_g, velocity of the amorphous/crystalline interface

υ_p, the pre-exponential factor

υ_1, threshold velocity

υ_p, plane Poisson coefficient

υ_s, sphere Poisson coefficient

ξ, dimensionless variable used for the K calculation

π, spreading pressure

π_A, spreading pressure of phase A

ρ, dimensionless parameter used for the stopping power determination

σ, scattering cross section

$(d\sigma/d\Omega)$, differential scattering cross section

σ_{max}, maxium contact pressure

σ^*, standard deviation of the distribution of the asperities heights

σ_m, mean contact pressure

σ_R, radial stress

σ_θ, angular stress

σ_Y, yield stress

τ_{max}, maximum shear stress

υ, velocity

υ_0, Bhor velocity

υ_1, threshold velocity

υ_g, velocity of the amorphous/crystalline interface

υ_p, the pre-exponential factor

φ_S, fraction of solid in contact with the liquid

$\sigma_{Z,}$ normal stress

Φ, fluence

Φ_{spec}, work function of the spectrometer

Ψ, plasticity index

Ω, solid angle

1 SCOPE OF THE THESIS

Human-made devices that contain parts or components with a characteristic length between 1 mm and 100 nm that are able to combine electrical and mechanical functionalities, are now a reality due to recent technologic developments [1]. These devices are designated as MEMS (Microelectromechanical systems) in the literature, and are already a well established reality, being present in a variety of different applications focused on the consumer, such as cars [2], cell phones [3] or DLP® (digital light processor) mirror arrays for projectors and TV [4] building a billion worth USD$ market [5].

However, until now, commercial successful MEMS have either very restricted lateral movements or no moving parts at all [6]. The microscopic characteristic length of MEMS devices leads to very high area-to-volume ratio values which dictate that surface forces such as, van der Waals [7], capillarity, surface tension [8] and friction, proportional to the area [9], become predominant over the inertial or even operating ones. The contacting surfaces of MEMS devices may experience high adhesion, which may lead to either stiction (permanent adhesion), or high friction, leading to failure by severe wear, imposing strong reliability issues to the contact-based MEMS commercialization.

Currently, MEMS industry is dominated by Si and Si-based materials, since the fabrication techniques used for these devices were inherited from the IC´s (integrated circuits) industry [10]. Different approaches have been studied and tested in both Si and even in operating MEMS devices, in order to overcome the adhesion and friction issues. The different studied approaches can be divided in three different categories: the chemical methods, physical methods and chemical-physical methods. The chemical methods consist in changing the surface properties, usually applying a coating that can be either hard, like SiC or DLC´s (diamond-like carbon) [11, 12], or low friction hydrophobic coatings such as SAM´s (self-assembled monolayer’s) or IL´s (ionic liquids) [13, 14], while physical methods consist in performing topographical surface changes in order to achieve simultaneously low adhesion hydrophobic surface [15, 16]. The chemical-physical methods encompass the combination of both chemical and physical ones [17, 18].

The surface properties of Si, or any other material, can be both chemical and physically changed by using a single technique: ion-implantation [19, 20]. Over the last 3 decades different elements have been implanted into Si in order to study the effect on different properties – see section § 2.2. However, as far as the author knows, ion-implantation has never been tested in MEMS devices, unlike the previous mentioned methods, having always remained nothing more than a possibility. More recently, Nakano *et al*. [21, 22] used ion-implantation and wet etching techniques to produce structures such as bouncing cantilevers, proving that ion-implantation is compatible with MEMS fabrication processes.

The present thesis aims to use the ion-implantation method to simultaneously improve wettability and nanowear properties of Si, in order to render Si as a possibility for contact-based MEMS applications. To reach such goal, different elements were implanted into Si, such as: Fe, C, co-implantations of Fe and C, and finally, co-implantations of Ti and C.

The elements were chosen based on different aspects, for instance, the Fe implantation into Si has been extensively studied in the past, but always seeking the formation of the low energy direct gap β – $FeSi_2$ phase [23, 24]. No tribological or mechanical studies have ever been made, with the exception of the author [25]. The C implantations were carried out seeking the good tribological properties of SiC [26] whereas the dual Fe and C implantation was investigated with the point of seeing if the properties of the single implantations were somehow additive and also, at the same time, fill one gap in the literature. The dual Ti and C implantations were made aiming to simultaneously form SiC, TiC and $TiSi_2$ phases, which are reported in the literature for having good mechanical properties, and also to investigate their respective nanotribological performance [27, 28].

Prior to the wettability and nanotribological evaluation, for each system, microstructural and structural characterization was preformed, using FEG-SEM (Field-emission gun scanning electron microcopy), GIXRD (Grazing incidence X-ray diffraction) and RBS (Rutherford backscattering spectrometry) techniques, for all implanted and annealed samples, in order to determine the phases present at each surface.

2 INTRODUCTION

2.1 STATE OF THE ART

2.1.1 INTRODUCTION TO MEMS\NEMS

The term MEMS (an acronym for Microelectromechanical systems) designate human-made devices that contain parts or components with a characteristic length smaller than 1 mm but larger than 100 nm, that are able to combine electrical and mechanical functionalities. Nanoelectromechanical systems (NEMS) refer to nanoscopic devices that have a characteristic length of less than 100 nm that also combine electrical and mechanical components [1]. In order to have a better perspective of the characteristic dimensions of these devices, Figure 1 compares the size of actual MEMS and NEMS with biological elements such as human air, red blood cells and DNA (deoxyribonucleic acid) molecules.

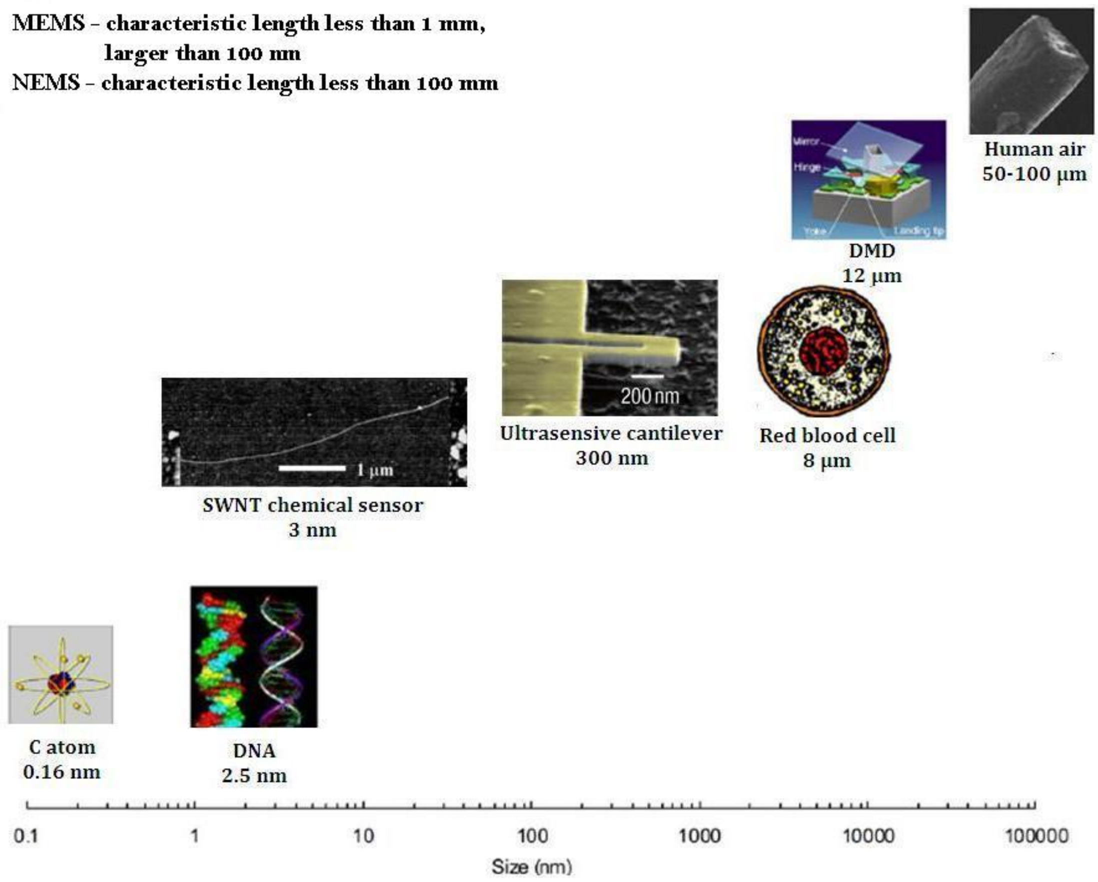

Figure 1. Size comparison of a DMD™ (Digital mirror device) and ultrasensive cantilever [29] MEMS devices and SWNT (single wall nanotube) chemical sensor NEMS [30] device with human air, red blood cell, DNA molecule and carbon atom. Adapted from [9].

The MEMS devices can be classified into 6 different categories according to their applications. The categories are the following [31]:

- Sensors: designed to sense changes in the environment and simultaneously interact with that same environment. The changes can be chemical, thermal or inertial.
- Actuators: designed to provide power or stimulus to other MEMS components devices.
- RF MEMS: designed to interact (filter, transmit, switch and manipulate) with radio frequency (RF) signals, e. g. antennas.
- Optical MEMS: designed to interact with light (direct, reflect, filter and amplify light), e.g., optical switches and reflectors.
- Microfluidic MEMS: designed to interact with fluid-based systems. The devices in this class include pumps, valves and channels fabricated to transport, eject and mix small volumes of fluids.
- BioMEMS: designed to interact with biological samples, more specifically, with proteins, biological cells, medical reagents and can be used for drug delivery analysis.

The MEMS devices are a well established reality that results from intensive research throughout the last 4-5 decades. Considered by many as the first MEMS device, the resonant gate transistor [32], a device that consisted of an out-of plane suspended cantilever over an electrode that moved based upon the applied voltage, was developed by Nathanson *et al*. in 1967. In the following decade other MEMS devices started to be developed in laboratory, such as pressure sensors, inkjet printheads, accelerometers and digital mirrors, but their respective commercialization in the 80´s and 90´s was only possible thanks to process developments in the IC´s industry, namely wet etching and surface micromachinig [33]. Currently, MEMS devices can be found in a huge variety of applications, including sensors for air-bag deployment, tire pressure monitoring and electronic stability control in automobiles [2], radio frequency (RF) switching devices in cell phones and other wireless communication devices [3], ink jet print heads, DLP® (digital light processing) mirror arrays for projectors and television [4]; providing electrical stimulus to pacemakers, drug delivery systems and lab-on-chip devices in biomedical applications [34] are just some few examples of a huge list. The wide-acceptance of the MEMS devices and their respective importance in the nowadays applications helped to build what is a now a billionaire industry. According to

Yole Développement´s research, in 2012 the MEMS market reached an amazing value of 11 billions US$ and global annual growth rates of 12 – 13 % were projected for the following years, until 2018, estimating to build a 23.5 billions US$ market by that time [5].

2.1.2 TRIBOLOGICAL ISSUES IN CONTACT-BASED OPERATION MEMS DEVICES

MEMS devices can be classified into 4 different types depending on the design complexity and respective operation mode. The different operation modes are highlighted on Table 1 as well as some examples of MEMS devices that fit on each category. Each class of devices has its own respective failure modes, being some of them shared among classes. The failures modes are mainly associated with operation mode and the respective surrounding environment. The failures modes can be: fracture, creep, stiction, wear delamination, among others [35]. In the present thesis we shall focus on the Type IV devices and their respective failure mechanisms.

Table 1. Classification of MEMS devices according their operation conditions [36].

Type	Description	Examples
I	Devices with no moving parts	Accelerometers, pressure sensors, ink-jet heads.
II	Devices with moving parts without rubbing or impacting surfaces	Gyroscopes, combo-drivers, resonators, RF MEMS
III	Devices with impacting surfaces	valve pumps
IV	Devices with moving parts with impacting and rubbing surfaces	Shutters, scanners, microgears, electrostatic rotors, optical switches

Commercially successful MEMS devices, to date, do not include the Type IV class devices. The available commercial devices are designed specifically to have either nonmoving parts or very restricted lateral motions [6]. The reason for such restrictive requirements can be explained by “scale effects” [7]. For instance, when the characteristic length of a device decreases from 1 m to 1 mm, the area of the device decreases by a factor of 10^6 whereas the volume decreases by a factor of 10^9. The resulting area-to-volume ratio change gives a result of 10^3 m^{-1}. The direct consequence of this size reduction is that surface forces such as van der Waals [7], surface tension, capillarity [8] and friction, which are proportional to the area, become 10^3 times greater when compared to volume forces such as the inertial and electromagnetic ones [9]. A graphical representation of this phenomenon is illustrated in Figure 2, where it is possible to see that for the macroscopic scales, gravity rules over adhesion, occurring an inversion at the microscopic scales. In Figure 2 it is also shown that the critical dimension where that inversion occurs is ≈ 1 mm, considering a perfect cube with a smooth surface [6].

The dominance of the surfaces forces over both inertial and operating ones causes that close or contacting surfaces of the devices to experience high adhesion phenomena, leading to *stiction*, or permanent adhesion (large static friction coefficient), preventing the device to performs his tasks, or high friction coefficients resulting in a catastrophic failure by excessive wear [37]. The stiction phenomenon is usually associated with the capillarity force, in fact the strongest surface force, for environments where RH (relative humidity) > 30 % is observed. Water vapor from the surrounding environment condensates, forming menisci between close or contacting asperities, leading to very large lateral forces to initiate the relative motion between surfaces [38]. The predominance of surface forces phenomenon in the micro/nanoworld was predicted decades before the first MEMS device was ever fabricated. Richard P. Feynman, physics Nobel prize laureate, stated in his famous 1959 lecture “There´s plenty of room at the bottom” [39]:

“It is interesting to consider what the problems are in such small machines. Firstly, with parts stressed to the same degree, the forces go as the area you are reducing, so that things like weight and inertia are of relatively no importance.”

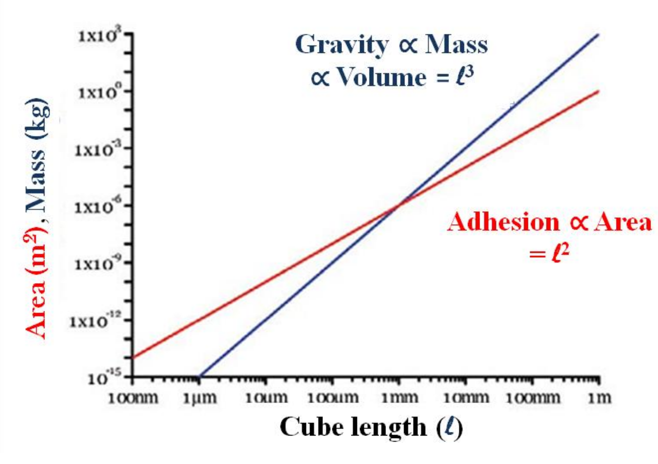

Figure 2. Logarithmic variation of gravity and adhesion for a cube as a function of the size (ℓ), adapted from [6].

Feynaman was already showing full awareness of the main challenges concerning small-scale devices operation. Up to date, these issues have not been completely cleared, still imposing huge reliability problems concerning life-time operations of contact-based MEMS devices, limiting their commercialization. The contact-based operation MEMS devices development (Type IV) started in the late decade of 1980 with the fabrication of the first ever silicon rotary elements made by Mehregany *et al*. at the ATT&T laboratories using silicon etching techniques [40]. These elements consisted of microgears and microturbines, Figure 3(a). The elements were manufactured separated from their place of operation, causing serious handling problems, and by air stimulations were able to reach a speed of 24000 RPM´s (revolutions per minute). Shortly after, Mehregany *et al*. [41] and Fan *et al*. [42] published for the first time the fabrication of movable micromechanical structures fully integrated, such as gears, sliders or springs, Figure 3(b), that no longer needed to be assembled. From this point on, researchers focused their attention towards the fabrication of motors. Fan *et al*. [43] built the first micromotor that operated under electrostatic-drive principles. The device consisted of a rotor with diameter of ≈ 60 µm surrounded by stator elements separated from the rotor by a distance of 2 µm. The application of voltage pulses to the stator elements in the proper sequence allowed the rotor to spin, Figure 3 (d). The micromotors were tested in air and only under high voltage application they would initiate motion, causing corona or even electrical breakdown in some cases. It is interesting to mention that these micromotors were already designed with some friction reduction conceptions. Nonetheless, the results clearly showed that friction related phenomena prevented the device from a regular operation. This was an event of extreme importance, the first experimental manifestation of friction-related problems in small-scale moving devices. This work served as a precursor for a series of friction and wear studies in the micro-scale devices, and even lead to the development of special devices to measure friction [44-47]. Despite the frictional issues several different types of micromotors were developed, a more detailed description of these devices can be found in [48]. The next evolutional step was given by Garcia and Sniegowski [49] with the fabrication and simultaneous preliminary testing of the first ever microengine in the mid 90´s. This device, the first of his kind, was directly linked to an output gear and converted linear motion from a combo-drive [50] actuator to rotational motion, Figure 3 (e). This microengine device was able to deliver torque to other micromechanisms. The tested microengines were able to achieve output angular speeds ranging from 30 to 300000 RPM´s. Nonetheless, tests conducted under a much more moderate speed, 1500 RPM´s, revealed limited life cycles, 10^5, before an increase of voltage was needed to continue the operation. Once again friction still played a critical role in the devices performance. Some minor changes allowed an increase of lifetime cycles before increasing the voltages, using silicon nitride on the side of the joints enabled $2.8x10^{6}$ cycles, whereas a $2x10^{-5}$ $m^{2}s^{-1}$ viscosity (20 centistoke) silicon oil allowed $12x10^{6}$ cycles without degradation under 1200 RPM´s. A fundamental study concerning microegines driving load gears was performed by Tanner *et al*. [51], with the objective of establishing a correlation between the lifetime of the microengine and his respective drive frequency or in other words, the microengine speed, Figure 3(f). The reported major failure mechanism for the operating MEMS was wear of the poly-Si between contacting surfaces. Considerable amounts of debris were formed, sometimes even after few operating seconds, leading to an erratic behavior and sometimes fracture of the pin joint in the drive gear, Figure 3 (f and g). This work was somehow a decisive proof of how unreliable these type of devices were, type IV class, being impossible to be commercialized. It is important to emphasize that the poor performance of the contact-based MEMS does not arise exclusively from the above mentioned scale-effects. Silicon as a material has its own limitations, properties such as, high hardness [52], low Young´s modulus [53], low fracture toughness [36], high surface energy [54], high friction and high wear rates [55] make Si definitely a poor tribological choice for contact MEMS devices. On the other hand, the present MEMS industry is currently dominated by Si and Si-based materials since the fabrication techniques used for MEMS devices were inherited from the IC´s industry [10]. This fact undeniably narrowed the range of possibilities for other materials to be considered for MEMS applications. Silicon became the focus of intense research, being the main objective of that research render Si more suitable for the contact-based operations MEMS. A more detailed description of this topic can be found in the following chapter.

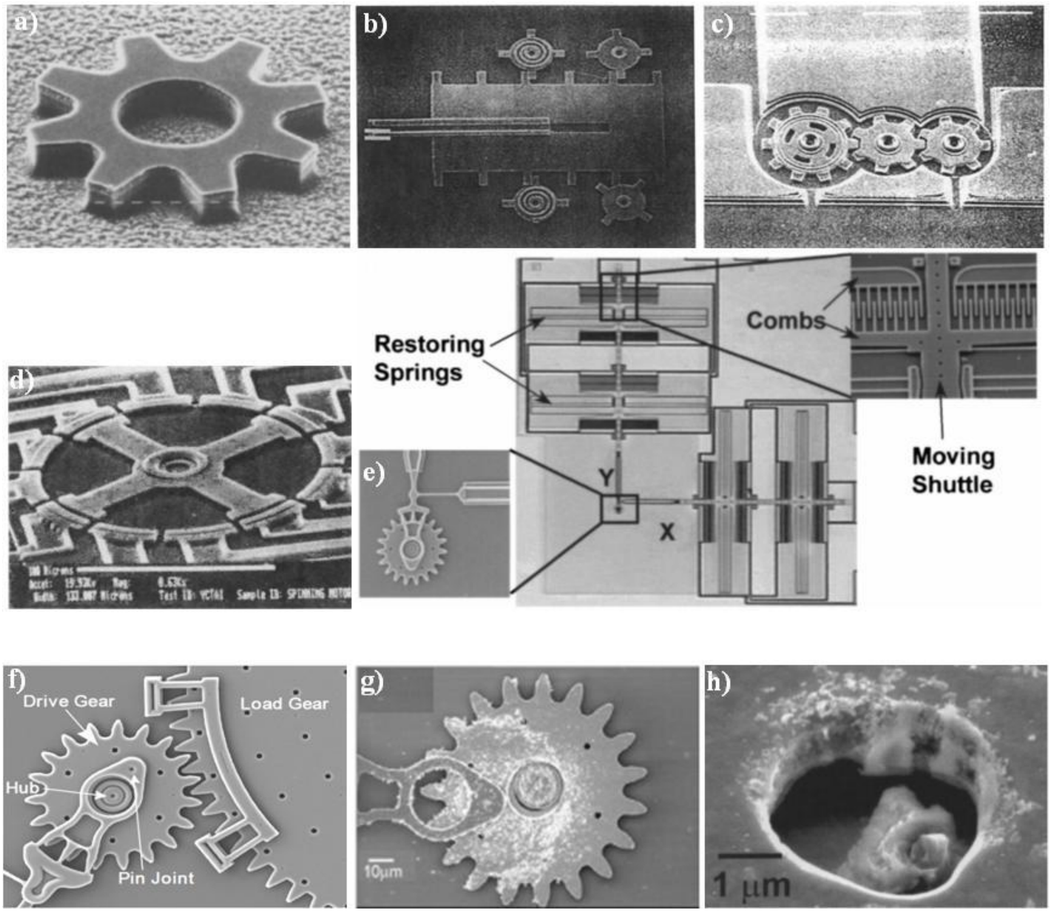

Figure 3. The evolution contact-based operation MEMS, (a) 300 µm gear [40], (b) gear slide combination [42], (C) a three gear-train, the smallest has a 125 µm in diameter [41], (d) A 12 stator, 4 rotor-pole micromotor (e) Sandia microengine with expanded views of the comb drive (top right) and the rotating gear (bottom left) [51], (f) Example of debris accumulation on a microengine stressed to 600.000 cycles at 1.8 % RH [56], (h) Severe pin hole damaged in the drive gear tested to failure (see Figure 3 (f)).

2.1.3 REVISION OF THE DIFFERENT APPROACHES TO OVERCOME MEMS TRIBOLOGICAL ISSUES

Over the last decades a lot of effort and research has been placed towards solving or minimizing the contact-based operation MEMS tribological issues specified in the previous chapter, namely, adhesion/stiction, friction and wear. The different main studied approaches can be classified into three main different categories, which are: chemical methods, when the surface properties are changed by chemical means including the formation of coatings; physical methods, when the surface is structured or changed topographically and finally chemical\physical methods when both strategies are used simultaneously. Some of these approaches have already been tested in MEMS devices while others never left the laboratories or are still waiting for an opportunity. The present and following chapters intend to provide the most significant achievements described in the literature concerning the optimization of Si tribomechanical properties.

2.1.4 CHEMICAL METHODS

As previously said, the chemical methods consist on changing the surface properties of Si by chemical means. One of the simplest methods that can be used consists on using a strong acid, usually HF (hydrofluoridirc acid), to etch the Si surface. This method has the advantage of being compatible with MEMS fabrication techniques, since HF etching is commonly used as a final step to release the MEMS devices from the substrate, by removal of the sacrificial deposited oxide layer [57]. Upon the removal of the oxide layer, the bare silicon surface are believed to be Si-H terminated [58], changing the hydrophilic character of the surface to hydrophobic [59]. The hydrophobic surfaces are welcome since they minimize capillarity adhesion. However, these surfaces are not stable enough, and with time, oxidation of the surface occurs by air and water contact, turning the surface hydrophilic again, as it was shown by Morita *et al*. [60] and, more recently by *Nunes et al*. [17].

Thinking in a more long-lasting and stable approaches, different types of coatings and strategies have been studied and considered in order to change the surface properties of Si. These can be classified into two different subcategories, the low adhesion/lubricant approaches and the high hardness and wear resistance ones, that the author shall address to in the same order.

Fluorocarbon films can be deposited on the surfaces [61] and have been considered for MEMS applications due to their superior surface proprieties, more specifically, low surface energy and high contact angle, stable until high temperatures, [62, 63] which makes them attractive candidates for solving the in-use adhesion and stiction issues. Man *et al*. [64] were able to deposit conformal thin fluorocarbon films with a thickness comprehended between 10 nm and 40 nm, respectively, and tested coated structures under severe conditions. For example, fluorocarbon coated cantilevers beams with a length comprehended between 10 µm and 350 µm, and with a gap of 1.5 µm were completely submerged showing no evidence of capillarity adhesion and accelerated aging tests showed that the films were able to withstand a limit temperature of 400 ºC. The wear performance of the films was also tested by means of a coated cantilever forced to contact a Si_3N_4 surface by means of an applied voltage. A 20 nm thick coating was able to remain hydrophobic even after 10 million cycles and at a temperature of 300 ºC it lasted around 5 million cycles. Smith *et al*. [65] tested fluorocarbon coatings in the field by coating a microengine. The thicker deposited films, around 100 nm, generated too much debris causing malfunction of the device. Reducing the thickness to 20 nm, a gear was able operate for 30 min at 15000 RPM´s. Preliminary tests determined a dynamic friction coefficient of ≈ 0.07 between the coated surfaces. Concerning the lifetime of the coated devices, no experiences were made by Smith and his collaborators, and as far as the author knows, no tribological studies of that kind were conducted so far until this point, lacking the definitive proof for the application of these films MEMS devices.

SAM´s coatings have been considered as an excellent lubricant for MEMS application. SAM`s consist of a single layer of organic molecules formed on a substrate in liquid or gas phase that typically possess two important groups, one is chemisorbed onto a surface, and then the terminal group that stays located at the top of the SAM´s. With the proper selection of the terminal groups the properties of the surface can be altered [66]. The SAM´s coatings not only can present low friction at the micro and nanoscale [13, 67, 68], but they can also possess low surface energy, conferring low adhesion and anti-stiction properties to the surface [69, 70], gathering the required properties for contact MEMS applications. Patton *et al*. [71] tested octadecyltrichlorosilane (OTS) SAM´s coating on a MEMS electrostatic lateral motor performance over a wide range of RH (%). The coated devices were able to achieve higher lifetimes when compared to the uncoated ones, but eventually succumbed to the same failure modes, that is, excessive wear in dry environments and stiction under high RH (%) once the coating either degraded or was removed, exposing the bare Si surfaces. The wear resistance of the SAM was not reliable/durable enough for the intended application.

Thinking in a strategy for a more long-term protection, Eapen *et al*. [72] studied the of effect a PFPE (perflouropolyether) lubricant, more precisely, Fomblin Zdol®, in the same type of electrostatic lateral output motors. This type of lubricants are widely used in magnetic rigid disks to reduce the friction and wear of the head–disk interface [73]. Experiments conducted on Si showed that these lubricants also possess low stiction, low friction and improved wear durability properties, being in theory good candidates for MEMS applications [74, 75]. The main advantage of the Fomblin Zdol® compared to SAM´s coatings relies on the fact that the lubricant can be chemically bounded and physically adsorbed in a surface at the same time, acting the latter as mobile phase that can replace the chemically removed species during the operation thus increasing the lifetime of the motor. However, the Fomblin Zdol® lubricated tested motors by Eapen *et al*. [72] showed a considerable variation in terms of performance. Some devices would operate for 16 minutes, already showing wear marks, while others were stopped by the operator after 720 minutes without showing any signs of failure or wear. The author attributed this variation of lifetimes as results of non-uniformity converge of the coating.

The concept of lubricants based on both bond and mobile species kept on being investigated. Eapen *et al*. [76] tested a different system, this time using hydrocarbon-based lubricants, more precisely, 1-decanol and 1,7-heptadiol as bound species, and pentaerythritol ester, cyclopentane, Penzane and a polysilane as a mobile phase. All the tested system combinations, again in a electrostatic lateral output motors, were able to achieve a higher number of cycles when compared to uncoated motors, however, some systems, in terms of average performance were basically the same as the Fomblin Zdol®, exhibiting high deviation that could almost reach double values of the average lifetime. The very high deviations were attributed to formation of non-uniform coatings resulting from the dip method.

Satyanarayana *et al*. [77] tested the tribological performance of SAM´s coatings overcoated with a PFPE lubricant, while Ma *et al*. [78] tested SAM´s coatings overcoated with hydrocarbon mobile lubricant, multiply-alkylated cyclopentane. These approaches were tested in laboratory conditions using tribometers (tribotesters), and not on MEMS and or electrostatic output motors. Nonetheless, promising results were attained, SAM´s coatings overcoated with a PFPE lubricant showed an increase of 30% of wear life when compared to PFPE coated Si. The SAM´s overcoated with the multiply-alkylated cyclopentane presented lower friction and a higher load carrying capacity when compared to the SAM´s alone. Using a slightly different route, and with simpler molecules, such as 1-penthanol, Asay *et al*. [79, 80] showed that sidewall friction devices (a detailed description of the device can be found [80]) could be lubricated via molecular adsorption, achieving significant increase in terms of operation cycles (reached 11 days without signs of failure). The effectiveness of the vapor phase lubrication relies on its continuous replenishment. During sliding contact, the adsorbed molecules may be desorbed, however the presence of vapor pressure of the respective lubricants species allows the removed species to be immediately replaced. The vapor phase lubrication has the advantage of being able to produce conformal films in complex devices, unlike the other classical vapor depositions techniques such as CVD (chemical vapor deposition) and PVD (physical vapor deposition). However, as previously said, a vapor pressure of the lubricant must always be present, once it ceases to exist, the lubrication stops. This fact may not be compatible with some MEMS applications.

IL´s or, ionic liquids, are another type of lubricants that have been considered to minimize the MEMS tribological issues based on their good tribological performance at the macroscale [81-83]. An IL consists of a synthetic salt with a melting point below 100 ºC, being termed room temperature IL´s synthetic molten salts with melting points at or below room temperature [84, 85]. Nainaparampil *et al*. [86] had the merit of being the first researchers to test the tribological performance of an IL, more precisely, 1,2-dimethyl–3-butyl imidazolium hexafluorophosphate (DMBI-PF6), at the nanoscale using a lateral electrostatic output motor. The strategy used was again the one consisting on both chemical bound and mobile phase. The uncoated devices worked for 87 minutes while the coated ones 1373 minutes. However, a large standard deviation was observed concerning the lifetime of the motors, being attributed to the formation of non-uniform coatings as a consequence of the dip method. The nanotribological properties of the IL´s became a subject of a more intensive study. Palacio *et al*. [87] and Bhushan *et al*. [88] studied the friction, adhesion and wear properties, using an AFM, of two different liquids, 1-butyl-3-methylimidazolium hexafluorophosphate (BMIM-PF_6) and 1-butyl-3-methylimidazolium octyl sulfate (BMIM-$OctSO_4$). The coatings containing a mobile phase presented lower friction, lower adhesion and a higher wear resistance when compared to uncoated and monolayer coated surfaces, presenting promising results. However, all these results were compared to a PFPE lubricant, Z-tetraol, showing a better performance but not significantly. Nainaparampil *et al*. [14] developed a method based on a atomic force microscopy (AFM) with a liquid cell to study friction and wear properties of surfaces lubricated with IL´s and compared the results with electrostatic lateral output motors. A good correlation was found between the “relatively cheap” AFM approach results and ones attained from the electrostatic motors. However the tested IL´s in the electrostatic motors did not perform better than the previous tested one [86].

Graphene is a one atom thick carbon sheet which forms the basis of graphite [89], one of the most common and famous solid lubricants [90]. However, only recently the nanotribological properties of graphene started to be investigated, since the scientific community was more focused on exploring other properties such as mechanical, thermal conductivity and high electrical conductivity [91-93]. Lee *et al*. [94] performed the first nanotribological study and showed that the friction behavior of graphite and graphene are different, despite having the same surface morphology. Lee *et al*. [95, 96] also reported that friction coefficient decreases monotonically with the number of graphene layers, but this situation only occurs when the graphene is not strongly bonded to the surface, in that condition the opposite trend is observed [97, 98]. As far as the author knows, up to date, the nanowear properties of graphene were only studied by Lin *et al*. [99]. The multilayer graphene not only exhibit low friction, but noticeable wear was only found after 100 cycles with a normal load of 5 µN. It was proposed that the wear of graphene resulted from the rupture of the in-plan bounds due to the shear tress. More tribological research is definitely needed to fully understand the tribological properties of graphene at nanoscale. The graphene approach, up to date, has not been tested in MEMS devices or lateral output motors, but considering the fact that graphene deposition can be achieved via CVD method [100] and its promising tribological properties, it should not take long to test this material in MEMS. Other strategies have been developed to use graphene as a lubricant, combining previous mentioned approaches that have been tested in MEMS. For example, Pu *et al*. [101] formulated a nanocomposite based on a dispersion of graphene sheets in an ionic liquid on a silicon surface and Ou *et al*. [102] linked reduced oxide graphene sheets to silicon by means of APTES ((3-aminopropyl)triethoxysilane) SAM. In both situations better micro/nanotribological properties were attained when compared to the graphene, IL or SAM alone. Combing graphene with an IL and a SAM not only lowered friction, thus increasing the wear resistance, but also increased the load carrying capacity of the system.

The poor tribological performance of SAM´s, IL´s and PFPE is related to their inherent low durability during testing and or operation. For this reason, a number of hard coatings have been explored in order to minimize friction and wear of MEMS devices. These hard coatings share a common drawback, which are the high temperatures needed to the deposition. Nonetheless, very interesting results were accomplished. One of the most interesting studied hard coatings were the DLC´s (diamond-like carbon). DLC´s consist of amorphous carbon (a-C) or hydrogenated amorphous carbon (a-C:H) with an high metastable fraction of sp3 carbon bonding (diamond) generally prepared by depositions process [103]. The DLC´s coatings have the advantage of combining good mechanical properties such as, high hardness and elastic modulus, 10-80 GPa and 200-900 GPa respectively [104], with good tribological properties, namely, low friction and wear rates both against himself as well as against other materials [105-107]. Smallwood *et al*. [12] tested very thin DLC´s films, 5 nm and 15 nm respectively, in a electrostatic lateral motor. The results were indeed quite promising. The coated MEMS showed significant improvement over the uncoated MEMS in the different environments. In air operation the coated devices reached 15x more operation cycles. Eapen *et al*. [108] combined a DLC coating with a PFPE lubricant, Fomblin ZDOL.

The coating plus lubricant approach behaved essentially the same as the DLC or ZDOL alone. Despite the promising results, one must also consider the fact that using deposition techniques is difficult to achieve conformal films in complex devices. The idea of using DLC as a structural material was never been much deepened, the high level of residual compressive stress in the DLC films has limited the practical applications of these materials to thin film hard coating. Despite that limitation, Chua *et al*. [109] was able to fabricated the first ever diamond-like amorphous cantilevers, 1.2 µm thick, with a resonant frequencies of 108 MHz, the double of same size silicon cantilevers. Even harder coatings have been studied and considered for MEMS applications, more precisely diamond, due to diamond superior both mechanical and tribological properties. Krauss *et al*. [110] deposited ultrananocristalline diamond (UNCD), with a grain size between 2-5 nm, on Si and using etching techniques was able to deposit thin films and also form diamond structures such as strain gauges or “propellers”. Fu *et al*. [111] were able to fabricate more complex structures such as gears and microengines similar to those mention before in Si, but the author did not test them. The field of diamond deposition indeed seems quite promising, however, so far, little research has been placed on both nanotribological and surface properties of the UNCD [112], the form of diamond that seems more suitable for MEMS applications. A more intense research concerning this topic is definitely needed. Other coatings not as hard as the DLC or even diamond were also considered. SiC (silicon carbide) possesses both superior mechanical and tribological properties than Si, as well as better nanotribological properties [26]. Compared to Si, SiC also possesses better properties such as, high thermal conductivity, ability to endure higher temperatures, slow passivation rate. These properties combined with the fact that the SiC deposition is compatible with MEMS fabrication techniques, led researchers to use SiC as tool for harsh environments where Si cannot perform [113]. For example, SiC coatings have been used for protecting Si against erosion and acidic environments [114, 115]. Fleischman *et al*. [11] showed that structural SiC devices such as microactuators could be made. The devices actuated under low voltages, 30 V, and had resonant frequencies in the range of 20-60 kHz. More SiC complex devices such as electrostatic motors were fabricated by Yasseen *et al*. [116], and tested in harsh environments, more specifically up to 500 ºC, the limit temperature until which the devices showed a stable operation [117]. Another example of a SiC device that was tested at high temperatures was the capacitive pressure sensor by Young *et al*.[118], showing sensing capability up to 400 ºC. The SiC approach shows indeed quite promising results, however, the deposition temperatures are still quite high, which, on one hand, makes difficult to conciliate SiC with Si or other materials and also, on the other hand, the nanotribological behavior of SiC still needs more research before a serious implementation. Mani *et al*. [119] tested the effect of a thin conformal W film by CVD, around 20 nm, on the microengines performance and compared the results against non-coated devices. The results were very surprising, while the uncoated devices operated only for an average of $4x10^5$ cycles, the coated ones achieved $2x10^6$ cycles. In some cases, motors were able to run until $1x10^9$ cycles without showing any signs of wear. Using ALD (atomic layer deposition) other authors were also able to form conformal hard thin coatings on complex devices. ALD is a chemical vapor deposition process that uses self-limiting surface reactions that can lead to atomic-layer controlled growth [120, 121]. Mayer *et al*. [122] deposited a 10 nm conformal film of Al_2O_3 on a microengine, showing that this deposition method is suitable for MEMS applications. Although the coated engines were not tested, preliminary results of the 10 nm coatings show low friction sliding against Si_3N_4 ball (≈0.3) and less wear debris formation when compared to the native-silicon oxide. Ashrust *et al*. [123] characterized a 10 nm film of TiO_2 using the same deposition technique. The TiO_2 film was harder and had a much smaller value of work of adhesion when compared to Si. The tribological response of the films was characterized using a side wall friction apparatus. The coated devices reach higher lifetimes when compared to the uncoated ones, and also against coated TiO_2 with a SAM deposited by vapor deposition. TiN hard thin films also have been considered. Although never tested in MEMS-like applications, the laboratory results, concerning both mechanical and tribological characterization at the micro/nanoscale show a great improvement comparing to bare Si [124, 125], proving to be an available option for further investigation.

Polymeric materials have also gained a wide acceptance in the MEMS, specifically in the BioMEMS and Microfluidic fields, where fluid transport and analysis are critical. Unlike Si, polymers have the advantage of being not only biocompatible, but also cheaper and compatible with simpler fabrication techniques [126, 127]. The investigation of polymers for BioMEMS and Microfluidic MEMS applications carried scientists to think of the possibility of coating Si or even substituting it in other MEMS applications. Tambe *et al*. [128, 129] studied that possibility, and performed a micro/nano adhesion study as well as the micro/friction of two polymers, PMMA (Polymethylmethacrylate) and PDMS (Polydimethylsiloxane) coatings. Comparing to Si, the polymer coatings presented a set of superior properties, namely, were more hydrophobic, with lower values of adhesion and also independent adhesion relative to both rest time and HR (%) and finally lower values friction coefficients at both micro and nanoscale. Another polymer considered for MEMS applications was the widely used photoresist SU-8 [130]. The SU-8 as a material, presents adequate surface properties for MEMS applications, low surface energy, high contact angle and low values of nanoscale adhesion [131], however presents poor tribological properties, high friction and wear rates [132]. Some efforts have been placed towards improving the SU-8 tribological response, for example, Jiguet *et al*. [133] reinforced SU-8 with SiO_2 nanoparticles, achieving higher elastic modulus and fracture toughness as well as lower wear rates while Singh *et al*. [134] tested a system of SU-8 plus PFPE lubricant, increasing the wear resistance by 10^3 cycles, using high loads. Saravanan *et al*. [132] formed a composite of SU-8 with PFPE and study the effect of incorporation of SiO_2 paricles, CNT´s (carbon nanotubes) and graphite. The incorporation of the PFPE lubricant in the SU-8 was able to reduce the friction coefficient from values of 0.82 to 0.11 or even smaller and increased the wear resistant 3 to 4 orders of magnitude. Another polymer was also considered. Satyanarayana *et al*. [135] studied the tribological performance of ultra high molecular weight polyethylene (UHMWPE) coated with PFPE lubricant. Again a great reduction in the friction coefficient was observed sliding against silicon nitride, from 0.6 to 0.08, as well as an increase of wear resistance. Tai *et al*. [136] reinforced UHMWPE with oxidized graphene (until 3%) and verified that the friction coefficient barely changed, however the wear rate decreased by 40%. Most of the tribological characterization of the polymeric coatings approach was carried out in laboratory under experimental conditions that are quite distant from the ones used in MEMS devices. Another drawback may rely on the mechanical properties, although the reinforcement strategies were able to increase them, the final value still may not be the most fit for contact-based operation MEMS.

2.1.5 PHYSICAL METHODS

The physical methods consist on performing topographical changes in a surface. These approaches have not been so extensively studied as the previous mentioned chemical methods. Nonetheless, a significant number of interesting results have been achieved, being worth to be mentioned.

The inspiration for surface texturization arose from nature´s lotus leaf and the so called famous lotus leaf effect [137]. The high roughness of the lotus leaf combined with a wax coating promotes a water repellent behavior, rolling off water from the surface. The roughness is key parameter for controlling the wettability. When water contacts with a rough surface it may assume either of two possible regimes [1], the homogeneous wetting, when the liquid establishes full contact with the surface grooves –Figure 4a); and heterogeneous wetting when air is trapped between the liquid and the grooves of the rough surface – Figure 4b).

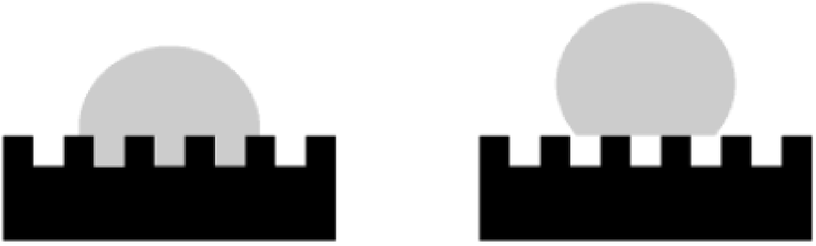

Figure 4. (a) A drop of water in full contact with the surface, according Wenzel model, (b) a drop of water in contact with both air and surface, according with Cassie-Baxter composite model.

According to Wenzel [138] analysis, the apparent contact angle in the homogenous regime, Figure 4a), can be express by

$$cos\theta^{w} = r_r cos\theta, \qquad \text{(Eq.1)}$$

where θ^{W} is the contact angle of the rough surface, θ the contact angle for the smooth surface and r_r the roughness ratio, defined as the ratio between the real and projected areas of the surface. If the θ is higher than 90 º, the roughing will increase the contact angle whereas the exact opposite happens in the case of θ being inferior to 90 º. For the heterogeneous case, the apparent contact angle can be calculated by using the Cassie - Baxter equation [139]

$$cos\theta^{CB} = -1 + \varphi_s(1 + cos\theta), \qquad \text{(Eq.2)}$$

where θ^{CB} stands for contact angle of the rough surface, φ_S the fraction of solid in contact with the liquid, and θ the contact angle in the respective flat surface. For this model small values of φ_S will generate a larger increase in the measured contact angle. Another important aspect is that since φ_S is always smaller than 1, unlike the previous model, the Cassie-Baxter model always predicts an increase of the contact angle independently of the value of θ [140]. Texturing a surface will enable to control the wetting behavior of a surface. The reduction of the wetting is important since it also reduces the menisci formation, hence minimizing the capillarity adhesion. On the other hand, roughening a surface will have, at the same time, the advantage of minimizing the Van der Waals attraction between contacting surfaces, as it can be seen in the following equation [141]

$$F_{vdw} = -\frac{HA}{6\pi z^3}, \qquad \text{(Eq.3)}$$

where is possible to see that the van der Waals forces are proportional to the shared area A, being H the Hamaker constant express in J, and z the separation distance between the two flat surfaces.

The texturization route was initially tested in Si. The texturization was achieved by different etching techniques [15, 57]. The results reported by Yeen *et al.* [15] showed that by forming a honeycomb-shaped grains in the surface, the work of adhesion was to be reduced by a factor of 20, according to his model, for a structured surface containing holes around 300 nm deep, measured by SEM analysis. Even though this specific value presents itself as big reduction, it is not very impressive if it is compared against SAMs OTS coatings on SiO_2 surface, where a reduction of the work of adhesion of factor of more than 1000 can be achieved [70]. Sundararajan and Bhusahn [142] published for the first time roughness parameters values of different areas of micromotors, using atomic force microscopy. The root mean square (RMS) values reported varied from 19 nm to 21 nm and the peak-to-valley distances ranged from 80 nm to 250 nm depending on the region where the measurements were done. The authors verified that silicon surfaces that were exposed to several etching steps during fabrication process presented higher values of both RMS and peak-to-valley distances when compared to surfaces that were covered and only released in the final stage of the fabrication. Since in that specific case of the studied micromotors, the contacting interfaces were only placed in contact at the very end of the process, this fact suggests that high friction values observed arise from the large real contact areas, as a result of the lower values of roughness of the surfaces, thus showing the importance of this parameter. Using deposition techniques some authors were able to structure different patterns on a a-Si film, deposited over a thermally oxide on a Si wafer, and characterize the respective nanotribological behavior. Zou *et al.* [16] formed dendrite shaped-like Si crystallites with an average roughness value of 27.7 nm, a value close to the ones measured in the micromotors [142]. The textured surface presented not only smaller values of adhesion but also smaller values of friction coefficient, for a wide range of forces, namely, from the few µN until close to 500 µN. Nair *et al.* [143] formed nano-textures consisting of sharp irregular nanopillars of poly-Si (111) with 200 nm and 400 nm in height. The structured surfaces like the previous mentioned ones, showed the benefits of the texturization. As a consequence of the contact area reduction, both adhesion and nanotribological properties were improved. However, one must take in consideration the fact that these improvements were achieved under laboratory testing conditions, using a triboindenter, thus quite distant from the real conditions on which contact based-MEMS are supposed to operate, making to some extend difficult to address how advantageous these approaches may in fact really be.

2.1.6 CHEMICAL AND PHYSICAL METHODS

The chemical/physical approaches are characterized by combining both changes in the surface properties as well as topographical changes, therefore combing some of the already mentioned strategies.

One of the easiest strategies to achieve such end was tested by Houston *et al*. [144], using a NH_4F surface treatment. The NH_4F solution not only has the ability to texture Si but at the same time also leaves the surface covered with Si-H bonds. Although the final surfaces were not hydrophobic, presenting a contact angle of 74º, the surface treatment was able to greatly reduce the work of adhesion of the surface, measured using cantilevers. However the surface was not stable, in air in contact with water vapor and oxygen, the surface native oxide grows loosing the and Si-H terminations, and the respective properties.

Surface texturization studies combined with chemical surface changes have been made with the point of minimizing menisci formation and, therefore, capillarity adhesion. Nunes *et al*. [17] textured Si using a femtosencond laser, roughening the surface at the micro and nanoscale. The final microstructure is formed by “worm” shaped-like features, with 3-5 µm of size, divided into smaller scale roughness of 700-800 nm perpendicular relative to the long axis of the “worm” pattern, as it can be seen in Figure 5. After the laser treatment, the samples were cleaned using the RCA (Radio Corporation America) procedure [145], which contains HF and enables the removal of the excess of debris formed during the laser treatment. The initial measured wettability angles varied from 110º to 135º. However, it was also shown that the angles were not stable with time, in fact, after a period of 20 h, upon the last HF cleaning step, the contact angle stabilizes in value close to ≈ 80º - Figure 6. This behavior was attributed to two different phenomena that occur at the same time. The Si–H groups present in the surface, due to HF, are not stable with time and tend to disappear, as the native oxide layer grows back again and hydrophilic Si-OH groups are formed, causing a decrease in the contact angle value. The measured 80º contact angle value, after 20 h, essentially corresponds to the single effect of the texturization, since the surface is most likely as much as hydrophilic as it was initially, prior to both laser and HF treatments. The initial contact angle for the Si <100> was around 33º, which tells one that the laser treatment was able to double the initial contact angle.

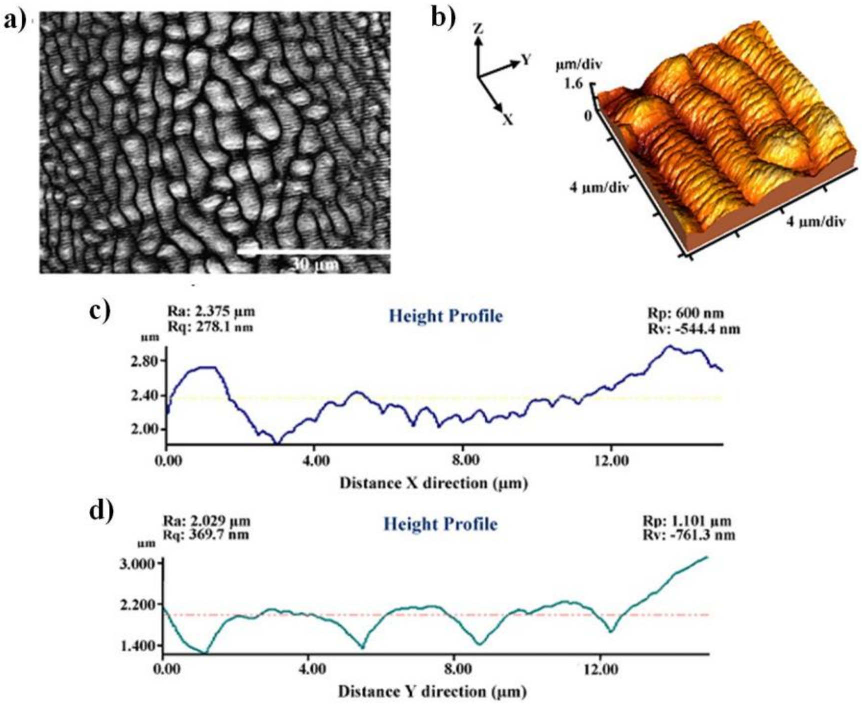

Figure 5.Si surface after a femtosecond laser processing (a) SEM micrograph of the global microstructure, (b) a detailed AFM image of the (a) image with a size 20x20 µm^2, (c) profile in the X direction of the (b) image, (d) profile in the Y direction of the (b) image. Image adapted from [17].

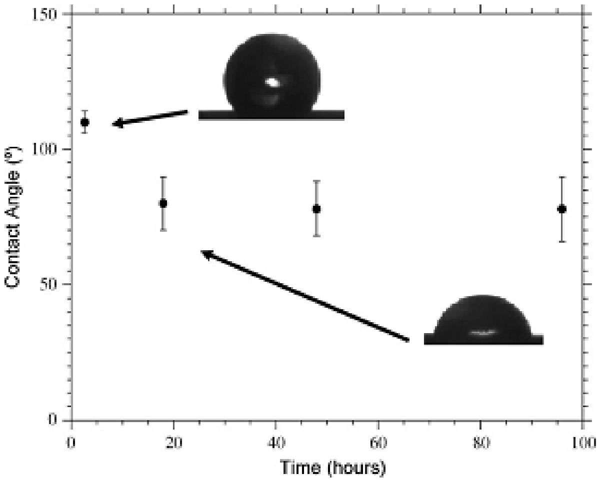

Figure 6. Evolution of the water contact angle on femtosecond laser treated Si samples during the four days after cleaning with the acid solution [17].

Cao *et al*. [146] performed nano/micro-texturing in Si using a variety of different consecutive steps, that evolved photolithography, DRIE (deep reactive ion etching) and wet etching with both HF and KOH. Cao *et al*. were able to achieve superhydrophobicity, that is, contact angles superior to 150º, with Si-H terminated surface due to HF cleaning steps. Looking for more stable surfaces, silicon have been pattern/textured by laser [140], anisotropic etching [147] and aluminum induced crystallization of a-Si and immediately coated afterwards by a low surface tension coating, typically a SAM coating, were not only able to achieve significantly high contact angles, in the order of 150º-160º, but also more stable with time.

Concerning the tribological performance of these textured and coated samples little has been made so far. Song *et al*. [18] tested the adhesion and microfriction properties of textured a-Si surface by aluminum induced crystallization coated with an OTS SAM coating. The a-Si features ranged from a size of 100 nm to 400 nm in height. The adhesion of the samples decreased as the water contact angle increased, and the values of the friction coefficient were always smaller when compared to the reference, the flat Si SAM coated sample, for all the tested normal loads, ranging from 200 µN to 1.5 mN. Shafiei *et al*. [148] replicated the lotus-leaf pattern on a electrodeposited nanocrystalline nickel surface, and with further deposition, formed new structures with 6 µm in height. Shafiei *et al*. verified that the structured surfaces presented initial lower dynamic friction coefficients values when compared to the flat surfaces. The explanation relies on the fact that the surface structures prevent the accumulation of wear debris at the interface. The lowest friction coefficients were attained for structured surfaces coated with a PFPE. The Ni surfaces were tested with a high normal load, 1 N, and reveal themselves quite promising, worth being explored at smaller scales.

Dual surface modifications have been performed on Si with the advantage of using MEMS compatible fabrication techniques such as lithographic and deep reactive ion etching. Regular patterns were formed on the surface, like pillars or channels, and then posterior coating of the textured surface with DLC or Z-DOL® coating [149, 150]. The micro/nanotribological characterization of the textured surfaces without any additional coating already presented much lower adhesion and friction coefficient values as a result of the decrease of the real contact area and consequent debris removal from the sliding interface, the latter effect being observed for higher loads in the mN range [150]. The additional coating of the surfaces enabled them to become hydrophobic and at the same time to lower the adhesion and friction coefficient values of the textured samples.

Polymeric surfaces have also been patterned. This can also be considered as dual surface modification since the pattern is performed on a polymeric film that coats Si. Singh *et al*. [151, 152] for example, studied the microtribological performance of different patterned PMMA films that consisted of reproductions of the lotus and colocasia leaf structures. The tribological characterization showed that the leaf replicas, with structures in the range of microns, presented lower friction coefficients when compared to the non-pattern film or Si. Other authors patterned and characterized PMMA and also other polymers such as polyurethane acrylate (MINS) and polystyrene (PS) with regular pillars structures, coating them afterwards with a SAM coating. The triple surface modification enabled to attain the lowest values of both adhesion and fiction coefficients, at the nanoscale, and at the same time, the highest contact angles [153, 154]. SU-8 coatings on Si have also been subjected to patterning and lubrication with PFPE [155-157]. The final results corroborate again the benefits of the triple surface modification. The tribological performance of the coatings was greatly improved, however it is important to standout that both coating thicknesses as well as the loads tested are still quite far from the ones required for MEMS applications.

2.2 ION IMPLANTATION: A TOOL TO TAILOR SURFACE PROPERTIES

The surface properties of a certain sample can be altered through the ion implantation technique. This specific method was deliberately not included in the above chapters, that is, in the chemical or physical methods for two reasons. The first reason is based on the fact that depending on the implantation conditions different properties can be changed. For instance, on one hand, calcium implantation on titanium alloys can improve the osseointegration on femoral implants [19], which can be considered a chemical change, while on the other hand, conical structures have been formed by high fluences implantations ($1x10^{16}$ to $2.8x10^{18}$ cm^{-2}) of cobalt on Si, SiO_2 and Si_3N_4 samples, tilted 30º, which can be considered physical-chemical change since both topographic and chemical changes occurred at the same time on the surface [20]. The second reason is based on the fact that ion implantation is the main technique used in the present thesis, thus being of relevant importance to reference the most important works published until this point regarding the optimization of the mechanical, tribological and wettability properties of Si by this method. These studies are summarized in Table 2 with the respective results achieved by other authors regarding the implantation of different elements into Si. Most of the presented studies were conducted with the specific objective to enhance the tribo/mechanical properties of Si for MEMS applications while a few others although conducted with different objectives were also considered by the author since involved both implantation and characterization.

The studies in Table 2 are presented in a chronological sequence starting from the mid 1980´s and finishing in 2009 thus showing 21 studies for a period of almost 3 decades. As far as the author knows up to date no tribological studies were performed concerning ion implantation with contact-MEMS operating devices unlike other mentioned approaches such as SAM´s or DLC´s. These facts enable to see that the ion implantation route for MEMS applications has been somehow relegated to a secondary plane. An important work developed by Nakano *et al*. [21, 22] showed that the ion implantation process combined with substrate etching can be used for MEMS and structures fabrication. Nakano *et al*. were able to fabricate a “mesh-like” structure as well as a cantilever by first implanting Si with different elements like Au or Ti, with high energies (MeV range) and fluences, through a mask with the pretended shape, etching afterwards the surrounded implanted zone with KOH. The etch rate is fluence dependent.

The present thesis aims to use ion implantation for the purpose of optimization of both micro/nanotribological and wettability properties of Si for MEMS/NEMS applications. With this in mid different species from the ones implanted until now were tested with the intention of adding valuable significant new data to the one existing already. Along the thesis and in the part of the analysis and discussion of the results, the results obtained in the present thesis will be compared or interpreted on the basis of the previous work. Therefore no further comments to the previous works on ion-implantation will be made at this point.

Table 2. Compilation of studies performed by ion implantation on Si to improve the mechanical, tribological and wettability properties with the respective attained results.

Element, Energy (keV)	**Φ ($x10^{17}cm^{-2}$)**	**Results**	**Reference**
N_2^+, 90	1-8	HV(Si)= 2000, HV(N_2^+) = 1300, from $4x10^{17}$ fluences on	Burnett [158]
C^+, N^+, 70	2	μ(Si)= 0.8, μ(C^+,N^+)= 0.1*	Brunei [159]
Ar^+, 70	1	μ(Si)= 0.9-1 to μ(Ar^+) = 0.3 in vacuum, μ(Si) = 0.7 to μ(Ar^+) = 0.55 in atmosphere conditions	Lekki [160]
C^+, 100	2	Decrease in the removed volume of 20-40%, nanowear tests	Miyamoto [161]
Ar^+, B^+, C^+, N_2^+, 70-200	0.05-5	μ(Si) ≈ 0.75, μ(Ar^+) ≈ 0.75, μ(N_2^+) ≈ 0.75, μ(N_2^+) ≈ 0.75, μ(B^+) ≈ 0.08, μ(C^+) ≈ 0.08 k(Si) ≈ 10^{-4} – 10^{-5}, k (Ar^+) ≈ $5x10^{-6}$, k (N_2^+) ≈ $6.5x10^{-6}$, k (B^+) ≈ $5.7x10^{-7}$, k (C^+) ≈ $5.1x10^{-7}$ mm^3/Nm	Gupta [162]
B^+, 200	0.05-5	10-15% increase of Hardenss, μ(Si) = 0.8 to μ(B^+)= 0.05, wear factor from $1.2x10^{-4}$ to $1.2x10^{-7}$ $mm^3N^{-1}m^{-1}$	Gupta [163]
C+, 100	1	H(Si) = 11.7 GPa, μ(Si)= 0.03, H(C^+) = 18 GPa, μ(C^+) = 0.02 and better nanotribological performance	Bhushan [164]
O^+, N_2^+, As^+, Ar^+, 200	0.1-5	O^+, N_2^+, increase the hardness as well as the resistance to deformation. As^+, Ar^+, decrease both hardness and deformation resistance	Gupta [165]
N^+, 35-150 vs 100	2.5	Significant wear resistant was achived by multiple energy implantation, when compared to Si or single energy implantation	Miyamoto [166]
C^+, N^+, 60	4-8	Better tribological performance of C^+ implanted samples when compared to the N^+ and (C^++N^+)	Kodali [167]
Ar+,250-1250	0.0005-5	E(Si) = 160 GPa, E(Ar) ≈ 125 GPa	Szabadi [168]
Ar^+, 3	0.18	More hydrophilic samples, whose contact angle increase with time in both air and Ar+ enviorment	Chassé [169]
C^+, N^+	3-6	H(Si) ≈ 12 GPa, θ(Si) = 51.9 º, H(C) ≈ 14.5 GPa, θ(Si) = 72.1 º, H(N) ≈ 13.2 GPa, θ(N) = 85.9 º	Ueda [170]
Si^+, 400	-	H(Si) ≈ 11GPa, H(Si^+) ≈ 9 GPa	Williams [171]
Si^+, 300 and 100	0.03	E(Si) ≈ 168.4 GPa, E(Si^+) ≈ 136 GPa. Results achieved by nanoindentation combined with finite element modeling	Follsteadt [172]
Ar^+, 110	0.005-5	Highest values of H and E achieved for the $1x10^{14}$ cm^{-2}. Better tribological performance starting from $1x10^{15}$ cm^{-2} fluence, with exception of the highest fluence, $5x10^{17}$ cm^{-2}.	Sun [173]
N^+	Not specified	Lower contact angles compared to the reference for all tested conditions	Wan [174]
Cr^+, 100	0.05-1	Lower values of H, E and higher nanofriction coefficients	Mishra [175]
N^+,100 and 300	-	θ(100 keV) = 57.3 º, θ(300 keV) = 46.2 º. Increasing the energy causes the hardness to increase	Fang [176]
Ar+, C+, N, Ne, 100	0.05-0.1	Only Ar did not increase both H and E. Only Ne did not increase the nanoscrath resistance	Xu [177]

* Implantation occurred at the same time as carbon layers are being deposited by controlled vacuum carburization.

2.3 TRIBOLOGICAL PRINCIPLES

2.3.1 SURFACE ROUGHNESS AND ROUGHNESS PARAMETERS

A solid surface, or more exactly a solid-air interface, regardless of the respective formation method, contains certain irregularities or deviations from a prescribed geometrical form. The high points on a surface are commonly designated to as asperities, peaks, summits or even hills while the low points are designated to as valleys [178], as it is represented in Figure 7a).

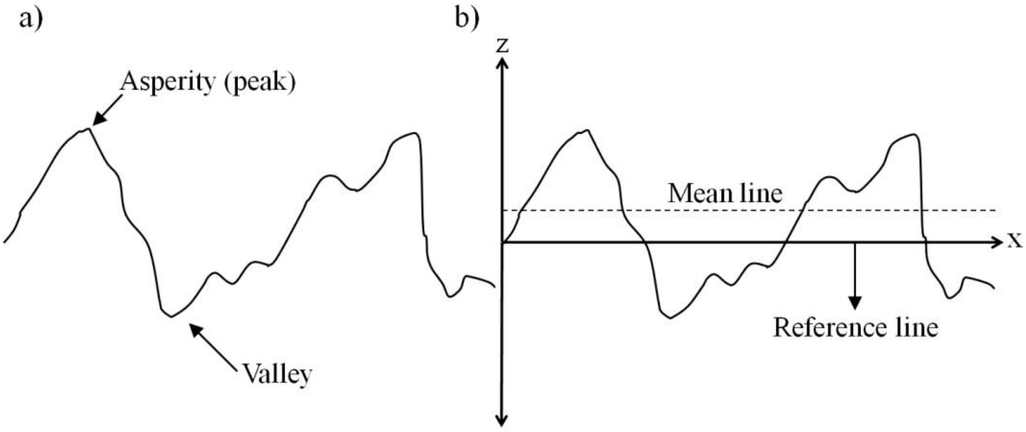

Figure 7. (a) schematic diagram of a rough surface, (b) schematic of a surface profile z(x), adapted from [178].

Surface roughness is normally associated to the variation in the height of the surface relative to a reference plane. It is measured either along a single profile or along a set of parallel line profiles, therefore constituting a surface map [178]. The surface roughness is commonly represented by three different parameters: average roughness or R_a, root-mean-square roughness (RMS) or R_q and the maximum peak-to-valley height or R_t [179].

Considering a surface profile, z(x) in which the profile heights are measured from a reference, as illustrated in Figure 7b), and where also the mean line, is represented, a line which divides the profile in equal areas above and below, both R_a and R_q roughness parameters can be calculated by the following expressions [178]:

$$R_a = \frac{1}{L_g}\int_0^{L_g} |z(x) - m_L| dx, \qquad \text{(Eq.4)}$$

m_L being expressed by

$$m_L = \frac{1}{L_g}\int_0^{L_g} z(x)dx, \tag{Eq.5}$$

and

$$R_q = \left(\frac{1}{L_g}\int_0^{L_g} (z(x))^2\, dx\right)^{\frac{1}{2}}, \tag{Eq.6}$$

respectively, being L_g the sample profile length and m_L the mean line. The maximum peak-to-valley distance or R_t parameter can be easily calculated by subtracting to maximum height of the profile the minimum one [179]

$$R_t = \max\big(z(x)\big) - \min\big(z(x)\big). \tag{Eq.7}$$

2.3.2 CONTACT BETWEEN SURFACES

The contact between two nominally flat solid surfaces, that are gently brought together, is first initiated by the highest of surface asperities. As the load (normal force) increases, an increment of the number contacts will occur as a result of more asperities being forced to come into contact, between the two surfaces [180]. The real contact area A_r, established upon contact, can be calculated by performing the sum of all areas of the respective contacting spots while the frequently designated term, nominal area A_n, corresponds to a conceptual area, that assumes two perfectly smooth contacting surfaces [181]. A schematic representation of two contact surfaces as well as of the latter mentioned concepts can be observed in Figure 8.

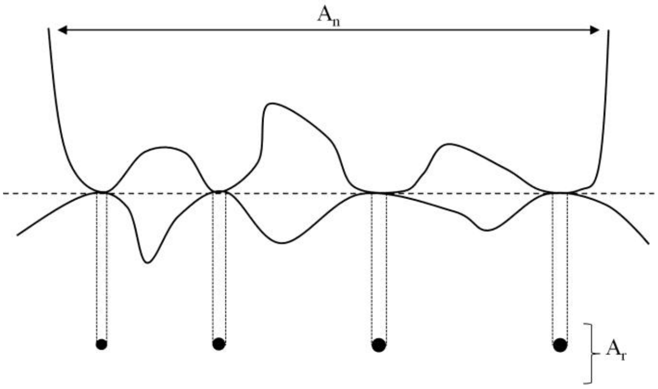

Figure 8. Schematic representation of an interface between two contacting solids surfaces where both real and nominal areas can be identified by A_n and A_r, respectively. Adapted from [180]

The contact of real surfaces is truly of complex nature. The contact is established by a large number of asperities that have different sizes and shapes that come into contact with the increasing of load. All these aspects bring extreme difficulties to address the topic thus being usual to perform some simplifications, for instance, it is common to consider the asperities to have a spherical shape. In the following sections of the thesis the simplified contact of single asperity will be addressed followed by the more complex case of multi-asperity contact.

2.3.2.1 Single asperity contact

The elastic contact between two solids, namely a sphere that represents an asperity and a plane, was first studied by Hertz [182]. According to Hertz, when a sphere summit is brought in contact with a flat surface with a determined load L, Figure 9, both surfaces deform to create a circular contact zone with a radius a_C, which is given by [183]

$$a_C = \left(\frac{3Lr}{4E_R}\right)^{1/3}, \qquad \text{(Eq.8)}$$

where r represents the radius of the sphere and E_R the reduced Young´s contact modulus of the two contacting materials given by

$$E_R = \left(\frac{(1-\nu_S^2)}{E_S} + \frac{(1-\nu_P^2)}{E_P}\right)^{-1}, \qquad \text{(Eq.9)}$$

where the subscripts S and P, designate both sphere and plane, and υ and E are the corresponding Poisson’s ratio and elastic modulus. The contact area, for this geometry, can be then easily calculated in the following way

$$\pi(a_C)^2 = \pi\left(\frac{3Lr}{4E_R}\right)^{2/3}, \qquad \text{(Eq.10)}$$

where is possible to observe that the area A, is $\propto L^{2/3}$. The elastic displacement between the two bodies is not uniform over the contact area, reaching the maximum value, h, precisely at center - Figure 9. The maximum displacement h, can be determined by [183],

$$h = \frac{{a_C}^2}{r} = \left(\frac{3L}{4E_R r^{1/2}}\right)^{2/3}. \tag{Eq.11}$$

and is related to the applied normal load L by the following expression[184]

$$L = \frac{4}{3} E_R r^{1/2} h^{3/2}. \tag{Eq.12}$$

The mean contact pressure exerted on the contact area, σ_m, can be calculated by dividing the applied load with the respective contact area,

$$\sigma_m = \frac{L}{\pi\left(\frac{3Lr}{4E_R}\right)^{2/3}} = \left(\frac{16LE_R^2}{9\pi^3 r^2}\right)^{1/3}. \tag{Eq.13}$$

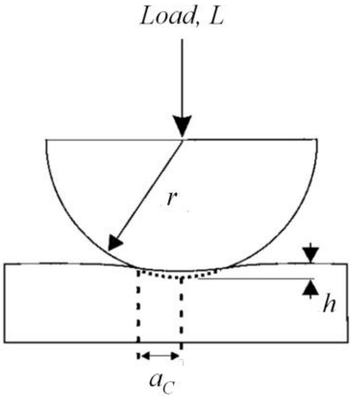

Figure 9. Schematic representation of the elastic contact of sphere with radius r, pressed with a load L against a smooth plane, where is also represent the respective contact radius a_C and maximum displacement h, adapted from [183].

The normal stress is not uniform over the established circular area of contract. The maximum contact pressure, σ_{max}, is reached at the center of the contact, having a value of 3/2 σ_m, falling to zero at the edge of the contact Figure 10a). The normal stress is compressive inside the contact areas changing to tensile outside. In opposition to what happens to the normal stress, the maximum shear stress, τ_{max}, is not located at the surface of contact, but rather a distance of $0.47a_C$ below it, as it can be seen in Figure 10b) and Figure 10c), where it reaches a value of 0.47 σ_m or, 0.31 σ_{max}, for a material with a 0.3 Poisson´s ratio [184].

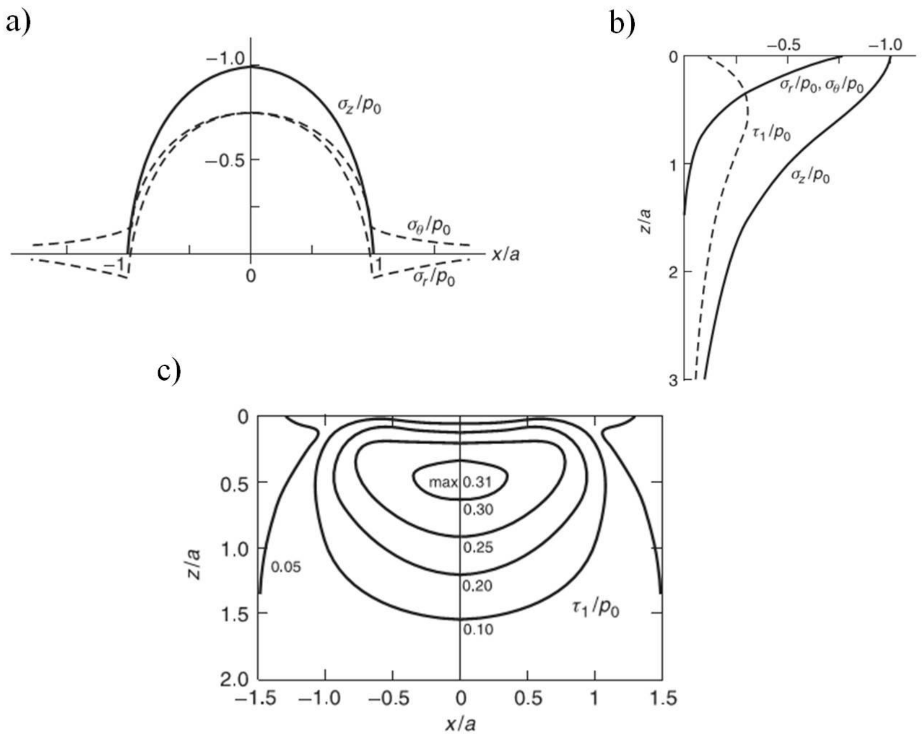

Figure 10. a) Stress distribution (σ_R, radial stress, σ_θ, angular stress and σ_Z normal stress in the *z* direction) at the surface of a plane induced by loading with a sphere and (b) under surface along the *z* axis, being τ_1 the main shear stress related to normal components by $\tau_1=|\sigma_Z - \sigma_\theta|$, c) contours of the principal shear stress τ_1 under surface. All stresses are normalized to normal stress, P_0; and the z and x axis normalized to the contact radius *a*, adapted from [180, 181].

In a situation where the load is increased beyond the elasticity limit, the asperities will plastically deform and plastic flow will occur at the contact. Assuming that the yield Tresca´s [185] criterion is applicable, the yield will occur when the maximum shear stress, τ_{max}, reaches a value of $\sigma_Y/2$, being σ_Y the uniaxial yield stress. Since the τ_{max} is equal to 0.47 σ_m, the plastic deformation will therefore initiate below the surface when the mean contact pressure reaches a value of $1.1\sigma_Y$. The plastically deformed created zone will be encapsulated by elastically strained material that will expand in close to a radial way by further increase of the normal load. In the limit situation, the plastic deformed zone will meet the surface, forming a fully plastic contact, being the mean contact pressure in this situation ≈ $3\sigma_Y$, remaining essentially constant even if the normal load keeps increasing [184]. The independence of the mean contact pressure, σ_m, from the normal load once a full plasticity is reached, allows to define the indentation hardness of the material, given by [184]

$$H_i \approx 3\sigma_Y, \qquad \text{(Eq.14)}$$

a relation known in the literature as Tabor law [186]. A schematic representation of both onset of plastic deformation and fully plastic contact can be observed in Figure 11, where the roles have been inverted, that is, the sphere is rigid and the plane deforms.

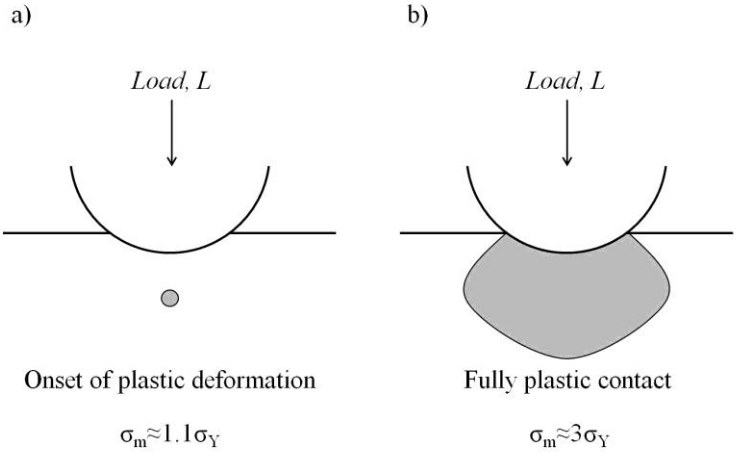

Figure 11. Schematic representation of a spherical asperity in contact with a body plane, a) beginning of plastic deformation at the maximum shear stress point b) fully plastic contact situation. Adapted from [187].

2.3.2.2 Multiple asperity contact

As previously said, the contact between real surfaces is of complex nature, being established by multiple asperities of different sizes and shapes that may undergo elastic or even plastic deformation. One of the most used statistical theories for the study of the contact of rough surfaces is the Greenwood and Williamson model [188], from now on abbreviated as GW, developed in 1966. The GW model is based on two assumptions/simplifications, which are the following:

- All asperities have spherical surfaces with the same radius, r_{asp}
- The asperities will elastically deform according to Hertz equations.

An example of a rough surface in contact with a rigid plane is illustrated in Figure 12. Considering that the height of an asperity above the reference plane has a values of z, and that the distance from surface to that same plane has a value of d, for a situation of $d<z$, the highest asperities will be under elastic deformation, according to the GW model and Figure 12.

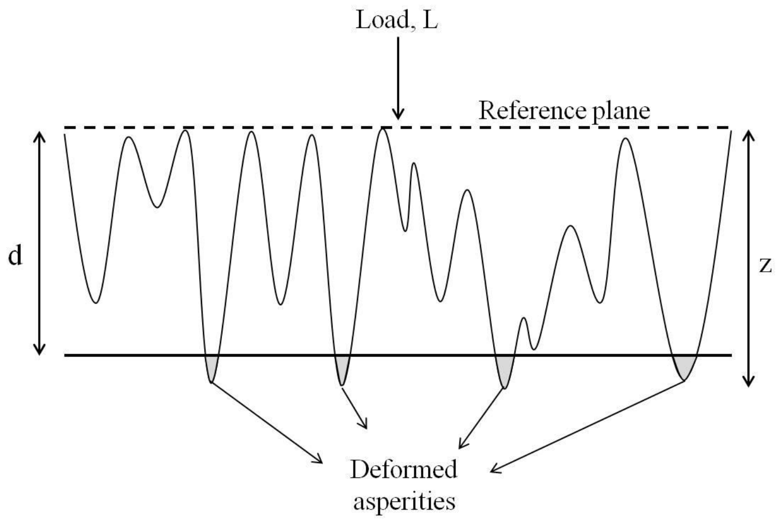

Figure 12. Schematic representation of a rough surface against a plane body by a load *L*, the grey zones indicates the deformed asperities.

The normal load that an individual asperity supports upon compression, according to the Hertz model, is given by the following expression [184]

$$L_A = \frac{4}{3} E_R r^{\frac{1}{2}} (z - d)^{\frac{3}{2}}. \qquad \text{(Eq.15)}$$

Assuming that the asperities heights can be described by a probability density function *P(z)*, the total number of asperities, n_A, that are elastically deformed for a given *d* (<*z*) can be calculated using the following expression

$$n_A = N_A \int_d^{\infty} \mathrm{P}(z) dz, \qquad \text{(Eq.16)}$$

being the N_A term the total number of asperities of the surface. The total load carried by all the asperities elastically deformed can be estimated using the two previous equations

$$L = \frac{4}{3} N_A E_R r^{\frac{1}{2}}. \int_d^{\infty} (z - d)^{\frac{3}{2}} \mathrm{P}(z) dz. \qquad \text{(Eq.17)}$$

Grenwood and Williamson solved the above equation using two different probability density functions, namely exponential and Gaussian, and realized that the real contact area is linearly proportional to the load for the exponential distribution and nearly linearly proportional for the Gaussian case. This situation is different from the single asperity case, where it was shown that the contact area is proportional to $L^{2/3}$ [184].

Despite being based on purely elastic contact, the GW model also allows one to predict the onset of plastic deformation of the contacting asperities. The proportion of asperities on contact that are subjected to plastic deformation depends on the plasticity index, Ψ, that is independent of the load, and can be calculated by the following equation [184]

$$\Psi = \frac{E_R}{H_i}\sqrt{\frac{\sigma^*}{r_{asp}}}, \qquad \text{(Eq.18)}$$

being H_i, the indentation hardness of the rough surface and σ^* the standard deviation of the distribution of the asperities heights. In a situation of $\Psi < 0.6$, the plastic flow of the asperities will only occur at very high values of nominal loads, whereas for $\Psi > 1$, the exact opposite occurs, that is, the asperities will be plastically deformed under the lightest of the loads.

2.3.3 ABRASIVE WEAR

The interaction between two contacting surfaces through sliding, rolling, or even impact, while in motion relative to one another, may lead to surface damage or material removal events, commonly known as wear. Wear can be classified in different types, essentially depending on the mechanism by which the material is removed. The main different types are: adhesive, abrasive, corrosive and surface fatigue. Other types of wear such as, fretting, erosion and cavitation can also occur. These latter types of wear do not represent themselves as distinct mechanisms of material removal, but rather a combination of adhesive, abrasive or corrosive wear mechanisms [180].

Abrasive wear occurs when the asperities of a hard rough surface, or hard particles encrusted on a surface, slide against a softer material, forming scratches by material removal. It may also occur as a result of a material removal or displacement from the contacting interface, generating wear particles that are free to roll and slide, a situation described in the literature as *three-body abrasive wear* [184].

A simple model to describe abrasive wear has been proposed by Rabiowickz [189], on which a hard conical asperity, sliding with a velocity V, promotes material removal of a soft smooth surface of hardness Hi. A schematic representation of the abrasive wear can be seen in Figure 13.

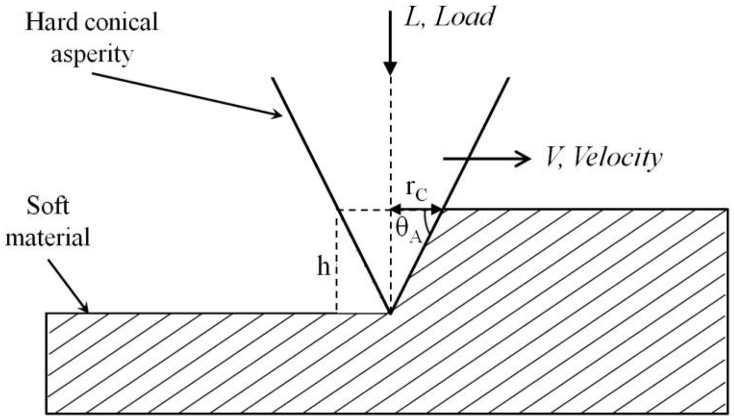

Figure 13. Schematic representation of abrasive wear where a hard conical asperity slides against a soft material.

The wear rate induced by the conical asperity on the soft material, defined as the total removed volume, dV_R, divided by the respective traveling distance, can be calculated by

$$dQ = \frac{dV_R}{dx} = r_C h = r_C^2 \tan\theta_A, \tag{Eq.19}$$

where r_C represents the contact radius and θ_A the angle-of-attack of the conical asperity.

Admitting a situation of fully plasticized contact, the total load supported by the represented conical asperity is given by

$$L = H_i area = H_i \frac{\pi r_C^2}{2}. \tag{Eq.20}$$

where only half of the area is considered since the contact with the softer material is established only by one side of the conical asperity. The combination of the previous equations allows one to achieve the following equation for the wear rate

$$dQ = \frac{2\tan\theta_A}{\pi}\frac{L}{H_i}. \tag{Eq.21}$$

Considering a more realistic case, where more asperities or hard particles contribute to the wear, the total wear rate can then be rewritten as

$$Q = \frac{2\,\overline{\tan\theta_A}}{\pi}\frac{L}{H_i}, \tag{Eq.22}$$

where $\overline{\tan\theta_A}$ represents the average slope of the multiple asperities or hard particle that belong to the harder surface. The above equation is usually presented in the literature in a different form, more specifically like

$$Q = K_{AB}\frac{L}{H_i}, \qquad \text{(Eq.23)}$$

being K_{AB} a dimensionless constant designated as abrasive wear coefficient which corresponds to

$$K_{AB} = \frac{2\,\overline{\tan\theta_A}}{\pi}. \qquad \text{(Eq.24)}$$

The wear rates predicted by Eq. 22 do not exactly match the experimental data, exhibiting much higher values then the ones attained experimentally. The source of overestimation is related to the fact that the Rabinowicz abrasive wear model considers that all the material removed by the hard asperities or particles, until a depth h, is taken away as debris particles (loose fragments) during the sliding, which essentially means that K_{AB} depends only of the geometry of asperities. However this is not necessarily truth. On one hand, considering a more realistic case, part of that material may simply plastically deform, during sliding, and only be partially removed, as it happens during the ploughing of ductile materials, resulting in a lower value of K_{AB}. On the other hand, the consecutive sliding cycles of the abrasive particles/asperities may lead to crack formation as a result of the stress concentration and lead to a surface wear fatigue events, meaning therefore that K_{AB} should take into consideration the critical number of sliding cycles to produce a fracture, or, in other words, it should take into consideration the fracture toughness of soft material. It becomes clear then that the K_{AB} does not strictly depend on geometrical factors of the asperities of the harder surface but rather from the properties of both materials that compose the tribological pair [181, 190].

Given the fact that both K_{AB} and H_i are directly related to the wear response of the softer material, it is quite common to merge these two quantities and represent the wear abrasive rate in more simplified form, namely,

$$Q = k_{AB}L, \qquad \text{(Eq.25)}$$

k_{AB} being called as specific wear coefficient factor given as

$$k_{AB} = \frac{K_{AB}}{H_i}. \qquad \text{(Eq.26)}$$

In opposition to wear coefficient K_{AB}, the specific wear coefficient k_{AB} is not dimensionless, being usually expressed in $mm^3/(m.N)$ or $m^3/(N.m)$. This parameter can be used as a criterion to compare the wear resistance of different materials, preferably within similar experimental conditions. For instance, materials with a specific wear coefficient of 10^{-14} $m^3/(N.m)$ or higher are usually not considered particularly wear resistant whereas values of 10^{-16} $m^3/(N.m)$ or lower are typical of high wear resistant materials. The main advantage of using the simplified formula of wear rate calculation – Eq. 25 hence the specific wear coefficient, respectively, lies on the fact that a wear characterization can be performed without a previous knowledge of the hardness of the softer material tested .

3 MATERIALS AND EXPERIMENTAL TECHNIQUES

3.1 MATERIALS

In the present work crystalline <100> silicon wafers, acquired from Si-mat (Silicon materials), were used. The specifications of the used silicon are presented in the Table 3.

Table 3. Specifications of the used silicon

Orientation	**Doping**	**Resistivity (Ω.cm)**	**Thickness (mm)**	**Diameter (mm)**	**Finishing**
<100>	p-type (Boron)	50-100	2.75 ± 25	100	One side polished

The quality of the Si surface finishing was verfied by AFM, as it can be seen in Figure 14a) and Figure 14b), where both AFM image and respective profile are represented. The calclualted roughness parameteres indicate a Ra of 0.18 nm and a RMS, or Rq, of 0.23 nm, being the peak-to-valey 2.21 nm - Figure 14a).

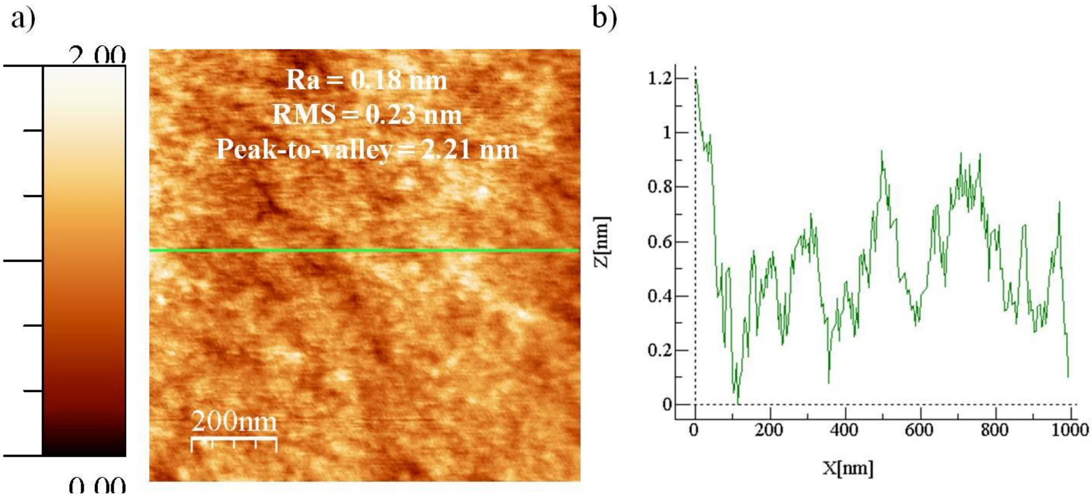

Figure 14. (a) 1x1 μm^2 AFM image of the used Si <100>, (b) height profile of the line in (a).

Previously to ion implantation and each characterization test the silicon wafers were cleaned with ethanol and distilled water, with the characteristic mentioned in Table 4. The distilled (De) and distilled and deionized (DeD) water were processed in the lab. The deionized water was made by passing the distilled water in a Mili-Q system. The final resistivity of the DeD water was ≈ 18.2 MΩ.cm at 25 ºC. In Table 4 are also present the characteristics of diiodomethane used for surface energy determinations experiments.

Table 4. List of reagents used

Reagent	Company	Purity (%)
Diiodomethane	Sigma-aldrich	99
Ethanol	Carlo Erba group	96

3.2 SAMPLE PREPARATION TECHNIQUES

3.2.1 ION IMPLANTATION

The ion implantation process was developed in the early 1970´s, appearing as natural solution to overcome the limitations of the used diffusion methods for electronic doping of materials. This process consists in the introduction of atoms into the surface layer of a solid substrate by bombardment of the solid with ions in the keV to MeV energy range [191]. For example, diffusion methods could not deliver the control confinement of dopants at the level needed both in concentration and depth confinement (because of the shorter characteristic length of the ion-implantation); created a higher concentration of dopants at the wafer surface and needed high temperature treatments, which damaged and contaminated the wafers. By solving all these problems plus adding other advantages, such as being compatible with the fabrication of smaller size and complex chips, ion implantation became the major technology used for semiconductor doping, becoming the basis of the modern IC´s manufacturing [192]. In order to have a better perception of the importance of the ion implantation in the evolution of the IC´s, in the 1970´s a n-type metal-oxide-semiconductor (MOS) required 6 to 8 implantation steps, currently, a modern complementary-metal-oxide-semiconductor (CMOS) IC with embedded memory may contain up to 35 implants [193].

It is undeniable that the primary application of ion implantation lies in the semiconductor industry, in fact it is the most profitable one. However, as surface treatment ion implantation presents several advantages when compared to other surface treatments such as coating. The advantages are, for example, the controlled addition of impurity ions, depth control by energy selection, multi-energy implants offer a depth tailored profile, small lateral spread of the implanted ions, solid solubility can be exceeded, bulk properties remain intact, no significant dimensional changes occur, compatible with low temperature, highly controllable and reproducible process, no adhesion problems since no sharp interface is formed and it is compatible with masks [194]. The combination of all these features extended the application of ion implantation to other fields of applications, which will be briefly mentioned. For instance , ion implantation has been tested and proved to be a good concept for improving both mechanical and tribological properties of steel tolls, improving the life of punches and dies for manufacturing aluminum beverages containers up to 6-10x when compared to un-implanted ones, increasing also the lifetime of injections molds for polymers and powder metals [195]. Intensive research and effort has been placed towards improving the corrosion behavior of iron, steels, stainless steels and aluminum. From 1985 to 2000 about 35 different elements have been implanted and studied aiming to achieve such goals [196].

Ion implantation has been also intensively tested in biomedical applications. It was shown that it can improve the properties of titanium and titanium alloys, used for orthopedic application [19, 197]. The addition of nitrogen showed promising results, increasing the wear resistance and wear-accelerated corrosion resistance in both saline and serum solutions in wide range of loads; the addition of calcium changes the cell-material interaction increasing the osseointegration and fluorine can act as a inhibitor of growth of *in vivo* bacteria [198].

In the present thesis ion implantation was the main method used for sample preparation. In the following chapters, the theoretical background of this processing method is concisely explained, as well as some features of the process.

3.2.1.1 Energy loss process and stopping powers

The specific energy loss; energy loss per unit of length, dE/dx, of an energetic ion moving through a solid, as occurs in implantation, is determined by screened Coulomb interactions with the substrate ions and electrons. It is common to discriminate two different mechanisms of energy-loss [199]:

(1) Elastic collisions between the nuclei, which corresponds to the Coulomb repulsion;

(2) Inelastic collisions with the electrons in the solid, which become ejected or detached from their atoms.

Considering the two above mentioned phenomena as independent and non-correlated, the total stopping-power of the moving ion in a solid, $\mathrm{d}E/\mathrm{d}x$, can then be expressed as

$$\frac{dE}{dx} = \left(\frac{dE}{dx}\right)_e + \left(\frac{dE}{dx}\right)_n, \qquad \text{(Eq.27)}$$

where the subscripts *n* and *e* denote nuclear and electronic collisions, respectively. The nuclear collisions are usually characterized by involving large energy-loss and significant angular deflections, being also responsible for the formation of lattice disorder by promoting the displacements of atoms from their respective lattice sites. Conversely, the electronic collisions involve much smaller energy-losses, minor deflection of the ion trajectory and negligible lattice disorder. In literature it is rather common to speak of energy-losses in terms of stopping cross-section *S*, which can be defined as a energy loss (per unit of length) per scattering center or atom of the solid, according the following equation [199]

$$S = -\frac{1}{N}\frac{dE}{dx} = S_e(E) + S_n(E) \qquad \text{(Eq.28)}$$

where *N* designates the atomic density of the solid, and $S_e(E)$ and $S_n(E)$ represent the respective electronic stopping and nuclear stopping cross-sections of the solid.

Concerning the determination of the stopping powers, Lindhard *et al*. [200] showed that for the sake of simplicity, it is convenient to introduce two dimensionless quantities, ε and ρ, which are related with both energy *E* and range *x* of the ion in the solid, given by the following equations,

$$\varepsilon = E\frac{a_{TF}}{Z_1 Z_2 e^2}\frac{M_2}{(M_1 + M_2)}, \qquad \text{(Eq.29)}$$

and

$$\rho = xN4\pi {a_{TF}}^2 \frac{M_1 M_2}{(M_1 + M_2)^2} \qquad \text{(Eq.30)}$$

where *N* represents the atomic density of the solid, Z_1, Z_2 and M_1, M_2 the atomic numbers and masses of both incoming ion and target ion of the solid, respectively, *e* the charge of the electron and a_{TF} the Thomas-Fermi screening radius expressed by

$$\mathrm{a_{TF}} = \frac{0.8853 a_0}{\sqrt{(Z_1^{2/3} + Z_2^{2/3})}} \qquad \text{(Eq.31)}$$

being a_0 a constant, the Bohr radius with a value of $0.529\text{x}10^{-10}$ m [201].

In the LSS theory, developed by Lindhard, Sharff and Schiøt [200], the electrons of the solid follow a Thomas-Fermi model, which can be considered to behave as an ideal gas. The resulting electronic losses are then the result of the interaction of the incoming ion with this gas. The electronic stopping power equation, derived by the authors based on the Thomas-Fermi potential, is the following:

$$S_e = -\left(\frac{d\varepsilon}{d\rho}\right)_e = K\varepsilon^{1/2}, \qquad \text{(Eq.32)}$$

where is possible to observe a linear relationship between the electronic stopping power and the velocity of the ions ($\varepsilon^{1/2}$ proportional to velocity, υ). The *K* in the above equation is expressed by

$$K = \xi_e \frac{0.0793(Z_1 Z_2)^{1/2}}{(Z_1^{2/3} + Z_2^{2/3})^{3/4}} \times \frac{(M_1 + M_2)^{3/2}}{M_1^{3/2} M_2^{1/2}}, \qquad \text{(Eq.33)}$$

being ξ_e a dimensionless variable with a value in the range of $Z_1^{1/6}$. The K parameter is essentially ion-solid dependent. The electronic stopping power expressed in Equation 32-33 is only valid for ion velocities υ, inferior to $\upsilon_1 = Z_1^{(2/3)}.\upsilon_0$, where υ_0 represents the Bohr velocity, ≈ $2.2\text{x}10^8$ cm/s [199], where most practical cases of implantation fit [202]. For velocities higher than υ_1, the charge state of the ion increases until untimely it becomes fully stripped of all its electrons. The moving ion can then be viewed as positive charge Z_1, moving with a velocity higher than the mean orbital velocity of the electrons of the solid. Under this high velocity regime, the electronic stopping cross-section decreases with the velocity since the particle spends less time in the vicinity of an atom. The electronic stopping power becomes essentially proportional to $(Z_1/\upsilon_1)^2$ and its overall behavior can be expressed by the following simplified expression in conventional energy unit rather than a reduced one [199]

$$S_e = -\left(\frac{dE}{dx}\right) = \frac{2\pi Z_1^2 e^4}{E} N Z_2 \left(\frac{M_1}{m_e}\right) \ln\left(\frac{2 m_e \upsilon^2}{I}\right), \qquad \text{(Eq.34)}$$

where m_e stands for the electron mass, and *I* the average excitation energy induced by the moving ion, that can be roughly estimated in electron-volt for most elements by ≈ $10Z_2$. The complete energy loss-energy equation often mentioned in the literature as the Bethe formula [199], has in considerations relativistic effects and corrections for the non-participant of the inner shell electrons. Nonetheless, for ions with atomic number $Z \geq Z_{He}$ and energies in the range of the few MeV, such as the RBS case for example, relativistic effects are insignificant and nearly all atoms contribute for the stopping power, $I=NZ_2$.

For the nuclear stopping power calculation, the LSS theory considers the interaction between the moving ion and the nuclei of the atoms of the solid as elastic collisions where the scattering events occur within the screened Coulomb field of the nuclei [202]. Using a Thomas-Fermi screening function, Lindhard, Sharff and Schiøt were able to find an expression for the nuclear stopping power [202]. Using a more refined approach, Ziegler, Biesark and Littemark substituted the Thomas-Fermi screening function with a universal screening one, determined by themselves, and were able to establish a universal nuclear stopping power equation with a higher degree of accuracy and for a wider range of energies [203, 204]. The determined universal nuclear stopping power equation expressed in reduced energies is given by [203, 204]

$$\mathrm{S_n} = -\left(\frac{\mathrm{d}\varepsilon}{\mathrm{d}\rho}\right)_{\mathrm{n}} = \frac{\log(1+1.1383\varepsilon)}{2(\varepsilon + 0.01321\varepsilon^{0.231226} + 0.19593\varepsilon^{0.5})}, \qquad \text{(Eq.35)}$$

which fits for most practical cases of implantation. For higher values of reduced energies, $\varepsilon \geq 30$, the nuclear stopping power is given by

$$\mathrm{S_n} = -\left(\frac{\mathrm{d}\varepsilon}{\mathrm{d}\rho}\right)_{\mathrm{n}} = \frac{\log(\varepsilon)}{2\varepsilon}. \qquad \text{(Eq.36)}$$

The variation of the nuclear stopping power in function of the square root of the squared energy is represented in Figure 15, where is also possible to observe at the same time, the electronic stopping variation for three different values of K according to the Equation 32.

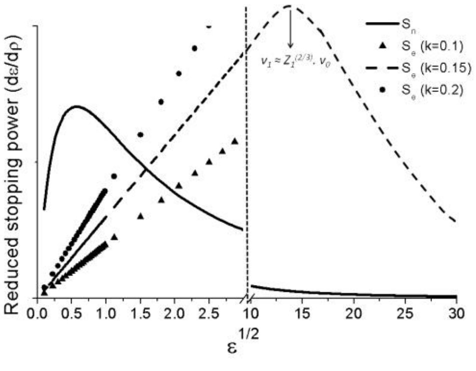

Figure 15. Variation of the nuclear and electronic stopping power (for K=0.1, 0.15 and 0.2) in function of the square root of the reduced energy adapted from [191].

3.2.1.2 Ion ranges and distributions in solids

The total distance traveled by an ion penetrating a solid, often called range *R*, can be calculated integrating the energy loss equation, Equation 27, using both electronic and nuclear stopping power from zero to the incident energy in the following way

$$R = \frac{1}{N}\int_0^E \frac{dE}{S_e(E) + S_n(E)}\,. \qquad \text{(Eq.37)}$$

However one must take in consideration the fact that the ion stopping inside a solid is a stochastic process resulting from a series of collisions and subsequent deflections. In fact, this means that two different ions, with the exact same energy and incident under the same angle, inside the same solid will not necessarily come to rest in the same position, giving rise to a statistical distribution [199]. Figure 16 (above) shows a 2D schematic representation of the path of three different incoming ions inside a solid. In Figure 16 (top) three different parameters are represented, the total distance traveled by an ion is represented by *R* (solid lines), the ion net penetration measured along a vector from the starting point to the ion´s end position, know as projected range, represented by R_p (dashed lines) and the projected range straggling represented by ΔR_p. The projected range analysis of multiple incident ions into the solid gives rise to a statically broad distribution just like the one observed Figure 16 (bottom) commonly referred as range distribution or range straggling, where $\overline{R_p}$ represents the most probable projected range often designated as average or mean projected range, and ΔR_p the standard deviation of the distribution.

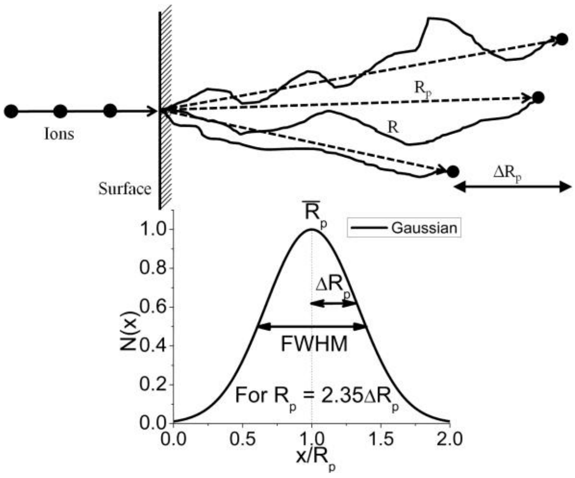

Figure 16.(top) Schematic representation of the course of ions traveling inside of a sample and representation of the range, projected range and range projected range straggling, (bottom) schematic representation of a Gaussian range distribution with Rp=2.35ΔRp adapted from [199].

Knowing both $\overline{R_p}$ (mean projected range) and ΔRp (projected range straggling) parameters makes possible to determine the spatial distribution of a determined implanted ion in a sample by the following equation [199]

$$N_{dis}(x) = \frac{\phi}{\sqrt{2\pi}\Delta R_p} e^{-\frac{1}{2}\left(\frac{(x-\overline{R_p})}{\Delta R_p}\right)^2}, \qquad \text{(Eq.38)}$$

where ϕ stands for the total implanted fluence and x the variable depth. Although this theoretical approach assumes a Gaussian shape for the depth distribution for the implanted ions, the occurrence of certain phenomena such as diffusion or channeling may induce some deviations to symmetry of the curve and also in the tails. Nonetheless, the Gaussian shape is still quite adequate as a first approximation for most practical cases of implantations [205]. A more precise alternative for the calculation of range parameters and respective implantation profiles can be easily be carried by using the freeware software SRIM (**S**topping and **R**anges of **I**ons into **M**atter) that is based on Monte-Carlo simulations [206]. In fact SRIM is a complex group of programs on which both stopping powers and ranges of ions (up to 2 GeV/amu) into matter are calculated using a quantum mechanical treatment of ion-atom collisions. The core of the SRIM is the TRIM (**T**ransport of **I**ons in **M**atter) program developed by J. F. Ziegler and J. P. Biersack, and these programs have been continuously updated over the years, the last update was made in 2003, regarding the stopping power calculations. The advantage of using the SRIM software relies on the fact that one not only can determine both lateral and 3-dimensional distribution profiles of implanted species, both on mono or multilayered samples, but also to extract all sort of information regarding the kinetic phenomena arising from the energy loss of an ion inside a solid, which include: target damage, sputtering, ionisation and phonon production [206]. The major drawbacks of this code are: it does not consider the crystalline structure effect the on the ion trajectories, there is no memory effect meaning that each event is independent of its predecessor and finally the fact that it does not account the changes induced in the solid by the impinging ions as the implantation progresses. Figure 17 shows a SRIM output result from a 150 keV Fe^+ implantation into Si, an implantation performed in this thesis, where it is possible to observe a depth distribution curve quite close to a Gaussian one. In Figure 17 it is also possible to observe the huge amount of information that can be retrieved from the same implantation upon selection: Ion recoil distribution, lateral range, ionization etc.

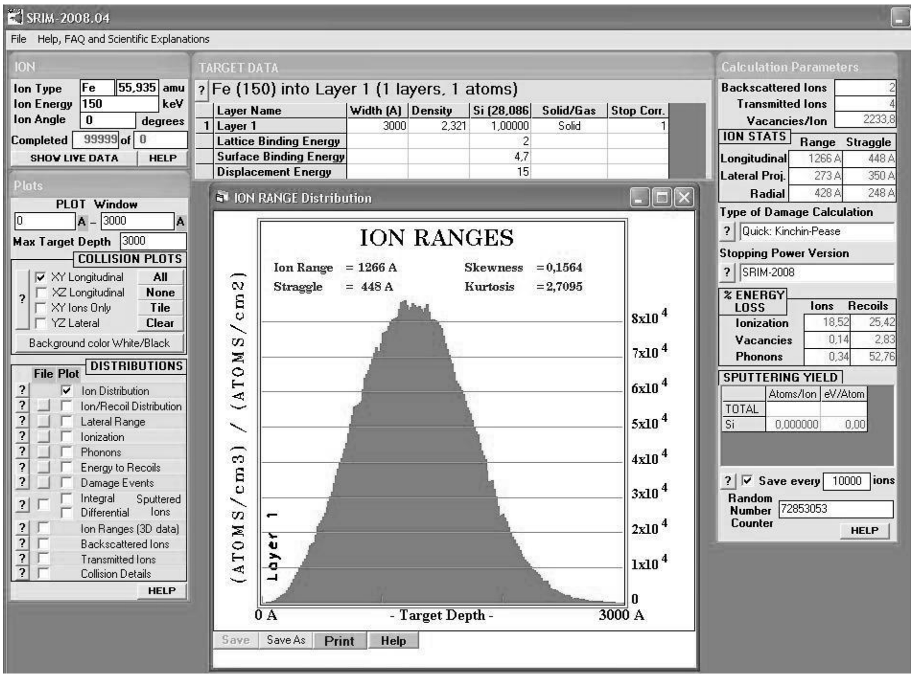

Ion Type: Fe 55,935 amu
Ion Energy: 150 keV
Ion Angle: 0 degrees
Completed: 99999 of 0

Fe (150) into Layer 1 (1 layers, 1 atoms)

	Layer Name	Width (A)	Density	Si (28,086)	Solid/Gas	Stop Corr.
1	Layer 1	3000	2,321	1,00000	Solid	1
	Lattice Binding Energy			2		
	Surface Binding Energy			4,7		
	Displacement Energy			15		

PLOT Window: 0 A – 3000 A
Max Target Depth: 3000

☑ XY Longitudinal
☐ XZ Longitudinal
☐ XY Ions Only
☐ YZ Lateral

	File	Plot	
?		☑	Ion Distribution
?	☐	☐	Ion/Recoil Distribution
?	☐	☐	Lateral Range
?	☐	☐	Ionization
?	☐	☐	Phonons
?	☐	☐	Energy to Recoils
?	☐	☐	Damage Events
?	☐	☐ ☐	Integral Differential Sputtered Ions
?	☐		Ion Ranges (3D data)
?	☐		Backscattered Ions
?	☐		Transmitted Ions
?	☐		Collision Details

Ion Range = 1266 A
Straggle = 448 A
Skewness = 0,1564
Kurtosis = 2,7095

Backscattered Ions: 2
Transmitted Ions: 4
Vacancies/Ion: 2233,8

ION STATS	Range	Straggle
Longitudinal	1266 A	448 A
Lateral Proj.	273 A	350 A
Radial	428 A	248 A

Type of Damage Calculation: Quick: Kinchin-Pease
Stopping Power Version: SRIM-2008

% ENERGY LOSS	Ions	Recoils
Ionization	18,52	25,42
Vacancies	0,14	2,83
Phonons	0,34	52,76

SPUTTERING YIELD

	Atoms/Ion	eV/Atom
TOTAL		
Si	0,000000	0,00

☑ Save every 10000 ions
Random Number Counter: 72853053

Figure 17: TRIM depth distribution output result for a 150 keV Fe$^+$ implantation into Si.

3.2.1.3 Amorphization and recrystallization

As the number of incident ions on the crystal increases the individual disordered track regions left unrecovered by each impinging atom begin to overlap. Above a certain number or fluence, often called in the literature as amorphization threshold, the crystalline structure of the solid is no longer able to accommodate the amount of defects generated, transforming the implanted zone into an amorphous layer. This presents perhaps the greatest disadvantage of the ion implantation process. In the past Christel *et al.* [207] used the dpa (displacement per atoms) parameter to propose displacement criteria for amorphization of silicon. A unit of 1 dpa means that, on average, every atom in the irradiated volume has been displaced once from its equilibrium lattice position. For more details consult reference [203]. According to the authors model, based on experiments of Si implantation onto Si, the authors established that 10% of displacements (or 0.1 dpa) of the lattice will render it amorphous. The experiments were performed at a temperature of 77 K, which in Si inhibits the self-annealing process and defect diffusion thus being the model independent of both implanted species mass and energy. The amorphous-to-crystalline transition in silicon subjected, (and vice versa) have been extensively studied in the past thus several theories have been published being very difficult to mention all of them. The author advises the consultation of review article [208] about the topic.

Figure 18 shows a schematic evolution for a 40 keV phosphorous implantation in Si, where a fluence of $4x10^{14}$ cm^{-2} is needed to form an amorphous layer. The generated amorphous phase is metastable; in fact, it has been pointed out that amorphous Si presents a Gibbs free energy of ≈ 0.12 eV/atom higher than crystalline Si. Since there is an energy difference between the crystalline and amorphous Si, providing thermal energy will act as driving force to order the amorphous phase thus reverting Si to a minimum energy state [209].

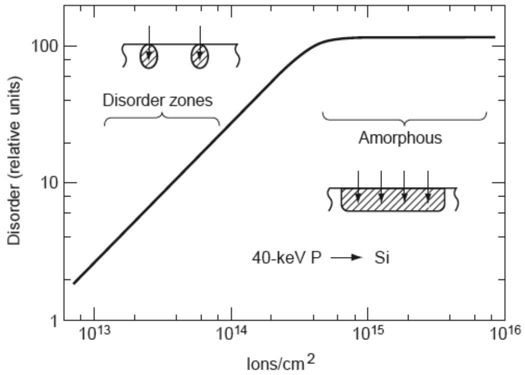

Figure 18. Schematic of disorder build up as a function of ion dose for 40 keV phosphorous ions incident on Si [199].

Performing a annealing on a self-implanted Si will induce recrystallization of the amorphous layer by means of what is designated in the literature as solid phase-epitaxy growth (SPEG) [210]. The crystalline substrate, below the amorphous zone, will act as a seed, and the crystal/amorphous interface advances towards the surface with the same crystallographic orientation as the substrate. Measurements performed on Si show that the growth velocity of the interface follows an Arrhenius-law type with temperature by the following expression [210]

$$\upsilon_g = \upsilon_p e^{\left(-\frac{E_a}{KT}\right)}, \qquad \text{(Eq.39)}$$

where υ_P represents the pre-exponential factor with a value of $3.1x10^8$ cm/s, E_a the activation energy with a value of 2.68 ± 0.05 eV, k the Boltzmann constant and T the temperature in K. The expression is valid for a temperature interval of 500 - 1000 ºC. The same authors verified that for different experimental conditions, that is Si amorphisized by a low fluence ($5x10^{14}$ cm^{-2}) 150 keV As^+ implantation, the same type of law is observed for a broader range of temperature 470 ºC to 1350 ºC, described by a single E_a of 2.7 ± 0.05 eV and υ_P of $3.68x10^8$ cm/s.

The addition of impurities in low concentrations affects the SPEG rate. Cseprei *et al* [211] verified that SPEG rate of pre-amorphisized Si, by self-implantation, was increased by a factor of 6 upon As^+ or P^+ implantations and by factor of 20 for a B^+ implantation, for impurity concentrations in the range of 0.2 – 0.5 atm %. Under similar experimental conditions and concentrations, other elements such as O, C, N and noble like Ar^+, Ne^+ and Kr^+ act as SPEG rate retarders, decreasing the SPEG rates from 3 times up to 9 times [212]. In the case of the impurity elements being in concentration higher than their solid solubility in the matrix, the SPGE tend not to occur, the diffusion processes may be difficult at the interface. In this type of situation, it is possible to observe an amorphous-to-polycrystalline transformation in the amorphous matrix upon the annealing. Nucleation phenomena occurs within the matrix forming a polycrystalline structure where once an amorphous structure existed [210, 213, 214]

3.2.1.4 LATR Ion implantation installations

The implantations of the Si wafers performed in the present thesis were carried out in the LATR (Laboratório de Aceleradores e Tecnologia da Radiação) facility located in the IST campus-Loures in Bobadela Figure 19a)b) - using a high fluence implanter Danfysik 1090, equipped with a CHORDIS (cold hot reflex discharge ion source) high current ion source, model 920. A schematic representation of the implanter can be found in Figure 20.

The ion implantation process will be briefly described in 5 different steps, which include: (1) - the ion formation and extraction, (2) - the mass separation, (3) - the post-acceleration, (4) - the focusing and scanning, and finally the (5) - chamber.

(1) Ion formation and extraction - the ion formation and extraction process begins by forming ions of the elements desired to be implanted, in the ion source -Figure 21) Figure 19c). The filaments in the ion source are placed under high current typically 100 -150 A in the presence of an inert gas usually Ar. The high current in the filaments will generate electrons via thermionic effect [215], that are forced to interact with the surrounding gas by a cylindrical magnet and an electric field thus generating a plasma. The target containing the elements desired to be implanted, in form of a disk, is placed in the holder and under a negative voltage, a common value, for example, for a Fe beam is around -200 V. The ions of the gas present in the plasma are then accelerated against the target promoting the sputtering of some of the target atoms. The sputtered ions as well as some gas ions go through a circular aperture with a 9 mm diameter and enter into the extraction/first acceleration zone, where are accelerated from 0 kV to a maximum of 50 keV (for single charge ions). In the middle of the extraction zone, there is a suppression zone at a negative potential so that the electrons resulting from the collisions of the accelerated ions with the respective surrounding surfaces are blocked and do not enter into the source and also to avoid the X-ray generation arising from the electrons deceleration.

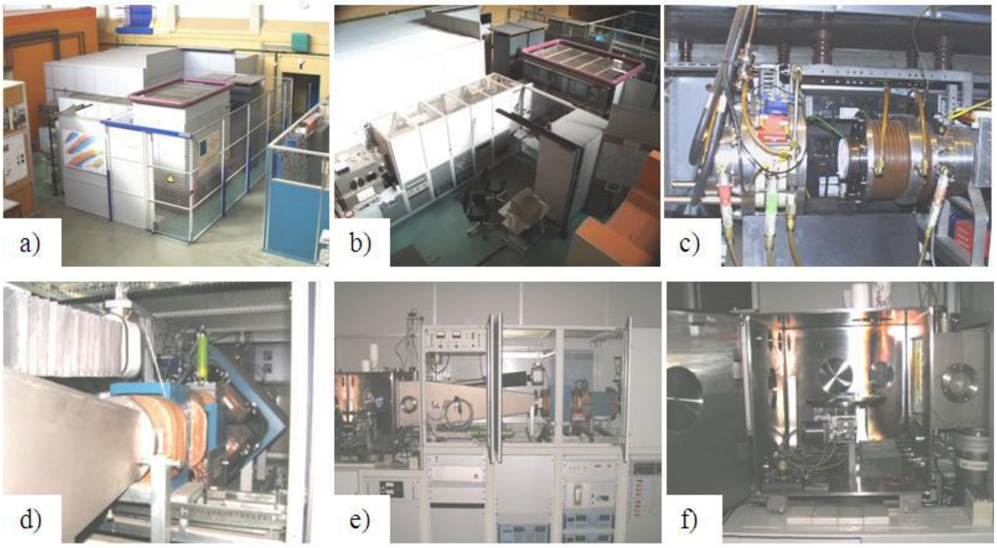

Figure 19. (a) and (b) General view of the ion implanter of the LATR facility, (c) close view of the ion source, (d) close view of the scanning magnet and the last quadrupole, (e) lateral view of the implanter from the focusing magnets to sample holder (f) close view of the sample holder plate.

(2) Mass separation - the accelerated ions are then propagate to the magnet analyzer- Figure 20- where the beam is deflected and “purified”. The presence of the magnetic field will separate the beam by masses, thus separating the desired ions from all the contaminations that may be present due to target sample or gas.

(3) Post-acceleration - once the masses are separated the post-acceleration stage follows. In this stage energy is added to the beam (already with an energy comprehended within 0 - 50 keV), up to a maximum of 160 keV, allowing a maximum implantation energy of 210 keV (for single charged ions). The added acceleration is provided by the acceleration tube, composed of 12 consecutive electrodes connected by 11 resistors of 12.5 MΩ. Each electrode will hold a fraction of the total voltage so that an axial uniform electric field is formed.

(4) Focusing and scanning – after the post-acceleration stage, there is need for reduction of the divergence of the beam. The beam crosses a zone where 3 magnetic quadropoles are present mounted in series which will converge the beam both vertically and horizontally - Figure 19d). With the aid of two magnets dipoles - Figure 19d), after the quadropoles, the focused beam is deflected to the sample in a simultaneous non-synchronized scanning mode, in the *x* and *y* direction. The beam scans the sample first in the x direction and then in the y one. The frequency of the horizontal scan varies between 0.1 Hz and 1 Hz while in the vertical direction between 1 Hz an 8 Hz. The scanning magnets are very important part of the process, since they must guarantee a uniform distribution of the beam in the samples.

(5) Implantation chamber – the final stage of the process where the beam finally reaches the samples with a dimension close to 1 cm^2. The implantation chamber has a cubic shape with a total volume of 0.7x0.7x0.7 m^3 - Figure 19f), with an entrance area of 40x40 cm^2. During the implantations the chamber is under vacuum in the range of 10^{-6}-10^{-7} mbar to avoid contamination from the atmosphere. The samples are mounted in a copper or stainless steel plate with a diameter of 40 cm. The samples can be heated up to 600 ºC by means of an oven or heated by the imposed current, or cooled down using liquid nitrogen reservoir that allows a minimum temperature of 200 K. The plate can be tilted, rotated and displaced, according to the needs, and can carry a maximum load mass of 50 kg.

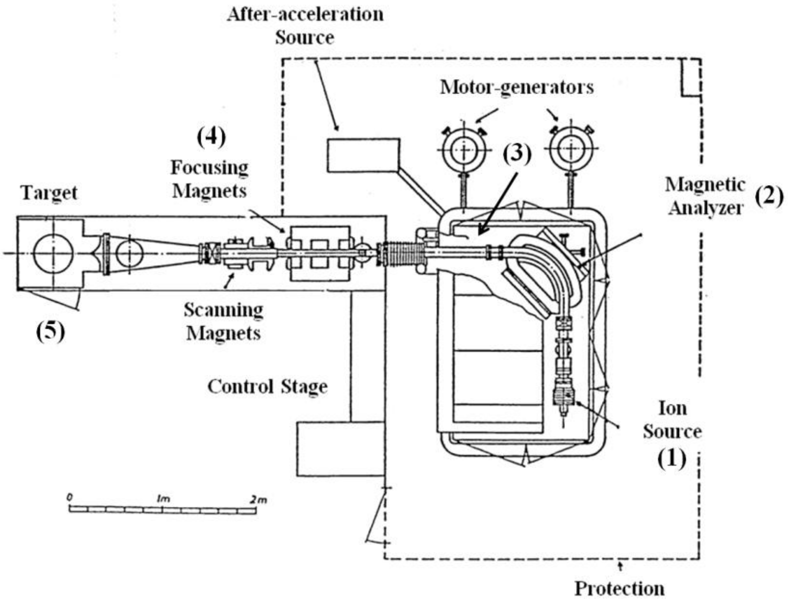

Figure 20. Schematic representation of the high fluence Danfysik 1090 implanter present in the LTAR facility.

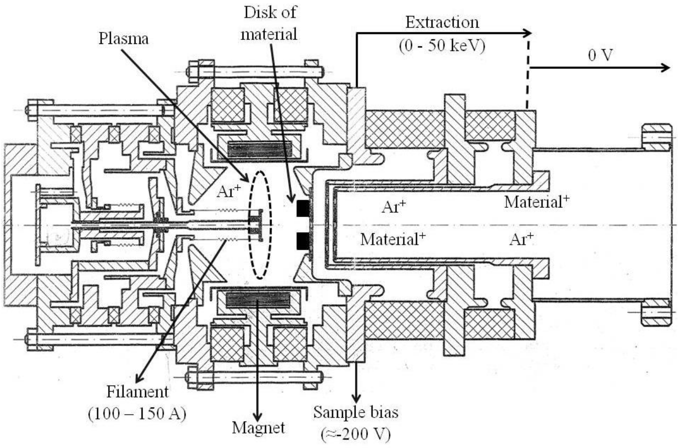

Figure 21. Cross-section drawing of the CHORDIS ion source present in the Danfysik 1090 ion implanter.

3.2.1.5 Ion implantation – experimental conditions and sample designation

The experimental conditions used for all the ion implantations made in the present work are described in Table 5, as well as the values of the projected range, R_p, and straggling, ΔR_p, values calculated using the TRIM-SRIM software. There are common traces to all implantations. All the implantations were carried out at room temperature, using current values within 10 μA and 300 μA, that never passed a deposited power density of 0.5 W/cm^2 thus not increasing the temperature during the implantation. All implantations were also carried under normal incidence (0º).

For the dual implantations cases, Fe^++C^+ and Ti^++C^+, the order of the implantation was the same for both systems. The wafers were initially implanted with C^+ and then implanted with the respective metallic ions.

For the sake of simplicity the author decided to implement a general designation for the samples to avoid the full description of type of implanted ion, fluence and annealing. For the single ion implantation cases, the nomenclature will be the following:

Nomenclature: Ion Fluence(L, M, H) T(or As)(550, 800, 1000)

First, the name of the ion is written in the conventional way, Fe or C, followed by three possible designations, L, M or H, which designate **l**ow (5x10^{15} cm^{-2}), **m**edium (5x10^{16} cm^{-2}), or **h**igh (2x10^{17} cm^{-2}) fluence. The annealing designation is written after a capital T followed by the respective temperature. An exception is made in the case of the as-implanted samples, instead of a T, an As will be written. The nomenclature for all single implantations is listed in Table 6.

For the double implantation case, the same methodology is used. Instead of writing the single ion, the two are written, like TiC or FeC. For the fluence specification, since there are only two different, the author shall use L for low (5x10^{16} cm^{-2}) and H for high (2x10^{17} cm^{-2}) fluence. The annealings are specified in the exact same manner as in the single implantation case. The nomenclature for all dual implantations is also listed in Table 6.

Table 5. Experimental conditions of all ion implantations processed for the current thesis.

Single implantations

Element	Energy (keV)	Rp (nm)*	ΔR$_p$ (nm)*	Fluence Φ (cm^{-2})	Temperature (ºC)
Fe$^+$	150	127.1	44.6	5x10^{15}	550 ºC, 800 ºC and 1000 ºC
				5x10^{16}	
				2x10^{17}	
C$^+$	25	83.1	32.8	5x10^{15}	
				5x10^{16}	
				2x10^{17}	

Dual implantations

Element	Energy (keV)	Rp (nm)*	ΔR$_p$. (nm)*	Fluence Φ (cm^{-2})	Temperature (ºC)
Fe + C	Fe $^+$: 170 C$^+$: 50	Fe$^+$: 142.3 C$^+$: 151.3	Fe$^+$: 49.0 C$^+$: 49.9	C$^+$:5x10^{16} Fe$^+$: 5x10^{16}	800 ºC and 1000 ºC
				C$^+$: 2x10^{17} Fe$^+$: 2x10^{17}	
Ti + C	Ti $^+$: 160 C$^+$: 50	Ti$^+$:151.8 C$^+$: 151.3	Ti$^+$: 51.8 C$^+$: 49.9	C$^+$:5x10^{16} Ti$^+$: 5x10^{16}	
				C$^+$: 2x10^{17} Ti$^+$: 2x10^{17}	

*Values determined by using the SRIM software considering a total number of 10^5 events.

Table 6. List of all samples abbreviated names according the nomenclature for both single and dual ion implantation

Single ion Implantation

Fluence	As-imp.	Ann. 550 ºC	Ann. 800 ºC	Ann. 1000 ºC
5x10^{15} cm^{-2}	(Fe or C)LAs	(Fe or C)LT550	(Fe or C)LT800	(Fe or C)LT1000
5x10^{16} cm^{-2}	(Fe or C)MAs	(Fe or C)MT550	(Fe or C)MT800	(Fe or C)MT1000
2x10^{17} cm^{-2}	(Fe or C)HAs	(Fe or C)HT550	(Fe or C)HT800	(Fe or C)HT1000

Dual ion Implantation

Fluence	As-imp.	Ann. 800 ºC	Ann. 1000 ºC
5x10^{16} cm^{-2} + 5x10^{16} cm^{-2}	(FeC or TiC)LAs	(FeC or TiC)LT800	(FeC or TiC)LT1000
2x10^{17} cm^{-2} + 2x10^{17} cm^{-2}	(FeC or TiC)HAs	(FeC or TiC)HT800	(FeC or TiC)HT1000

3.2.2 VACUUM ANNEALINGS

The implanted samples were annealed in a tubular furnace shown in Figure 22 that can reach a maximum temperature of 1300 ºC. The procedure to perform the annealings will be now described. The samples are placed in a pure silica tube that is connected to a vacuum pump that can reach pressures of 2x10^{-6} mbar to 8x10^{-6} mbar. The furnace possesses a set of wheels which makes it movable. Upon reaching the desired values of temperature, and pressure, the furnace is moved towards the sample. The temperature of the annealings is monitored using a type K thermocouple that is positioned and secured closed to the tube by means of tungsten wires. The annealings in the present work were performed at various temperatures, namely, 550 ºC, 800 ºC and 1000 ºC for periods of 30 min under vacuum conditions. The samples were annealed in a specific position, more specifically; the polished faces of the samples were facing each other during the annealing, in order to minimize surface oxidation.

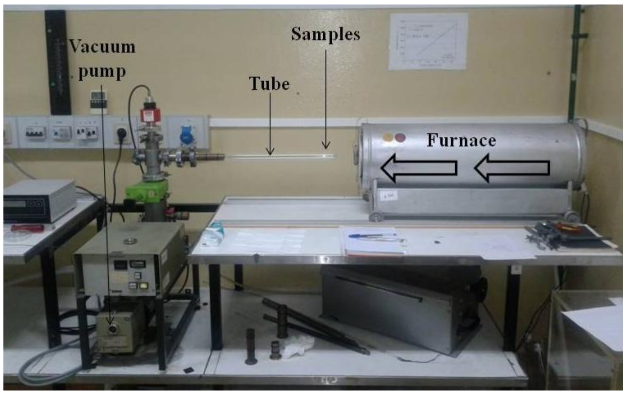

Figure 22. Tubular furnace used for the vacuum annealings.

3.2.3 SAMPLE CLEANING PROTOCOLS

In the present chapter the cleaning procedures will be described for the techniques where it plays an important role on the discussion. The experimental conditions used in the ion implantation will also be detailed and nomenclature for the samples will be defined for the sake of simplicity.

3.2.3.1 Contact angle determination

For the water contact angle measurements the samples were cleaned in several steps.

1) The samples were placed in glass beaker containing a diluted solution of Extran® which was placed under sonication for 5 min.

2) After 5 min. of ultrasound emersion, the samples were removed and rinsed with distilled water.
3) The samples were then ultrasound emersion with distilled (De) water 7 times for periods of 10 minutes. After each period the samples were rinsed with De water.
4) The samples were sonicated with distilled and deionized (DeD) water 5 times for periods of 10 min. each step. Between sonication periods the sample were rinsed with DeD water
5) The samples were sonicated with ethanol for 5 min. and dried with dry gaseous nitrogen.
6) The samples were placed in a vacuum oven over night to dry. No temperature was applied.

In order to have a good statistics, after the water contact angle experiments the sample were rinsed with DeD water, and the procedure was repeated starting from point 4.

The diiodomethane contact angle measurements, for the surface energy determination, were carried out after the water contact angle determination. Once again, after the water contact angle measurements, the samples were rinsed with DeD water and the cleaning procedure was repeated starting from the point 4.

3.2.3.2 Annealings

The implanted wafers were cut using a diamond cuter with the author wearing rubber gloves to prevent eventual fingerprints laying and contamination. The cut samples were sonicated for 5 min in ethanol and dried under nitrogen. The silica tube where the samples are positioned was cleaned in its first use, again using ethanol and sonication. Before starting the annealing the vacuum pump stays on for at least 8 hours to be sure that the vacuum is stabilized.

3.2.3.3 Depth-sensing indentation

Before the depth-sensing indentations, the samples were sonicated with ethanol for 10 min. and dried in vacuum oven during the night. The samples were then glued with a very thin double-side duck-tape in a squared aluminum support to gain the sufficient height for the sample holder of the apparatus.

3.3 CHARACTERIZATION TECHNIQUES

3.3.1 SCANNING ELECTRON MICROSCOPY

The scanning electron microscope (SEM) represents one of the most versatile available characterization instruments for examination and analysis of the microstructure morphology for several different types of samples. The SEM takes advantage of using electrons for imaging in opposition to conventional optical microscopes that use light. The main advantages of the SEM when compared to optical techniques are: higher magnification range (10x-10.000), the possibility to take three dimensional-like images (higher depth of field) and finally the ability to take topographic as well as chemical information from the samples [216].

A schematic representation of the SEM is shown in Figure 23. Electrons are generated either by thermionic effect, in conventional SEM´s, or by field emission, in field emission gun SEM (FEG-SEM), and are accelerated between a cathode and an anode with a voltage in the range of 0.1 kV and 50 kV, having the anode a hole that allows the electrons to continue through the column towards the sample. In Figure 24 it is possible to observe the two different electron guns, which in fact constitute the main difference between a conventional SEM and FEG-SEM one. The FEG-SEM system has the advantage of not needing any sort of heating to promote electron emission, instead, a high electric filed is concentrated in the sharp tip (Figure 24b) which not only significantly reduces the work function of material thus enhancing the electron emission, but also significantly increases the spatial resolution, since the electron beam is generated from the sharp tip rather than a wide filament [217] - Figure 24a).

Once formed, the electron beam diverges when passing through the anode, being necessary afterwards a set of condenser lenses to collimate the beam using magnetic fields Figure 23. The final spot size of the beam in the sample depends on the electron source and respective number of condenser lenses. Values from 1 nm to 10 µm can be found [218]. The collimated beam is then directed to the sample by a system of scanning coils. This deflection system of the SEM causes the beam to move through a series of discrete locations along a series of parallel lines in the sample, until forming a rectangular raster. Finally, the electrons are collected by the respective detectors. Simultaneously, the same scan generator creates a similar raster on the view screen where the final image of the sample can be seen. All this process, from electrons production until they reach the detectors is carried under vacuum, so that electrons are not scattered by air molecules [216].

The interaction of the electron beam with the sample will generate the emission of various different types of radiation, Figure 25, which can be collected upon having the proper detectors, however, concerning SEM imaging, the backscattered electrons BSE and the secondary electrons SE signals are the ones most commonly used. The BSE signal corresponds to electrons from the primary beam that penetrates the specimen and suffer single-large angle or multiple small angle scattering events, leaving the specimen with relatively high energies, a fraction of the energy of the primary beam. Since materials with high atomic numbers backscatter more effectively the electrons from the primary beam, the BSE signal allows one to extract compositional information, that is, to distinguish zones with different atomic numbers [219]. The SE are generated by the interaction of the primary beam electrons with the weakly bound outer shell electrons from the specimen by means of inelastic scattering events. The weakly bounded electrons receive enough energy resulting from the collisions to be freed from the respective atoms and are released from the specimen with a small amount of kinetic energy that is strongly attenuated with the distance travelled. Only the SE that are emitted from the near surface, (<10 nm), are able to escape the specimen and be detected, being this kind of signal typically used to extract topographical information from the sample [216].

In the present thesis two different SEMs were used, a Hitashi S2400 with an accelerating voltage of 25 kV and field emission JEOL 7001F with an accelerating voltage of 15 kV.

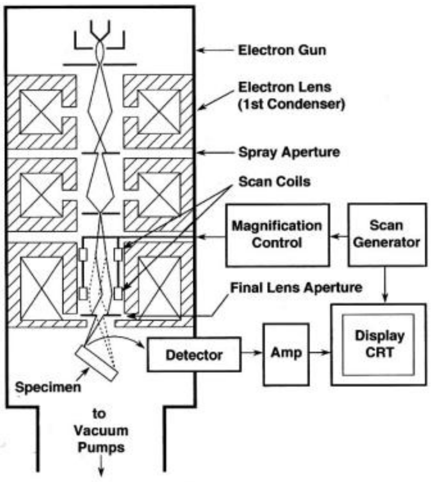

Figure 23. Schematic representation of a scanning electron microscope [216].

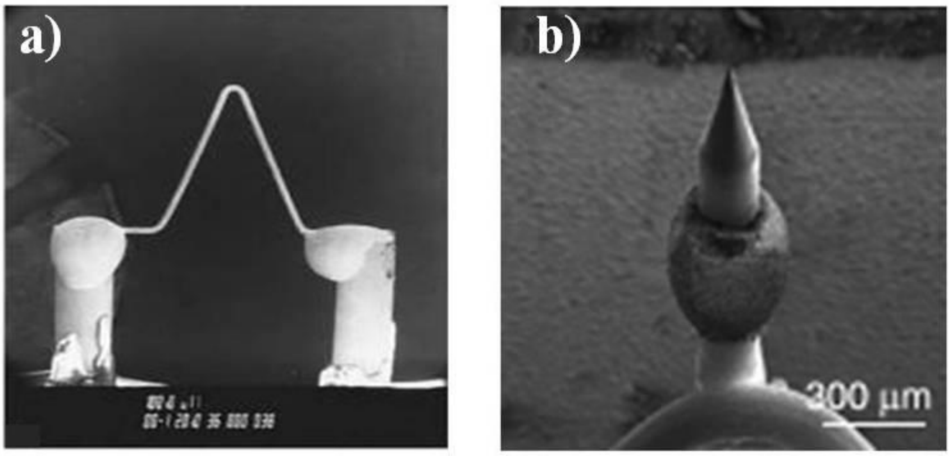

Figure 24. (a) Conventional tungsten hairpin filament electron gun [216], (b) filed emission gun with extreme sharp tip [220].

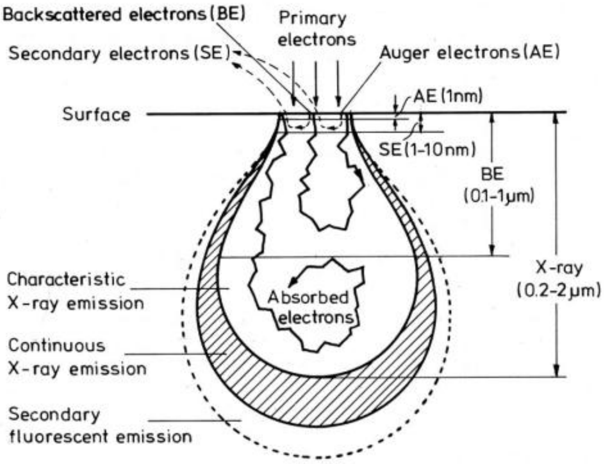

Figure 25. Illustration of the several different signals generated by the electron beam-specimen interaction in the Scanning electron microscope [201].

3.3.2 ATOMIC FORCE MICROSCOPY

The atomic force microscope (AFM), is a part of a larger family of instruments termed scanning probe microscopes (SPM), invented in the 1980´s, that perform surface characterization using very small probes. The AFM itself was developed in 1986 by Binnig, Quate and Gerber [221] and was naturally developed to overcome the limitations of the scanning tunneling microscope, that could only perform surface characterization of electrically conducting samples. The first ever AFM was only used for a few experiments, however, the results presented had such an impact upon the scientific community that this first instrument now resides in the science museum in London [222]. A schematic representation of an AFM is represented below in Figure 26a).

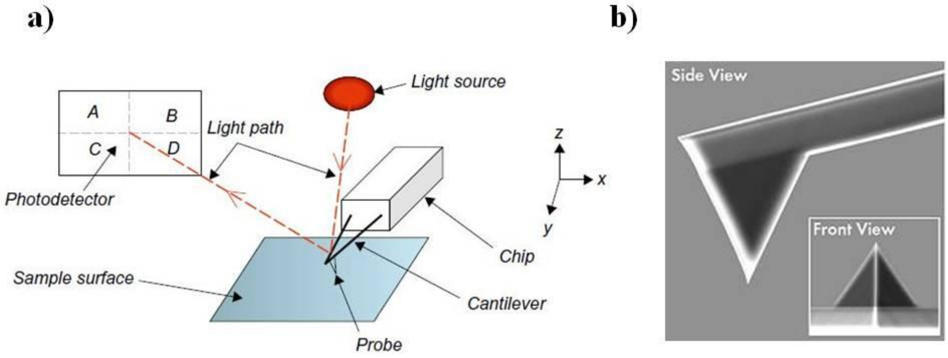

Figure 26. (a) Atomic force microcospe schematic [223], (b) a real non-contact tip [224].

The AFM is composed of four major components: (1) the arm or cantilever, which can be of either V or rectangular shape; (2) the tip or probe that is mounted in the extremity of cantilever and directly interacts with the sample; (3) the piezoelectric scanner which allows movement in the XY and Z direction and finally, (4) the optical system, composed of a light source, usually a laser and the respective photodetector, normally a photodiode that is divided in four quadrants, A, B, C and D, as it can be seen Figure 26a) that allows to determine both z-position of the tip or the cantilever torsion based on the signal position in the detector.

The AFM images are formed by performing a raster scan pattern, typically with the same dimensions in *x* and *y* direction, as it is represented in Figure 27a). The piezoelectric actuator moves either the tip or the sample in the *x* direction, represented as fast scan direction in Figure 27a), collecting the respective information for each point (represented by dark points) for example, the z - position. Once the line scan reaches the end, it comes back to the starting point, and the scanner moves the tip in *y*, represented as slow scan direction, repeating the same process. The image is acquired by the repetition of this sequence until the end, represented with an X in Figure 27a). The total number of lines for an image is a parameter that can be defined by the operator, determining in fact the resolution of the image. The values can vary from 64 to 2048 lines.

There are three main AFM operation modes that are directly related with the tip – sample distance separation, thus depending on the magnitude of the surface forces (Van der Waals) established between tip and surface - Figure 27b).

The three operating modes are: the contact mode and the dynamic mode, which can be subdivided in two different modes, the intermittent contact mode and non-contact mode respectively. In the contact-mode operation the cantilever does not oscillate during the scanning, unlike the other two modes. The tip is brought directly into contact with sample. In this case, due to the small distances, the repulsion forces arising between the tip and the sample are dominant over the adhesive ones - Figure 27b). There are different contact modes, the constant force and variable force one; however, the one most often used is the constant force one which, being also the one that was used in the present thesis thus the one that will be briefly explained. In the constant force mode, the tip is placed in contact with the sample with a defined force by the operator, the set-point. This selected force will create a deflection upon the cantilever. When a sample is scanned according to Figure 27a), with the help of a feedback system loop, whenever a change of deflection, hence force, occurs due to changes in z-height, the feedback loop will restore the original predefined set-point, for each scanned point. The changes in the z-height for each *x,y* position of the scan enable to create the final topographical image of the sample [223]. In the intermittent-contact mode, also designated as tapping mode, the tip interacts intermittently with the sample. In this mode, as it can be seen in Figure 27b), the tip experiences both repulsive and adhesive forces as the cantilever oscillates. The intermittent operation mode starts by placing the cantilever to oscillate freely far away from the surface, in a frequency close to the resonance frequency, and choosing the respective amplitude set-point, which typically is half of the amplitude of the chosen frequency. While approaching the sample, the tip will start to feel the surface forces, which will restrict the amplitude of vibration of the cantilever, and the cantilever is placed to oscillate at the chosen set-point. As the surface is scanned, the oscillatory amplitude of the cantilever changes as it encounters the surface topography. The feedback loop will promote the adjustment of the distance, guaranteeing that the oscillating amplitude is maintained constant during the scan whenever changes in the z-height of the piezoelectric are performed. Then the image construction follows the same principle as in the contact mode case. In the non-contact mode the cantilever is forced to oscillate far away from the surface but with much smaller amplitude than in the tapping case. As the probe approaches the surface, the long-range adhesive interaction - Figure 27b), will cause a detectable shift in the cantilever´s oscillation frequency. The detection of the shift allows the z-positing of the cantilever to be adjusted so that the cantilever remains out of contact with the surface by means of the feedback loop [223].

In the present thesis a Vecco^{TM} DI CP-II AFM was used. The images were acquired in two main different modes, tapping and contact-mode, using standard commercial Bruker silicon tips such as MPP11 (C_n=20 N/m) and MP31 (C_N=0.9 N/m), respectively.

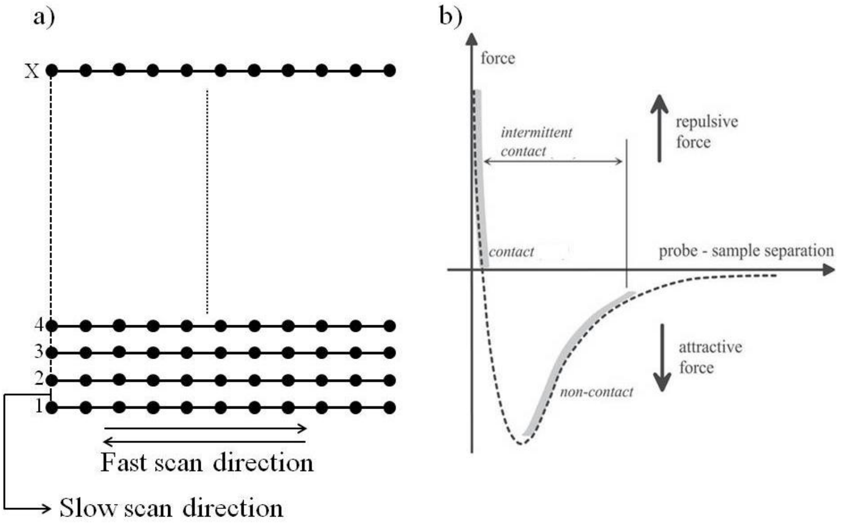

Figure 27. (a) Schematic representation of Raster scan for image acquisition, (b) diagram illustrating the force regimes under which each of the three most common AFM imaging modes operate [225].

3.3.3 ATOMIC FORCE MICROSCOPY-BASED NANOWEAR

Looking to the atomic force microscope as only a microscopy tool is quite restrictive concerning the full potential of the instrument. The main advantage of the AFM, compared to others microscopic techniques, relies on the fact that the images are built based on a direct interaction between the tip and the surface at small scales. AFM´s have been used and modified to perform different types of characterization, such as, for example, mechanical, by allowing the determination of properties such as hardness and Young´s modulus [226, 227]. The AFM has also been extensively used for the study of friction and wear phenomena at the very small contact scales [105, 228-230] in which the AFM tips can be used to simulate a sharp single-asperity travelling over a surface.

In the present thesis nanowear experiments were performed using two different AFM´s. A Vecco^{TM} DI CP-II atomic force microscope with a commercial Veeco^{TM} diamond tip was used for the characterization of the single Fe^+ implanted samples and a Nanosurf AFM with a commercial Microstar^{TM} diamond tip was used for the characterization of all the other implanted samples. A schematic representation of a typical nanowear scan as well as micrographs of the different diamonds tips used is shown in Figure 28.

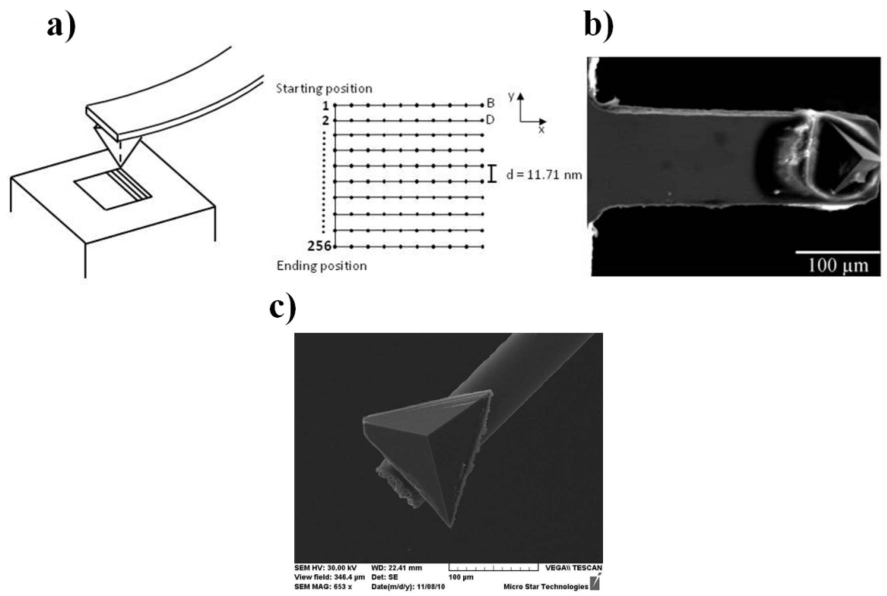

Figure 28. (a) Schematic representation of nanowear scan, (b) SEM micrograph of the DNISP diamond tip used in the nanowear scans, (c) Microstar diamond tip used on the nanowear scans, mounted on a sapphire cantilever.

The characteristics of both cantilevers and diamond tips used are presented in Table 7. The nanowear characterization scans were performed in 3x3 µm^2 areas with a speed of 6 µm/s and a constant loads between 2 µN and 8 µN, when using the Veeco Cp – II AFM, while a speed of 1.2 µm/s and loads that varied from 8 µN to 70 µN were used when using the Nanosurf AFM. Before the nanowear experiments, the sensibility of each cantilever was properly calibrated in a sapphire sample. The normal force applied by the AFM is given by the formula below, resulting from the multiplication of three different factors which are:

$$L = C_n S_Z U_{(A+B)-(C+D)}, \qquad \text{(Eq.40)}$$

the spring constant of the cantilever, C_n, given in Table 7, the sensitivity of the photodetector S_Z, that is determined by performing a force plot in the calibration sample and corresponds to the inverse of the slope of the linear contact region of the force-plot, and finally the measured signal variation, $U_{(A+B)-(C+D)}$, according to the detector represented in Figure 26a). A sapphire calibration sample was chosen since it is very a stiff sample, thus giving a linear response in contact region of the force plot.

The scans were performed with a resolution of 256 lines. The final worn areas were then observed in the same AFM in contact mode using silicon standard tips MPP31 with a 100 nN normal force. The total volume removed, V_R, for each nanowear scan was calculated based on the following equation

$$V_R = A_S . d_{ave}, \tag{Eq.41}$$

where A_S stands for the area of the scan, in this case 9 µm^2, and d_{ave} for the average depth after each scan, calculated from 8 height profile measurements. The wear rates, Q, were calculated by dividing the total worn volume V, by the total sliding distance D. The total sliding distance, D, can be easily calculated by multiplying three parameters: the length of the scan, L_{gth} of the scan, a factor of 2 since the tips performs each line of the scan twice, and finally the resolution of the scan, r_{es}. The wear rate can be then given by

$$Q = \frac{V_R}{D} = \frac{V}{2L_{tgh}r_{es}}, \tag{Eq.42}$$

where the length L_{gth} and resolution r_{es} of the scan have assume values of 3 µm and 256 lines, respectively, which correspond to the experimental conditions used in the present thesis.

Table 7. Characteristics of the AFM tips and cantilevers used in the nanowaer experiments.

	Veeco™ DNISP		**Microstar™ TD**	
	Cantilever	**Tip**	**Cantilever**	**Tip**
Material	Stainless steel	Diamond	Sapphire	Diamond
Geometry	Rectangular	Triangular pyramid	Rectangular	Triangular pyramid
Dimensions	Length, l = 340 – 350 µm Width, w = 112 – 115 µm Thickness, t ≈ 13 µm	Height, h ≈ 45 µm Tip angle ≈ 93º ** Tip radius*** R ≈ 325 nm ±145 nm	Length*, l = 508 µm Not measured Thickness, t ≈ 21 µm*	Height* h ≈ 104 µm Not measured Tip radius*** R ≈ 57 nm ±13 nm
Elastic properties	Spring constant C_n* = 188 N/m	-	Spring constant C_n*= 177 N/m	-
Resonant frequency	f_0*= 61 kHz	-	f_0*= 60 kHz	-

***** Values specified by the manufacturer
** Angle between a face and the opposite edge of the pyramid
******* Value obtained from SPIP™ software

3.3.4 X-RAY DIFFRACTION

X-ray Diffraction (XRD) is a powerful nondestructive characterization technique used to uniquely identify the crystalline phases present in materials and also to measure the structural properties of those same phases, such as, strain state, grain size, epitaxy, phase composition, preferred orientation, and defect structure [231]. The diffraction effect can only be observed when electromagnetic radiation impinges on periodic structures with a characteristic dimension in the order of the length scale of the wavelength of the incoming radiation. Since interatomic distances in both crystals and molecules vary within a range of 0.15 – 4 nm, the corresponding photon energies in the electromagnetic spectrum with the wavelength of x-rays ranges between 0.3 and 8 keV, respectively [232].

The diffraction phenomena of x-rays by crystals are directly related to certain phase relations between two or more waves. The differences in phase and amplitude between waves directly arises from the different path lengths traveled by each wave [233]. The geometrical relation that describes the x-ray diffraction as result of constructive and destructive interference interaction of waves is know in the literature as Bragg´s law [234].

$$n\lambda = 2dsin\theta^{d}, \qquad \text{(Eq.43)}$$

where d represents the interplanar distance given by

$$d = \frac{a}{\sqrt{h^2 + k^2 + l^2}}, \qquad \text{(Eq.44)}$$

where h, k and l are Miller indexes of the Bragg´s plane. For a cubic system, being a the cell parameter. The Bragg´s equation can be then rewritten as

$$sin\theta^{d} = \frac{\lambda\sqrt{h^2 + k^2 + l^2}}{2a}. \qquad \text{(Eq.45)}$$

Fundamentally this law provides the needed conditions so that a plane wave can be diffracted by a family of planes within the crystalline structure of the solid. A geometrical description of the diffraction phenomenon can be found in Figure 29, where two electromagnetic waves impinge on a crystalline sample with an incident angle θ, relatively to the crystallographic planes separated by a distance d.

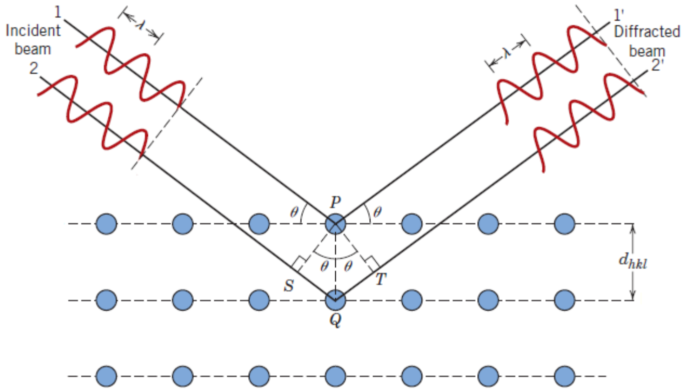

Figure 29. Schematic representation of the diffraction phenomenon of electromagnetic waves by atomic planes [235].

In the present thesis the samples were characterized in most cases by grazing or glancing incidence x-ray diffraction (GIXRD) instead of the typical Bragg-Brentano ($\theta - 2\theta$) configuration because of the small depth of the implanted regions. The GIXRD is a very useful method for thin film or thin surface layers characterization, which is the case of the implanted/annealed samples studied in the present work. The configuration of a GIXRD is shown in Figure 30a). In a GIXRD measurement the angle between the incoming beam and the sample surface is very small, close to a few degrees or even less, which increases the path of the x-ray in the thin film. The difractogram acquisition is performed in a way such that α, the grazing angle, is kept constant while the detector is moved along the 2θ circle. This represents the major difference when compared to the ($\theta - 2\theta$) scans, where θ is continuously changing during the measurement. The scattering angle, 2θ in the grazing incidence geometry also corresponds to the angle between the outgoing beam and the direction of the incoming beam whereas the angle between the surface and the outgoing beam is $(2\theta - \alpha)$ [232].

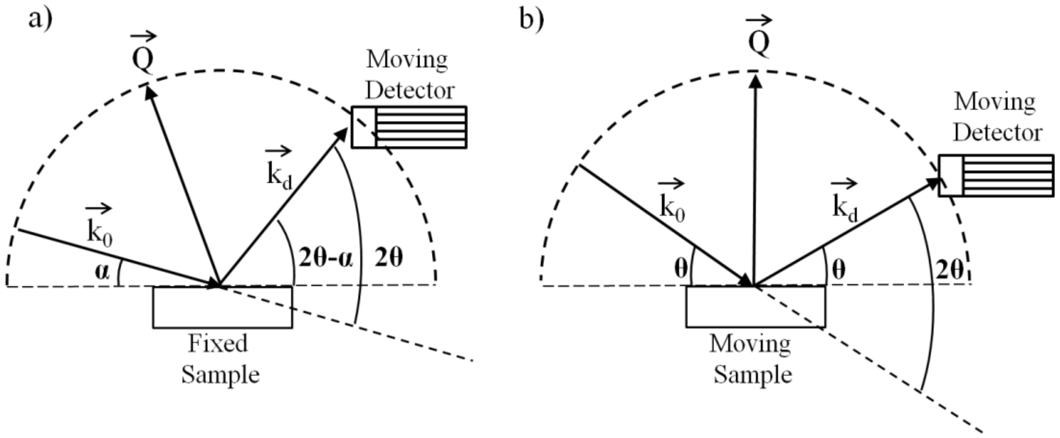

Figure 30.(a) Schematic representation of a GIXRD geometry, (b) schematic representation of Bragg-Brentano geometry.

There is a direct consequence in acquiring a difractogram with a fixed grazing incidence angle. While for a ($\theta - 2\theta$) scan the direction of the scattering vector $\vec{Q}$, defined by the wave vector difference, - Figure 30a) remains perpendicular to the surface, in the case of GIXRD this does not happen. This means that the angle between the diffracting lattice planes and the sample surface vary during the course of a GIXRD measurement. The GIXRD measurements are best performed in polycrystalline thin films since the reflections for a determined Bragg angle θ, are caused by sets of lattice plans that are neither parallel with the surface nor with each other. In fact, epitaxial or highly textured films may not show any reflection under grazing incidence geometry [236].

In the present thesis the grazing X-rays diffraction measurements were carried out using a Bruker D8 Discover apparatus with a Göbel mirror and a nickel (Ni) filter. The X-rays were generated by a Cu source with a Kα radiation ($\lambda_{\mathrm{AVERAGE}}$ = 1.5418 Å), that has two components, Kα_1 (1.5405 Å) and Kα_2 (1.5443 Å). The chosen grazing angle was 1.5º. The Peaks identification was carried out using the *Pearson´s Crystal data – Crystal structure for inorganic compounds, version 1.0* software [237].

3.3.5 RUTHERFORD BACKSCATTERING SPECTROMETRY

The Rutherford backscattering spectrometry (RBS) is a widely used surface analysis technique where a beam of highly energetic low mass ions is used as a probe to perform the sample characterization. The principles of the RBS technique are relatively easy to follow. Typically, a beam of $^4He^+$ ions with an energy comprehended between 1-3 MeV are directed into a sample. Aside other interactions, ions collide elastically with the atoms within the sample and are scattered back into a suitable detector, typically a Si detector, which measures the energy of the particles that reach it. Based on the information collected, the energy, one is able to perform not only the compositional analysis of the sample but also to extract information regarding the elements distribution within the sample and the sample thickness [238].

The RBS technique is based on four basic physical principles [239]:

(1) Kinematic factor – The kinematic factor K_i relates the initial energy of the incoming ions E_0 with their energy after the elastic collision with the atoms of the solid E_1 by the following expression

$$E_1 = K_i E_0. \qquad \text{(Eq.46)}$$

A schematic representation of the collision can be found in Figure 31. Based on the conservation of kinetic energy and momentum one can find the following expression for K_i

$$K_i = \left(\frac{M_1 cos\theta + (M_2^2 - M_1^2 sen^2\theta)^{\frac{1}{2}}}{M_1 + M_2} \right)^2, \qquad \text{(Eq.47)}$$

where M_1 and M_2 represent the mass of the incoming ion and the mass of the target, respectively, and θ the backscattering angle of the incoming ion.

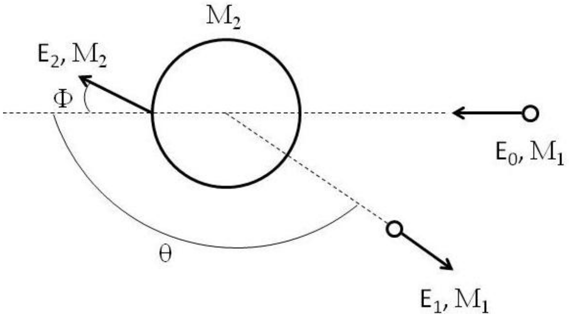

Figure 31. Schematic representation of an elastic collision between an incoming ion of mass M_1 and energy E_0, with a target atom at rest with a mass of M_2.

The kinematic factor is used to perform isotope/mass identification, since E_0 is known and E_1 and θ are experimentally set, the only unknown parameter being M_2, that can be determined using the above equations thus finding the target element .

(2) Scattering cross section – The scattering cross section parameter reflects the probability of the occurrence of a scattering event, described above, for a specific angle θ, which is typically the detector angle of the experimental setup. Considering Q_i, the total number of incident particles in a sample with a know thickness and density, t and N, respectively, the total number of detected particles that reach the detector with the energy within an interval of $[E_j, E_{j+r}]$, for a given solid angle Ω, is given by [239]

$$Y = \Omega Q_i N t \sigma, \qquad \text{(Eq.48)}$$

where σ represents the scattering cross section that is defined by the following integral

$$\sigma = \frac{1}{\Omega} \int_{\Omega} \frac{d\sigma}{d\Omega} d\Omega. \qquad \text{(Eq.49)}$$

For small values of Ω, which fits most of the experimental situations it is then more convenient to use the differential scattering cross section, which is given by the following expression in laboratory frame [239],

$$\frac{d\sigma}{d\Omega}=\left(\frac{Z_1Z_2e^2}{4E}\right)^2\frac{4}{sen^4\theta}\frac{\left(\left(1-\frac{M_1^2}{M_2^2}sen^2\theta\right)^{\frac{1}{2}}+cos\theta\right)^2}{\left(1-\frac{M_1^2}{M_2^2}sen^2\theta\right)^{\frac{1}{2}}}, \tag{Eq.50}$$

where Z_1 and Z_2 represent the atomic number of both incident ion and target ion, respectively and E the incident energy of the ions. The above equation shows that the differential cross section is directly proportional to Z_2^2. This shows that heavy atoms are more efficient scattering centers than light elements thus allowing understand that RBS technique is more sensible to heavy elements than light ones.

(3) Energy loss and stopping power – The average energy loss by a particle moving in a dense medium or stopping power is a parameter of great importance to perform in-depth analysis. As previously said, when the incident particle penetrates into a solid, it interacts with both nuclei and electrons of the target. For the RBS case, since light ions are used and energies are in the MeV range, the nuclear stopping can be neglected. In Figure 32a) is represented a scheme of an ion travelling inside a solid with the respective energy variation. The energy-loss of an ion just before an impact after having travelled a distance $x/cos\theta_1$ can be given by the following expression

$$E=E_o-\int_0^{\frac{x}{cos\theta_1}}\frac{dE}{dx}d\mathrm{x}. \tag{Eq.51}$$

Since the RBS is a surface characterization technique, where most of the backscattering events occur in the surface or near surface region, it is a plausible approximation to consider the energy-losses (dE/dx) within the solid as roughly constant (surface approximation) [239]. The above equation can then be written as

$$E=E_o-\frac{\Delta x}{\cos\theta_1}\left(\frac{dE}{dx}\right)_{in}, \tag{Eq.52}$$

where for the surface energy approximation $(dE/dX)_{in}$ is calculated for $E=E_0$. Using an analogous line of thought, it becomes easy to write the energy equation for a particle after the scattering event at a depth *Δx*, having in consideration the energy lost in the impact and the energy lost during the exit path

$$E_1 = K_i E - \frac{\Delta x}{\cos\theta_2}\left(\frac{dE}{dx}\right)_{out}, \qquad \text{(Eq.53)}$$

eliminating *E* from the above equations one can get

$$K_i E_o - E_1 = \left[\frac{K_i}{\cos\theta_1}\left(\frac{dE}{dx}\right)_{in} + \frac{1}{\cos\theta_2}\left(\frac{dE}{dx}\right)_{out}\right].\Delta x, \qquad \text{(Eq.54)}$$

the energy parameter K_iE_0 represents the edge of the backscattering spectrum in Figure 32b), and corresponds to the maximum detected energy resulting from the scattering on surface elements. Introducing the symbol *ΔE*, as the difference between K_iE_0 and E_1 the above equation is rewritten as

$$\Delta E = [S].\Delta x, \qquad \text{(Eq.55)}$$

where *[s]* is called the energy loss factor or simply *S* factor. The *[S]* is given by

$$[S] = \left[\frac{K_i}{\cos\theta_1}\left(\frac{dE}{dx}\right)_{Eo} + \frac{1}{\cos\theta_2}\left(\frac{dE}{dx}\right)_{K_iE_0}\right]. \qquad \text{(Eq.56)}$$

It is possible to write the above equations in terms of stopping cross section rather than in terms of energies-loss *(dE/dx)*

$$\Delta E = [\varepsilon].N\Delta x, \qquad \text{(Eq.57)}$$

where

$$[\varepsilon] = \left[\frac{K_i}{\cos\theta_1}(\varepsilon)_{in} + \frac{1}{\cos\theta_2}(\varepsilon)_{out}\right] \qquad \text{(Eq.58)}$$

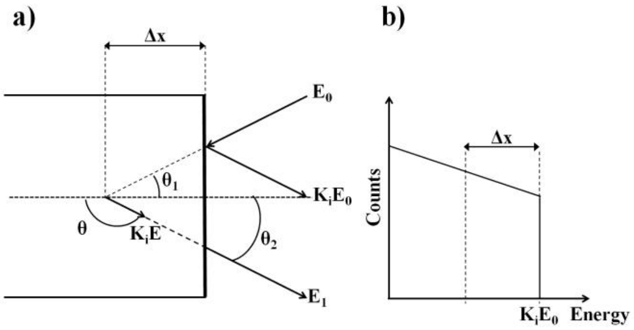

Figure 32. (a) Schematic representation of a projectile inside a solid, (b) schematic representation of an RBS spectra.

(4) Energy straggling – The last important parameter for the RBS technique is the energy straggling. When a beam of particles moves through a medium each particle will suffer individual encounters. Despite the fact that initially all particles had the same energy, these events will generate an energy broadening of the beam. This effect is commonly designated as energy straggling, and can be calculated by [239]

$$\delta E_S = \left((8ln2)4\pi e^2 Z_1^2 Z_2 N x\right)^{1/2}. \qquad \text{(Eq.59)}$$

The above formula shows that this phenomenon is energy independent, depending mainly from the target nature *(Z_2Nx)*

3.3.5.1 Ion channelling

When a well-collimated beam of ions is incident on a single-crystal target along one of its major crystallographic axes or planes (perfectly aligned), the charged particles will experience a steering force induced by the collective potential of the regular crystal structure. Thus, the periodic rows of atoms and planes of the crystalline structure of the target form channels that guide and keep the moving particles confined within these channels [240]. This phenomenon is designated channeling and it is represented below in Figure 33.

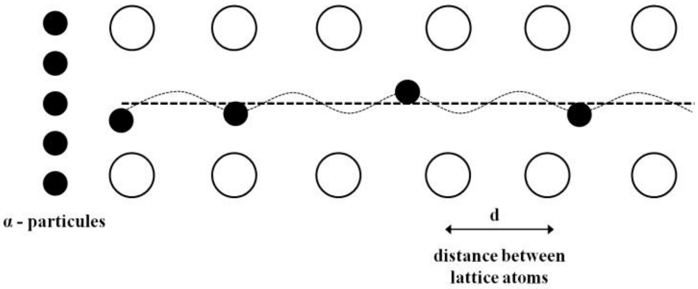

Figure 33. Schematic representation of the channeling effect of α-particles.

The fraction of channeled ions may reach impressive values of 95-98 % for target samples of high crystallinity quality. The channeled ions are very sensitive to very small displacements of the target atoms from their respective lattice positions, thus providing information on the crystalline quality and defects [241]. Figure 34 schematically represents the difference between a “channeled” or as typically called aligned spectrum and a random spectrum, for two different set of samples: a crystal and a damaged crystal. The random spectrum designates a spectrum that was not aligned with any particular crystallographic direction of the sample. The small peak observed at the higher energy for the aligned spectra of the perfect crystal, Figure 34a), is called the surface peak. The surface regions of the crystals are typically imperfect regions with displaced atoms, thus backscattering a large portion of the beam. As the beam penetrates into the solid more ions from the beam are deflected to random directions, due to lattice imperfections or defects or even due to beam divergence, causing an increase in the number of counts. For the damaged crystal case, Figure 34b) which is a typical case of implanted samples, it is possible to observe a broad peak corresponding to the highly defective/damaged region of the crystal, from where a significant part of the beam is scattered. In these situations the alignment is performed in the region immediately behind the defective zone, which brings an extra difficulty to aligned the sample

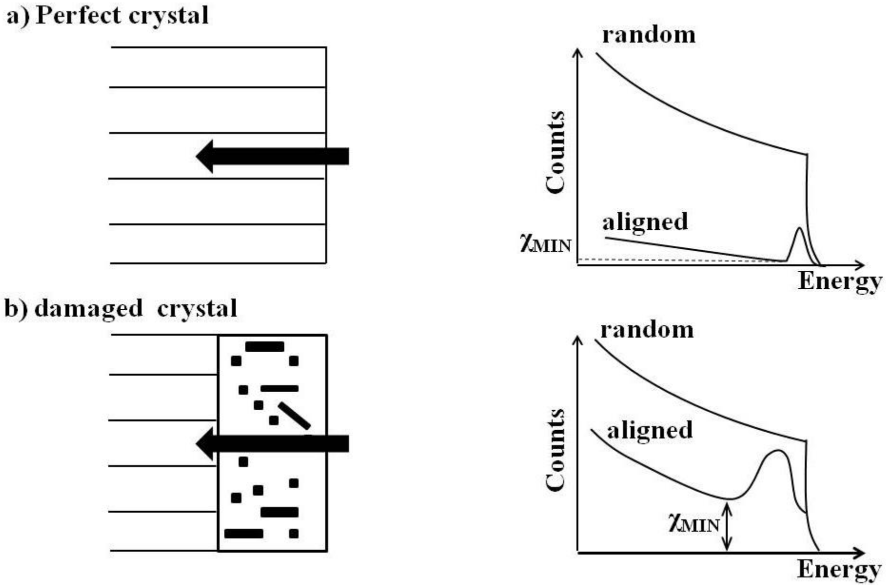

Figure 34. Schematic representation of the channeling in two different situations and respective RBS spectra representation (a) perfect crystal, (b) damaged crystal, adapted from [241].

3.3.5.2 LATR RBS/-channeling installation

The RBS and RBS-C measurements of the present work were performed using a Van de Graff accelerator with energy of 2 MeV using a beam of He^+ particles. The Van de Graff accelerator of the LATR facility can reach a maximum energy of 2.5 MeV for single charge ions, allowing also to use a H^+ beam. A schematic representation of the experimental installations is shown in Figure 35 and will be briefly explained. A more detailed description can be found in [202, 242].

The $^4He^+$ beam of particles generated in (1) is guided to RBS-C line by means of application of magnetic field (2) (4.809 kG for the 2.0 MeV $^4He^+$ beam) and reaches the slits (3)(S_1 and S_2) which constitute a part of the beam stabilizer system, being respective current measured in a beam-stopper tantalum that is electrically connected to a charge integrator. The beam is then collimated using a set of collimators (4) with a section area of 1 mm^2 separated by distance of 2.45 m that guarantees a maximum angular divergence of ≈ 0.02º.

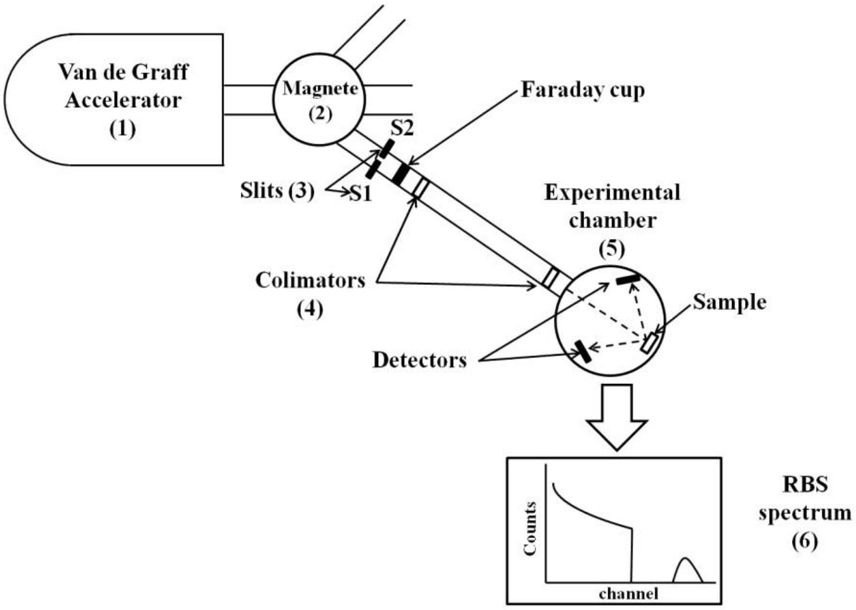

Figure 35. Schematic representation of the RBS-channeling installations at the LATR facility, adapted from [243].

The samples are placed in the sample holder attached to a goniometer in the experimental chamber (5). The goniometer, controlled by a PC, enables to rotate the sample in two different axes, the vertical one, commonly represented by θ which rotates in the horizontal plane (with small increments of 0.04º) and horizontal plane Φ, that rotates in the in the vertical plane (with small steps of 0.02º). During the measurements the experimental chamber is placed under vacuum, 10^{-6}-10^{-7} mbar by means of a turbomolecular rotary pump set and the sample holder is placed under a polarization of ≈ +200 V, to minimize the emission of secondary electrons while beam interacts with the sample. The experimental chamber used in the present work has an IBM geometry. In the experimental chamber three solid-state detectors are present at three different positions to the incoming beam direction: one at 140º, with an energy resolution of 12 keV and solid angle of ≈ 4 msr; two at ±165º, with energy resolution of 12 keV and solid angles of 11.4 msr. The RBS spectra presented were obtained using the detector at -165º with a total charge of 5 µC.

Some of the experimental RBS spectra were simulated using the NDF© code [244] to evaluate both implanted profiles and to confirm the implanted fluences. The NDF© is a worldwide known code developed by Barradas, Jeynes and Webb to specifically analyze ion beam characterized samples data, like extract element depth profiles, under techniques such as: RBS, ERDA (elastic recoil detection analysis), PIXE (particle induction X-ray emission) and non-resonate NRA (nuclear reaction analysis) where beams with an energy in the order of MeV´s are used. The analysis can be carried for any ion or target and any geometry, having as an advantage the possibility to perform different types of simulations for different samples at the same time.

3.3.6 WETTABILITY AND SURFACE FREE ENERGY

The contact angle determination represents one of the most inexpensive and easiest existing methods for surface characterization. As simple as placing a drop of liquid upon a surface, the direct observation of the liquid interaction with the solid allows one to extract relevant information concerning the studied samples, namely concerning his wettability nature, hydrophobic or hydrophilic. Since this technique is sensitive to the first few surface monolayer's of the solid, the contact angle determination is also suitable to characterize thin-films. Besides the contact angle, one may also determine the surface energy of a solid surface, this will be explained ahead.

3.3.6.1 Surface tension and surface free energy

The wettability measurements of a surface, by a determined liquid, are based in a triphasic equilibrium established in the line of contact or wetting perimeter between the solid/liquid/vapor. The established equilibrium can be expressed in terms of surface tensions. The surface tension is a physical quantity that may be interpreted as a force per unit length or energy per unit area, (J/m^2 or N/m). For a better perception of these two different conceptions one may follow the next example. Let's take into consideration the classical experiment of a soap film initially in equilibrium that is stretched over a movable wire frame - Figure 36. The work needed to increase the area of the film by a $dA = 2L_d dx$ (two surface areas are created, top and bottom) due to the actuation of the force F is given by [245]

$$dw = Fdx = F\left(\frac{dA}{2L_d}\right) = \gamma . dA, \qquad \text{(Eq.60)}$$

where γ represents the surface tension. Looking to the above equation is plain to see that the surface tension may correspond simultaneously to the force per unit of length that acts parallel to the surface or the work/energy that must be supplied to system to increase the surface area by one unit.

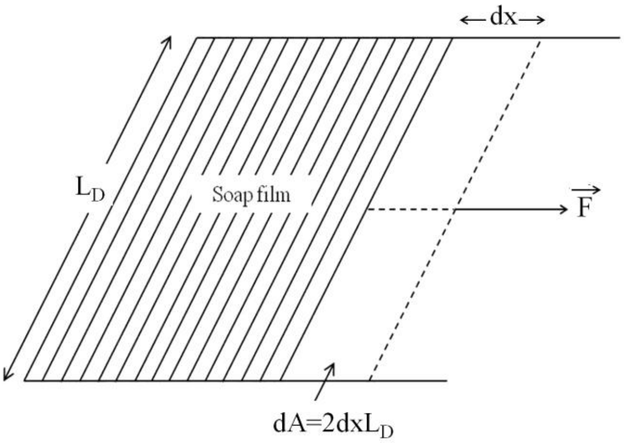

Figure 36. A schematic representation of a soap film stretched across a wire frame with one movable side.

From a molecular point of view the concept of surface tension must be interpreted in a different way. For molecules it is generally energetically more favorable to be surrounded by other molecules. Within the "bulk" liquid the molecules are attracted to each other by different types of interaction such as van der Waals or hydrogen bond, for example. At the surface, the molecules are only partially surrounded by other molecules since the total number of neighboring molecules is smaller comparatively to a molecule within the liquid. This places a surface molecule in an energetically unfavorable situation. In order to bring a molecule from the bulk to the surface, work has to be done. From this point of view the surface tension γ, can be interpreted as the energy required to bring molecules within the liquid to the surface and create new surface area. For this reason, the surface tension is often termed also as surface free energy. For one component liquids, surface tension and surface free energy are equal, but the same does not happen to crystalline solid surfaces. For this reason, in terms of nomenclature, in the present thesis, the term surface tension was adopted explicitly for liquids and the term surface energy or surface free energy was adopted for solids [245-247].

3.3.6.2 Young´s equation

When a drop of liquid is placed upon a solid surface the triple interface, formed between the solid, liquid and surrounding gas will move in response to forces arising from the three interfacial tensions until an equilibrium position is reached. A schematic representation of this situation is shown in Figure 37, where a drop of liquid (L) is placed on a flat solid surface (S) in contact with the vapor of the liquid (V) which corresponds to the third phase. The angle, θ, established between the solid surface and the tangent to the liquid surface at the line of contact with the solid is known as contact angle, and depends on both liquid and solid properties [248]. The classic energy balance for this situation, for an idealized interface between an ideal non-deformable solid, an infinitely deformable liquid and a gas, is given by the Young´s equation,

$$\gamma^{LV} cos\theta = \gamma^{SV} - \gamma^{SL}, \qquad \text{(Eq.61)}$$

where γ^{LV}represents the surface tension of the liquid in equilibrium with his vapor, θ the contact angle, described above, γ^{SV} the surface free energy of the solid in equilibrium with the vapor and finally γ^{SL} the interfacial tension between the solid and the liquid.

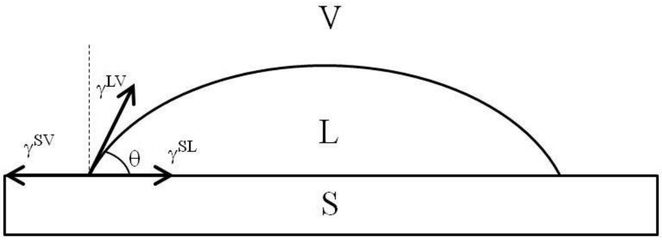

Figure 37. Forces acting at the triple interface for a drop liquid on flat solid surface.

The contact angles can be calculated directly applying the Young´s equation, if several assumptions are valid. These assumptions are for example [249]: the solid surface is rigid and non-deformable; the solid surface is immobile and cannot re-orient in response to the liquid; the solid surface is smooth, (RMS values < 0.1 nm); the solid surface is homogenous and uniform thus lacking heterogeneous domains or contaminants; the liquid phase surface tension is known and remains constant, disregarding the possibility of contamination from both solid and vapor, which will change the surface tension; the solid and liquid phases do not interact beyond the three-phase equilibrium (no surface swelling) and, finally, the spreading pressure on the solid for the liquid on the solid is zero, meaning that liquid vapor does not adsorb on the solid surface to change the solid surface-free energy.

In terms of laboratory conditions it is very hard to conciliate all the mentioned assumptions. In the past some changes have been made to account for the influence of other parameters such as roughness (see section § 2.1.5.) Despite the distance from ideal conditions, the Young´s equation has been widely used [250].

3.3.6.3 Work of adhesion and work of cohesion

In this section some important concepts will be introduced for understanding the surface free energy determination. In terms of thermodynamics, the work of adhesion W_{AB} refers to the free energy difference between two different states, the first, when two different phases A and B are in contact in equilibrium and the second comprising the two phases separated in equilibrium in vacuum, that is, in equilibrium with their own vapor - Figure 38a). The work of adhesion is defined in terms of the surface energies according to the following expression [251]

$$W_{AB} = \gamma_A + \gamma_B - \gamma_{AB}, \qquad \text{(Eq.62)}$$

where γ_A and γ_B represent the surface energies of two different phases A and B, and γ_{AB}represents the respective interfacial energy between the two phases. From an analogous point of view, the work of cohesion refers to a situation where there is only one phase present (Figure 38b), and so is defined as

$$W_{AA} = 2\gamma_{a.} \qquad \text{(Eq.63)}$$

The term “work of adhesion” is sometimes used also to designate the free energy difference, not between the two phases A and B in contact in equilibrium and the two phases separate in equilibrium in vacuum, but rather between to two phases A and B in contact in equilibrium and two phases separate in the same enclosure equilibrium with the vapor present. The work of adhesion under these conditions can be written as [251]

$$W_{AB}^{*} = \gamma_{AV} + \gamma_{BV} - \gamma_{AB}, \qquad \text{(Eq.64)}$$

γ_A differs from γ_{AV} by the spreading pressure, π_A, which can be interpreted as the lowering of the surface energy of material in vacuum by adsorption of the vapor

$$\pi_A = \gamma_A - \gamma_{AV}, \qquad \text{(Eq.65)}$$

with,

$$W_{AB} - W_{AB}^{*} = \pi_A + \pi_B. \qquad \text{(Eq.66)}$$

The spreading factors are of difficult determination and for the sake of simplicity, in most general cases, these terms are neglected [252]. Considering a realistic example of a drop of liquid on a surface, in equilibrium with the vapor, the work of adhesion is then described by

$$W_{SL} = \gamma_{SV} + \gamma_{LV} - \gamma_{SL}. \qquad \text{(Eq.67)}$$

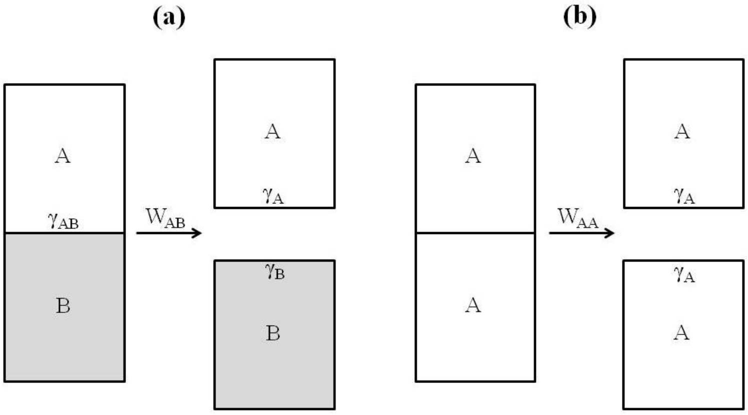

Figure 38. Schematic representation of (a) work of adhesion, (b) work of cohesion.

3.3.6.4 Methods for surface energy determination

The basis for the surface energy determination, of the most used methods, are based on the pioneer idea developed by Fowkes [253, 254], that states the surface tension of a liquid or surface energy of a solid, results from a sum of independent components, associated with specific interactions, as it is shown in the following equation

$$\gamma_S = \gamma_S^d + \gamma_S^p + \gamma_S^H + \gamma_S^i + \gamma_S^{ab} + \gamma_S^0 = \gamma_S^d + \gamma_S^{nd}, \qquad \text{(Eq.68)}$$

where γ_S^d, γ_S^p, γ_S^H, γ_S^i and $\gamma_S^{ab}$are the dispersive, polar, hydrogen (related to hydrogen bonds), induction and acid base components, respectively, while γ_S^0 designates all remaining interactions. For the sake of simplicity, it is rather consensual to group al the none-dispersive interactions in above equation in one term, γ_S^{nd}, thus converting the above equation into

$$\gamma_S = \gamma_S^d + \gamma_S^{nd}. \qquad \text{(Eq.69)}$$

Fowkes mainly researched two phase systems containing both nonepolar liquid and solid, in which the dispersion interactions, corresponding only to London interactions, appear. Considering such a systems Fowkes determined the interfacial surface energy by the following expression [255, 256]

$$\gamma_{SL} = \gamma_{SV} + \gamma_{LV} - 2\sqrt{\gamma_{SV}^d \gamma_{LV}^d}, \qquad \text{(Eq.70)}$$

where the superscript *d* indicates the dispersive components of both solid and liquid. In the case of one of the phases being polar, the above equation presents also a good approximation [255, 256].

Owens and Wendt [257] developed a new method for the surface energy calculation changing at some extent the ideas proposed by Fowkes. Owens *et al*. assumed that all the different components in which a surface energy could be decomposed, Equation 68, with the exception of the dispersive one, could be associated to a single term, the polar interaction γ_S^p. By doing so, the surface energy calculation is made taking into consideration both dispersion and polar intermolecular forces (due to Keesom and Debye interaction) that operate across the interface. The authors defined the work of adhesion between solid and liquid as

$$W_{SL} = 2\sqrt{\gamma_{SV}^d \gamma_{LV}^d} + 2\sqrt{\gamma_{SV}^p \gamma_{LV}^p} \qquad \text{(Eq.71)}$$

where the superscript *d* and *p* designate both dispersive and polar components. The solid-liquid interfacial tension can be written, according to Eq. 67 as

$$\gamma_{SL} = \gamma_{SV} + \gamma_{LV} - 2\sqrt{\gamma_{SV}^{d}\gamma_{LV}^{d}} - 2\sqrt{\gamma_{SV}^{p}\gamma_{LV}^{p}} \qquad \text{(Eq.72)}$$

Combining the above equation with the Young´s equation, Equation 61, one can obtain the following expression

$$\gamma_{LV}(1 + cos\Theta) = 2\left(\sqrt{\gamma_{SV}^{d}\gamma_{LV}^{d}} + \sqrt{\gamma_{SV}^{p}\gamma_{LV}^{p}}\right) \qquad \text{(Eq.73)}$$

From the above equation is possible to determine both dispersive and polar components from a determined surface. In order to do so, one must measure the contact angle with two different liquids from which the polar dispersive components are known and also the respective interfacial energy between those two same liquids. The surface components can be then determined solving a system of equations

$$\begin{cases} \gamma_{w}(1 + cos\Theta_{\mathrm{w}}) = 2\left(\sqrt{\gamma_{SV}^{d}\gamma_{w}^{d}} + \sqrt{\gamma_{SV}^{p}\gamma_{w}^{p}}\right) \\ \gamma_{DD}(1 + cos\Theta_{\mathrm{DD}}) = 2\left(\sqrt{\gamma_{SV}^{d}\gamma_{DD}^{d}} + \sqrt{\gamma_{SV}^{p}\gamma_{DD}^{p}}\right) \end{cases}, \qquad \text{(Eq.74)}$$

where the subscript w and DD designate both water and diiodomethane, the liquids used in the present thesis. For this method of surface energy calculation, the liquids choice must have in consideration a liquid with a dominant polar component and the second one with a strong dispersive one. Other liquids could also have been used as long as the requirements were fulfilled. Some flaws have been pointed out to the Owens-Wendt method, also known as geometric mean method, concerning the nature of the initial assumptions, more precisely the nature of the forces that act across the interface solid/liquid and should be taken into account in the work of adhesion. What Owens-Wendt designate as polar component is more likely to be a non-dispersive component that includes a broader range of interactions than van der Waals forces, for instances, asymmetric electron donor-electron interactions whose participation in the work of adhesion cannot be described by a geometric mean expression [258]. Nonetheless, the method has been defended by the practical point of view, not only for being mostly intuitive and mathematically convenient, but also in the specific case where one does not intend to assign any precise physical significance to the polar nondispersive term, but rather consider it as adjustable parameter that allows to estimate the amplitude of the deviation of the solid from a purely dispersive one [258]. The Owens-Wendt method was the method adopted for the energy calculation in the present thesis.

3.3.6.5 Determination of diiodomethane polar and dispersive components

Before the calculation of the surface energy of the samples, the properties of the acquired diidomethane, distilled two consecutive times for impurity removal, were evaluated. Both surface tension and interfacial tension, with water, were determined using the pendent drop method. The measured values presented some deviations when compared to the reference values (Table 8). For that reason it was decided to determine both polar and dispersive components of the diiodomethane rather than using the common literature values. The determination of the polar and dispersive components for the geometric mean method can be made by solving a set of two equations

$$\begin{cases} \gamma_{w/DD} = \gamma_{LVw} + \gamma_{LVDD} - 2\left(\sqrt{\gamma_{LVw}^{d}\gamma_{LVDD}^{d}} + \sqrt{\gamma_{LVw}^{p}\gamma_{LVDD}^{p}}\right) \\ \gamma_{LVDD} = \gamma_{LVDD}^{d} + \gamma_{LVDD}^{p} \end{cases} \qquad \text{(Eq.75)}$$

To solve the system of equations, the author assumed the polar and dispersive components of the water from the literature [259]. The values used of the dispersive and polar components of water, as well as the respective calculated components of the diiodomethane are listed in Table 9

Table 8. Comparison between the experimental and literature values of the diiodomethane surface tension and interfacial tension with water

	Surface tension (mN/m)	Interfacial tension with water (mN/m)
Reference Diiodomethane [260]	50.2	48.2
Experimental values	48.2 ± 0.2	51.5 ± 0.3

Table 9. Surface Free Energy Components for the liquids tests, water and diiodomethane

Liquid	Surface free energy ($mJ.m^{-2}$)	Dispersive component, γ^d ($mJ.m^{-2}$)	Polar component, γ^p ($mJ.m^{-2}$)
Water [259]	72.8	21.8	51.0
Diiodomethane	48.2	44.4	3.8

3.3.7 WETTABILITY MEASUREMENTS – SESSILE DROP METHOD

The contact angle measurements made in the present thesis were performed using the sessile drop method. This specific method was chosen due to its experimental simplicity. The procedure for the contact angle determination, according to this method, is as simple as placing a drop of liquid in a horizontal surface and to directly or indirectly determine the corresponding angle between the solid and the respective liquid. The direct angle measurements can be made by simply taking a picture of the drop and measuring the respective angle whereas the indirect angle determination is based on equations. The contact angles determined in the present thesis were all calculated using an indirect method. The indirect contact angle determination was based on the Laplace´s capillarity equation, represented below

$$\Delta P = \gamma_{LV}\left(\frac{1}{R_1}+\frac{1}{R_2}\right), \qquad \text{(Eq.76)}$$

where ΔP represents the pressure difference at the liquid/vapor interface, γ_{LV} the surface tension of the liquid, and R_1, R_2 the curvature radius of the main interfaces. The strategy employed for the contact angle determination is based on the construction of a function which expresses the error between the experimentally observed profile of a drop and a theoretical Laplace´s curve, thus representing a solution of the Laplace´s capillarity equation [261]. In order to this method to be applied no other forces can be acting on the system beside the gravitation one, and a proper system of differential coordinates must be used. For a more detailed description of the coordinate system can be found in [261]. All these calculations were performed using the software *ADSA-P*, (Axissymmetric Drop Shape Analysis-Profile) developed by Neumann and his collaborators [262]. The software can calculate simultaneously the radius, volume, surface tension, surface area and contact angle, by just giving an input of the gravity acceleration, liquid density and some coordinates corresponding to some experimental points of the drop.

A schematic representation of the experimental setup for the contact angle determination is represented in Figure 39. The samples were placed in a chamber (Ramé-hart®, 100-07 model), with two quartz widows, and the drops were placed on the sample using a microsyringe, which allows to regulate the volume of the drop. Once the drops contact with the surface, a set of images are acquired using a JVC color TK-1070 video camera, that is coupled to a Wild M3Z microscope that enables the magnification of the drop. The contact angle measurements performed in the present thesis with both water and diiodomethane were carried out at room temperature for 30 seconds.

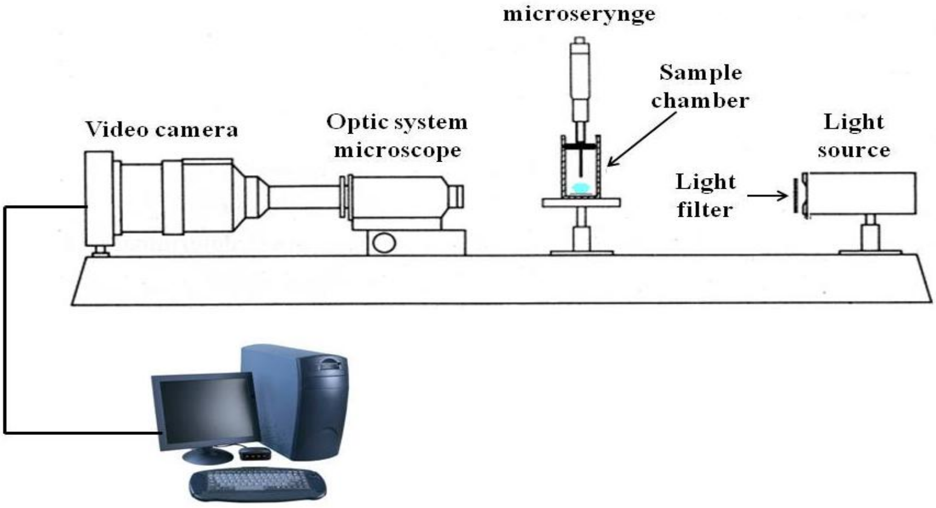

Figure 39. Schematic representation of the experimental setup for the contact angle measurements.

3.3.8 X-RAY PHOTOELECTRON SPECTROSCOPY

Surface analysis by x-ray photoelectron spectroscopy (XPS), also known as electron spectroscopy for chemical analysis (ESCA) is performed by irradiating a sample with monoenergetic x-rays and analyzing the electrons emitted [263]. The photoelectric effect represents the basis of this technique. When a photon having an energy E_{photon}, impinges on a sample surface, as schematically displayed in Figure 40, an electron bound to the nucleus with a binding energy, E_b, is ejected with a kinetic energy E_k, related by:

$$E_{photon} = h\nu = E_b + E_k + \phi_{spe}, \quad \text{(Eq.77)}$$

where ϕ is the work function of the spectrometer (not of the material). The above equation can be rewritten as:

$$E_b = h\nu - E_k - \phi_{spe}, \qquad \text{(Eq.78)}$$

and

$$E_k = h\nu - E_b - \phi_{spe}, \qquad \text{(Eq.79)}$$

From the above equations is possible to observe that E_b and E_k vary in a symmetrical way. In a photoelectron spectra, the intensity of ejected electrons as a function of their binding energy is registered [264].

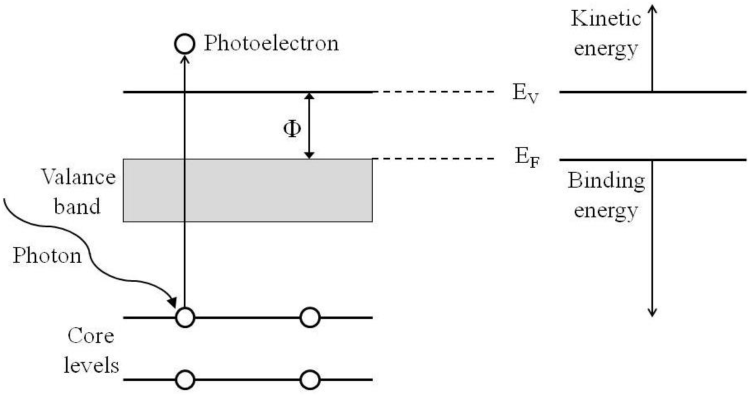

Figure 40. Schematic of the photoemission process, adapted from [265].

The study “objects” of this specific spectroscopy technique are the photoelectrons issued from the atomic core, having binding energies (BE) to the respective nucleus smaller than the exciting energy. The characteristic BE of the core electrons, represent a true fingerprint of the atom where they are issued from, are obtained by the difference between the incident X-photon energy and the corresponding kinetic energies Figure 40. Spectra are then obtained through the representation of the electron intensity versus BE [264].

The analysis of the characteristic peaks of BE allows the clear identification of all elements by their core photoelectrons, with the exceptions of the hydrogen and helium, which correspond to elements where the core electrons are nonexistent. Furthermore, despite the large invariance of the core electrons upon chemical bonding formation, small variations in BE (chemical shifts) can be detected, which provides further relevant information concerning the chemical surrounding of the inspected element. For instance, for an electron donor (a more electronegative element) the chemical shift will be positive (BE increases), whereas for an electron acceptor (a less electronegative element) the chemical shift will be negative (BE decreases). The additional information provided by the chemical shift as well as the ability of this technique to distinguish different oxidation states for a given element, largely contributes to classify XPS as a powerful analytical and elemental tool [264].

The mounting schematically represented in Figure 41b) is the model XSAM800, from KRATOS, shown in Figure 41a). The whole setup must be under ultrahigh vacuum conditions (usually around 10^{-7} Pa). The excitation radiation is in the X-ray range of the electromagnetic spectrum and the used anodes were magnesium and aluminium, which emit radiation with energies of 1253.6 and 1486.6 eV, respectively. For all the samples the charge shift was corrected using as reference the binding energy of aliphatic C 1s (285 eV).

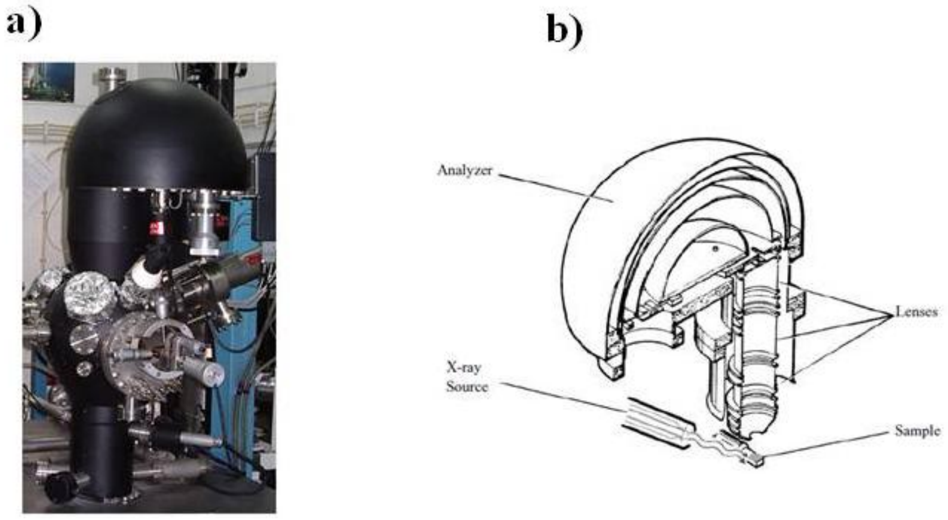

Figure 41.(a) Photograph of a XSAM800 KRATOS spectrometer, (b) Simplified cross-section of an XPS spectrometer with a dual anode X-ray source and without monochromator [264].

3.3.9 DISPLACEMENT SENSING INDENTATION

The displacement sensing indentation method was developed to simultaneously determine both hardness, *H*, and Young´s modulus, *E*, resulting from a cycle of indentation, loading and unloading, respectively, which is schematically represented in Figure 42a) and Figure 42b). The curves are generated by a continuous monitoring of the indenter, controlled by a piezoelectric, with the respective displacement. As the indenter is pressed into the sample both elastic and plastic deformations occur, resulting in a formation of a hardness impression with the shape of the respective used indenter. Upon the withdrawal, only the elastic portion of the displacement is recovered thus allowing the determination of respective Young´s modulus.

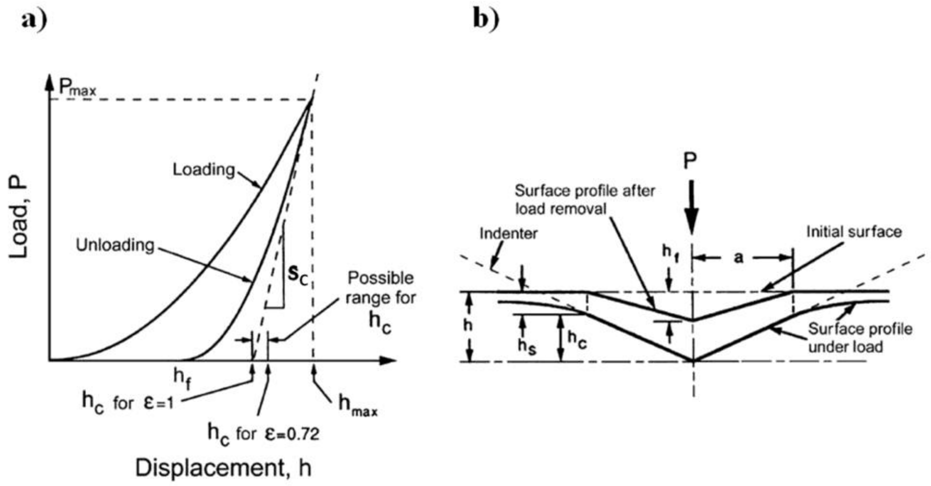

Figure 42. (a) Schematic representation of typical load–displacement cycle ,(b) the deformation pattern of an elastic –plastic sample during and after indentation (h$_{max}$ – maximum depth, h$_c$ – contact depth, h$_s$ – surface displacement at the contact perimeter, h$_f$ – final depth after elastic recovery, S$_c$ – initial unloading stiffness) [266]

The hardness, or often designated indentation hardness, resulting from a cycle of indentation can be calculated by dividing the indentation load, L_{max}, used during the measurement, with the projected contact area of the indentation. This value represents the mean pressure that a material can support under the load. The indentation hardness can be then calculated from the Figure 42a) at the peak load by the following expression [266]

$$H_i = \frac{L_{max}}{A_p}, \qquad \text{(Eq.80)}$$

where A_P stands for the projected contact area. The calculation of the projected contact area from a curve load-displacement curve can only be calculated if one knows the contact depth, h_c, Figure 42b) which will be discuss afterwards.

The elastic modulus of the sample calculation starts with the determination of the initial contact unloading stiffness, S_c, which corresponds to the slope of the initial portion unload curve (dP/dh) Figure 42a). The contact stiffness, S_C, can also be calculated in function of the projected contact area and Young´s modulus by the following expression [266]

$$S_c = 2\beta E_R \sqrt{\frac{A_P}{\pi}}, \qquad \text{(Eq.81)}$$

where β is a constant that depends on the geometry of the indenter and E_R represents the reduced Young´s modulus, previously defined in Eq. 9 in section § 2.3.2, on which one must use the known values of both Poisson´s ratio and elastic modulus of the diamond indenter, 0.07 and 1141 GPa respectively. The determination of the Young´s modulus from the above equations is then dependent from the determination of the projected area and contact stiffness from load-displacement curve. Oliver and Phar [266] figured out that the unloading curve from a cycle indentation is not linear as it appears in Figure 42a), following instead a power dependence described by the following equation

$$L = B(h - hf)^m, \tag{Eq.82}$$

where B and m are empirically determined fitting parameters. According to Oliver and Phar [266] the initial unloading stiffness, S_i, is then calculated by differentiating the above equation at the maximum reached depth, h_{max}

$$S_c = \left(\frac{dL}{dh}\right)_{h=h_{max}} = Bm(h_{max} - h_f)^{m-1}. \tag{Eq.83}$$

The Doerner and Nix [267] method for calculating the stiffness, by fitting a line tangent to the initial unloading curve was the method used by the software apparatus for the Young´s modulus calculation. This method assumes that during unloading, the area of contact between the indenter and the sample remains constant while the indenter is removed. Despite this type of behavior being characteristic of a flat cylindrical punch, Doerner and Nix experimentally observed that the initial portion of the unloading curve of some materials (mostly metals), with different indenter geometries, such as Berkovich indenter, presented also a linear behavior, thus justifying the application of the method defended by the authors.

For a correct determination of the contact stiffness one must take in consideration the apparatus or machine compliance, that is, the elastic displacement per unit of applied load. The total compliance of the system C_t, corresponds to sum of the contact compliance, C_c, with the machine compliance, C_m [181, 266]

$$C_t = C_c + C_m. \tag{Eq.84}$$

Given that the compliance consists in the inverse of the stiffness, the contact stiffness is then given by the following expression [181, 266]

$$S_c = \left(\frac{1}{S_t} - C_m\right)^{-1}. \quad \text{(Eq.85)}$$

The machine compliance can be determined by performing a linear regression of S_T^{-1} in function of load $L_{max}^{-1/2}$ according to the following expression,

$$\frac{1}{S_t} = C_m + \frac{\sqrt{\pi}\sqrt{H_i}}{2E_r\sqrt{L_{max}}}. \quad \text{(Eq.86)}$$

The determination of the projected contact area is based in the determination of a polynomial function that relates the area of the indenter in function of the depth. This procedure is carried away in a sample with a known Young´s modulus and Poisson´s ratio. The A_P is then given by [181, 266]

$$A_p = \frac{\pi}{4}\left(\frac{S_c}{E_r}\right)^2. \quad \text{(Eq.87)}$$

For a series of different loads, the contact depth parameter, h_c Figure 42b), is calculated. The contact depth is given by

$$h_c = h_{max} - \epsilon\frac{L_{max}}{S_C}, \quad \text{(Eq.88)}$$

where ϵ is a constant that depends in the shape of the indenter. Finnaly, plotting Ap vs h_c for each load, one will be able to extract (by fitting) the corresponding polynomial function which describes the project area in function of the depth, typically given by [181, 266]

$$A_p(h_c) = C_0h_c^2 + C_1h_c + C_2h_c^{\frac{1}{2}} + C_3h_c^{\frac{1}{4}} \ldots + C_8h_c^{\frac{1}{128}}, \quad \text{(Eq.89)}$$

where C_1 to C_8 are constants.

In the present thesis a Shimadzu DHU-211S apparatus using a Berkovich indenter with 115° between faces was used for the determination of both hardens and Young´s modulus. The measurements were performed with a maximum load of 5 mN, using a constant rate of 0.2926 mN/s. The maximum load was kept for 20 seconds. Prior to the measurements, both compliance and indenter area function were calibrated, using hard steel and silica glass BK7 samples.

4 RESULTS AND DISCUSSION

In the following chapter the results relative to the characterization of the different implantations sets will be presented and discussed. For organization purposes the results and respective discussion will be divided by implanted element or elements. The implantation conditions as well as the respective fluences were displayed in the previous chapter in Table 5.

4.1 FE^+ IMPLANTATION RESULTS

4.1.1 STRUCTURAL CHARACTERIZATION

In the present chapter the results relative to the Fe^+ implantation will be displayed. In Figure 43 and Figure 44 it is possible to observe the microstructural evolution of the low-medium ($5x10^{15}$ cm^{-2} and $5x10^{16}$ cm^{-2}) and high fluence ($2x10^{17}$ cm^{-2}) of the Fe^+ implantations during the annealings at 550 ºC, 800 ºC and 1000 ºC, respectively. For the sake of simplicity, the micrographs relative to as-implanted state are not shown since no morphological changes could be observed in SEM when compared to the Si <100> reference sample, and also since the Ra values of the as-implanted samples were close to the Si one, around 0.23 nm. The samples annealed at 550 ºC also do not show any microstructure, the small circular features present in Figure 43 and Figure 44, at this specific temperature, are relative to impurities or contaminations that were used with the purpose of facilitating the focus of the respective micrographs.

In Figure 43 it is possible to observe that the low and medium fluence samples show a similar evolution with the annealing temperatures. As previously said, no microstructures are observed after the annealing at 550 ºC whereas at 800 ºC both fluences show very small precipitates with dimension smaller than 50 nm. At 1000 ºC significant change can be seen. Note that the micrographs presented in Figure 43 for this temperature have a lower magnification for a better perception of the microstructures. In the low fluence case, it is possible to observe the formation of large regular precipitates, with a parallelepiped shape, surrounded by much smaller ones. An interesting perspective of these parallelepiped precipitates can be seen in Figure 45 (left). The micrograph was attained by tilting the sample 70º relative to the horizontal plane and shows that the precipitates can reach a height in the order of the micrometers. The medium fluence sample exhibits also large precipitates, but with an irregular shape when compared to the low fluence sample. A larger number of small precipitates can be observed surrounding the larger ones, which is expected since the medium fluence is one order of magnitude higher than the low one.

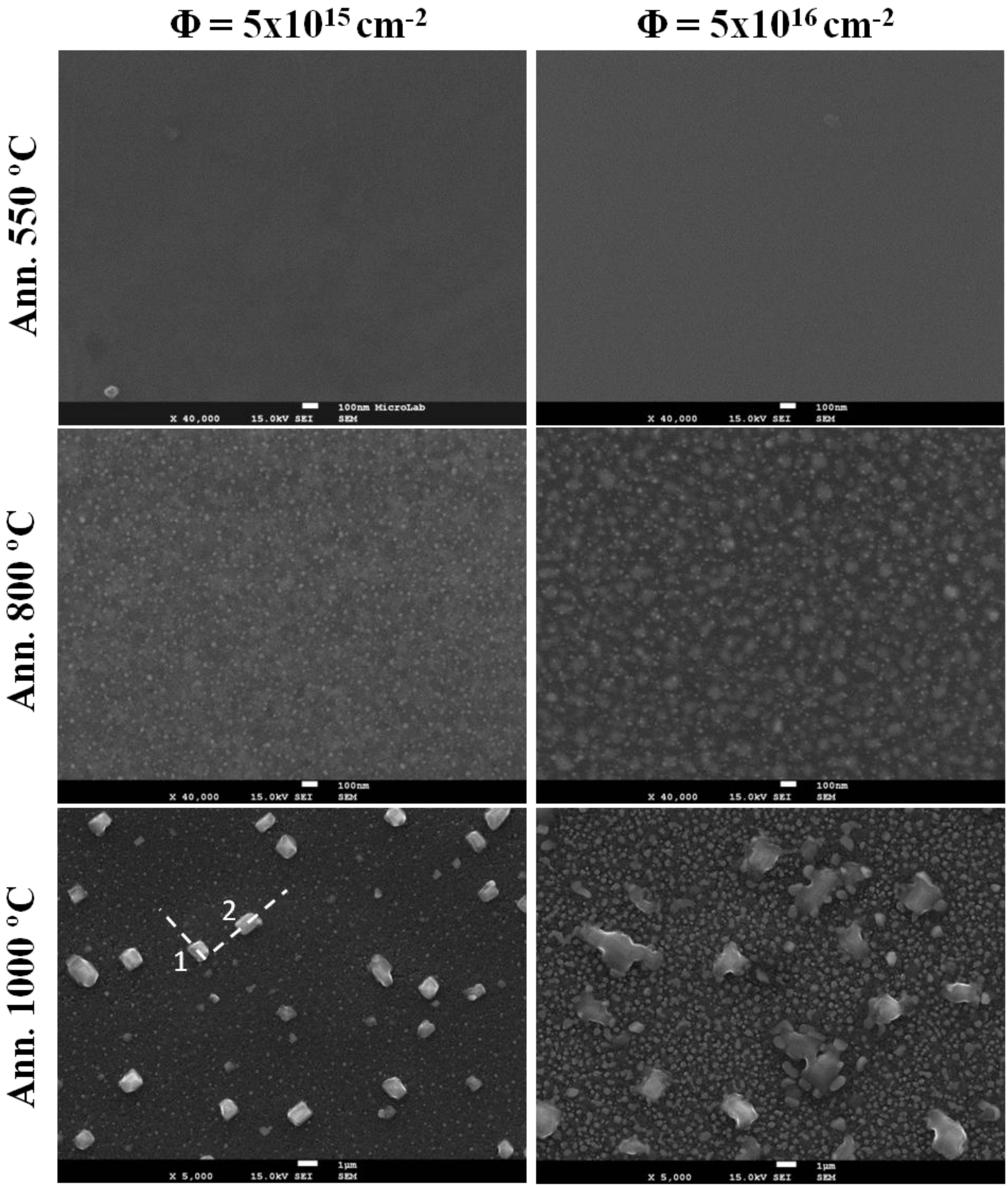

Figure 43. Micrographs relative to the microstrucrtual evolution of the low and medium fluence (5x10^{15} cm^{-2} and 5x10^{16} cm^{-2}) Fe$^+$ implantation at the annealings temperatures of, 550 ºC, 800 ºC and 1000 ºC respectively.

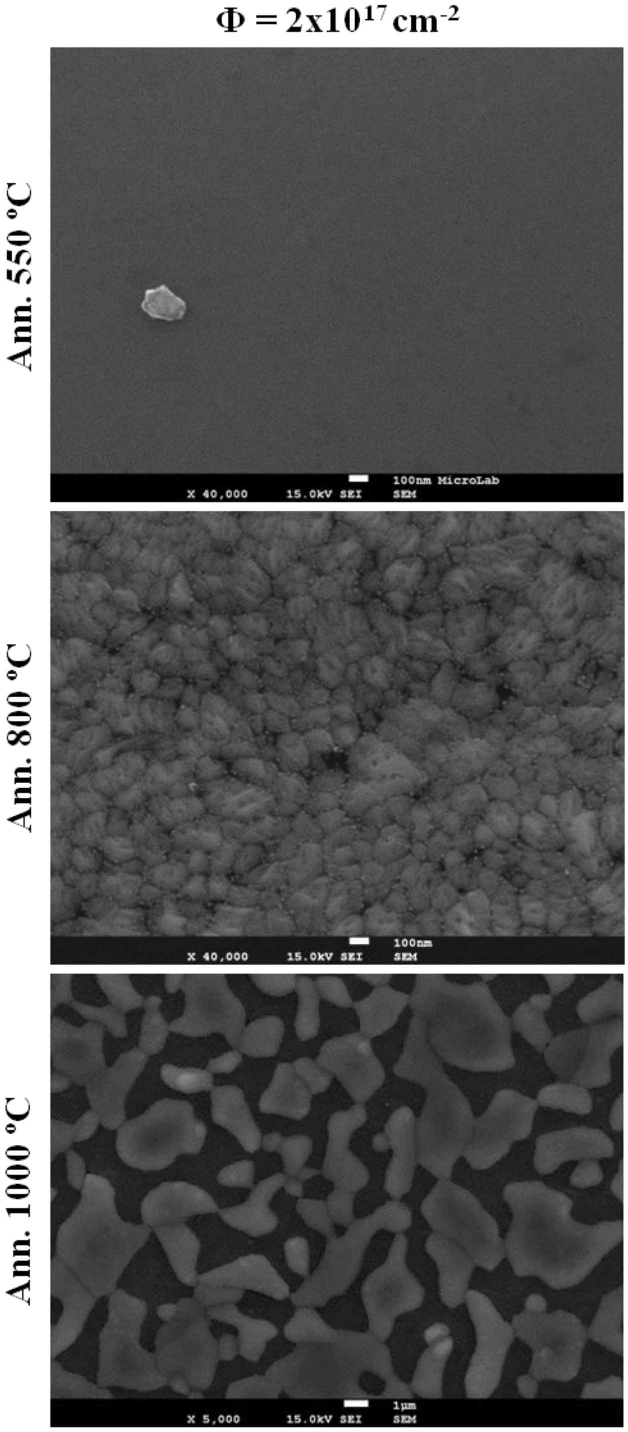

Figure 44. Micrographs relative to the microstrucrtual evolution of the high fluence (2x1017 cm^{-2}) Fe$^+$ implantation at the annealings temperatures, of 550 ºC, 800 ºC and 1000 ºC respectively.

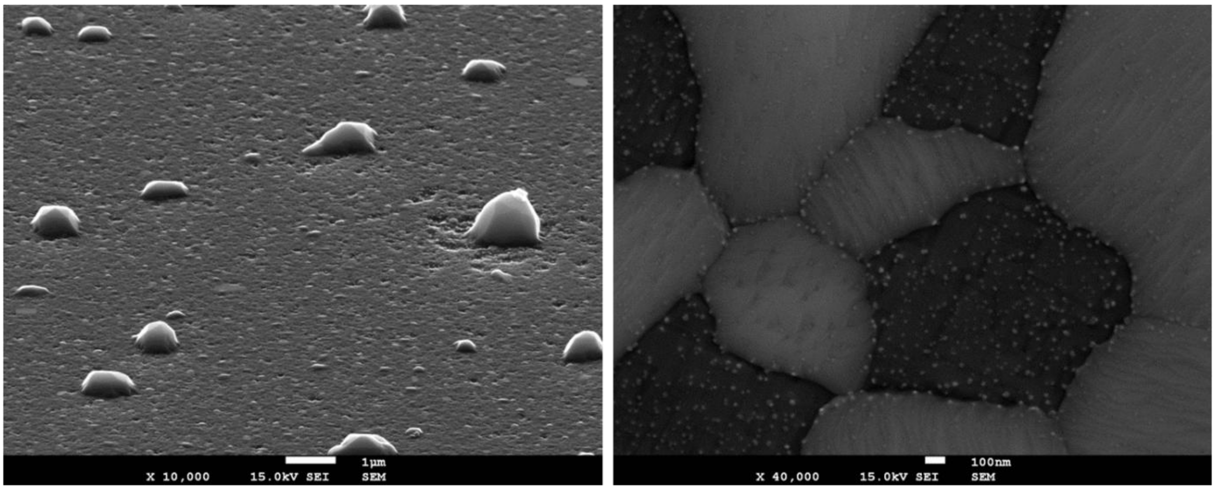

Figure 45. (Left) Micrograph of the low fluence Fe$^+$ implantation annealed at 1000 ºC tilted 70 º, (right) micrograph of the high fluence Fe$^+$ implantation annealed at 1000 ºC.

The microstructural evolution with temperature of the high fluence Fe$^+$ implanted samples, shown in Figure 44, follows a different development when compared to the low and medium fluence. Although in Figure 44 no microstructure is observed after the 550 ºC annealing, using an AFM it was possible to observe a microstructure that consists of large grains, which indicates that a new phase is being formed –Figure 46 (left). A more detailed view of the grains formed in FeHT550 sample can be seen in Figure 46 (right). At the 800 ºC annealing, the surface is fully covered with small precipitates with an approximate dimension of 100 nm whereas at 1000 ºC a radical change in the microstructure is observed. The precipitates microstructure evolves to a biphasic structure (Figure 44), where it is possible to observe both bright and dark different zones.

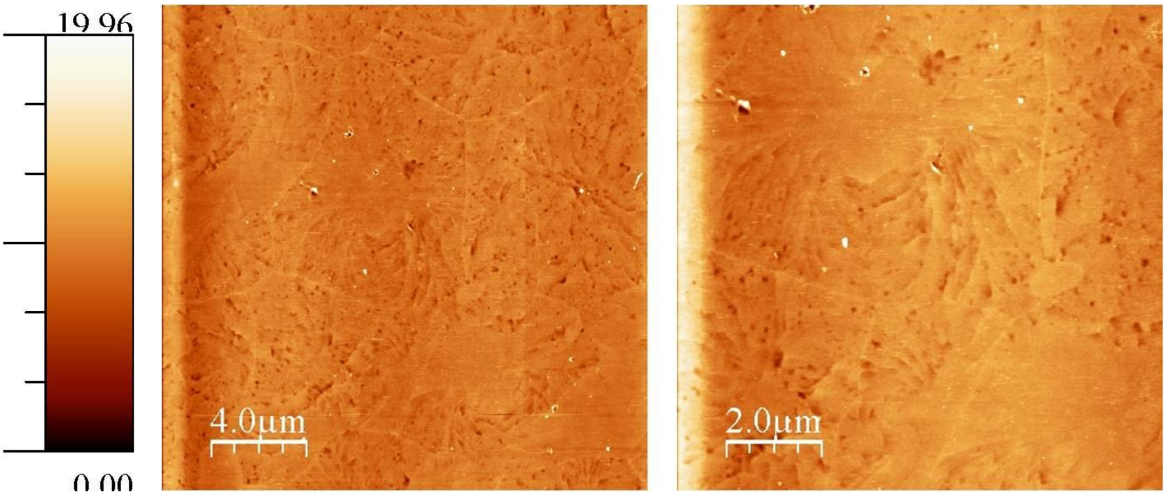

Figure 46. (left) 20x20 μm^2 AFM image of the FeHT550 sample, (right) 10x10 μm^2 image of the FeHT550 sample.

GIXRD measurements were performed to identify the phases observed in both SEM and AFM microscopes. The GIXRD results are presented in Figure 47a)-c) corresponding to the low, medium and high fluence, respectively. A common feature is seen for all the three difractograms, the fact that no peaks were observed for the respective as-implanted samples. For the low implanted fluence case, no peaks were observed for all the annealing temperatures despite the presence of some precipitates at both 800 ºC and 1000 ºC. The most plausible explanation for the absence of the diffraction peaks at those temperatures is most likely the small size or density of the precipitates formed, which do not seem to present themselves enough to build an XRD signal. For both medium and high fluences, respectively, diffraction peaks can be observed. However some differences can be seen. For instance, at a temperature of 550 ºC, only the high fluence sample exhibits diffraction peaks, corresponding to the orthorhombic semiconductor $\beta - FeSi_2$ phase. The high fluence sample was the only one to exhibit a polycrystalline microstructure as shown in Figure 46. At 800 ºC both medium and high fluence samples reveal the presence of the $\beta - FeSi_2$ phase, the diffraction peaks being more intense for the higher fluence. The annealing at 1000 ºC produces new phases. For the medium fluence sample, one can observed the presence of 4 peaks corresponding to the $\beta - FeSi_2$ phase and a very low intensity peak corresponding to the $\alpha - FeSi_2$ tetragonal metallic phase while for the high fluence sample one can only see the presence of $\alpha - FeSi_2$ peaks. For the FeHT1000 sample, in Figure 45 (right) it was possible to observe a microstructure composed of two different phases, a white and a dark one respectively.

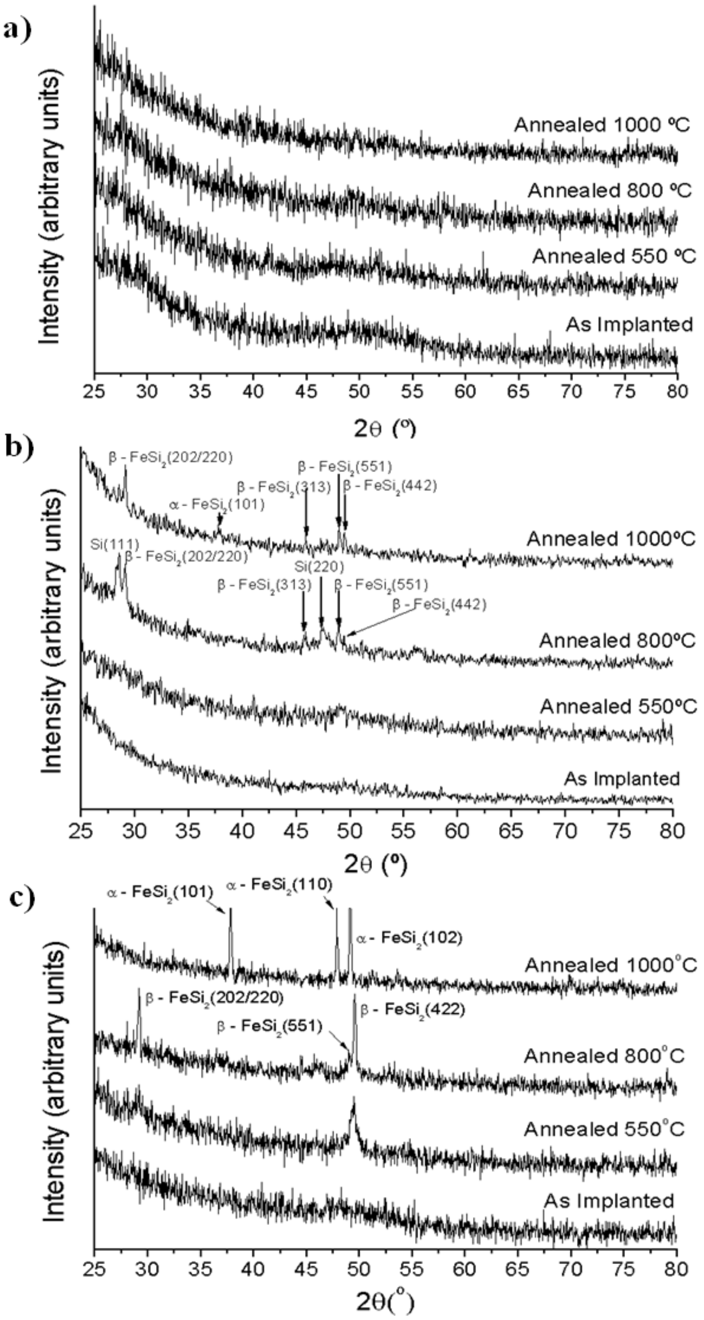

Figure 47. GIXRD difractograms of the Fe+ implanted samples with the respective annealing temperatures, (a) low fluence, (b) medium fluence and (c) high fluence.

An EDS analysis was performed in different spots of the sample, in both white and dark zones respectively. The results are presented in Figure 48, where is possible to see the different spots where the EDS was performed as well as the resulting atomic percentages of both Si and Fe. The spots that present the higher content of Fe element coincide with the white zones, suggesting that this phase corresponds to the α – $FeSi_2$ silicide. For the spots corresponding to the dark zones, it corresponds mainly to Si. The exception is the spot number 4, present in a dark zone but with Fe content close to white zones. The examination of the EDS scanned area by a secondary electron micrograph showed that in fact the spot number 4 hit a border of white/dark zone. The Fe concentrations in the white spots are very low, in fact never reach a 10 at % value. One must take into consideration that the EDS analysis reaches a depth in the couple of microns range, whereas the Fe content is expected to be located in the first few hundred nanometers counting from the surface. The atomic % Fe values read are essentially diluted in a huge concentration of Si.

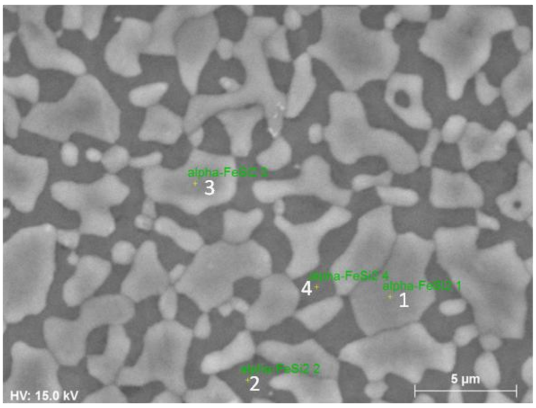

Spot	Atomic % Si	Atomic % Fe
1	92.17	7.83
2	99.39	0.61
3	92.46	7.54
4	94.67	5.33

Figure 48. EDS analysis performed on the FeHT1000 sample (left) different spots where EDS was performed, (right) atomic precentages given by the EDS analysis.

RBS characterization was performed to all fluences and respective annealings. The RBS spectra are presented in Figure 49a)-c), corresponding to the low, medium and high fluence respectively. The spectra of the 550 ºC annealed samples, for each fluence, were not represented since they are quite similar to the as-implanted ones. For the same reason for each fluence only the Fe peaks of the aligned spectra are represented since the random and aligned spectra fully overlap in the Fe peak, with the exception of the as-implanted case. This fact allows one to understand that the phases and precipitates formed upon the annealings did not grow in an epitaxial way with the Si substrate. The low and medium fluence samples, Figure 49a) and Figure 49b), show an identical evolution with temperature. For these samples, it is possible to observe that as temperature increases, recrystallization of the amorphous induced phase, ranging from channels 350 – 450, occurs, with a clear advance of the amorphous\crystalline interface and a simultaneous sweep of Fe towards the surface, detected by the shifts of the Fe barrier towards higher values of energy. For the high fluence case, an advance of the amorphous layer is not observed, but rather it's disappearing, most likely as a result of the formation of $\alpha - FeSi_2$ and $\beta - FeSi_2$ phases detected in GIXRD. A common feature to all fluences, although more easily seen in both medium and high fluence, is the decrease in height of the Fe signal after the 1000 ºC annealing along with the broadening of the peak, showing a clear diffusion of Fe towards the bulk. Using the surface approximation, it was possible to achieve a first rough approximation of the thickness of the amorphous layers of the as-implanted samples. The values attained were 200 nm, 230 nm and 270 nm for the low, medium and high fluence respectively. The sweep of Fe during the recystallization is most likely associated with different solubility values of Fe in both crystalline and amorphous Si. This type of behavior has been reported in the past with different species [210].

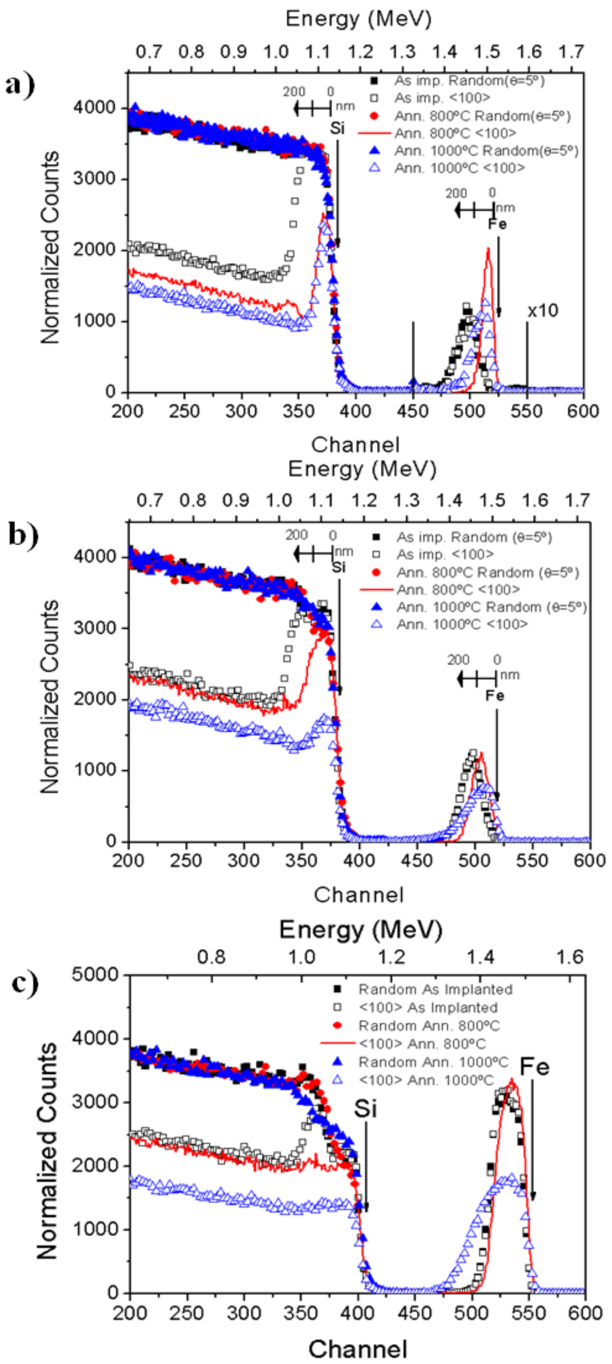

Figure 49. RBS spectra of the Fe implanted and annealed samples, (a) low fluence, (b) medium fluence, (c) high fluence.

4.1.2 MECHANICAL PROPERTIES AND NANOTRIBOLOGICAL STUDIES

The changes introduced on the mechanical properties, more precisely hardness and Young´s modus, of the Fe implanted samples were studied for all fluences and annealings. As a preliminary test, a few indentations were performed on the reference Si and also on the high fluence Fe samples using a 100 mN load. The SEM micrographs are displayed in Figure 50. Figure 50 clearly shows that both implantation and annealings promoted a change in deformation behavior. In the reference Si, Figure 50a), radial cracks can be seen as well as an increase of height in the zone surrounding the indentation. For the high fluence Fe implanted samples different deformation behavior can be observed. For instance, the as-implanted sample, Figure 50b), not shows only a huge amount of plastic flow in the edges of the indentation but also does not evident radial cracks. The same happened to the other as-implanted samples of lower fluences. After the annealing at 550 ºC a fracture type behavior can be seen, with the removal of a substantial amount of material in the surrounding of the indentation while after the annealing at 800 ºC no fractures or cracks are seen. After the annealing at 1000 ºC a mixed behavior is observed. For most of the indentations made, a plastic flow could be seen as well as some fractures, as illustrated in Figure 50e).

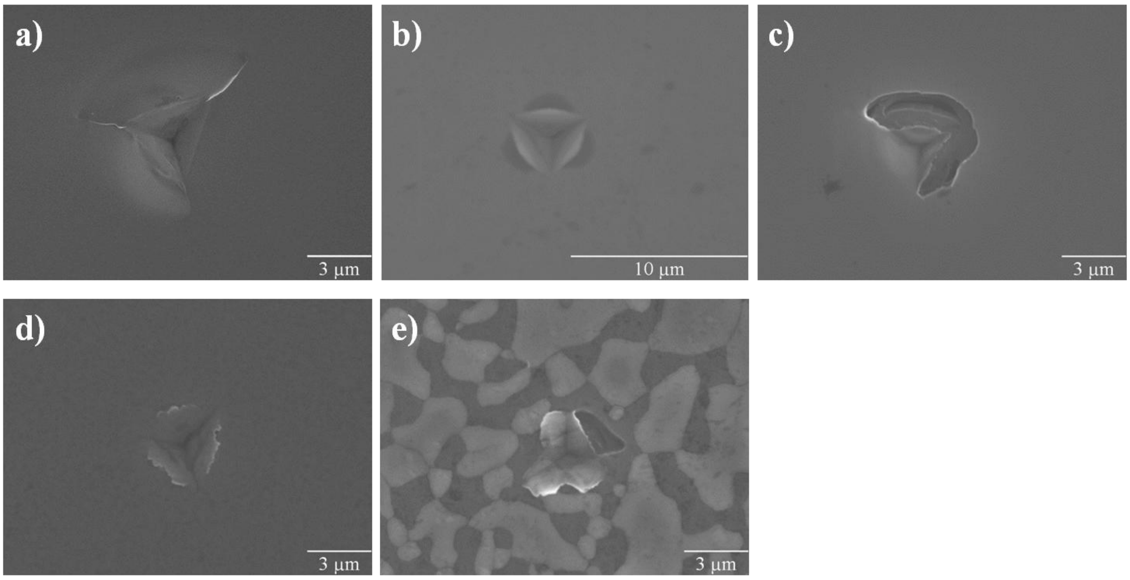

Figure 50. 100 mN indentations micrographs performed on (a) reference Si, (b) high fluence Fe as-imp, (c) high fluence Fe ann. 550 ºC, (D) high fluence Fe ann. 800 ºC, (e) high fluence Fe ann. 1000 ºC.

The hardness and Young´s modulus were determined using a much lower normal force, 5 mN, than the one used in the indentations in Figure 50, 100 mN, in order to analyze the respective implanted zones of each sample. The results are displayed in Figure 51, where for each sample 10 measurements were made. A general look into Figure 51 shows that for all fluences and respective annealings, only minor increases were observed for hardness while for the Young´s modulus no increases were actually observed but rather a larger number of decreases. In terms of hardness and Young´s modulus Figure 51 shows that the as-implanted samples show indeed a lower value when compared to the reference, being this behavior more easily seen for both low and medium fluences. The annealings and respective recrystallization of the amorphous induced phases promote indeed changes in the mechanical properties relative to the as-implanted ones. Looking to the low fluence sample, Figure 51a) and b) the hardness and Young´s modulus recover, being the hardness value quite close to the Si one and the elastic modulus always slightly lower than the reference. For the medium fluence, a recovery of the mechanical properties is observed for the 550 ºC and 800 ºC annealing while at 1000 ºC a new significant decrease is observed. The high fluence sample follows a similar behavior, at 550 ºC and 800 ºC a recover is seen in the mechanical properties, while at 1000 ºC the hardness slightly decreases and Young’s modulus slightly increases comparing to the 800 ºC.

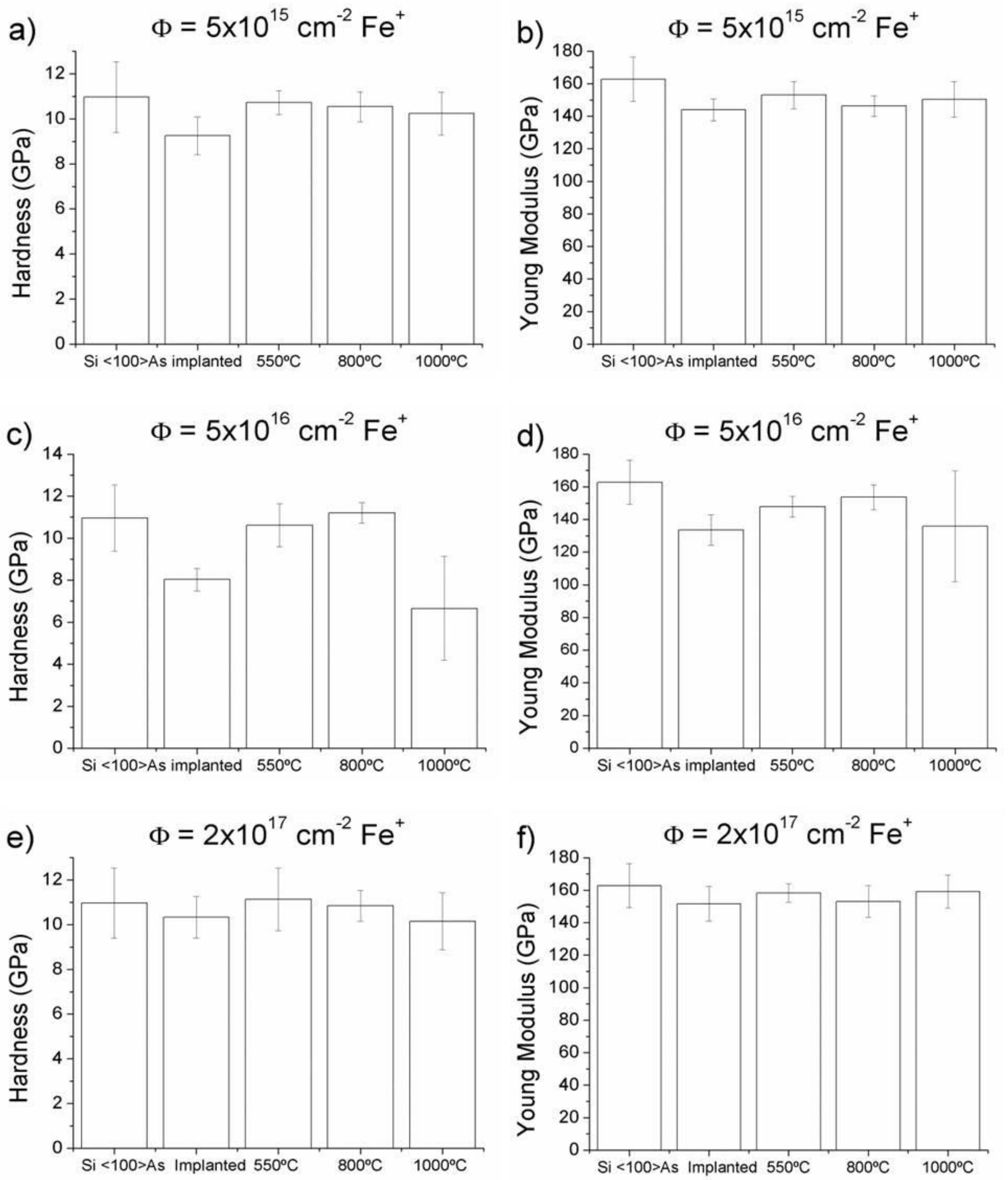

Figure 51. Hardness and Young´s modulus of 150 kev Fe$^+$ ion implanted Si(100) with a fluence of 5x10^{15} cm^{-2} (a and b); 5x10^{16} cm^{-2} (c and d); and 2x10^{17} cm^{-2} (e and f) measured with 5 mN normal load, for both the as-implanted state and all annealing temperatures.

The nanotribological properties of the Fe implanted samples were also studied. More specifically, the nanowear properties of the high fluence Fe samples. The nanowear scans performed in the as-implanted and on the 800 ºC and 1000 ºC annealed samples can be seen in Figure 52.

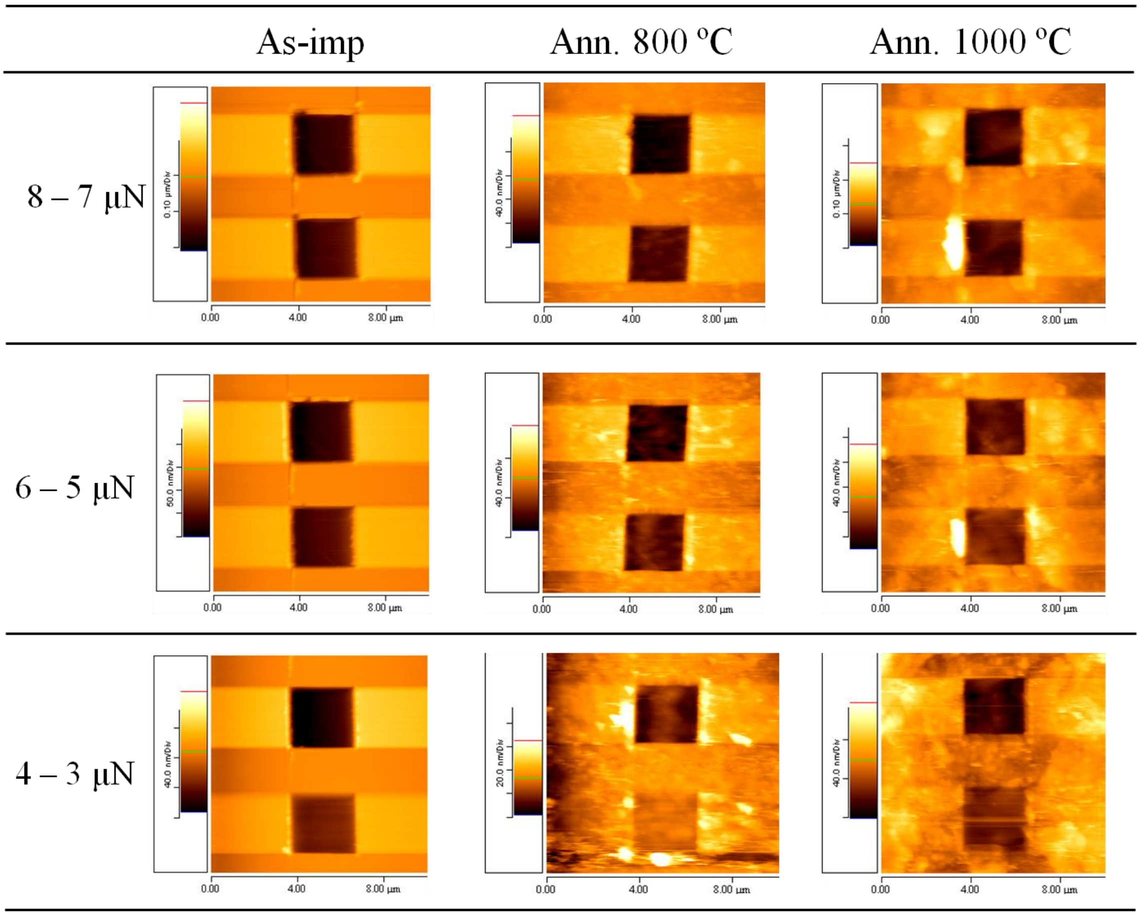

Figure 52. Nanowear scans performed with a DNISP diamond tip for the high fluence Fe implanted samples, as-implanted, annealed at 800 ºC and 1000 ºC for a load range of 3 - 8 µN.

The scans were performed over a 3 × 3 µm^2 area, and the corresponding measured depths as well as calculated wear rates for each sample are plotted in Figure 53. The lines in Figure 53 are guidelines, thus not representing any kind of fit. The scans were performed with a diamond tip and the load varied from 3 to 8 µN. In Figure 53 it is possible to see that the as-implanted sample stands out from all the others. This sample, exhibits the highest wear rates and depths throughout the load range studied. This behavior is most likely associated with the induced amorphous layer detected in the RBS results. In the previous figure, it was observed that a small change in hardness and Young´s modulus was observed for this sample. Upon the annealings the wear rates change to lower values. Both 800 ºC and 1000 ºC annealed samples show lower values of wear rate for almost the whole load range, comparatively to the reference Si. This result is most likely associated with the recrystallization and formation of new phases such as the β and α silicide phase. From the nanowear results presented in Figure 53 it was possible to calculate not only the wear coefficients but also wear threshold for each of the characterized samples, by performing a linear regression for each corresponding sample. The calculated specific wear coefficients are shown in Figure 54. The as-implanted sample shows the highest specific wear coefficient, which is in good agreement with the results of the nanowear scans in Figure 53, while the annealed samples presented the lower values. The lowest value corresponds to the 1000 ºC Fe implanted sample, despite the fact that for the lower loads the 800 ºC sample presented slightly lower wear rate values. In fact, in Table 10 one can see that the 800 ºC annealed sample presents indeed the highest value of wear threshold while the as - implant one as expected, presents the lowest one, being the only sample that presents a wear threshold lower than 1 µN. Figure 53, Figure 54 and Table 10, show that comparing to the reference Si, the as – implanted sample exhibits the worst nanotribological performance, considering the studied samples, while the best nanotribological performance was achieved for the annealed samples. However, among the annealed samples, one cannot clearly identify the best one. For instance, the 1000 ºC presents the lower wear rates for the higher studied loads and presents the lowest value of specific wear coefficient while the 800 ºC presents lower wear rates for lower loads and presents the highest wear threshold.

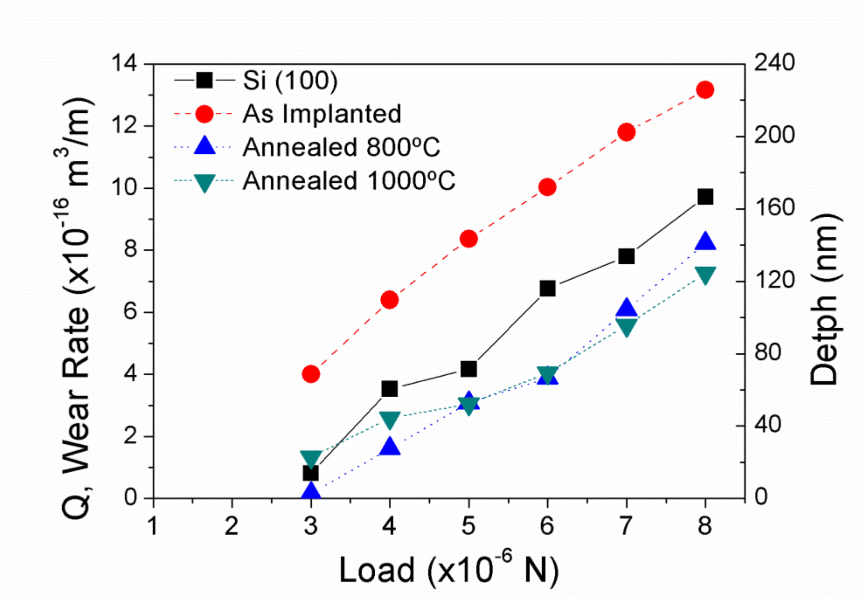

Figure 53. Nanowear results of the high fluence Fe$^+$ implanted samples, wear rate and depth vs Load.

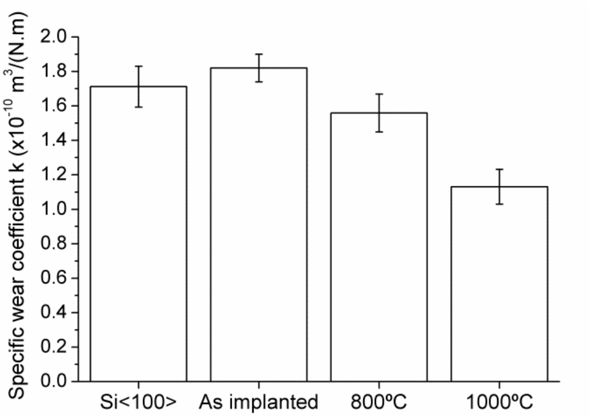

Figure 54. Calculated specific wear coefficients for the reference Si <100>, high fluence Fe as-implanted, annealed at 800 ºC and 1000 ºC, respectively.

Table 10. Calculated wear threshold for the Nanowear characterized samples

Sample	Si <100>	As-implanted	Ann. 800 ºC	Ann. 1000 ºC
Wear Threshold (µN)	2.30 ± 0.42	0.57 ± 0.26	3.04 ± 0.46	1.98 ± 0.54

4.1.3 WETTABILITY STUDY

Contact angle measurements were performed with both water and diiodomethane to evaluate the wettability behavior of the implanted and annealed samples and also to determine the corresponding surface energy. The results are summarized in Figure 55, where on the left side the wettability measurements for water are represented and, on the right one, the determined surface energies, dispersive components and polarities. The respective polar components of the samples were not represented to avoid too much information displayed on the chart. These components can be determined indirectly by subtracting the values of the dispersive component from the values of surface energy.

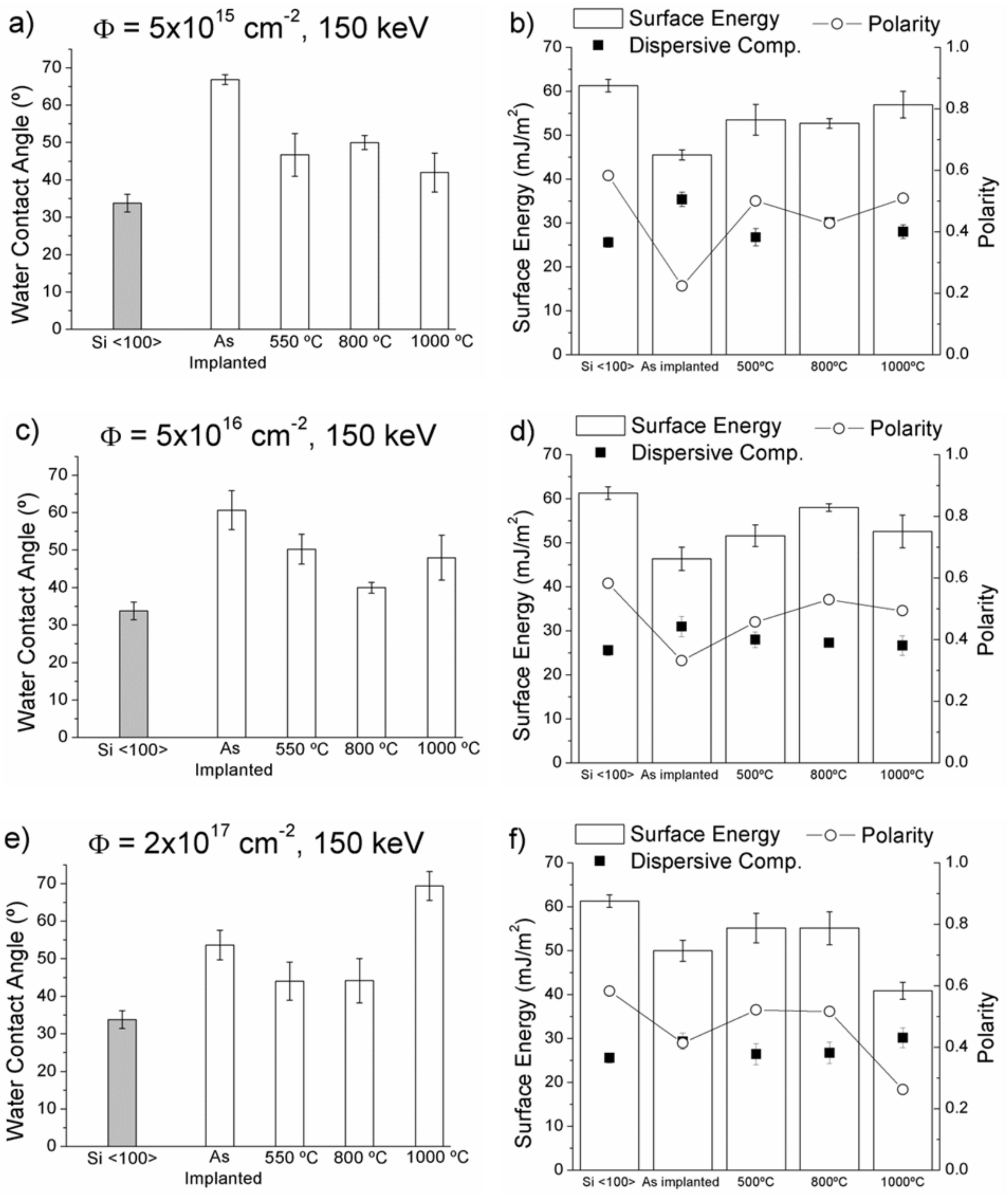

Figure 55. Water contact angle, surface energy, dispersive component and polarity of (a,b) low fluence (c,d) medium fluence, (e,f) high fluence, of the Fe$^+$ implanted and annealed samples.

For both contact angle and surface energy determination a reference Si <100> sample was used for comparison purposes. Looking to Figure 55a)b) and c), one can observe that the implantation of Fe into Si can induce significant changes in the water contact angle. Comparing the as-implanted samples for each fluence one can find a trend. The low fluence sample presents the higher contact, ≈ 67 º, which represents almost the double of the reference Si <100> ≈ 34 º. As the fluence increases, one can observe a decrease of the contact angle, around 60 º for the medium fluence and 53 º for the high fluence one, respectively. The increase of the contact angle is accompanied by a decrease in the surface energy. One can also observe that, comparing to reference Si, the polar and dispersive components of the surface energy change to opposite. The polar component is higher on the reference Si but upon implantation, its value decreases, contributing less to the total value of surface energy. Upon the annealing, considering the low and medium fluence samples, one can observe a decrease of the contact angle comparing to respective as implanted samples but still higher than the Si reference. These fluences have in common the fact that they are not enough to produce a continuous silicide film on the surface. The annealings, as it was observed in the RBS results (Figure 49) cause a segregation of Fe towards the surface, and lead to the formation precipitates, like it was show in the SEM images before, Figure 44. The final outcome is a decrease in the surface energy, where both polar and dispersive components share almost an equal value.

The high fluence shares almost the same behavior of the lower fluences. At the 550 ºC and 800 ºC, there is a decrease of contact angle, and an increase of the surface energy, to the same values. For both annealings, as it was observed under GIXRD characterization before, Figure 47, the same phase is present at the surface, the β – $FeSi_2$ phase, although with a completely different morphology. The surface energy of the β – $FeSi_2$ phase is not significantly different from the Si reference, however a change of 15 º in contact angle is observed. For the high temperature annealing, at 1000 ºC, one can see quite a significant change, an increase of contact angle of ≈ 25 º compared to the other annealed samples. The surface energy decreases from 55 mJ/m^2 to 40 mJ/m^2 compared to the other annealed samples. The high temperature annealing corresponds to the sample that presented the lowest value of the polar component, thus polarity, within this fluence. The 1000 ºC sample does not present continuous film on the surface unlike the others annealings. Both contact angle and surface energy are a result of combining both Si and α – $FeSi_2$ silicide phase.

4.1.4 DISCUSSION

The present chapter of the thesis aims to discuss in detail the experimental results previously shown.

A great deal of research has been placed towards characterizing Si surfaces implanted with Fe (e.g [268-270]). However, most of those studies do not use the scanning electron microscopy, but different characterization techniques like TEM (transmission electron microscopy) [271], Mössbauer spectroscopy [272] or quite different experimental conditions, such as, for instance, laser treatment [273, 274], or IBAD (ion beam assisted deposition) [275], thus imposing a certain difficulty to establish a comparison. As far as we know, microstructures such as the ones presented in Figure 43 for both low and medium fluence at 1000 ºC were firstly published in the aim of the present work [17], taking into the consideration the experimental conditions used. Microstructures such as the one observed in Figure 44, corresponding to the high temperature annealing have already been reported in the literature. Although using different experimental conditions, implantations at 350 ºC, higher fluences and energies [276, 277]. The final microstructures identified were quite close to the ones found in this work, composed of both dark and white zones, with different contents of Fe.

The GIXRD of the Fe implanted and annealed samples shown in Figure 47 seem to reveal a slightly different evolution with the temperature for the medium and high fluence. The high fluence Fe sample seems to follow the binary alloy Fe – Si phase diagram shown in Figure 56. The transition of β to α – $FeSi_2$, according to the diagram, occurs at 937 ºC. Below and above this temperature the high fluence shows the corresponding β and α – $FeSi_2$ phases while the medium fluence sample shows the presence of both β and α at 1000 ºC. It has been shown before that the implantation of Fe for fluences even higher than the highest one used in this work, can slightly change the transition temperature to a lower value. Katsumata *et al*. observed the transition β to α transition at 930 ºC [278]. The presence of β – $FeSi_2$ above the eutectoid temperature has been reported before in the literature [279, 280]. Gao *et al*. [279] suggests the presence of β phase at higher temperatures as a result of partial transformation of the α phase during cooling. Since it has been proven that the α to β transition is a process with a relatively slow kinetics [281] it is also plausible to think that not all β transformed into α initially. As for the low fluence sample it is rather difficult to compare if it follows or not the binary Fe –Si phase diagram since no peaks were observed for all annealing temperatures despite the observation of some precipitates at 800 ºC and 1000 ºC. The lack of the peaks was attributed before to low density of the formed precipitates which was not enough for a XRD signal. However, the 2θ – θ (Bragg - Brentano) scan was performed on all Fe implanted samples annealed at 1000 ºC. At this temperature the low fluence sample revealed the presence of only one peak, aside from the ones expected of the Si, at 2θ = 17.3º, corresponding to most intense peak of the α – $FeSi_2$ phase, the (001) reflection. According to the phase diagram the α – phase forms at 937 ºC. The presence of the XRD peak tell us that the α - phase, most likely the regularly shaped precipitates present in Figure 43, were grown under a specific orientation relative to the substrate. Looking with attention to the precipitates at 1000 ºC (precipitate 1 and 2 marked in Figure 43) for the low fluence case, one can see an angular relation between different precipitates, considering the precipitates long axis. Between 1 and 2 one can measure 90º. The same angular relationship was observed by Gao *et al*. [279] in α – $FeSi_2$ precipitates under TEM plain-images observation. The precipitates were less thick than the ones observed in the present work, which is probably explained by the different experimental conditions used. For the precipitates at 800 ºC no XRD extra measurements were performed. However, it is plausible to think that the precipitates correspond to β – $FeSi_2$ phase according to phase diagram the results of and both medium and high fluences. The medium fluence also presented the same peak corresponding to the α – $FeSi_2$ (001) phase. Although the precipitates are not as regular as the ones presented in the low fluence at 1000 ºC case, a sort of close orientation can still be found but just for some cases. As for the high fluence sample at higher temperature, more peaks of α – $FeSi_2$ were detected but with intensities much lower when compared to peak detected in the other fluences. The α – $FeSi_2$ phase formed for the higher fluence is most likely polycrystalline instead of having a preferential orientation with the substrate.

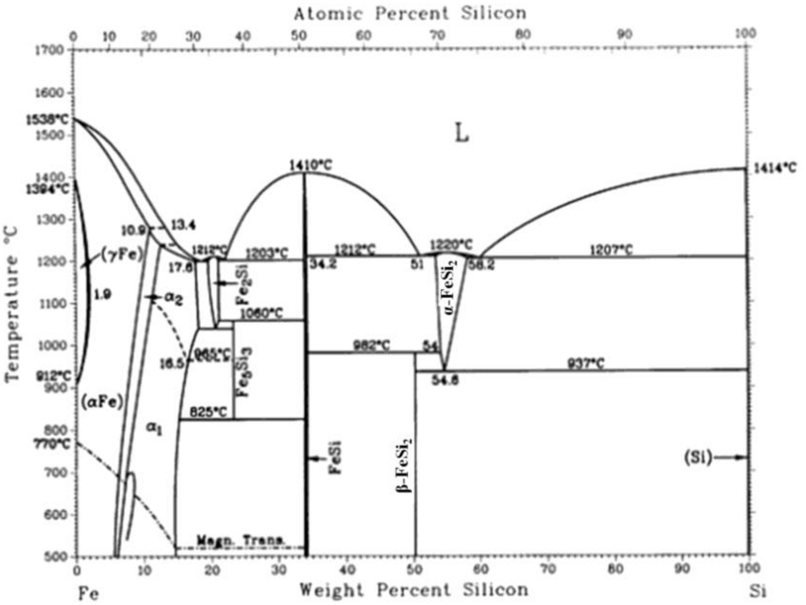

Figure 56. Binary alloy Fe - Si phase diagram, adapted from [282].

The RBS spectra presented in Figure 49 shows a common trace for all fluences in the as-implanted state, which is the presence of an amorphous phase. This result agrees with previous works published by several authors [283] who predicted a critical fluence for amorphization of Si of approximately $2.5x10^{14}$ cm^{-2}. All the implanted fluences were higher than to this value. The medium and high fluence spectra were all simulated using the WINDF/NDF© code [244] to obtain information on the profile and damage depth. The simulated spectra for the higher fluences can be seen in Figure 57. The simulated spectra confirmed the values of the respective implanted fluences, $5x10^{16}$ cm^{-2} and $2x10^{17}$ cm^{-2}. For both medium and high fluences, the as-implanted fit allowed one to realize that the Fe signal reaches a depth of 210 nm and 230 nm, respectively. Upon the annealing at 800 ºC, based on the fit of the medium fluence sample, it was possible determine that the β – $FeSi_2$, in form of precipitates in the Figure 43, appears within the first ≈ 115 nm, as result of the advance of the recrystallization front observed in the aligned spectra in Figure 49b). At 1000 ºC, again based on the fit results, a silicide seems to be present until a depth of ≈ 170 nm. Beyond this point a diffusion tail is observed, until very deep depths, ≈ 400 nm. It is plausible to think of different silicides, with different values of stoichiometry, since the atomic % of Fe is quite low and decreasing with depth. For the high fluence the result from the fits revealed the presence of silicides phases with a stoichiometry of 1 – Fe to 2 – Si, corresponding to both α and β phases. For the 800 ºC, a continuous film of β – $FeSi_2$ is present at the surface, with a thickness of ≈ 100 nm, followed by a second layer of β – $FeSi_2$ plus Si until a depth ≈ 130 nm. For the high temperature of annealing a similar behavior is observed similar to the medium fluence at the same temperature but with a much more silicide phase in the higher fluence sample. The spectum simulation showed the presence of the silicide in the surface in a concentration higher than Si until a depth of ≈ 86 nm. Looking to Figure 44, the white zones, corresponding to the silicide occupy a greater fraction of the image. According to the simulation the silicide is present to a depth of ≈ 360 nm.

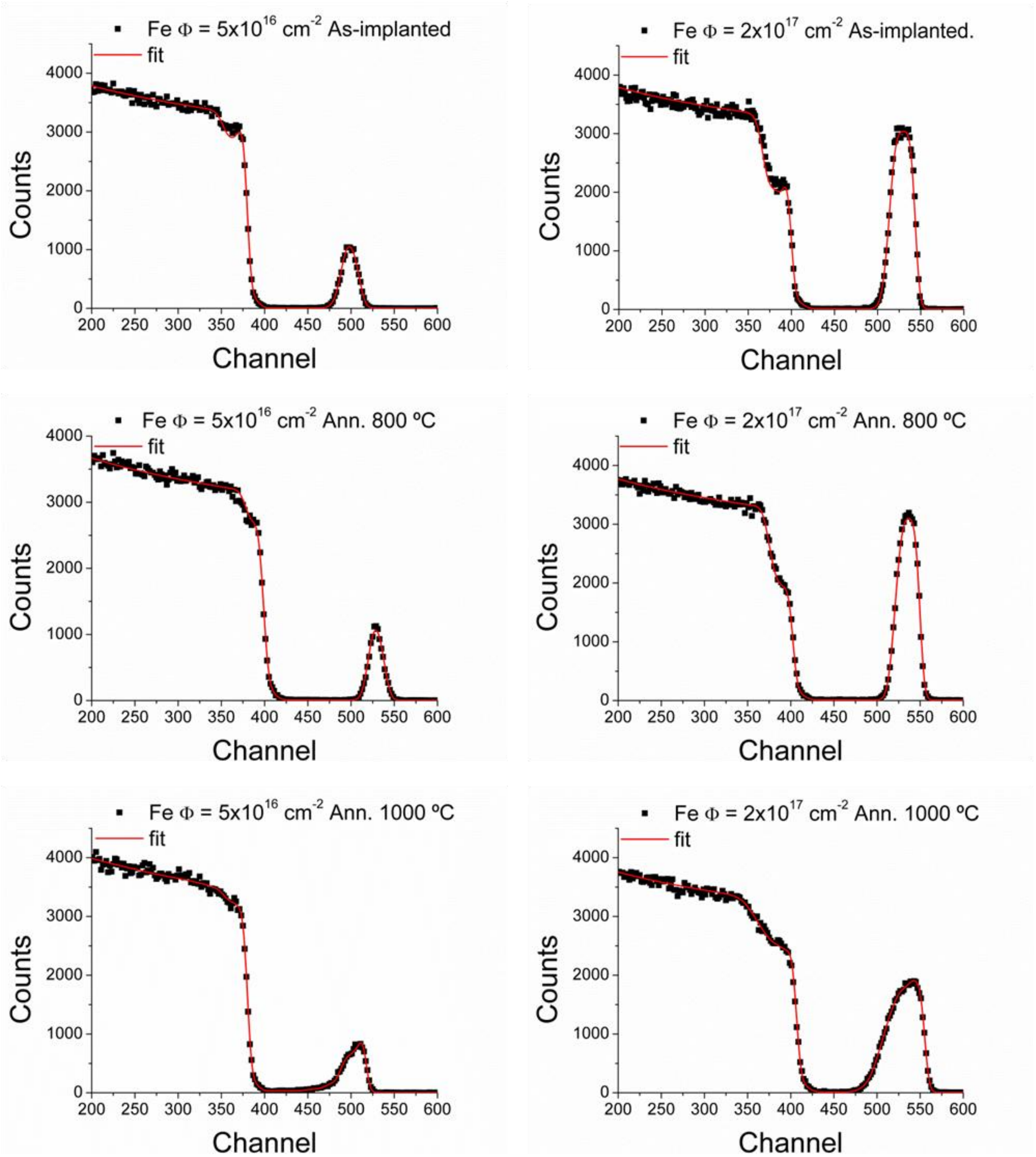

Figure 57.Random and NDF© simulation of the medium and high fluence Fe implanted and annealed samples RBS spectra.

The measured mechanical properties of the Fe implanted and annealed samples in Figure 51, were all compared to the values of hardness and Young´s modulus of a Si <100> wafer. The respective measured values of both hardness and Young´s modulus were 10.96 ± 1.58 GPa and 162 ± 13 GPa. These values are in good agreement with the ones published in the literature that report that Si hardness ranges from 10 – 12 GPa [284, 285] and a Young´s modulus of 169 ± 2 GPa [285, 286]. The decrease of hardness and Young´s modulus observed for the as-implanted samples is directly related to formation of the amorphous layer induced by the implantation. Extensive work has been placed on the study of mechanical properties of amorphous Si, a – Si (from now on abbreviated in this form). The literature shows that a – Si either produced by self ion implantation or deposition, always presents lower values of hardness, from 8 GPa to 9 GPa [168, 284], and Young´s modulus, 120 GPa to 140 GPa [168, 287], when compared with the crystalline Si, c – Si. The difference between the c - Si and a - Si mechanical properties has been explained by the difference in the deformation mechanism. It is known that c - Si suffers a multiple phase transformations under indentation conditions and also anvil-diamond tests [288, 289]. Under pressure, the diamond cubic Si - I transforms to β – Sn tetragonal structure, also designated as Si - II. Upon pressure release, the Si - II phase can transform to either a - Si or other metastable phases such as body-centered cubic phase, bc8 or Si - III, or rhombohedral r8 or Si – XII [290, 291], depending on experimental conditions. Indentions performed on a - Si [284, 292] show that such phase transitions do not occur, being stated by the authors that deformation mechanism in a – Si results of plastic deformation as consequence of the higher number of dangling bonds induced by ion implantation, which may help the plastic flow, as it can be observed in Figure 50b). The indentations performed on as-implanted samples reach a maximum depth of ≈ 140 nm, thus being well within the respective amorphous layers measured by RBS of 210 nm, 230 nm and 270 nm, for the low, medium and high fluence respectively. Comparing all as-implanted samples, the smallest decrease in hardness is observed for the high fluence. Although the hardness value is slightly higher than the ones previously mentioned, 8 - 9 GPa, where the values of both low and medium fluence fit, values of 10.6 GPa have also been reported [172], being quite close to the ones obtained for the high fluence, 10.3 GPa. Upon the annealings the mechanical properties of the Fe implanted samples are recovered. The reason for such recovery lies on the recrystallization of the amorphous induced phase. Using Si self implantation, Williams *et al*. [284] observed an increase of hardness from 9 GPa to 10 GPa upon a 450 ºC annealing for 30 min, being the reference value ≈ 10.5 GPa while Follstaedt *et al*. [172] observed a full recovery of the hardness values upon 1 h annealing at 500 ºC but the same did not happen to elastic modulus, that recovered from 130 GPa to 148 GPa, being the reference value 168 GPa. Both authors performed Si self-implantation. Szabadi *et al*. observed an increase from 120 GPa to 130-140 GPa in the elastic modulus upon amorphization with Ar and annealing at 530 ºC. The results in Figure 51 are in good agreement with the previously mentioned results. Both hardness and Young´s modulus show a great recovery upon annealing, being however the Young´s modulus values slightly lower than the reference. The sample that presents the highest deviation from the reference values is the FeMT1000 one. This result can be explained by the sample´s microstructure. The large irregular precipitates visible in Figure 43 are quite close to each other. Some of the performed indentations hit those same precipitates, which originated a large standard deviation since the precipitates do not form a stable surface to perform indentations. For the FeLT1000 sample, despite the large precipitates observed in Figure 43, these were quite distant from each other, which enabled to perform the indentations between precipitates. The FeHT800 sample, unlike all low and medium fluences, shows the presence of a continuous film on the surface of $\beta - FeSi_2$, rather than isolated precipitates. The mechanical characterization shows that both hardness and Young´s modulus do not differ much from the reference Si. The indentations for this sample reached a maximum depth 100 – 120 nm, which, according to the RBS spectra simulation is basically in the limit of the $\beta - FeSi_2$ film. The results are then influenced by the substrate properties. However, as far as the author knows, the mechanical properties of β - $FeSi_2$ have never been experimentally determined. Tani *et al*. [293], using density functional theory (DFT) calculations, estimated a value of 339 GPa for elastic modulus of the β - $FeSi_2$ phase, while Nakamura *et al*. [294] using extreme low loads evaluated the hardness and Young modulus of non-crystalline or amorphous $FeSi_x$ formed by facing target sputtered method, as around 10 GPa, while the values of elastic modulus were reported to be larger than carbon-based materials. The value of hardness does not differ much from the one attained by the other, slightly higher, however the phase is amorphous, thus is expected that the mechanical properties may be different from the crystalline phase ones, as it was observed for the silicon case previously. Both authors agree in a quite high elastic modulus. However, despite the fact that the indentations were in the limit of the film, if the elastic modulus of the β - $FeSi_2$ phase was indeed that high, the author strongly believes that a greater influence should be visible in Figure 51. More experimental work is needed to evaluate the true mechanical properties of the β - $FeSi_2$ phase. The FeHT1000 sample also presents a silicide on the surface however, as it can be seen in Figure 44, it does not form a continuous film. The hardness value is lower than the reference while the Young´s modulus has quite a close value.

The RBS results previously showed that the silicide phase reaches a depth of 200 – 300 nm, being the indentations within this interval. However the surface must likely acts as "composite" since both phases are present, and most likely both phases were indented simultaneously. Regarding the mechanical properties of the α - $FeSi_2$, only one reference published by Mikehine *et al*. [295] could be found, where the author reports a hardness and elastic modulus of 5.6 GPa and 108 GPa, respectively. The α - $FeSi_2$ phase from the reference was produced by induction melting, which differs a lot from the method used by us to achieve the same phase. Comparing the attained results for α - $FeSi_2$ with ours, it seems that Si greatly influences the results. Again, like in the β - $FeSi_2$ case, more experimental results are needed to confirm the mechanical properties of the α - $FeSi_2$ phase, so that a proper discussion can be made.

In order to analyze the nanotribological response of the high fluence Fe implanted samples (Figure 52 and Figure 53) the author used the Hertz model [182, 296]. In Figure 58 it is plotted the mean pressure and respective contact radius as a function of the normal load according to the Hertz model equations, described in detail in section § 2.3.2.1 of the present thesis. The values used for both Young´s modulus and Poisson coefficients were 1141 GPa and 0.07 for the diamond [297], and 163 GPa and 0.28 [298] for the Si, being the used value of Young´s modulus the one determined experimentally by the ultramicroindentation tests. In Figure 58 it is also represented the plasticity limits. The $1.1\sigma_Y$ and $3\sigma_Y$ in Figure 58 represent the critical mean pressure for the onset of plasticity and the critical mean pressure for a fully plastic contact, respectively, described in detail in section § 2.3.2.1 of the thesis. The value of σ_Y was calculated from the hardness values of the Si <100> sample from Figure 51, according to the Tabor relation, $H = 3\sigma_Y$ [186].

According to Figure 58, the onset for plastic deformations intercepts the Hertzians load curve for a 5 µN value. In a first approximation, below this value it should not be expected the occurrence of wear, since no plastic deformation is expected. However, Figure 53 shows the opposite, for the Si <100> sample, where wear is detected until a load of 3 µN, being the calculated wear threshold around 2.30 µN, as it can be seen in Table 10. The Hertzian calculations were not performed for the implanted and annealed samples. No significant changes should be expected, except maybe for the as-implanted one, which exhibit a lower value of both hardness and Young modulus, so most likely the model would fit more accurately. The values of contact radius in Figure 58 do not reach high values (< 30 nm), in fact, taking in consideration that the maximum shear stress under the indenter occurs at a depth $0.47a_C$, with a value of $0.47\sigma_M$, the maximum shear stress occurs inside the amorphous layer of the as-implanted sample and within the films of β and α $FeSi_2$ phases. The samples that presented the best nanotribological performance were the ones annealed, at 800 ºC and 1000 ºC respectively. Looking to Figure 53, where the wear rates are plotted vs the applied load, one can see that for lower loads, the 800 ºC sample exhibits lower wear rates. Nonetheless, when normal loads of 5 µN and 6 µN are reached, the wear rate values are overlapped. Beyond this point the 1000 ºC sample shows the lower wear rates. Figure 52 shows that the annealed samples for the low loads, unlike the Si or as - implanted samples, do not show a flat bottom, but rather a bottom where some features can be seen. These same features, can affect the measured value of depth and thus the calculations of the wear rates. For loads higher than 6 µN, all samples seem to exhibit a similar value slope. This might indicate that for the higher loads the results may be influenced by the Si substrate. For a better interpretation of the nanotribological results, the author decided to use the Greenwood and Williamson criteria [188], described in section § 2.3.2.2 of the thesis. Based on this model, it is possible if upon contact, that the asperities of the sample (the diamond tip is much harder than the samples used) are under plastic or elastic deformation. The values used for the hardness and reduced Young's modulus were calculated based on Figure 51, the values of average roughness, R_a, and asperity radius were calculated using an AFM and finally, for the standard deviation of the asperities heights, σ, an approximation was used, like the one Graça *et al.* [229] performed. Considering a Gaussian distribution of asperities heights, the σ value can be approximated as $\approx 1.25R_a$. The plasticity index, Ψ, calculated for all samples, was higher 10. According to Greenwood and Williamson criteria, for $\Psi > 1$, the asperities will deform plastically under even the lightest of loads, thus meaning that most of the contacting asperities during the nanowear measurements were under plastic deformation. This result is quite in good agreement with the attained results. However, Table 10 shows the values of the respective wear thresholds for each sample. For instance, for Si <100> sample, the wear threshold has a value of 2.3 µN. In Figure 59 it is possible to see that for 1 and 2 µN, no wear was detected on the topographical image, the loads are below the threshold limit, nonetheless, the corresponding lateral force image shows exactly where the nanowear scans were performed. According to the Greenwood and Williamson wear should still occur. It may have occurred, at scale that one cannot achieve using an AFM. In fact, the nanoscale mechanisms of friction and wear are still unclear, being highly dependent on the experimental conditions used [299], which presents itself as major difficult to a more elaborated discussion of the results.

The calculated values for the specific wear coefficients varied within an interval of [1.1 – 1.8]x10^{-10} m^3/(N.m). The value for the reference Si was ≈ 1.7x10^{-10} m^3/(N.m). This value is different from the ones published in the literature, Khurshudov *et al*. [300] using also a diamond AFM tip, estimated a wear rate of ≈ 4.5x10^{-13} m^3/(N.m) under scratching test conditions, while Wang and Kato [301] 2.3x10^{-14} m^3 using a pin-on-disk tester with a much higher load than the one used by the author, 100 mN. The value measured by the author is quite distant from the values of literature, this fact, most likely arises from the different experimental conditions used and different diamond tip characteristics. According to the literature, materials with specific wear coefficients in the range of 10^{-14} m^3/(N.m) or higher, are not considered as particularly wear resistant, for such designation, specific wear coefficients of 10^{-16} m^3/(N.m) are expected [302]. The measured values are quite distant from the ones previously mentioned from the literature. The Fe implantation and respective annealings were not able to substantially increase the wear resistance of Si.

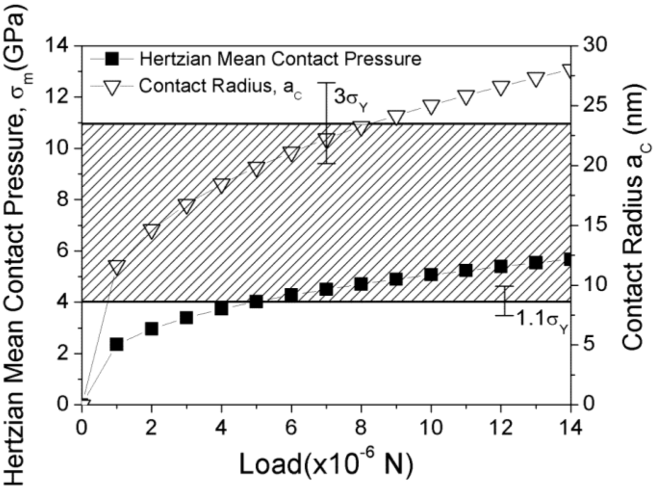

Figure 58. Calculated Hertzian loads and contact radius for a load range comprehended between 0 and 15 µN, for the Si <100> sample.

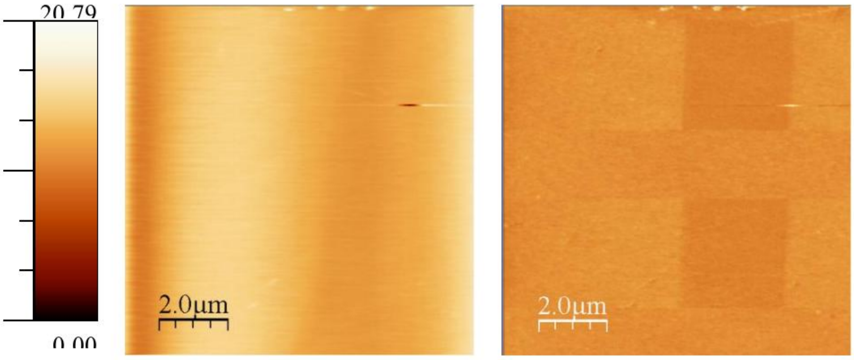

Figure 59. (left) topographical image of nanowear scan with 1 and 2 µN load for the Si <100> sample, (right) corresponding lateral force image.

For the study of the influence of the Fe implantation on both wettability and surface energy of Si, Figure 55, a Si <100> reference sample was used, as previously mentioned. The literature values of contact angle and surface energy for Si tend to vary quite significantly, since each author uses different surface cleaning procedures and, in some cases, different approaches for surface energy determination. Contact angles for Si can range from 0º to 20º [131, 303] while surface energies from 49.3 75 mJ/m^2 to 75 mJ/m^2 [131, 303, 304].

However, Levitin *et al*. [305] used similar experimental conditions, and the measured values for both water contact and surface energy were, 31.8º and 64.5 mJ/m^2, which are very close to the ones achieved in our work 34º and 61.3 mJ/m^2 [305].

The results from Figure 55 show that upon the implantation of Fe the samples become more hydrophobic, that is, have a higher water contact angle compared to the Si reference. Figure 55 also shows that the increase of the contact angle is inversely proportional to the implanted fluence. The increase of the contact angle is most likely being caused by two different effects. On one hand, as it was observed before in the RBS results, that all fluences have an amorphous surface, on the other hand, Fe is present, and is expected to be in higher concentrations with increasing fluence. The low fluence as-implanted sample, presents the highest contact angle and shows the highest decrease in terms of surface energy, and at the same time, the lowest value of polar component of the surface energy (Figure 55). According to the Owens-Wendt method, the one used, the polar component is essentially a non-dispersive component that includes a broader range of interactions than the van der Waals forces, like asymmetric electron donor-electron interactions. These interactions seem to contribute less to the total surface energy upon implantation, though increasing with the fluence. The Si reference sample, for instance, has a higher polar component compared to the dispersive one. The implantation of Fe seems to invert the initial situation due to a combination of amorphous structure and Fe presence. Upon the annealings both low and medium fluence show a decrease in the contact angle, corresponding to an increase of the surface energy. The RBS results show that for these two fluences, Fe is swept to the surface while the recrystalization front advances. Although the 550 ºC annealed RBS spectra were not presented, the low fluence shows a higher migration of Fe towards the surface compared to other fluences. The annealed samples have then, compared to the respective as-implanted ones, not only a higher concentration of Fe at the surface, forming silicide phases in precipitates form, but also no longer an amorphous surface but a recrystallized one. All these effects seem to affect the wettability behavior of once as-implanted samples, rendering them more hydrophilic, however, still with a higher contact angle than the reference. For the high fluence Fe samples one can see that from the as-implanted to the 550 ºC and 800 ºC, a small decrease in the contact angle is observed. It is interesting to see that both contact angle and surface energy are essentially the same. At 800 ºC, as it was observed in the GIXRD and AFM results, Figure 47 and Figure 46, only one phase is present, the β – $FeSi_2$, and covers all surface. The determined contact angles and surface energy are then from the β – $FeSi_2$ silicide phase. The properties have not been reported before, though, as far as we know are novel results arising from the present work. At 1000 ºC, an increased of the contact angle is observed, accompanied by a decrease in the surface energy, comparatively to the other temperature annealings. Like in the case of the as-implanted samples, at this temperature the polar component of the surface energy is quite small, becoming the dispersive component the most significant component of the surface energy. At 1000 ºC, as it was observed in the SEM, the surface is composed by two different phases, Si and α – $FeSi_2$. The observed increase of the contact angle may be associated with the multiple different interfaces Si/α – $FeSi_2$ across the surface.

4.2 C$^+$ IMPLANTATION

4.2.1 STRUCTURAL CHARACTERIZATION

In the present chapter the results relative to the C$^+$ implantation will be displayed. The microstructures of the C$^+$ implanted and annealed samples were observed under the FEG-SEM. The attained microstructures are present in Figure 60. Unlike the Fe implantation case, microstructures could only be observed after the 1000 ºC annealings and only for the medium and high fluence, respectively. These samples, the medium and high fluence, were annealed with the respective implanted surface facing against each other. The surface morphology of both samples is presented in Figure 60. The samples presented a circular mark, in the center of the sample, and a “grayish” zone in the surrounding area. The microstructures of the two zones are different. For the medium fluence, in fact, no microstructure was observed in center zone whereas precipitates with dimensions close to ≈1 µm were seen in the periphery. For the high fluence case, a set of two different precipitates were observed, with different dimensions. In the central area, the precipitates range within of ≈ 50 – 100 nm (rough estimation based on Figure 60) while in the periphery zone the precipitates can reach a dimension of ≈ 500 nm. The reason for this behavior is still unclear.

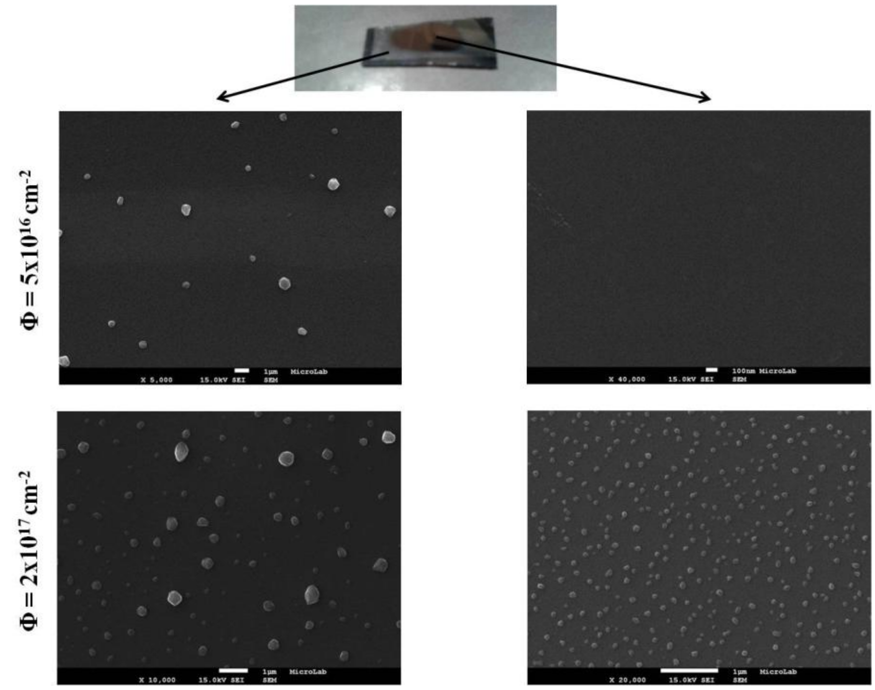

Figure 60. (top) Schematic representation of the 1000 ºC medium and high fluence samples, (below) SEM micrographs of the different zones, center and periphery, of the medium and high fluence 1000 ºC annealed samples.

GIXRD measurements were performed on the C^+ implanted and annealed samples to identify the phases that were formed. The GIXRD results are presented in Figure 61. Looking into the figure one can observed that no peaks are observed for all fluences and all studied temperatures. Even in the cases where some precipitates were observed, such as the cases of the medium and high fluence at 1000 ºC. Although not shown in the present thesis, the author also performed 2θ – θ scans (Bragg – Brentano) on these same samples. The only peaks that could be observed were corresponding to Si. If precipitates could have been seen under this geometry, the precipitates had grown epitaxially with substrate. However, the lack of peaks under the different scan geometries enables one to understand that there is not enough material density to form a XRD signal.

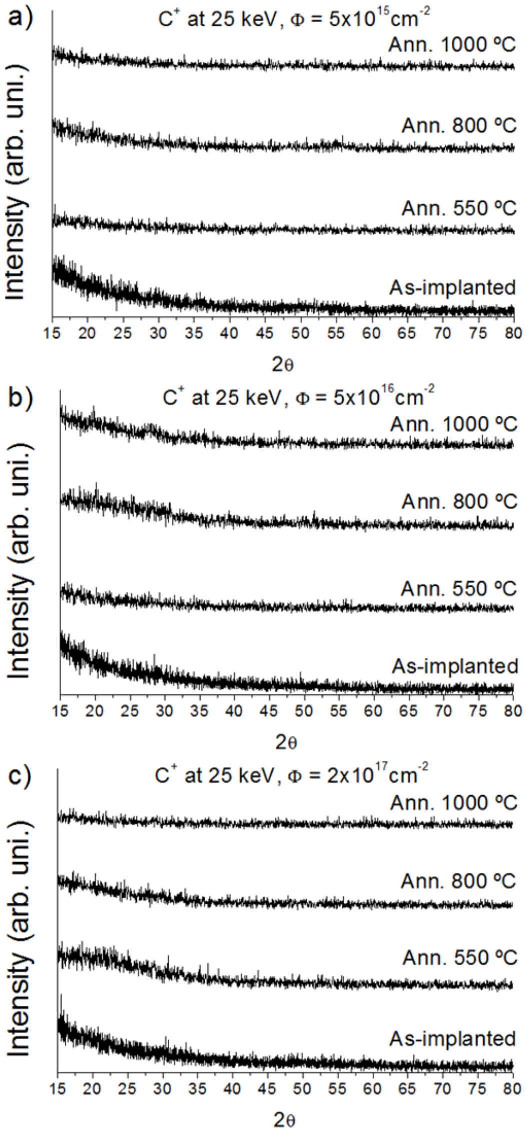

Figure 61. GIXRD results (θ = 1.5º) for the (a) low fluence, (b) medium fluence and (c) high fluence C^+ implanted and annealed samples.

RBS measurements were made on the carbon implanted and annealed samples, for all fluences and are displayed in Figure 62. Again, like in the case of the Fe implantations, the author decided not to present the spectra of the 550 ºC annealed samples for the sake of simplicity. The corresponding spectra were quite similar to the as-implanted ones. In Figure 62 it is possible to observe, in the respective as-implanted spectra, that an amorphous layer was formed for each implanted fluence. Using the surface approximation, the thicknesses of induced amorphous layers were calculated. The calculated values were ≈ 95 nm, 140 nm and 170 nm for the low, medium and high fluence respectively. One can also see that the low fluence sample presents a different behavior upon annealing relative to other two fluences. In the low fluence case as the temperature rises, one can see that the amorphous layer recrystillazes and the sample recovers the initial cristallinity. The calculated minimum yield for the as-implanted state was ≈ 33 %, decreasing to 22 % after 800 ºC annealing and 11 % for the 1000 ºC annealing. For the medium and high fluence respectively, only a very small recovery is observed with the increasing of the temperature, of just a few nanometers. What was an amorphous layer upon annealing became most likely a polycrystalline zone that “dechannels” the incoming beam, a phenomenon already described in the literature [306]. The detection of C signal under RBS characterization could only be observed for the high fluence sample at 1000 ºC. The sample presents precipitates of different dimensions, as it can be seen in Figure 60. Despite the fact that the medium fluence also presented precipitates at the same temperature, no signal in the RBS was detected. The small value of scattering cross section of C makes it difficult to see the C signal on the RBS spectra for the samples implanted with lower fluences.

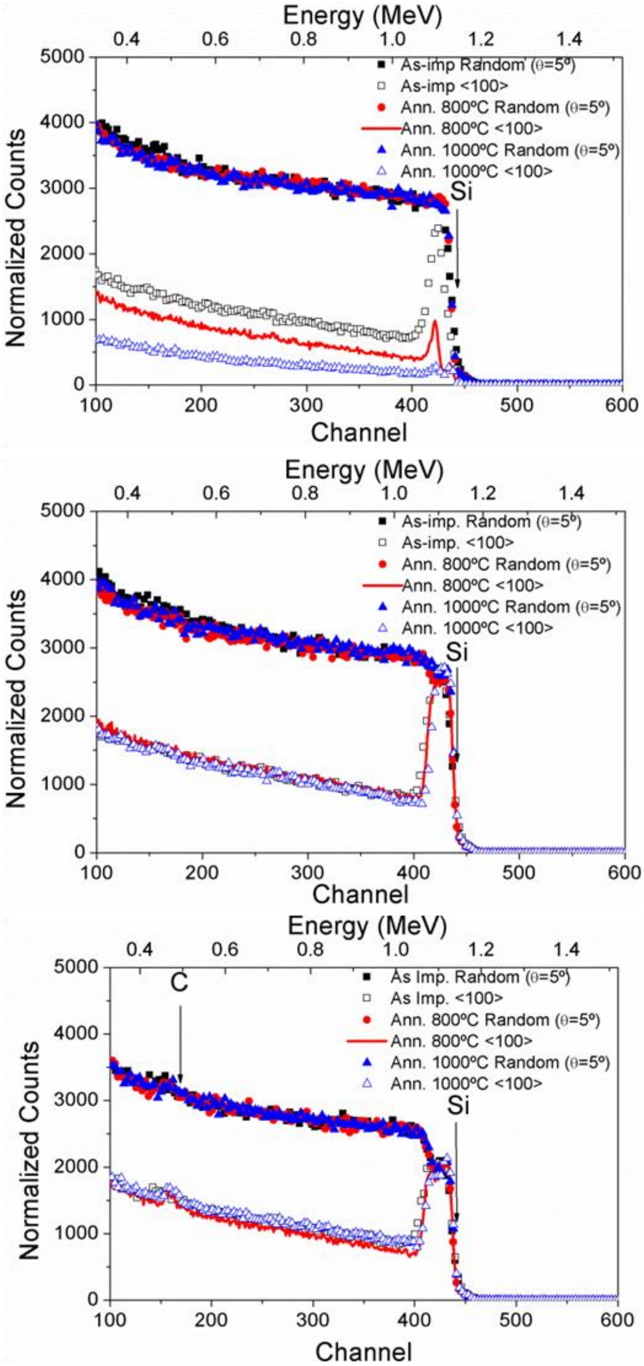

Figure 62. RBS spectra of the carbon implanted and annealed 800 ºC, 1000 ºC samples (top) low fluence, (middle) medium fluence and (bottom) high fluence.

XPS measurements were performed in some of the C$^+$ implanted and annealed samples. The main objective was to identify the precipitates observed under SEM characterization that did not present any XRD signal. The XPS measurements were performed then on the high fluence as-implanted and 1000 ºC annealed samples, while for the medium fluence one only the high temperature annealing was made. The XPS spectra corresponding to C, Si and O peaks are detected in Figure 63 while the respective atomic concentrations of the identified species are presented in Table 11. Observing the column corresponding to the C peaks, for all samples in Figure 63, one can observe a peak belonging to the C contamination, which corresponds to several different species indentified in Table 11, and a C-Si peak belonging to SiC, thus allowing the XPS characterization to identify the precipitates observed by SEM (Figure 60) as SiC. Figure 63 shows that for the high fluence sample, the transition from the as-implanted state to the annealed one induces a change in the form of C-Si peak, from a shoulder type to a peak shape. In the case of the medium fluence of CMT1000 sample, as expected, the peak is less evident compared to the higher since this sample has a lower content of C. The middle column of Figure 63 shows the Si peaks indentified, corresponding to both the "metallic" and oxidized state of this species. Table 11 shows that relative to silicon oxide both stoichiometric and non stoichiometric oxides species are present in the surface of all XPS characterized samples.

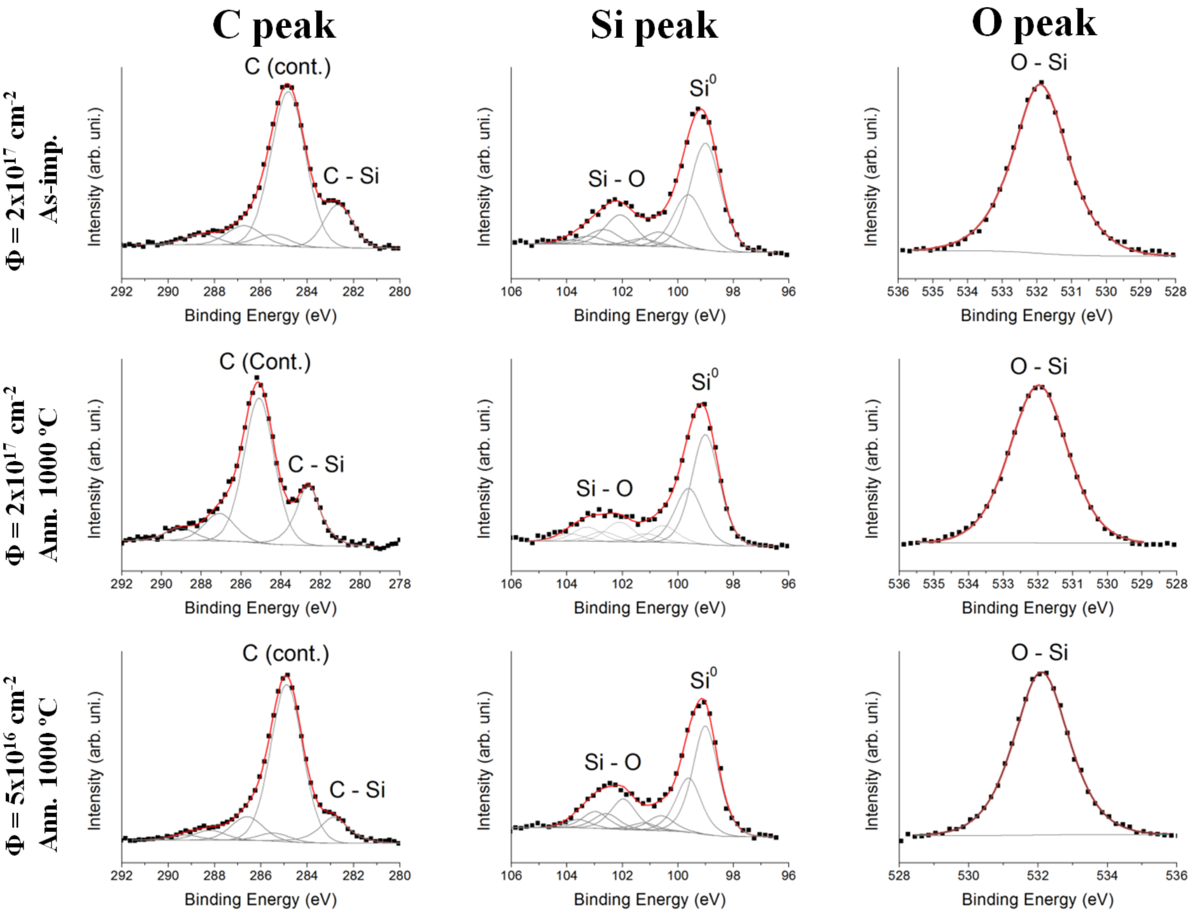

Figure 63. XPS Spectra corresponding to the C, Si and O peaks of the high fluence as-implanted and 1000 ºC annealed samples and medium fluence carbon implanted at 1000 ºC. The points represent the experimental data, the grey lines represent the components of the fit that is represented in a black line.

Table 11. Atomic concentration and ratios of the identified species under XPS characterization

Element	**$\Phi = 5x10^{16}$ cm^{-2} Ann. 1000 ºC**	**$\Phi = 2x10^{17}$ cm^{-2} As-imp.**	**$\Phi = 2x10^{17}$ cm^{-2} Ann. 1000 ºC**	**species**
Si	18.8	22.0	26.0	Si
	2.6	3.0	4.0	Si-C
	5.3	6.3	4.6	SiO_x (x<2)
	2.9	1.7	3.4	Si-O (SiO_2)
O	29.6	30.3	32.2	O - Si
N	1.4	1.6	1.8	R-NH2 (peak not shown)
C	4.6	5.5	5.7	C-Si
	26.8	23.5	16.0	C-C, C-H
	1.4	1.7	1.8	C-N
	4.1	2.9	3.1	C-O
	1.7	1.6	1.4	C=O
Ratios				
C/Si	1.76	1.84	1.45	
Si-C/C-Si	0.54	0.54	0.69	
C-Si/C (total)	0.12	0.16	0.20	
Si-C/Si (total)	0.09	0.09	0.10	
C-Si/Si (total)	0.15	0.17	0.15	
O/Si	1.00	0.92	0.85	
C-N/N	0.97	1.00	1.00	

4.2.2 WETTABILITY STUDY

The influence of C implantation and annealing on both wettability behavior and surface energy of Si is shown on Figure 64. The reference values of Si present in Figure 64 are exactly the same as the ones showed previously for the Fe implantations. The results suggest a trend. The as-implanted samples, for each implanted fluence, exhibit a higher contact angle compared to reference Si. The contact angles increase from ≈ 30º to 60º almost 70º whereas the surface energy decreases from ≈ 60 mJ/m^2 to ≈ 40 mJ/m^2. The C implanted sample with the highest contact angle is the medium fluence implanted one, followed by the low and high fluences, respectively. The effect of annealing of the C implanted results in a decrease of the contact angle corresponding to an increase of the surface energy. The low fluence sample, Figure 64, shows quite an interesting evolution with the increase of temperature, an almost monotonic decrease of the contact angle. For the others fluences a more “abrupt” fall of the contact angle is observed for all annealings relative to the as – implanted state. The 550 ºC and 800 ºC annealed samples tend to have similar contact angles, while for the higher annealing temperature, 1000 ºC, a small decrease is again observed. The effect of the decrease of the contact angle with the increase of annealing temperature is directly related with the increase of the surface energy of these samples, as it can be seen in the right column of Figure 64.

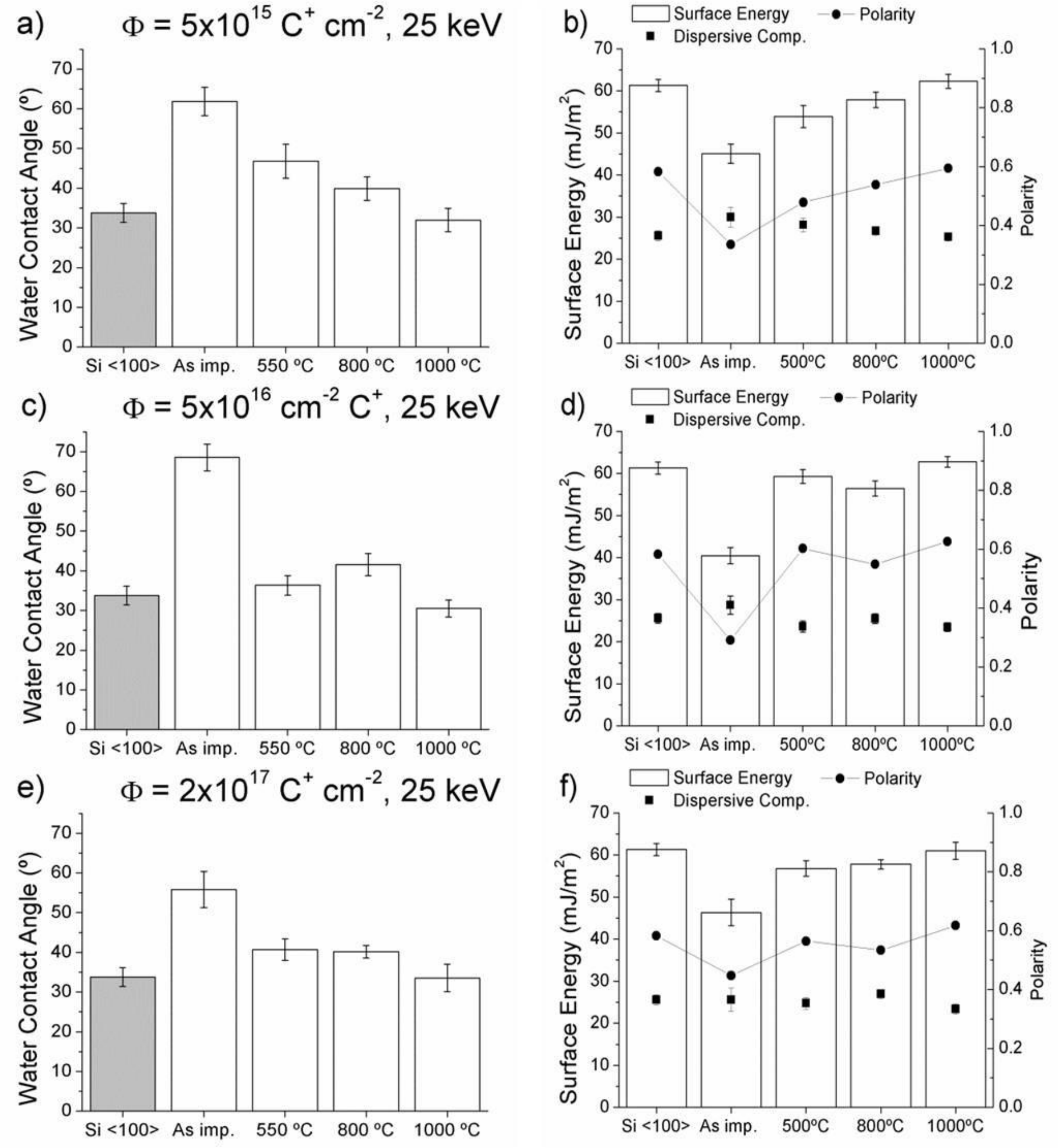

Figure 64. Water contact angle, surface energy, dispersive component and polarity of (a,b) low fluence (c,d) medium Fluence, (e,f) high fluence, of the C^+ implanted and annealed samples.

4.2.3 NANOTRIBOLOGICAL STUDY

Nanowear studies were conducted on the high fluence single C^+ implanted and annealed samples, with the exception of the 550 ºC annealed one. The nanowear scans corresponding to the Si <100> are shown in Figure 65 whereas the ones corresponding to C implanted samples are represented in Figure 66. The nanowear experiments on the C implanted samples were carried on using the Nanosurf AFM with a Microstar® diamond tip.

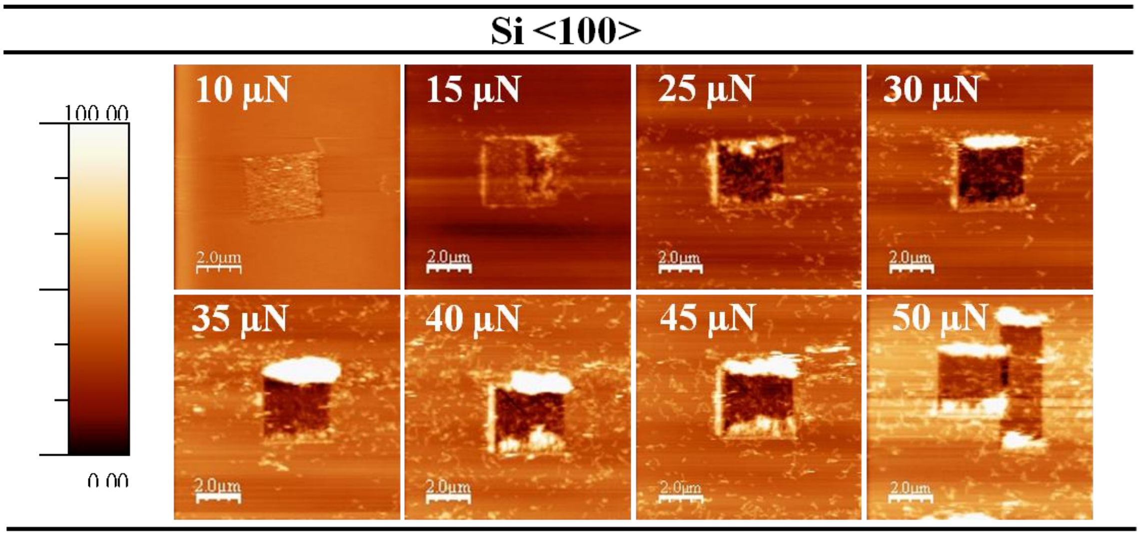

Figure 65. Nanowear scans of the Si <100> sample. The normal load of each scan is indicated on the top left corner (height color scale in nm).

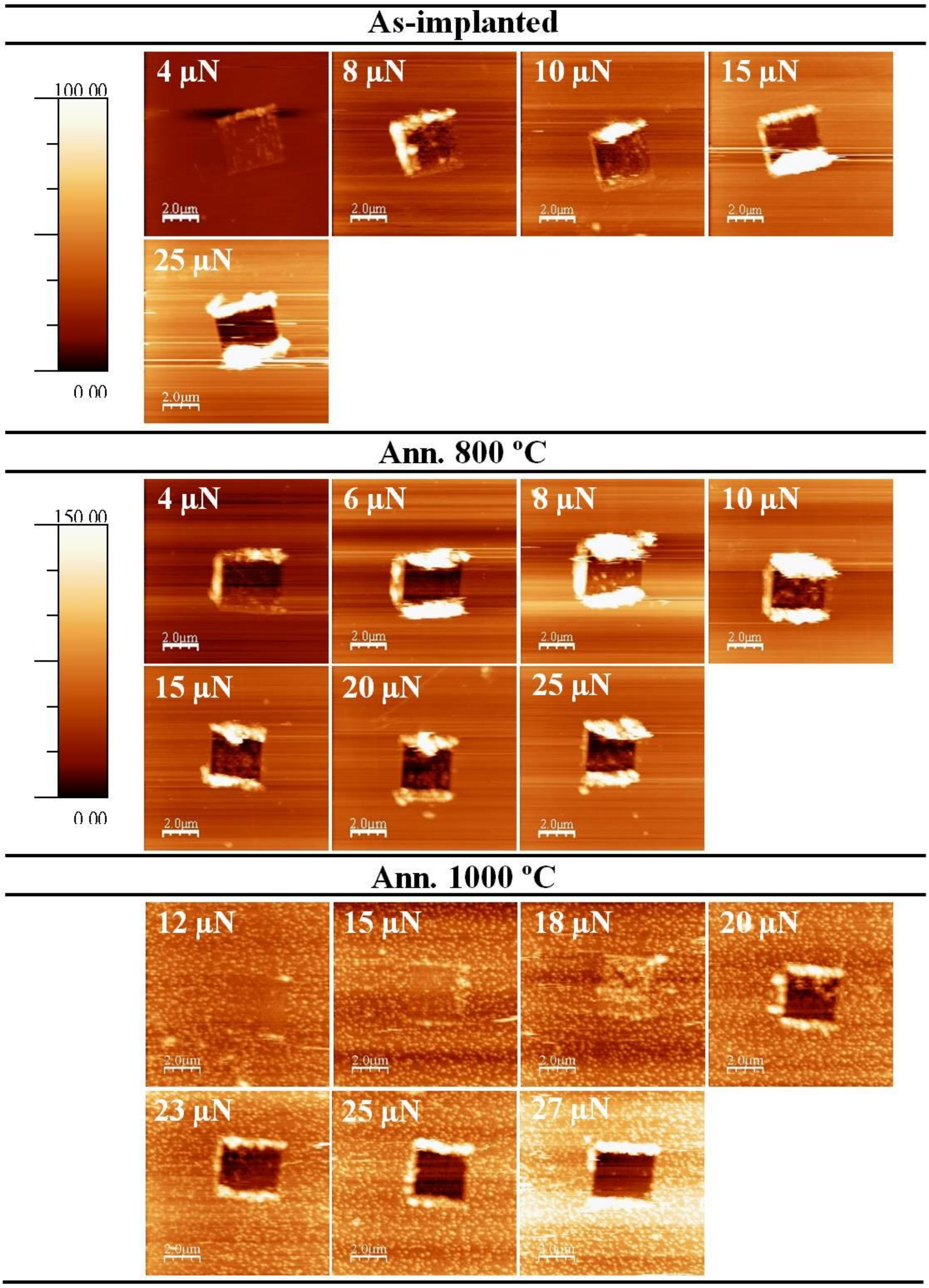

Figure 66. Nanowear scans for the high fluence C$^+$ implanted samples: as-implanted, annealed at 800 ºC and 1000 ºC. The normal load of each scan is indicated on the top right corner (height color scale in nm).

Looking into Figure 65, corresponding to the Si nanowear scans, one can observe an interesting aspect. For the lower load, 10 µN, no depression or crater is actually seen but rather a square with worm-shaped protuberant features inside. These features are actually above the surface and can be observed in more detail in Figure 67, with the corresponding profile. The same features are also present at 15 µN, but this time, they do not fully cover the wear scan, since a crater can be observed on the right side of the scan. The 10 µN to 15 µN scans seem to show the wear initiation of the Si sample. Starting from the 25 µN scan, craters can be observed, for all loads, with a huge amount of debris surrounding the scans. For the highest load, it is possible to observe rectangular wear scan on the side of the scan measurement.

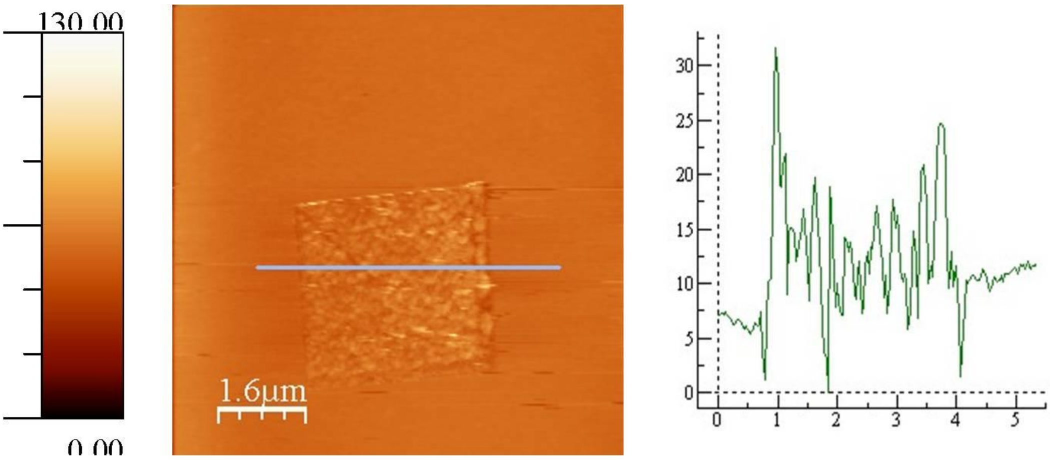

Figure 67. (left) Zoom scan of the 10 µN nanowear scan of the Si sample, (righ) profile of the line of the left image (height color scales in nm).

As for the C implanted samples, Figure 65, one can observe some interesting differences when comparing to Si. Both as-implanted and 800 ºC annealed samples start to present wear at much lower loads, whereas the exact opposite happens for the 1000 ºC annealed sample, where wear only starts showing at 20 µN. It is curious to observe that for the high temperature annealing, at 18 µN, the same type of features that appeared in the Si sample appear again, just before wear starts to initiate. These were not observed for the other implanted samples, maybe lower loads were needed in order to do so. Regarding the debris, the implanted samples exhibit as much as the Si one. It seems in fact that for the Si case the debris tend to present a higher degree of adhesion towards the substrate. Multiple scans were made in order to sweep the scanned areas before taking the final image (the same number for each sample), but Si debris are still present surrounding the scanned area at the higher loads.

The wear rates of both Si and C^+ high fluence implanted samples were calculated based on the average dimensions of the worn scans (Figure 65 and Figure 66). The results are presented in Figure 68a), where is also possible to observe the calculated specific wear coefficients, for each sample respectively. Looking into Figure 68a) one can easily see that the carbon implanted samples do not present wear rates lower than Si reference, being the exception the CHT1000 sample at the lower normal loads. Figure 68a) also shows that all samples present a linear relationship Wear rate – Load, with the exception of one, the CHT800 sample. For this specific sample one can see that at a load of 10 – 15 µN, a transition occurs, and the wear rates start to increase less with the increase of the load. Before the transition one can see that the CHT800 sample presents a value of specific wear coefficient that is more than two times higher than the value of Si whereas after the transition the value is significantly reduced, becoming even lower than the Si reference value - Figure 68b). As it can be seen in Figure 66 and Figure 68a, the wear of the CHT1000 sample initiates at a high load, around 18 – 20 µN. However, this same sample is the one that presents the highest value of k.

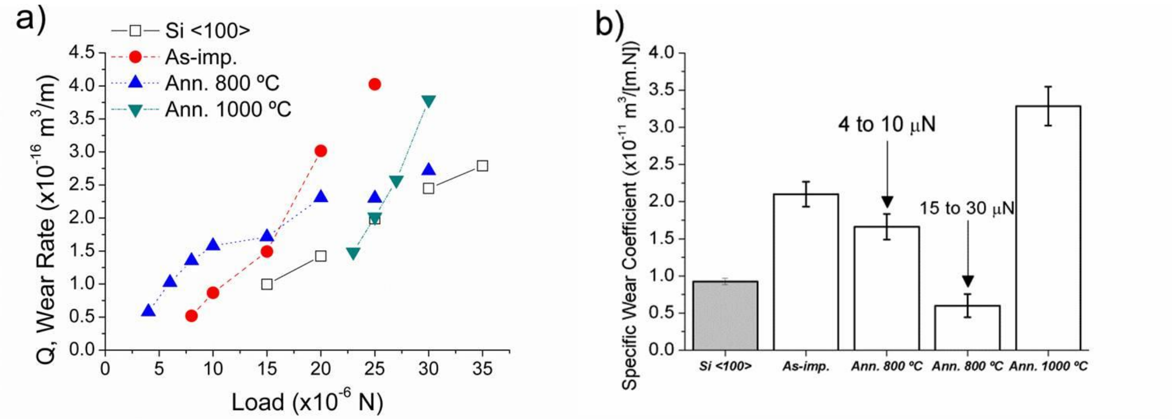

Figure 68.(a) Calculated wear rates of Si and C$^+$ implanted and annealed samples, (b) calculated specific wear coefficients of the Si and C+ implanted and annealed samples.

4.2.4 DISCUSSION

The FEG-SEM microstructural analysis of the C implanted and annealed samples showed microstructures only for the medium and high fluences, after 1000 ºC annealing. The literature published on the topic: silicon implantation by carbon; shows that implantation of C into Si forms SiC layers or precipitates [307-311] depending on the implanted fluence and energy, buried under the Si surface. For C implantations at low energies, typically below 50 keV we observe microstructures at the surface [312, 313]. The results presented are within the latter category, where surface microstructures are formed (Figure 60). Markwitz *et al.* [313] implanted Si with a fluence of 7.6x10^{16} cm^{-2} (with a 10 keV energy), quite close to the medium fluence of our study, 5x10^{16} cm^{-2}, and also observed the presence of nanoprecipitates at the surface. The precipitates formed for the medium fluence are considerably larger. The annealings conditions used by Markwitz *et al.* were considerably different, using an EBA (electron beam annealing) annealing at 1000 ºC for 15 seconds. Also Hopf *et al.* [312], observed different microstructures but using implantations at high temperatures and quite higher fluences.

The XRD characterization of the C implanted samples did not show the presence of any peak, for all fluences and respective annealings, Figure 61. Although not shown in the present thesis, the author also performed 2θ – θ scans (Bragg – Brentano) on these same samples. The only peaks that could be observed correspond to Si. If precipitates could have been seen under this geometry, the precipitates had grown epitaxially with substrate. However, the lack of peaks under the different scan geometries enables one to understand that there is not enough material density to form a proper XRD signal. Despite the fact that the XRD measurements did not allow the identification of the observed precipitates for the higher temperatures, it is a known fact that SiC can form spontaneously in a Si – C solution, since the Gibbs free energy of the SiC compound is -70.385 kJ/mol and -40.973 kJ/mol at temperatures of 300 K and 2200 K, respectively [314]. This is also confirmed by the binary C - Si phase diagram [282], Figure 69, where it is possible to observe that SiC is the only phase expected to be formed. The precipitates are formed most likely due to low limit value of C solubility in Si, 10^{-3}–10^{-4} at %C, in the temperature range of 1200 ºC to 1400 ºC [315], forming a supersaturated solution rather than a solid solution, where the impurity C is diffused/segregated towards the surface with the temperature, forming the observed precipitates.

Unlike in the Fe implantation case, the author did not perform simulations of the attained RBS spectra concerning the C implanted and annealed samples. The reason for such lies on the fact that using Windf/NDF© software it is quite difficult simulate the back end of the spectra, where the C signal is present, and that could only be observed for the high fluence case.

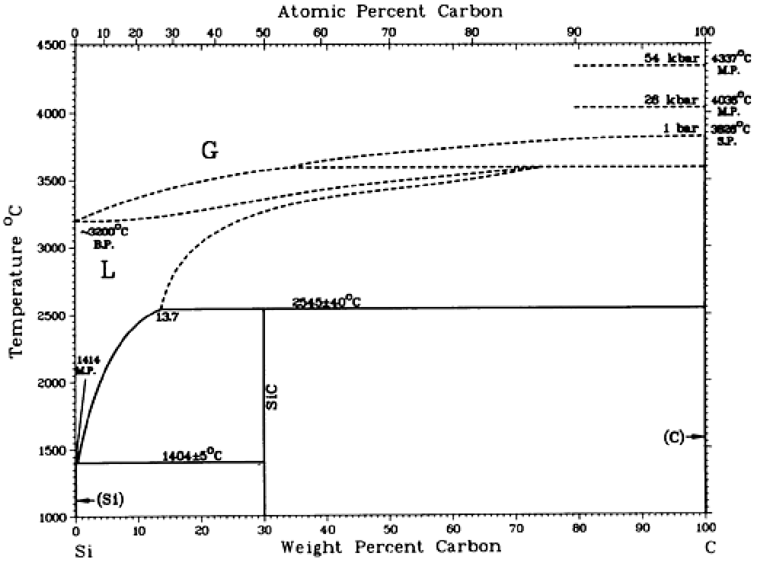

Figure 69. Binary alloy C - Si phase diagram [82].

Relatively to the XPS data, Table 11 enables one to understand the effect of the high temperature annealing of the high fluence carbon implanted sample based on the calculated ratios, present at the bottom of Table 11. The first calculated ratio, corresponding to total carbon divided by the total detected Si, C/Si, shows that for the high fluence case there is a decrease from the as-implanted to the 1000 ºC annealed sample, having the CMT1000 sample a close value compared to high fluence as-implanted one. The decrease of the ratio value may lead one to think that for the high fluence case there is an actual decrease in the concentration of C in the surface upon the annealing. However, a closer look into Table 11 tells us that the CHT1000 sample presents the lowest value of total C, since it has the smallest concentration of C-C-C-H, while the concentration of the other C species is relatively similar within all samples. This fact also affects the second calculated ratio, the C-Si/C (total) one, which may lead one to think that concentration of SiC increases with the temperature. The following calculated ratios, the Si-C/Si (total) and C-Si/Si (total), which are not affect by the decrease of the contamination carbon of the CHT1000 sample, show identical values (for each specific ratio) for the three studied samples. On one hand, this fact tells one that the amount of Si-C or C-Si for the high fluence case, barely increase with annealing while on the other hand, the concentration of SiC for both medium and high fluence carbon annealed samples is essentially the same, despite the fact that more precipitates can be seen in the CHT1000 sample. The ratio between the Si bound to carbon, and the carbon bound to Si (Si-C)/(C-Si), enables one to see the evolution of the SiC formation with the increasing temperature for the higher fluence case. The initial ratio value for the CHAs sample is 0.54, reaching a value of 0.69 at 1000 ºC for the CHT1000 sample. The evolution of the ratio values shows that initially, in the as – implanted sample mostly clusters of C are present, with some content of Si. As the temperature raises, the ratio value increase, meaning that Si content of the cluster of C is increasing. However the ratio value attained after the 1000 ºC annealing is still a bit distant from 1, meaning that stoichiometry of the SiC phase present after the 1000 ºC annealing for the higher fluence is not 1:1, the one more or less expected from the SiC phase. The same happens for the SiC of the CMT1000 sample, that presents a ratio value of 0.54.

The author also tried to study the effect of oxidation with the increase of temperature using the XPS data, using the O/Si ratio present in Table 11. The O/Si ratio shows an odd trend. Although the ratio values do not significantly diverge within the studied samples, one might expect that the 1000 ºC annealed samples to exhibit the highest ratio values. In fact, the medium fluence annealed sample shows the highest ratio value, but the high fluence annealed sample shows exactly the opposite, the lowest ratio value. Finally, the as-implanted sample shows an intermediate ratio value between the annealed samples. Based on these O/Si values it becomes quite hard to fully understand the oxidation trend. The results seem to indicate that with the increase of temperature oxidation occurs, but not in a significant way.

The effect of C implantation on the wettability behavior of Si is shown in Figure 64. It is possible to observe that the implantation of carbon renders the Si surfaces more hydrophobic compared to the reference. Comparing just the three as – implanted samples, corresponding to the three different implanted fluences, one can see that the contact angle increases from the reference sample to the low fluence one, increases again but slightly with the fluence for the medium fluence sample decreasing afterwards for the highest fluence. The increase of the contact based on C implantation in Si has been reported before in the literature by Wang *et al*.[170], having observed a similar behavior compared to the one achieved by the author, that is, an increase of the contact angle with the implantation fluence but a decrease for the highest fluence, although using a different orientation of Si, Si <111>. The increase of the contact angle of the as–implanted samples is directly related with the decrease of the surface energy of the implanted samples, Figure 64. It is also possible to observe that the implantation besides lowering the surface energy, it significantly reduces also the value of the polar component of the total surface energy. This also happened in the case of the Fe implantations, although the contact angles achieved with Fe were slightly lower. Another identical behavior between the Fe and C implantations, Figure 55 and Figure 64, is the decrease of the contact angle upon the annealings, with the exception of the FeHT1000 sample. The initial thought of the author was that with the increase in temperature, the oxidation of the surface would occur causing the contact angle to decrease, as it can be seen in Figure 64 for all fluences. It is well known that OH groups form on Si surfaces rendering surfaces hydrophilic. In the past, wettability studies have been made in oxidized Si, revealing contact angles that vary between 11.4º and 47º, depending on the oxidation conditions [60, 316, 317]. The experimental results relative to contact angles are within this interval. However, unlike the Fe implantation case, XPS measurements were performed on some of the C implanted and annealed samples. The results, previously shown and discussed, revealed themselves quite contradictory. Compared to an as–implanted sample, the 1000 ºC medium fluence annealed sample presented a higher degree of oxidation while the high fluence annealed at the same temperature revealed a smaller degree of oxidation. However, the contact angles between these two samples were quite identical, which may indicate that the influence of oxidation of Si may not be the only parameter influencing contact angle. In the literature contact angles of SiC surfaces can vary from 58º to 70º [318, 319], being quite distant from the values of the 1000 ºC annealed samples, ≈ 30º, that presented some SiC precipitates. Studies show that SiC spontaneously oxidizes even in ambient air [320, 321] preferably on the superficial Si. The oxidation of the SiC will form hydroxyl groups on the surface, which make it more hydrophilic. Other authors deliberately formed hydroxyl groups on the SiC surface by using H_2O_2 [322] or HF [318] solutions, achieving contact angles of 13º or 38º, depending on the SiC orientation [318]. The oxidation of SiC will also affect the contact angle measurements since more hydroxyl groups will be present at the surface making it more hydrophilic.

The nanotribological characterization of the C$^+$ implanted samples, as well as the Si <100> one, revealed the presence of some worm-shaped features that were protuberant above the surface level in the respective scanned areas, having these features appeared in the Si and CHT1000 samples, respectively, as it was observed in Figure 65, Figure 66 and in more detail in Figure 67. These types of features were first observed in Si by Kaneko *et al*. [323] after some nanowear tests using a diamond tip, and have been denominated in the literature as hillocks. Although initially Kaneko and Anddoh thought that these features appeared as a result of chemical reactions between the tip and the surface - oxidation [324], more recent studies show that these hillocks can also form not only in Si in vacuum but also in already oxidized surfaces such as quartz [325, 326].

So far, it has been acknowledged that the upheaval of the hillocks correspond to a pre-stage of wear of Si, before the removal of the material, being this one major difference between the wear of Si at the macro and nanoscale. The results published by Yu *et al*. [326-328] showed that the upheaval of the hillocks is mainly caused by the mechanical interaction between the tip and sample, depending on the load, number of cycles, velocity of the scan, distance and surrounding environment. The hillocks were composed of a – Si, right above a plastic deformed layer that contained defects. The authors attributed the upheaval of the hillocks as a result of a volume expansion resulting from the phase transitions: Si – I diamond to Si – II Tin and finally to a – Si. In order for this transition to occur, the Hertzian pressure on contact should reach values in the range of 11 – 13 GPa [326, 327]. However, the same authors also observed the occurrence of hillocks for cases where the Hertzian pressure was quite lower than the latter presented values, around 3.5 GPa, [327]. The Si phase transitions under scratching test conditions are different from the ones that occur during the indentation. Under scratching conditions a diamond Si structure can be directly converted into a – Si [327], being also noticed by the authors that the lower the speed scans are the thicker the amorphous layer is. The attained hillocks in the Si sample appeared at loads in the range of 10-15 µN while for the CHT1000 one at ≈ 18 µN. As it was mentioned before, the hillocks represent the first stage of wear, before the material removal. Since the wear threshold of the CHT1000 sample is higher than the Si one, most likely due to the presence of the SiC precipitates, it is easily understandable why the hillocks appeared at a higher load.

The mean contact Hertzian pressures were calculated for the Si sample since a completely different diamond tip was used. The equations of the Hertz model have been previously described in section §2.3.2.1 of the thesis. The used value of the reduced Young´s modulus is exactly the same as the one earlier used in the nanotribological characterization of the high fluence Fe implanted samples, see section §4.1.2. For the mean contact Hertzian pressure calculations it was needed to determine the tip radius. Using the SPIP® commercial Software, that uses the blind reconstruction method [329] for the radius calculation, a value of 57 nm was attained - Table 7. The calculated Hertzian mean contact pressure in function of the load is shown in Figure 70 alongside the plasticity limits and contact radius, as it was shown in the previous case of the Fe implantation - Figure 58. Comparing Figure 58 with

Figure 70, where the respective Hertzian loads were calculated for the different diamond tips used for the nanowear characterization, DNISP and Microstar, one can see a significant difference. The calculated Hertzian loads for the Microstar diamond tip - Figure 70 are around three times higher when compared to the ones calculated for the DSNP tip - Figure 58, considering the same load range, 1 – 15 µN. The main difference for Hertzian pressure calculations lies on the radius, which is around 6 times lower in the Microstar tip thus giving higher values of pressure. In opposition, the contact radius values shown in Figure 58 are almost the double of the ones in Figure 70, again considering the same range, 1 – 15 µN. The reason lies again on the tip radius, the only different parameter for the contact radius calculation.

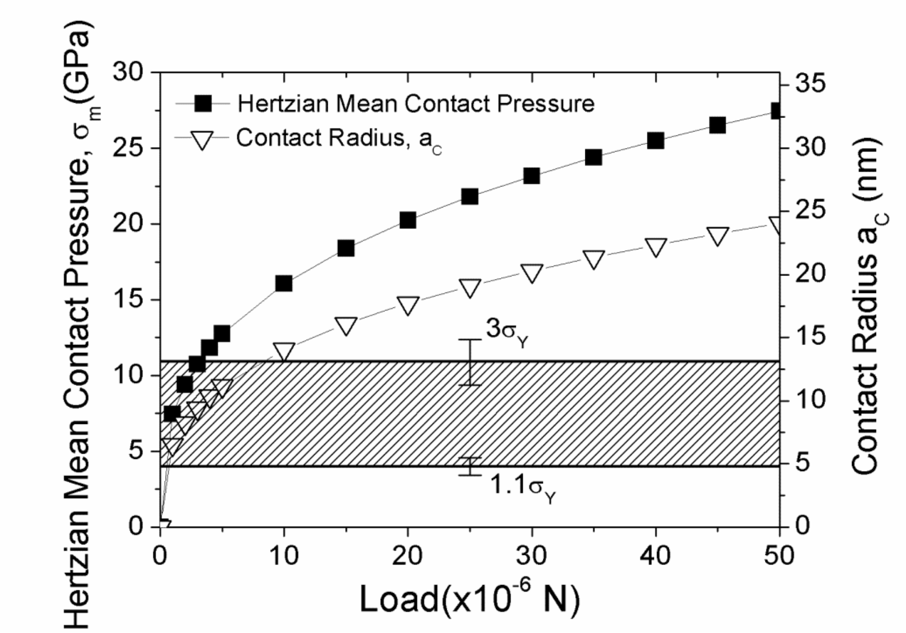

Figure 70. Hertzian mean pressure variation in function of the load for Si nanowear experiments carried out in the Nanosurf apparatus.

Despite the differences on the nanowear experimental conditions used in the present work, it is possible to observe that the Si <100> wear rate variation as a function of the load exhibit always a linear relationship: Figure 68a) and Figure 53. Under similar conditions, Myamoto and Kaneko observed for Si a different relationship, more close to a polynomial or exponential variation [161, 166]. The calculated specific wear coefficient for Si in the Nanosurf AFM was 8x10^{-12} m^3/(m.N), around two orders of magnitude lower than the one calculated in the Vecco CP-II AFM, ≈ 1.7x10^{-10} m^3/(N.m). The 8x10^{-12} m^3/(m.N) value does not also match the values reported in the literature by Khurshudov *et al.* [300] using also a diamond AFM tip ≈ 4.5x10^{-13} m^3/(N.m) and Wang and Kato [301] 2.3x10^{-14} m^3/(N.m) using a pin-on-disk tester, still being one or two orders of magnitude lower. Despite that difference, the value calculated using the Nanosurf was definitely closer to values reported in the literature, when compared to the one calculated using the Vecco AFM.

For the C$^+$ implanted samples, more specifically the CHAs one, in Figure 68a) one can observe a linear wear rate variation with the applied load, presenting always higher values of wear rate when compared with Si reference. From the RBS spectra in Figure 62c) the amorphous layer induced by the implantation extends to ≈ 170 nm. Since the highest load used for this sample was 25 µN, where depth of ≈ 45 nm was reached, the nanowear scans were always within the amorphous layer and apparently behind the C concentration peak, placed at 83 nm according to SRIM calculations The XPS characterization of the CHAs sample revealed that SiC is already detected in this sample, but with a stoichiometry that is different from 1:1, as it can been seen in Table 11 in the (Si-C/C-Si) ratio. Despite the presence of SiC, no improvements were achieved concerning the nanowear resistance. Ueda *et al*. [170] implanted C into Si using the plasma immersion implantation technique and observed an increase of hardness, although not as high as it was expected when compared to the SiC one. Ueda *et al*. attributed the difference to the fact that the SiC formed is in an amorphous state, thus not possessing the same mechanical properties as crystalline SiC. Myamoto *et al*. [161] performed nanowear experiments with C$^+$ implanted Si and an increase of wear resistance was observed but only when the depths reached were close to the peak of C concentration. Prior to that point the implanted sample presented higher wear rates. In the present work the single high fluence Fe as-implanted sample also presented the worst wear resistance (Figure 53). As it was seen and discussed before, in the Fe results/discussion (section §4.1 and §4.1.4), the a – Si phase (with Fe) has the worst mechanical properties when compared to c – Si, lower hardness and Young´s modulus. It seems that the same happens with the carbon implantation, despite the presence of SiC within the amorphous layer. Upon the annealings at 800 ºC and 1000 ºC, the nanowear resistance of the C implanted samples changes significantly. The 800 ºC sample presents a nonlinear wear rate variation. As it can been seen in Figure 68a) at a load of 15 µN, a change in the nanowear behavior occurs. It seems that the sample is composed of two different layers, a more superficial one that exhibits not only higher wear rates than the reference Si but also higher than the as-implanted sample, and a buried layer with a higher wear resistance. Since the CHT800 sample does not present any microstructure, the better nanotribological properties at the higher depths are most likely associated with the formation of a more stable stoichiometry SiC, enhanced by the annealing.

The nanowear scans in Figure 66 show that above 8 μN structures are seen on the bottom of the scanned areas. The specific wear coefficient of this sample, considering only the range above the 15 μN, was the lowest measured value within the C implanted samples, thus showing the significant wear resistance of the buried layer. More difficult to explain are the worst tribological properties of the surface layer. After the annealing it is expected that the initial a – Si layer recrystallizes - Figure 62, thus being the properties of the recrystallized Si closer to the Si reference one. However this does not seem to happen. In order to find some answers we perform some Raman studies. The spectra obtained can be seen on Figure 71 and they can actually help to explain the worst nanotribological properties of the top surface layer of the CHT800 sample. The represented scans spectra only contain information regarding a 200 cm^{-1} to 1050 cm^{-1} range, above this value no information could be retrieved. In Figure 71 it is possible to observe clear differences between the reference Si and the as-implanted sample. The Si peaks at 300 cm^{-1}, 520 cm^{-1}, 620 cm^{-1} and a band centered at 970 cm^{-1} show a much lower intensity upon implantation and a new peak emerges at 472 cm^{-1}, referenced in the literature as belonging to the a – Si phase [330-332]. Upon the annealing at 800 ºC one can see that the peak at 520 cm^{-1} increases in intensity and that the 300 cm^{-1} peak and the band at 970 cm^{-1} start to emerge again, indicating recrystallization of the a – Si phase. However, the a – Si peak still remains, but slightly shifted, positioned now at 482 cm^{-1}. The growing of the Si peak at 520 cm^{-1} and the shift of the a – Si phase seem to indicate that either the recrystallization of the Si was not completed or the recrystallized silicon is most likely highly concentrated in defects. At the higher temperature, 1000 ºC, the a – Si peak merges with the Si 520 cm^{-1} peak, forming a tail, and the intensity of the others Si peaks increase. The presence of the a – Si peak, even if in the form of a tail, is still representative of some degree of disorder in the Si phase. Intarasiri *et al*. [333], just like the author observed the same tail in Raman spectroscopy after C implantation and annealing at the same temperature for 60 min. The HRTEM characterization of the sample showed the presence of some disordered Si, containing some defects. Based on the Raman results, the lower nanowear resistance of the top surface layer of the CHT800 sample may possibly be associated with the fact that Si phase present at the surface is highly disordered or with a high concentration of defects, thus presenting significantly different properties from the reference Si.

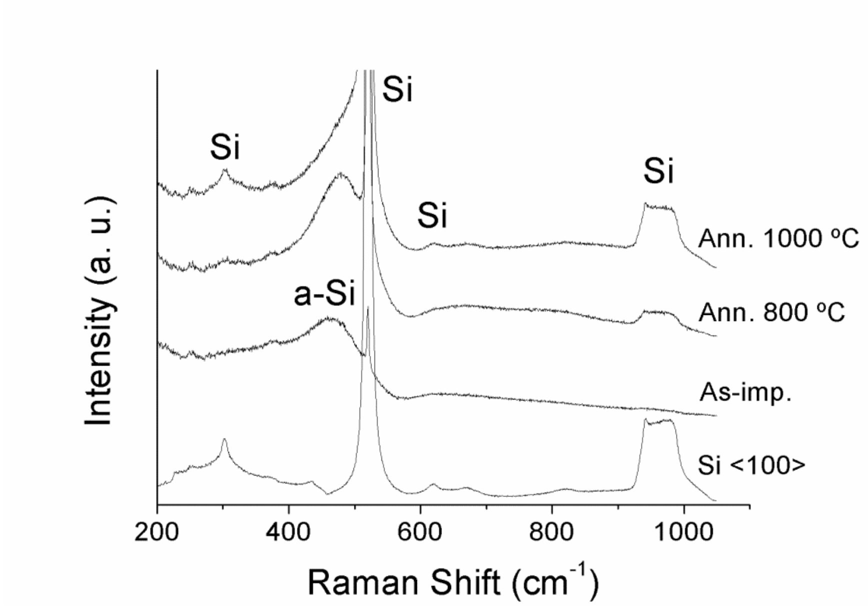

Figure 71. Raman spectra of the Si <100> and C$^+$ implanted samples at 25 keV with a fluence of $2x10^{17}$ cm^{-2} and after annealing at different temperatures.

4.3 DUAL IMPLANTATION OF FE$^+$ AND C$^+$

4.3.1 STRUCTURAL CHARACTERIZATION

The microstructural characterization of the dual Fe and C implanted samples is shown in Figure 72, Figure 73 and Figure 74. Again, like in the previous implantations cases, regarding the single implantation of Fe and C, no microstructures were observed in the as-implanted samples for the two chosen implanted fluences. Figure 72 shows the microstructure of both low and high fluence dual Fe and C implantation after a 800 ºC annealing. It is possible to observe a very similar microstructure, composed of small precipitates of similar dimensions for both fluences, but present at a larger number for the high fluence case, Figure 72(right).

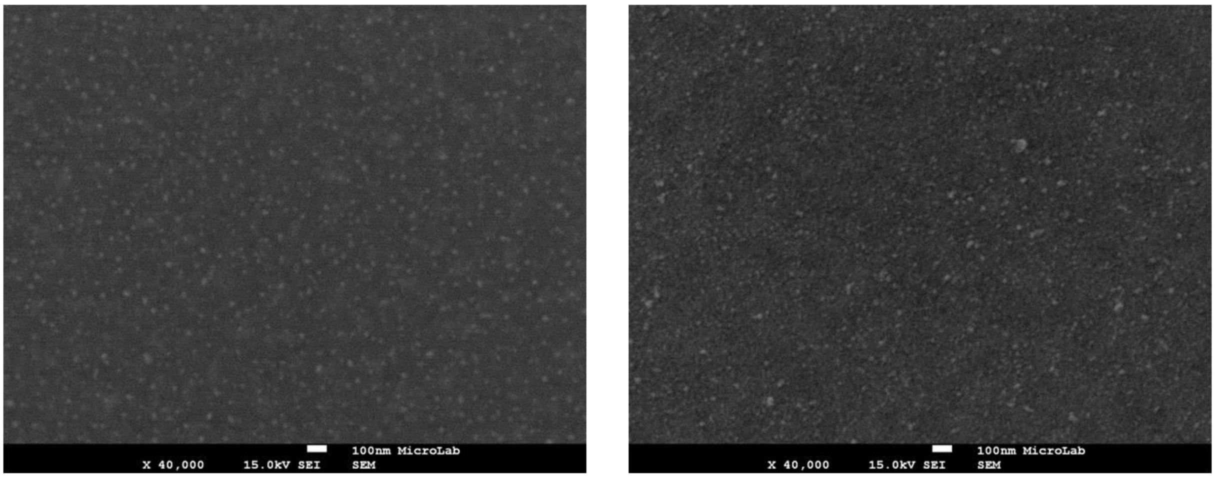

Figure 72. (left) Microstructure of dual implanted sample $\Phi = 5x10^{16}$ (Fe + C) cm^{-2}, at 170 keV and 50 keV, respectively, annealed at 800 ºC for 30 min, (right) microstructure of dual implanted sample $\Phi = 2x10^{17}$ (Fe + C) cm^{-2}, at 170 keV and 50 keV, respectively, annealed at 800 ºc for 30 min.

As for 1000 ºC annealings, the attained microstructures are presented in two different figures: Figure 73 for low fluence and Figure 74 for high fluence, respectively. After the 1000 ºC annealing, the low fluence sample presents a centered circular zone with a coloration close to that of Si, while the surrounding area presented a more “grayish” tone, just like the schematic representation presented before in Figure 60 regarding the single C implantations. The top of Figure 73 shows the microstructure of the central area whereas the bottom shows the microstructure outside of the central zone. The microstructures are not significantly different. Outside the central area one can observe not only the presence of larger precipitates of dimensions of ≈ 1 µm but also small precipitates with ≈ 10 nm, that do not appear in the central/interior one zone of the sample.

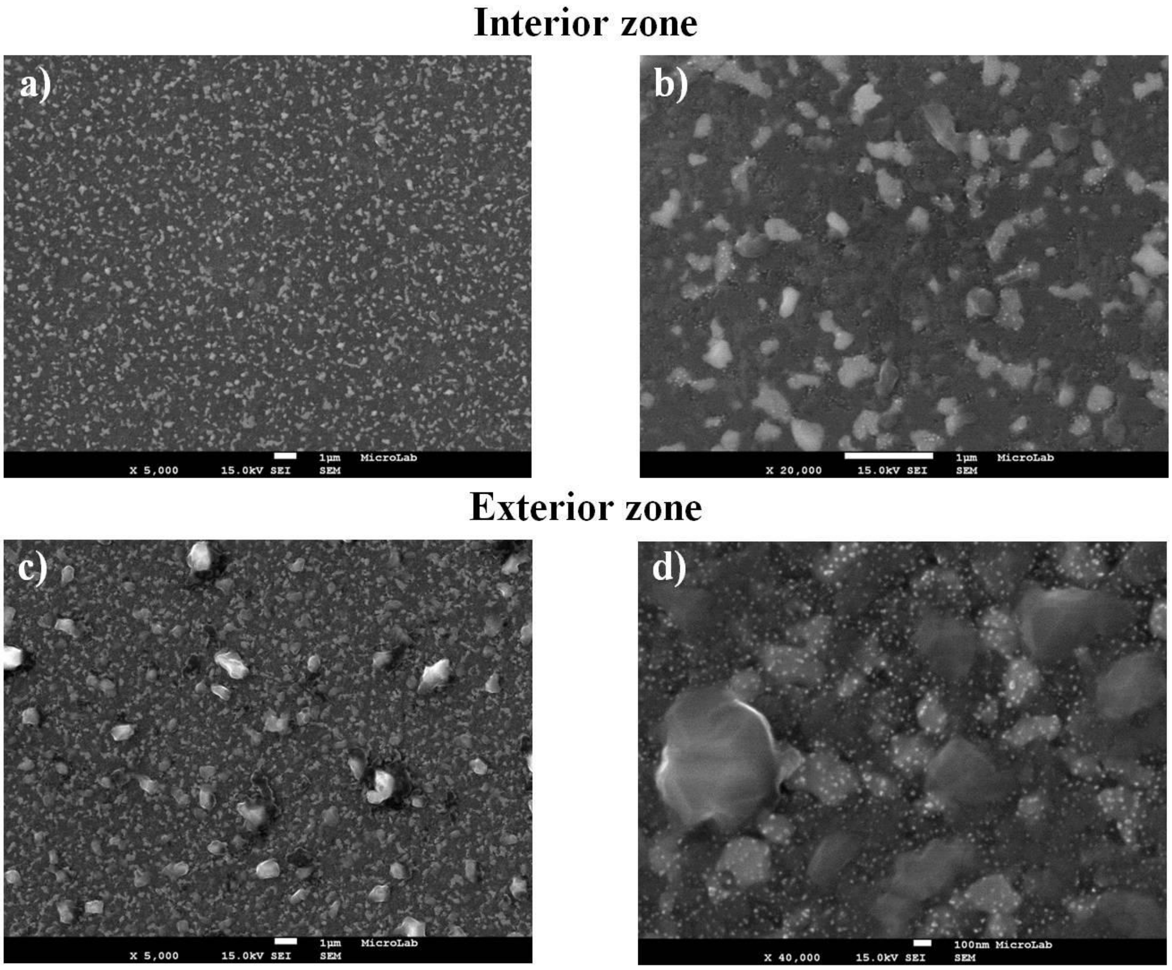

Figure 73.(a) Microstructure of dual implanted sample $\Phi = 5x10^{16}$ (Fe + C) cm^{-2}, at 170 keV and 50 keV, respectively, annealed at 1000 ºC for 30 min, in the interior zone, (b) higher magnification of a); c) microstructure in the exterior of the central circular zone, (d) higher magnification of c).

Unlike the low fluence case, the 1000 ºC annealing of the high fluence dual implanted sample did not reveal zones with a different coloration where different microstructures could be observed. Instead only one microstructure was observed - Figure 74. In Figure 74 it is possible to see that the microstructure of the FeCHT1000 sample is composed of three different phases. A dark one, the matrix, a white one, contained within the dark matrix phase and finally the third one, the large irregular precipitates, with dimensions in the range of ≈ 1 µm that reach considerable heights relative to the surface.

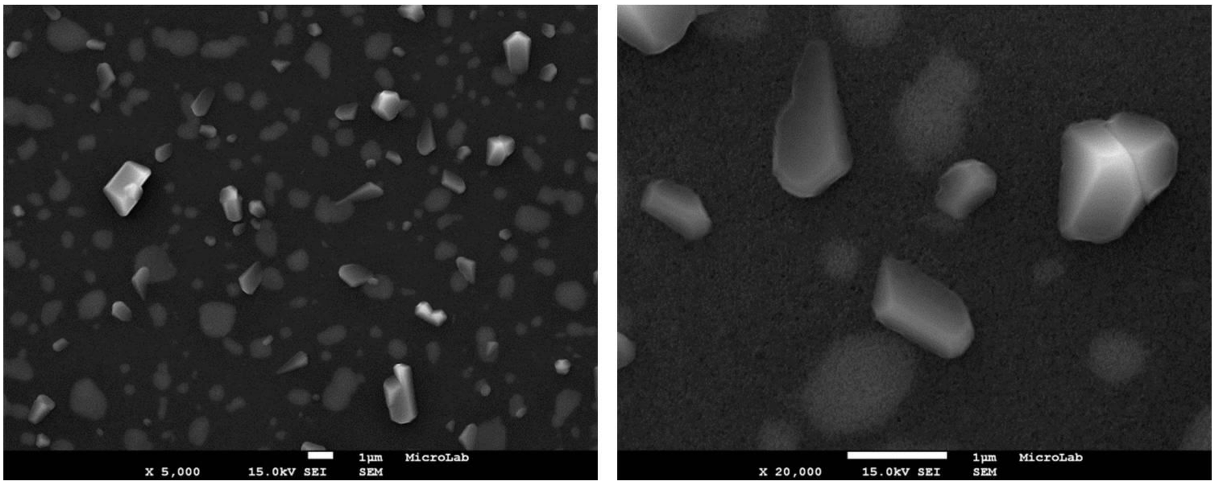

Figure 74. Microstructure of dual implanted sample $\Phi = 2\text{x}10^{17}$ (Fe + C) cm^{-2}, at 170 keV and 50 keV, respectively, annealed at 1000 ºc for 30 min, Dual implantation of Fe$^+$ and C$^+$.

GIXRD measurements were performed on the dual Fe and C implantations, for both fluences, in order to see the phase evolution with the temperature. The GIXRD results are presented in Figure 75. Figure 75a) shows the phase evolution of the sample implanted with the lower fluences of both C and Fe. No peaks are observed for the as-implanted sample while at 800 ºC two phases are observed, Si, which presents the most intense observed peaks, and the β – FeSi$_2$ phase, identified by the presence of the (202) and (422) reflections, the ones with the higher intensity of the corresponding silicide phase. At the higher temperature, 1000 ºC, three phases were detected. The most intense peaks observed correspond to the Si phase and α – FeSi$_2$ phase, the high temperature silicide. With a much smaller intensity at position of $2\theta = 35.5^o$ it is also possible to observe the presence of one peak of the SiC phase, corresponding to the (111) reflection. This peak was confirmed by performing a zoom (not shown) in the $2\theta = 35.5^o$ region. Although the peak intensity did not clearly standout from the background noise, it shows with a measurable width.

The phase evolution of the high fluence dual Fe and C implanted sample with the temperature - Figure 75b), follows an identical behavior compared to the lower fluence one. Again, no peaks are observed on the as-implanted sample. The same silicides can be seen at the same temperatures, that is, β – FeSi$_2$ silicide at 800 ºC and α – FeSi$_2$ at 1000 ºC. At 1000 ºC it is also possible to indentify the presence of a small peak corresponding to the SiC phase, at $2\theta = 35.5^o$, corresponding to the most intense peak of the phase.

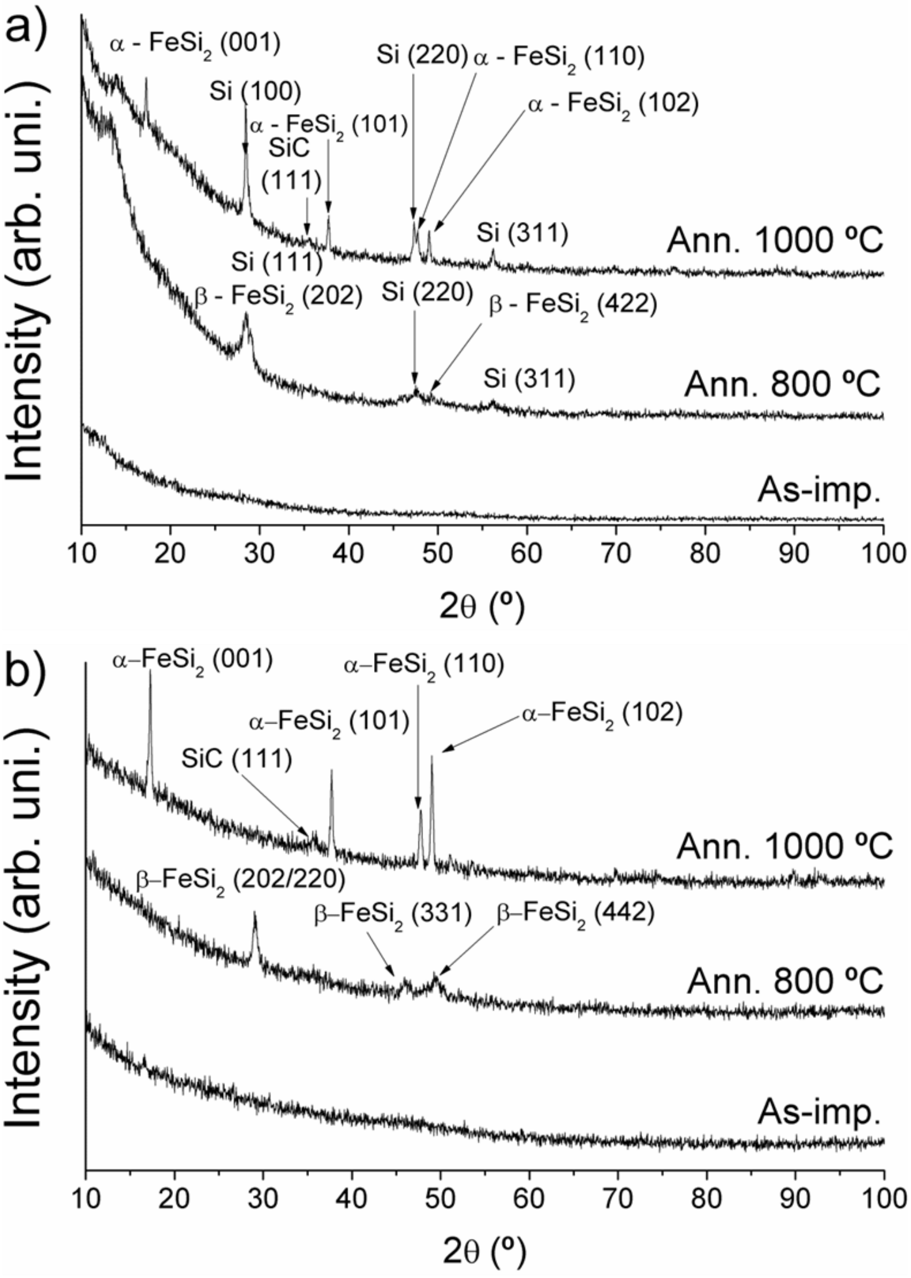

Figure 75. GIXRD (θ = 1.5 º) results of the dual Fe and C implanted and annealed samples at 800 ºC and 1000 ºC (a) $\Phi = 5\text{x}10^{16}$ (Fe + C) cm^{-2}, at 170 keV and 50 keV, (b) $\Phi = 2\text{x}10^{17}$ (Fe + C) cm^{-2}, at 170 keV and 50 keV.

RBS measurements were performed on the dual Fe and C implanted samples, like in case of the single implantations of the same elements. The results can be seen in Figure 76. The channel scale for both figures is significantly different as a result of having used different values of electronic gain. Again, for a better global perception of the figure, the Fe peak of the aligned spectra were not represented.

In Figure 76, for both studied fluences, it is possible to observe the presence of an amorphous layer that reaches a thickness of ≈ 250 – 300 nm, calculated using the surface approximation. Upon the annealings, for the low fluence case, Figure 76a), it is possible to observe that the amorphous-crystalline interface barely moves for both annealings, most likely indicating the formation of a polycrystalline zone since diffraction peaks were detected under the GIXRD characterization and also according to published results from the literature [214, 306]. Figure 76a) also shows that the shape of the Fe peak changes significantly with the temperature. At 800 ºC is possible to see that the profile actually narrows, increasing the concentration of Fe at the peak, while a small portion of the peak extends to surface, meaning that a small amount of Fe migrated to surface. As for the higher temperature, 1000 ºC, a broadening of the peak can be observed, being the concentration of Fe higher on the surface compared to the 800 ºC sample. For the high fluence samples, Figure 76b), it is possible to observe a more significant advance of the amorphous/crystalline interface occurs at the higher temperature, 1000 ºC, when compared to the 800 ºC annealing. In the higher fluence, it is interesting to observe that the concentration of Fe does not seem to diffuse to the surface. From the as-implanted sample to the 800 ºC it is possible to see a change in the shape of the Fe peak, changing from a close-to Gaussian profile to a rectangular shape, suggesting a formation of a film at the surface. At 1000 ºC, a significant decrease in the height of the Fe peaks is observed. This decrease in height is accompanied by the formation of a diffusion tail in the spectrum, meaning that Fe is diffusing towards the bulk rather than the surface.

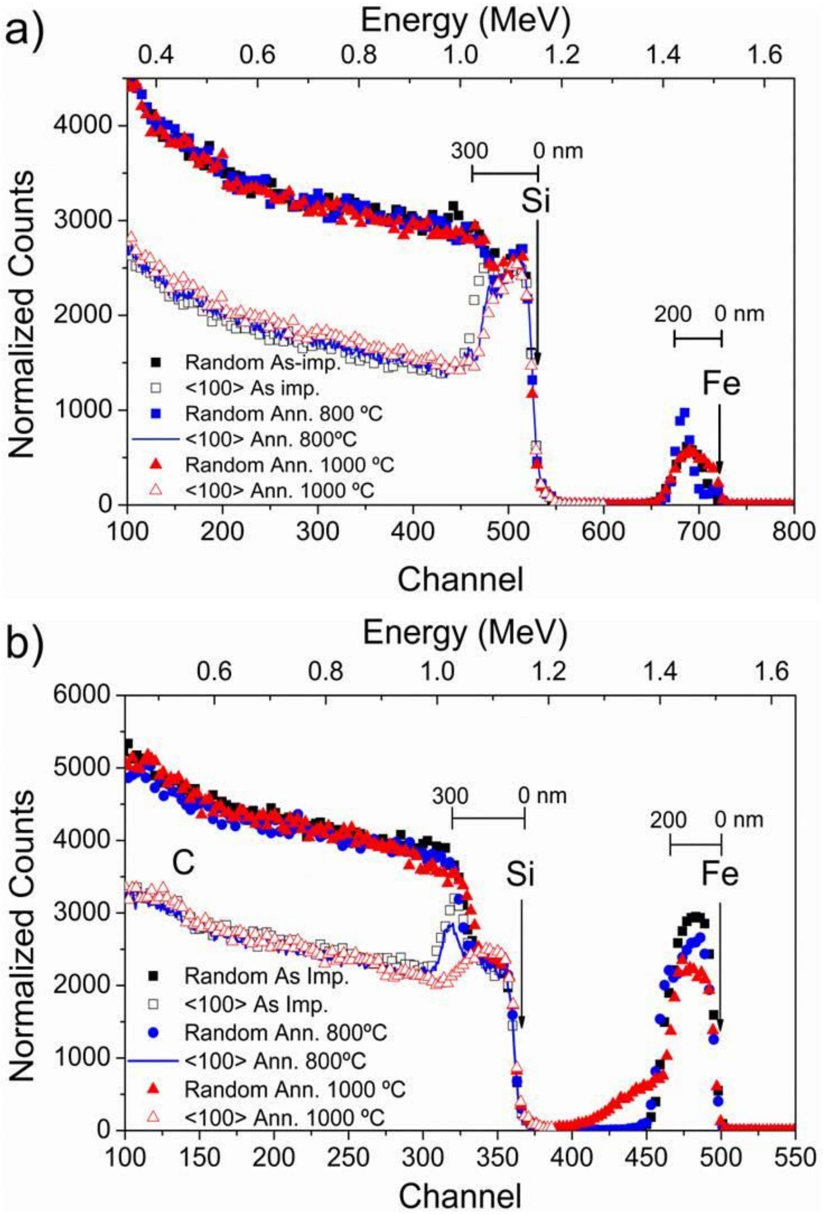

Figure 76. RBS spectra of dual Fe and C implanted and annealed samples, at 800 ºC and 1000 ºC, acquired with alpha particles and with a total charge of 5 µC, (a) $\Phi = 5\text{x}10^{16}$ (Fe + C) cm^{-2}, at 170 and 50 keV, (b) $\Phi = 2\text{x}10^{17}$ (Fe + C) cm^{-2}, at 170 and 50 keV.

XPS characterization was performed for all the high dual Fe and C implanted samples. The main objective was to confirm the presence of SiC phase since only a low intensity peak could be observed under the GIXRD characterization at 1000 ºC - Figure 75. The attained XPS spectra are presented in Figure 77.

The Si 2p region was fit with 4 doublets with a spin-orbit shift of 0.6 ± 0.1 eV and an area ratio Si 2p$_{3/2}$/Si 2p$_{1/2}$ = 2. The component Si 2p$_{3/2}$ was centred at 99.5 eV (used as reference), 100.85 ± 0.1 eV, 102.5 ± 0.1 eV and 103.6 ± 0.1 eV. They are assignaed, respectively, to silicon in the form of pure Si, SiC, SiO$_x$ (x<2) and SiO$_2$ or SiO(OH)$_2$ [334].

The C 1s region was fit with 4 components centred at 282.7 ± 0.2 eV, 285.0 ± 0.2 eV, 286.9 ± 0.1 eV and 288.9 ± 0.2 eV assigned, respectively to C bound to Si, C sp^3 bound to C or/and H, C singly bound to O and carbon in a neighborhood very rich in oxygen (singly bound to 3 oxygen atoms or singly bound to one and doubly bound to another). For sample annealed at 1000 ºC, a fifth peak at very low binding energy (~281 eV) was needed to a good fitting. It is tentatively assigned to C-Fe [334].

Fe 2p$_{3/2}$ region was fit with 4 components centred at 706.6 ± 0.1 eV, 708.2 ± 0.1 eV, 709.5 ± 0.1 eV and 711.2 ± 0.1 eV. They are assigned, respectively, to Fe^0, Fe bound to Si and/or C, FeO, and Fe_2O_3 and/or FeO(HO) [334].

Finally, O 1s region was fit with a single peak centred at 532 ± 0.1 eV assigned to a mixture of oxides already mentioned when describing the other XPS regions.

The XPS spectra relative to both C and Si peaks clearly show the presence of the SiC for the as-implanted sample as well as in the annealed ones; a clear increase in the relative amount of SiC is observed for the one annealed at 1000 ºC.

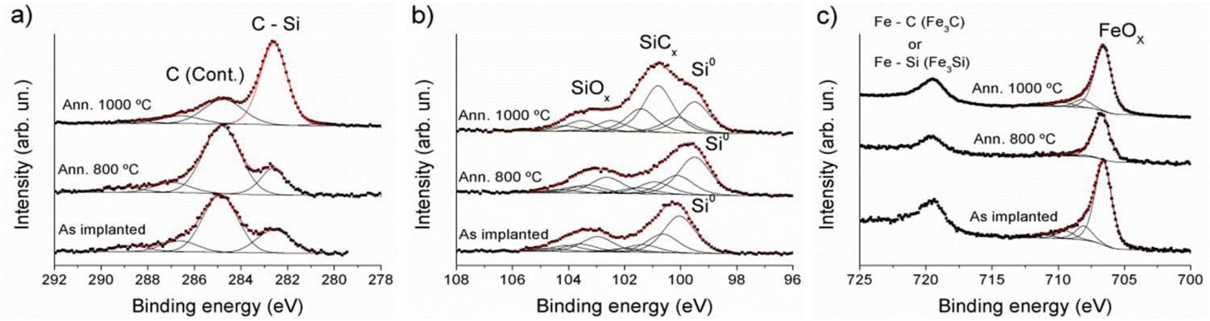

Figure 77. XPS spectra corresponding to (a) C 1s, (b) Si 2p and (c)Fe 2p regions for the $\Phi = 2x10^{17}$ cm^{-2} Fe$^+$ + C$^+$ dual ion implantation and respective annealings

The binding energies as well as the respective atomic concentrations for each identified specie are displayed in Table 12 where also some ratios were added.

Table 12. XPS binding energies (± 0.2 eV) and atomic percentages (±1 %) for the high fluence dual Fe+ and C+ implantation sample as-implanted and annealed at 800 ºC and 1000 ºC

	BE, eV	As-implanted	Annealed at 800 ºC	Annealed at 1000 ºC	Assignment
C 1s0	280.9			0.39	**C**–Fe
C 1s1	282.7	7.2	6.1	17.8	**C**–Si
C 1s2	285.0	18.5	21.6	7.7	C–C,**C**–H (cont.)
C 1s3	286.9	3.3	3.3	2.5	**C**–O
C 1s4	288.9	1.5	1.7	0.73	O–C=O, CO_3
Si $2p_{3/2}$ 1	99.5	10.9	10.4	7.4	Si–Si
Si $2p_{1/2}$ 1	100.1	5.5	5.2	3.7	
Si $2p_{3/2}$ 2	100.8	2.3	3.3	11.1	Si–C
Si $2p_{1/2}$ 2	101.5	1.1	1.7	5.6	
Si $2p_{3/2}$ 3	102.5	4.5	4.4	2.6	SiO_x
Si $2p_{1/2}$ 3	103.2	2.3	2.2	1.3	
Si $2p_{3/2}$ 4	103.6	1.8	1.8	2.6	SiO_2+$SiO(OH)_2$
Si $2p_{1/2}$ 4	104.2	0.88	0.91	1.3	
O 1s	532.3	33.5	34.5	31.0	
Fe $2p_{3/2}$1	706.6	5.2	2.5	3.4	Metallic Fe
Fe $2p_{3/2}$2	708.2	0.87	0.09	0.47	**Fe**–C + **Fe**–Si
Fe $2p_{3/2}$3	709.5	0.49	0.09	0.23	**Fe**O
Fe $2p_{3/2}$4	711.2	0.24	0.09	0.11	**Fe**$_2$O$_3$ + **Fe**O(OH)
Ratios					
Si–C/**C**–Si		0.47	0.82	0.94	
Fe ox/Fe tot		0.11	0.06	0.08	
Siox/Si tot		0.32	0.31	0.22	
C ox/Ctot		0.16	0.22	0.27	
Fe/C		0.22	0.09	0.15	
Fe/Si		0.23	0.09	0.12	

4.3.2 WETTABILITY CHARACTERIZATION

The wettability behavior of the dual implanted samples with Fe and C was investigated by means of contact measurements with both water and diiodomethane. The corresponding surface energy of all of the dual implanted samples was also determined. The results are summarized in Figure 78.

From Figure 78 it is possible to observe that both fluences exhibit the same trend in terms of contact angle variation, but with more significant angle variation for the lower fluence case. In comparison to reference Si, the implantation of both elements, Fe and C, increases the contact angle to ≈ 60º and ≈ 50º for the lower and higher implanted fluence respectively. The highest contact angle for each fluence occurs after the 800 ºC annealing. The low fluence sample exhibits an "almost-hydrophobic" behavior. The average contact angle measured was around ≈ 85 º, but some drops reached 92 – 93º values. For the higher fluence the maximum attained contact angle was ≈ 75º. Upon the high temperature for both fluences a decrease in the contact angle is observed, being much more significant for the low fluence case where a drop from 85º to 35º is observed while for the higher fluence the decrease of the contact is half of the low fluence, around 25º. In Figure 78b) and d) is represented the surface energy variation of the dual implanted samples. The surface energy variation follows the exact opposite variation as the contact angles. The lowest value reached of surface energy was ≈ 28 mJ/m^2 for the FeCLT800 sample, rendering the sample almost hydrophobic. For both implanted fluences one can see that polar component reaches the lower value precisely after the 800 ºC annealing, where the higher contact angles were observed.

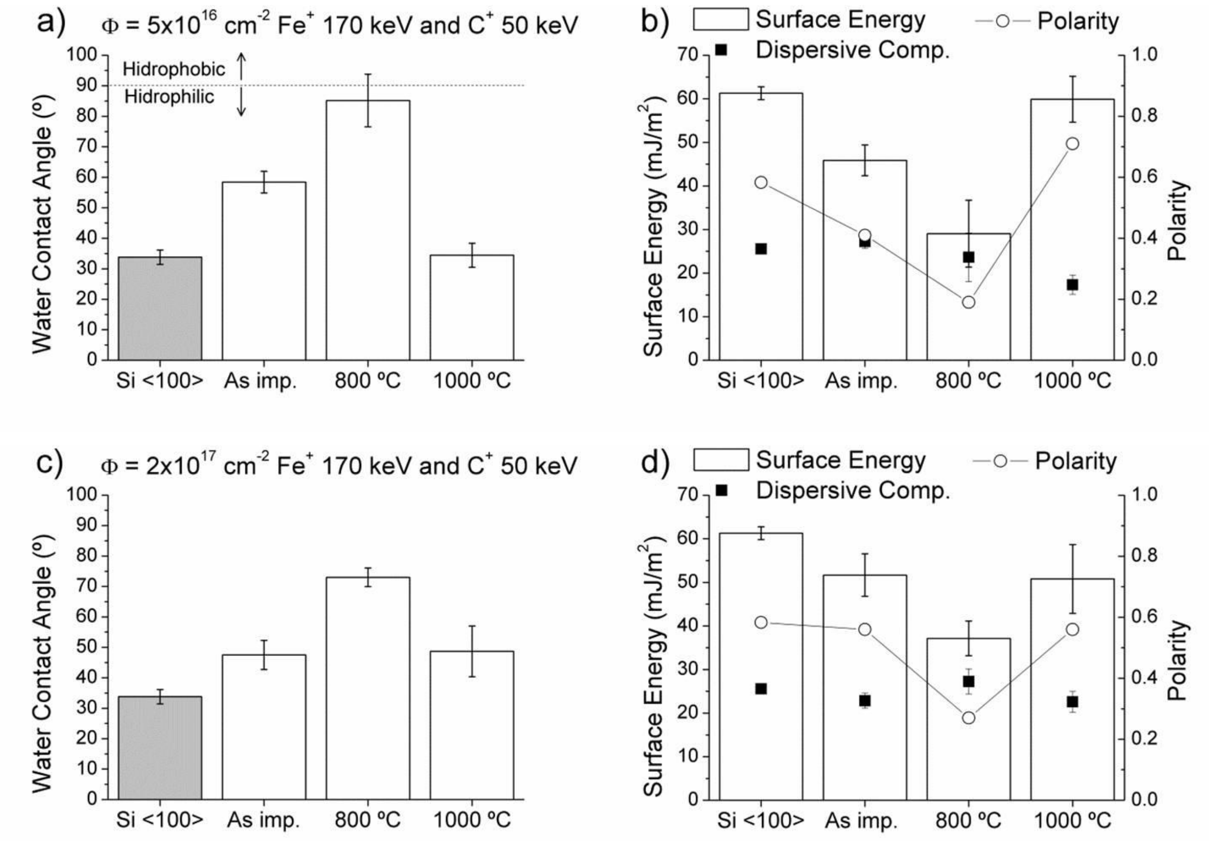

Figure 78. (a) Water contact angle of the dual Fe and C and annealed samples with a fluence of Φ = 5x10^{16} cm^{-2} (b) Surface energy, dispersive component and polarity of a), (c) Water contact angle of the dual Fe and C and annealed samples with a fluence of Φ = 2x10^{17} cm^{-2} (d) Surface energy, dispersive component and polarity of c).

4.3.3 NANOTRIBOLOGICAL STUDY

The nanowear resistance of the dual Fe and C implanted samples was studied for both low and high fluences using a Nanosurf AFM with a Microstar® diamond tip. The corresponding nanowear scans, for the different normal loads, can be observed in Figure 79 and Figure 80, respectively. The nanowear scans of the low Fe and C dual implanted samples in Figure 79 show that the as-implanted sample behaves quite differently from the annealed samples. The as-implanted sample does not seem to show any depressions/craters in the respective scanned areas, in fact the scanned areas present features that are at surface level or even above. For this specific sample, it seems that wear did not occur, at least until 35 µN. For the annealed samples the elevated features are also present but before wear initiation. At loads in order of the 10 µN the annealed samples start to exhibit wear and craters/depression become visible.

The nanowear scans of the high fluence dual Fe and C implanted samples, Figure 80, show that both as-implanted and 800 ºC samples initiate wear at a load of 10 µN, where it is possible not only to observe depressions but also the presence of some features similar to the hillocks observed for Si. For the 1000 ºC the wear seems to initiate a little earlier, since at normal load of 10 µN a deep crater/depression can be observed. It is important to standout that nanowear scans and respective volume calculations for this specific sample were quite troublesome due to the presence of large and extremely high precipitates. Nonetheless the author did his best efforts to properly calculate the respective depths for each load.

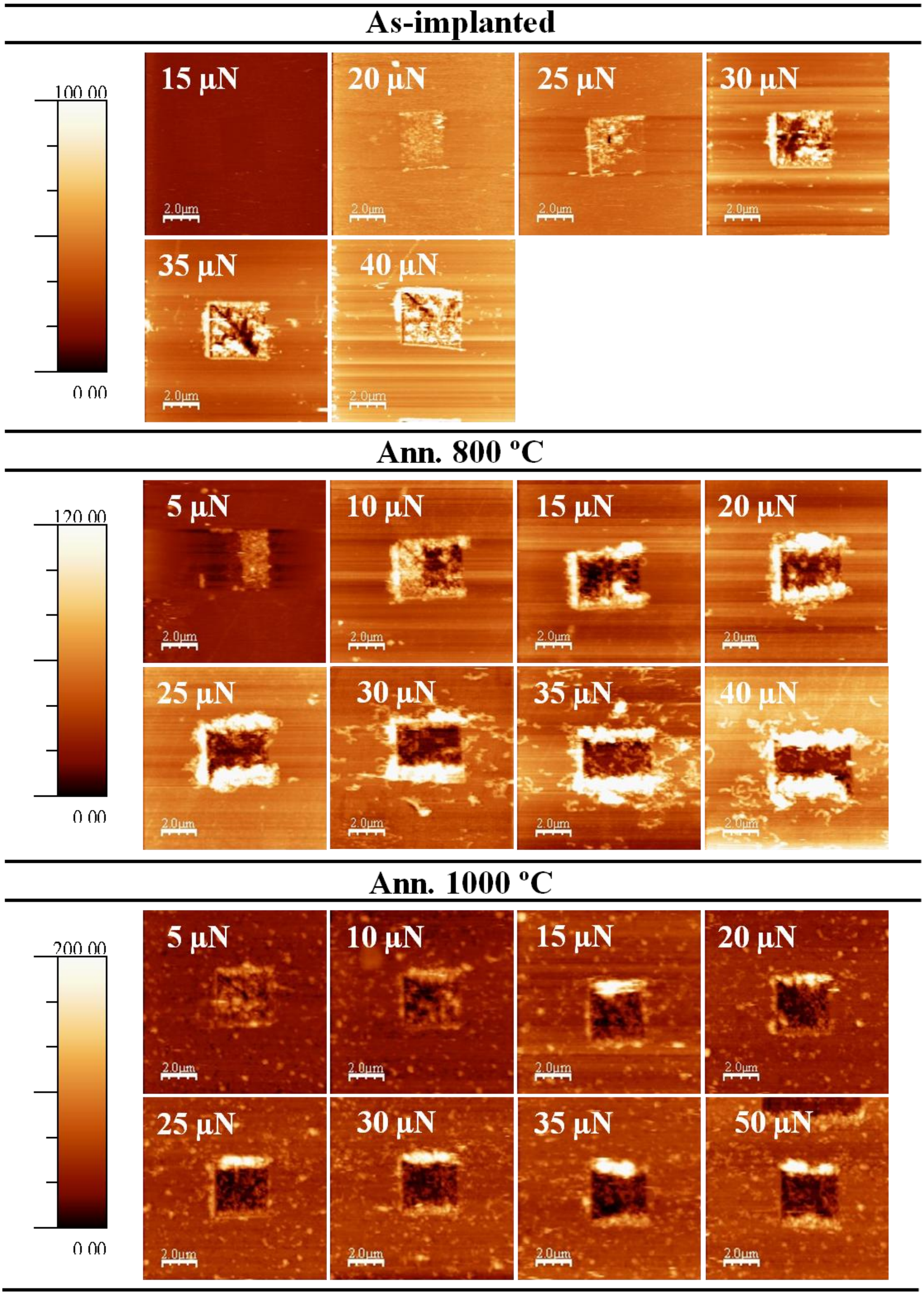

Figure 79. Nanowear scans of the Φ = 5×10^{16} cm^{-2} dual Fe (150 keV) and C (50 keV) implanted and annealed samples, at both 800 ºC and 1000 ºC, for the different applied normal loads (height color scales in nm).

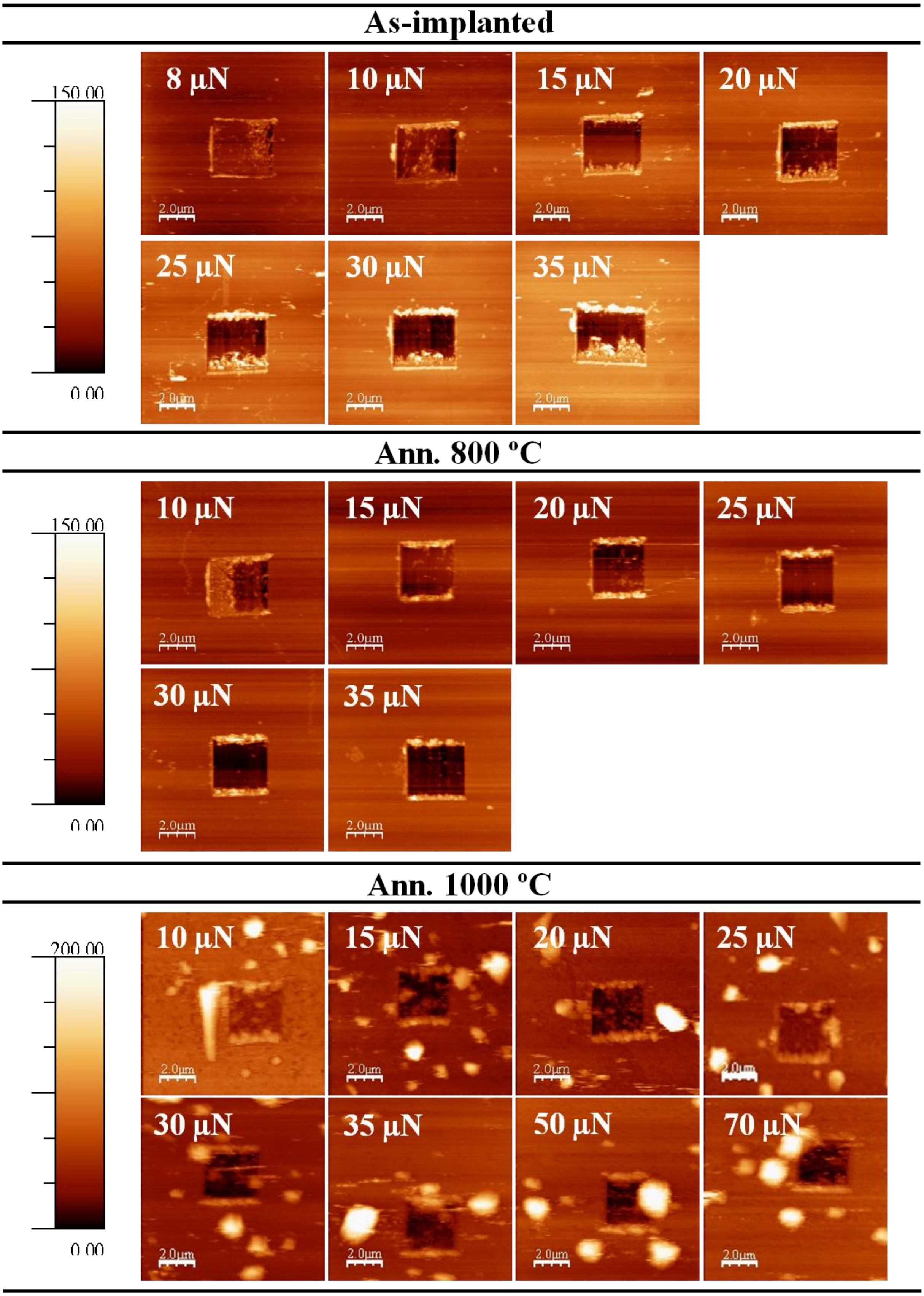

Figure 80. Nanowear scans of the Φ = 2x10^{17} cm^{-2} dual Fe (150 keV) and C (50 keV) implanted and annealed samples, at both 800 ºC and 1000 ºC, for the different applied normal loads (height color scales in nm).

From the AFM images presented in Figure 79 and Figure 80, the wear rates and specific wear coefficients were calculated. The results for both fluences are summarized in Figure 81. In Figure 81a) and Figure 81c), the respective values of wear rate and specific wear coefficient of the as-implanted sample are represented, despite the fact that no depressions were attained. The depth values used for the wear rate calculations for that specific sample consisted in the deepest measured depth, and are estimation. By using these values a linear relationship is still observed. As for the annealed samples, regarding the low fluence dual Fe and C samples, in Figure 81a) it is possible to observe that the calculated values are almost overlapped for all the load range. For the lower loads, 10 – 20 µN the calculated wear rates are higher than the reference Si, whereas at a load of 25 µN a transition occurs and the wear rates from this load on become lower when compared to the Si. The calculated specific wear coefficients in Figure 81c) show quite well these wear differences before and after the 25 µN load. The specific wear coefficients decrease in value, decreasing more in the 1000 ºC case. Globally, it is interesting to observe that the calculated specific wear coefficients are always lower than the Si reference, even in the lower load regime.

The wear rate variation for the high fluence dual Fe and C implanted samples in Figure 81b) shows that both the as-implanted and 800 ºC samples exhibit a linear relationship with the load. The as-implanted seems always to present higher wear rates than the reference while the same happens for the 800 ºC sample, but for the lower loads. Beyond the 20 µN an inversion occurs and wear rates become lower than the Si ones. The wear rate variation for the 1000 ºC sample exhibits a slightly different behavior when compared to the previous samples. At the lower loads one can observe that the wear rates seem to be like almost constant, independent of the load until a load of 30 µN is reached. For higher loads, the wear rate seems to present a linear-like behavior, and lower wear rates are attained for the higher applied normal forces. The corresponding specific wear coefficients were determined and are represented in Figure 81d). The as-implanted specific wear coefficient is indeed quite close the Si one, the wear rates slopes are quite similar. Upon the annealings, one can observe a decrease of the specific wear coefficient with the increase of the temperature. Being at 800 ºC the specific wear coefficient value close to half of the Si one and at 1000 ºC around half of the 800 ºC one.

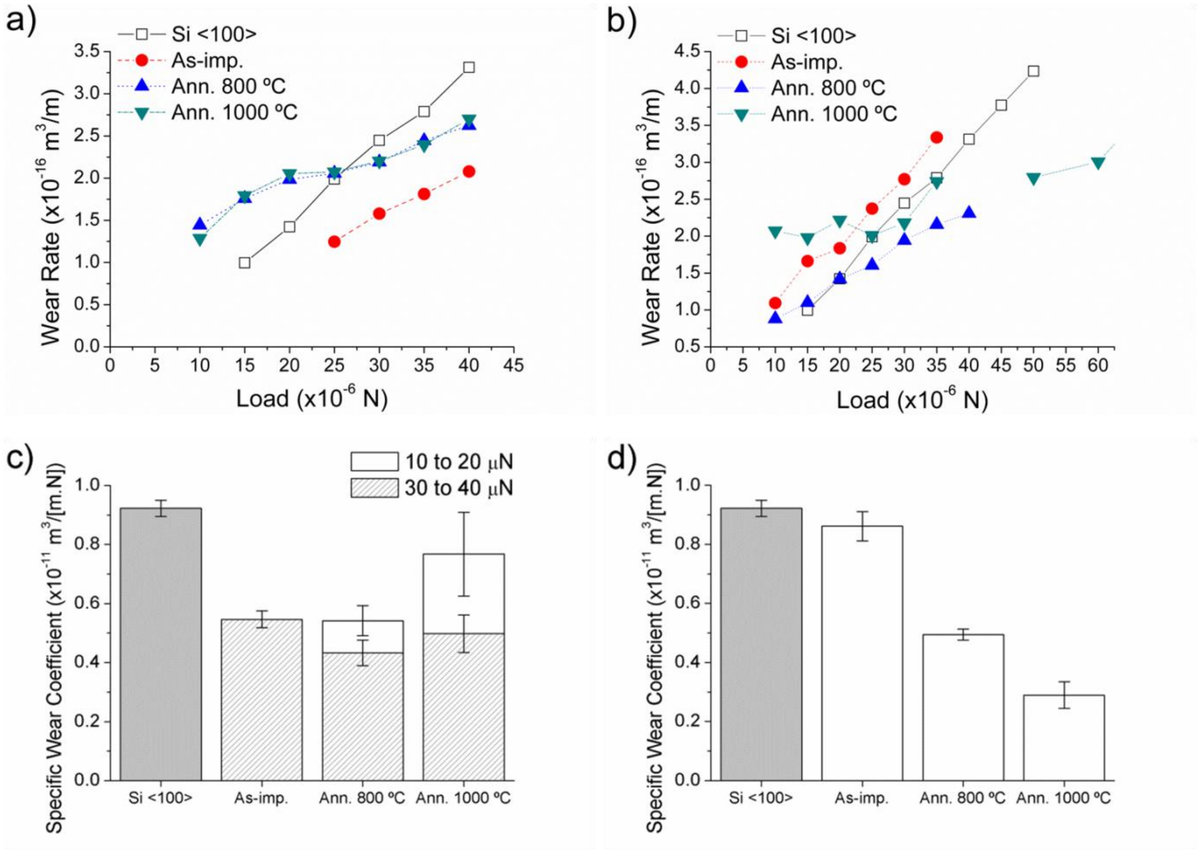

Figure 81. Calculated wear rates for (a) low fluence dual implanted and annealed samples, (b) high fluence dual Fe and C implanted and annealed samples; specific wear coefficients for (c) low fluence dual Fe and C implanted and annealed samples, (d) high fluence dual Fe and C implanted and annealed samples.

The nanotribological characterization of the dual Fe and C implanted samples revealed how both elements work together in terms of nanowear resistance, for both low and high fluences. For all studied dual Fe and C samples, one presented a behavior different from all others: FeCLAs one. Instead of depressions/holes which enable to calculate the corresponding worn volume, the scanned areas were full of hillock features - Figure 79. These features are quite identical to hillocks previously observed in Si and CHT1000 samples. As it was mentioned before, these features represent a pre-stage of wear. From a load ≥ 30 μN the hillocks show some signs of disruption, in opposition to what was previously observed in Figure 67, where they fully cover the surface, although for a much lower load value. It seems that for this sample a clear transition from hillocks to wear did not occur. The results were repeated, for the same load range, and the outcome was exactly the same. Unfortunately no other characterizations techniques were used for this specific sample, aside the ones presented previously, to understand why the tribological behavior was different relative to the other samples. Regarding the annealed samples, for the low dual Fe and C fluence, one can observe that the wear rate variation follows quite a similar trend for both annealing temperatures.

Initially, at lower loads, the wear rates are higher than reference, inverting this trend after a load of 25 µN. The GIXRD results of the annealed samples - Figure 75, show that for each temperature different phases are present, aside from the Si common to both, more precisely β – $FeSi_2$ and α – $FeSi_2$ at 800 and 1000 ºC, respectively. The morphology of the surface is also quite similar, consisting of small precipitates - Figure 72 and Figure 73, although in a higher density for the 800 ºC case. The nanowear scans for the higher temperature did not encounter any of the larger precipitates seen in Figure 73. The higher wear rates at lower loads may be associated with the surface precipitate removal, which will work as third body, enhancing wear. For the higher loads, the lower wear rates can be associated with the increase of the concentration of the implanted species.

It is interesting to compare the dual high fluence Fe and C implantation results with the single Fe and C implanted ones, since the same fluence was used. The main limitation in the comparison will be the fact that Fe single implantations were carried out in a different AFM with a different diamond tip, in a different load range. Comparing the respective dual and single as-implanted samples, one can see that single leads to lower wear resistances when compared to Si. The inferior mechanical properties of the amorphous layer induced by the implantation seem to rule the behavior of the samples despite the implanted elements. However it is unclear why the same did not happen for the lower dual Fe and C implanted sample, since both same elements and amorphous layer are present. At the 800 ºC annealing one can observe that the nanowear behavior follows more a similar trend with the Fe single implantation rather than the C implantation, a linear tendency is observed starting from low loads. This was somehow expected, since both dual and Fe single implantation at that temperature have the same phase present the β – $FeSi_2$ silicide phase. For the highest applied normal loads, the depths were in the order of 30 – 40 nm. Looking into Figure 82, one can see that these depths probably correspond to the surface layers of the β – $FeSi_2$ silicide phase, it seems to extend to deeper depths. However, the single C implantation shows that at 800 ºC starting from 15 µN load, higher nanowear resistance is achieved. The global good nanowear resistance displayed by the dual Fe and C implanted sample at 800 ºC, starting from low loads, is definitely achieved by the combined effect of the implanted elements.

As for the 1000 ºC sample, a complete different behavior is observed when compared to the single implantations. In Figure 81b) it is observed that for the lower loads the wear rates seem to display a rather like constant trend, almost if independent of the applied normal load, which did not happen for the single implanted cases. The surface morphology of the dual implanted sample is quite identical to the Fe case, with the exception of the large precipitates and lower content of the white phase, indentified as α – $FeSi_2$ in the surface. The single Fe implantation displayed a close-to-linear wear rate behavior, exhibiting slightly higher rates than Si at the lower loads, but inverting this tendency afterwards. It is rather difficult to point out the reasons why for the lower loads the wear rates exhibits a constant trend. On one hand, it has been reported that the α – $FeSi_2$ phase has worse mechanical properties than Si [295], but since the surface show less content of the silicide phase, one should expect the dominance of the mechanical properties of Si. There is the possibility of the α – $FeSi_2$ phase removal acting like a third body which might significantly increase the wear rates. The nanowear scans in Figure 80 show that scanned areas have features at the bottom, showing that there are different zones with different tribological properties within the same surface. The same was not observed for the 800 ºC or as-implanted samples. At the higher loads, 50 – 70 µN, one can see that the wear rates become significantly lower than the Si ones. This decrease is most likely associated with the presence of a higher content of SiC upon deeper layers, which significantly increases the nanowear resistance. Looking into Figure 81d) one can see that the FeCHT1000 sample presented the lowest specific wear coefficient value among the dual high fluences Fe and C samples, despite the terrible wear resistance at lower loads.

4.3.4 DISCUSSION

As far as we know, studies involving dual ion implantation, using different elements, are almost inexistent in the literature. The only works involving simultaneously Fe and C were either the implantation of carbon into Fe rich films [335], or the exact opposite [336], in considerably different experimental conditions than the ones used by the author. This being said, the author will carry the discussion of the Fe and C dual implantations results based on the single implantations of both Fe and C.

In terms of microstructure, directly comparing the dual implanted micrographs (Figure 73 and Figure 74) with the single implanted ones, (Figure 43, Figure 44 and Figure 60) it is easily seen that the dual implanted microstructures are mostly identical to the single Fe ones, but with small changes, most likely induced by the presence of carbon. The microstructure observed after the 800 ºC annealing, for the lower dual implanted fluence, consists on small precipitates with lower dimensions than the ones observed for the same fluence single Fe implanted microstructure. As previously mentioned, no microstructures were observed at 800 ºC for the C single implantations. For the same temperature but for the higher dual implanted fluence, the microstructure is again composed of small precipitates, with dimensions in the range 10 – 20 nm, fully covering the surface. Comparing with the single Fe implantation microstructure, where precipitates of 100 – 200 nm were observed, these precipitates are much smaller. As for the higher temperature, the observed microstructure of the dual low fluence samples (Figure 73) is quite identical to the single Fe implantation one (Figure 43). However, it is interesting to see that both dual Fe and C and single C presented similar “macrostructure”, that is, the surface with two different tones of color where different microstructures were observed. The different tones were not observed for the high fluence dual implantation case after annealing at 1000 ºC, as it was for the single C implantation one. Again, the dual Fe and C microstructure presented several similarities with the single Fe implantation, namely, the presence of dual white/black microstructure that fully covered the surface - Figure 44. However, in the dual implantation case the white phase does not seem to form a continuous network, but rather islands in the dark matrix and also large irregular precipitates are present.

The GIXRD phase evolution of the dual Fe and C implanted shown in Figure 75 is similar to the Fe single implantation one, Figure 47. For the 800 ºC annealing, the exact same phases can be identified for both single and double implantations – recrystallized Si and β –

$FeSi_2$ silicide. The main differences appear at higher temperature, 1000 ºC. The low dual fluence implantation, Figure 75, shows the presence of Si, α – $FeSi_2$ and possibly SiC phase, as it was explained before in the results section. The high fluence dual implanted sample, at 1000 ºC, shows the presence of both SiC and α – $FeSi_2$ while in the single implanted one only the α – $FeSi_2$ phase is seen. The author searched for the ternary Fe – Si – C diagram to see which possible phases could be expected. Unfortunately such ternary diagrams, within the plausible range of composition of the studied samples and for the right temperatures were not found or even may not exist. The XPS data presented in Table 12 also shows the presence of a Fe – Si and Fe – C compounds, (Fe_3C or Fe_3Si) that could not be fully determined. This phase did not appear in the difractograms in Figure 75, most likely because of its low concentration. The results presented in Table 12 also seem to give an explanation why the SiC phase only appears at the higher temperatures, despite the fact that according with the biphasic Si – C diagram, Figure 69, it should appear at lower temperatures. The ratio between the Si bound to carbon, and the carbon bound to Si (**Si**–C/**C**–Si)), Table 12, enables one to see the evolution of the SiC formation with the increasing temperature. The initial value, in the as-implanted state, is 0.47, showing, after implantation, the presence of clusters of carbon with low content in Si. As the temperature increases, the values of the ratio increase: 0.82 at 800 ºC and 0.94 at 1000 ºC. At 1000 ºC, the ratio is already close to the stoichiometry of 1:1 present in SiC. The exact same ratio was calculated previously for the single high fluence C as – implanted and annealed at 1000 ºC and also for the CMT1000 sample. The result is expressed in Table 11. The ratio values were the following: 0.54 and 0.69 for the CHAs and CHT1000 and finally 0.54 for the CMT1000 sample respectively. For single C high fluence implantation, it is possible to see that ratio is slightly higher compared to the dual implanted sample, however, at 1000 ºC the ratio value is smaller. The SiC formed for the C and Fe dual implantations at the higher temperature presents a stoichiometry closer to 1:1, meaning that the addition of Fe seems to indeed aid somehow the SiC formation.

The RBS spectra for the dual Fe and C implantations were simulated using the NDF© code. Both experimental and simulated spectra for the two implanted fluences and respective annealings are presented in Figure 82. In the top right corner of each spectrum of Figure 82 it is also represented the simulated result of the Fe signal in function of depth. The simulations enabled to confirm the implanted fluences of Fe for all samples with the exception of the FeCLT800 sample. The simulation revealed a fluence of $4.6x10^{16}$ cm^{-2}, around 8 % less than the expected value, $5x10^{16}$ cm^{-2}. The smaller value of fluence may be related to the fact that the sample was extracted too close to the edge of the implanted wafer. The other pieces of the exact same wafer, that were annealed, were extracted from a more central position and presented the expected fluence value. The C fluence was measured for the higher fluence sample FeCHT1000, Figure 82)f) since the C region of the spectrum is well fitted. A fluence value of 2.5x10^{17} cm^{-2} was determined, being higher than the expected one, 2x10^{17} cm^{-2}. In the other same fluence samples, FeCHAs and FeCHT800, the C region of the RBS spectra were not well fit and the corresponding simulated values were far from 2x10^{17} cm^{-2}. However, the C implantations are relatively easier to perform and control in comparison to other elements such as, Ti or W, thus being more or less expected the same implanted fluence value for these samples. The corresponding amorphous layers of the dual implanted samples were also calculated using the surface approximation equation, just like in the previous implantations. The attained values comprehended between 245 and 285 nm for the low and high dual Fe and C implantation, respectively.

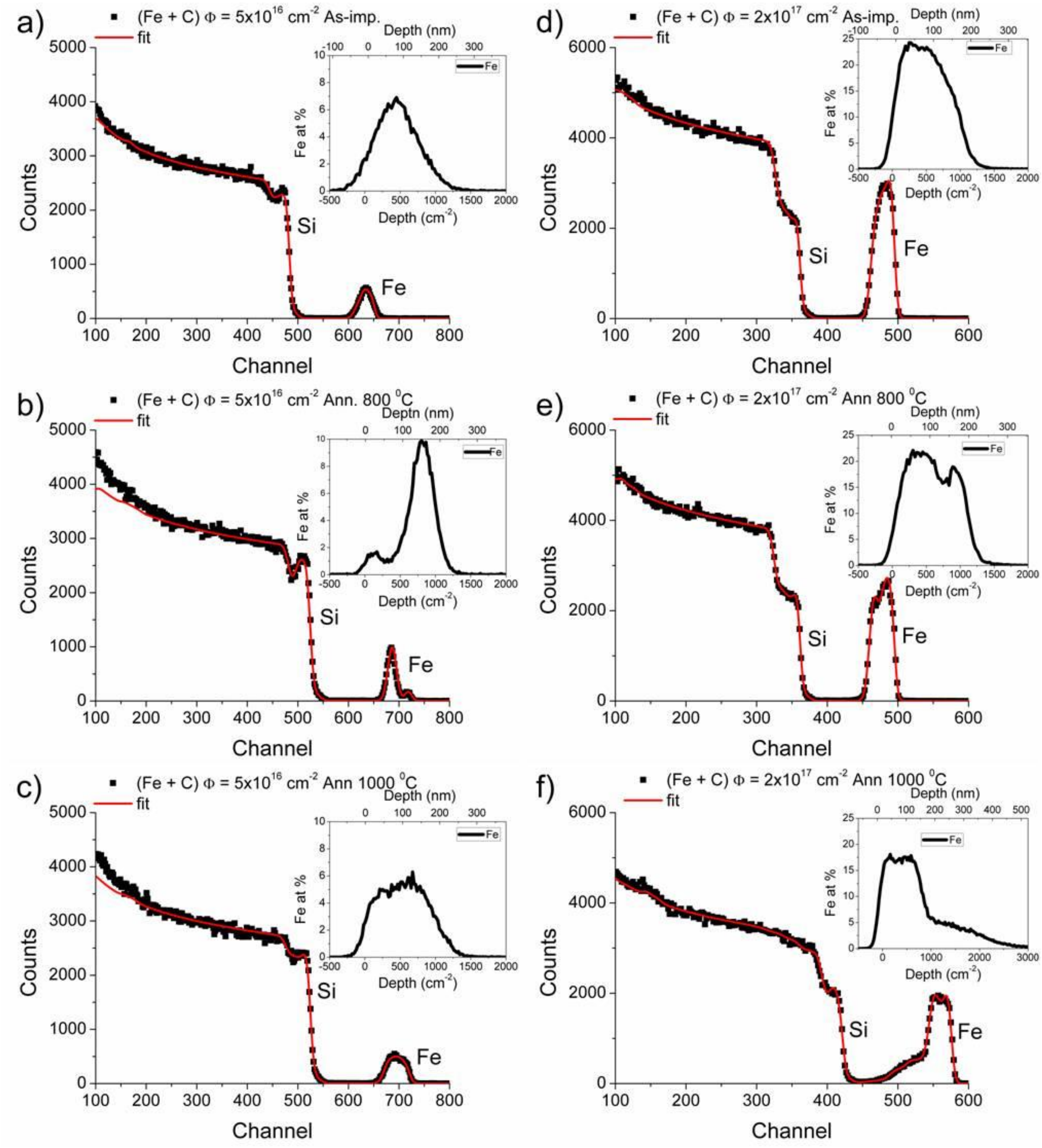

Figure 82. NDF simulations of the dual ion implanted Fe$^+$ and C$^+$ spectra, low fluence (Φ = 5x10^{16} cm^{-2}) (a) as-implanted, (b) annealed at 800 ºC (C) annealed at 1000 ºC; high fluence (Φ = 2x10^{17} cm^{-2}) (d) as-implanted, (e) annealed at 800 ºC (f) annealed at 1000 ºC.

The influence of the dual implantation on the wettability response of the samples is shown in Figure 78. Just like in the case of the single implantations of both elements Fe and C (Figure 64 and Figure 55), the as - implanted samples exhibit a higher contact angle compared to Si reference. Another common feature when comparing to single implantations is the fact that with the increase of ion fluence lower contact angles are achieved. The main differences between the single and double implantations arise after the annealings. While for the single implantations the 800 ºC annealing promoted a significant decrease in the contact angle, compared to respective as - implanted samples, for the dual implanted case the exact opposite occurs. In fact the dual low fluence samples almost became hydrophobic, presenting an average contact angle of ≈ 85 º ± 8º, having some water drops reached contact values above 90º, while the same did not happen for the higher one. This constitutes an outstanding result and one of the greatest achievements of the present thesis. As far as the author knows, and according to Table 2, this is the highest ever reported contact angle in Si involving exclusively the ion-implantation method, being slightly above 85 º, which was the maximum value found by the author, achieved by means of Nitrogen implantation and reported by Uueda *et al.* [170]. Contact angles of this magnitude could definitely reduce drastically the capillary adhesion of the contact-MEMS devices, which still imposes itself as one major obstacle for the commercialization and reliability of these devices. For the higher temperature annealing, 1000 ºC, the dual implanted samples show a decrease in the contact angle compared to the 800 ºC contact angle, being a more drastic drop for the low fluence case.

The observed difference in the wettability behaviour between single and dual implantations cannot be simply explained by the presence or not of a specific phase. Considering the medium and high fluence single Fe implantation, one can see that $\beta - FeSi_2$ phase presented a low contact angle whereas the $\alpha - FeSi_2$, although hydrophilic presented a higher contact angle. For the dual implantations this same order is completely inverted. For the dual implanted case, at least for the higher temperatures, the $\alpha - FeSi_2$ phase does present itself only with Si and SiC phase. It is interesting to observe that for the single case of C implantations, whenever the SiC phases was present, in the form of precipitates, the contact angles were also quite smaller when compared to the as – implanted sample. As it was mentioned before, the contact angles reported in the literature concerning the SiC phase varied between 58 – 70º, which does not seem to corroborate well with the reported results. The explanation may be associated with the fact that contact angles were measured on continuous films instead of precipitates on a Si hydrophilic surface. For the dual implanted Fe and C case, at 800 ºC where the highest contact angles were achieved, for each respective fluence, the SiC phase was not detected under the GIXRD measurements. However, the XPS results show that C – Si peak is present, but with a stoichiometry different from 1:1. This result should also be applicable to lower dual Fe and C implantation case, but confirmation is needed by XPS. The increase of the contact angle may be then associated with the fact of non-stoichiometric SiC phase being present, or, with some of the implanted carbon that may be actually “doping” the β – $FeSi_2$ phase. The XPS data presented in Table 12 also shows that with the increase of the temperature no signification oxidation occurs. Comparing all the ratios (element Ox)/ (element tot), one can directly see that with the increase of temperature carbon is the element that gets more oxidized, comparing to Si and Fe. This may also have an effect in the wettability behavior of the dual implanted samples.

The surface energy variation of the dual implanted Fe and C samples shown in Figure 78 presents some similar features compared to single implantations. For both implanted fluences, one can see that the dispersive component of the surface energy tends to present an almost constant value close to both Si reference and single implantations. The surface energy variation occurs due to significant changes in the surface energy polar component value minimum at 800 ºC for the higher contact angles.

The nanotribological characterization revealed how both elements work together in terms of improving the nanowear resistance, for both low and high fluences. For all studied samples, one presented a behavior different from all others: FeCLAs one. Instead of depressions/holes which enable one to calculate the corresponding worn volume, the scanned areas were full of features. These features are quite identical to hillocks previously observed in Si and CHT1000 samples. As it was mentioned before, these features represent a pre-stage of wear. From a load $\geq 30\ \mu N$ the hillocks show some signs of disruption, in opposition to what was previously observed in Figure 67, where they fully cover the surface, although for a much lower load value. It seems that for this sample a clear transition from hillocks to wear did not occur. The results were repeated, for the same load range, and the outcome was exactly the same. Regarding the annealed samples, for the low fluence, one can observe that the wear rate variation follows quite a similar trend for both annealing temperatures. Initially, at lower loads, the wear rates are higher than the reference ones, inverting this trend after a load of 25 µN. The GIXRD results of the annealed samples (Figure 75), show that for each temperature different phases are present, aside from the Si common to both, more precisely β – $FeSi_2$ and α – $FeSi_2$ at 800 ºC and 1000 ºC, respectively. The morphology of the surface is also quite similar, consisting of small precipitates (Figure 72 and Figure 73), although in a higher density for the 800 ºC case. The nanowear scans for the higher temperature did encounter some of the larger precipitates seen in Figure 73. The higher wear rates at lower loads may be associated with the surface precipitate removal, which will work as third body, enhancing wear. For the higher loads, the lower wear rates can be associated with the increase of the concentration of implanted species.

It is interesting to compare the dual high fluence Fe and C implantation nanowear results with the single Fe and C implanted ones, since the same fluence was used. The main limitation in the comparison will be the fact that Fe single implantations were carried out in a different AFM with a different diamond tip, in a different load range. Comparing the respective dual and single as-implanted samples, one can see that lower wear resistances are attained when compared to Si, more evident in the case of the single as-implanted samples. The inferior mechanical properties of the amorphous layer, induced by the single implantation, seem to rule the tribological behavior of the samples despite the implanted elements. Nevertheless, the same did not happen for the lower dual FeCHAs sample, where an amorphous layer is also present. The wear rate variation of the FeCHT800 sample (Figure 81b) follows a linear trend with the load, a behavior that is more identical to that of the Fe single implantation case than to the single C implantation one, at the same temperature. This was somehow expected, since both dual and Fe single implantation at that temperature have the same phase present the, β – $FeSi_2$ phase. For the highest applied normal loads, the depths were in the order of 30 – 40 nm. Looking into Figure 82, one can see that these depths probably correspond to the surface layers of the β – $FeSi_2$ phase, which seems to extend to deeper depths. However, the single C implantation shows that at 800 ºC starting from 15 µN load, higher nanowear resistance is achieved. The global good nanowear resistance displayed by the dual Fe and C implanted sample at 800 ºC, starting from low loads, is definitely achieved by the combined effect of the implanted elements.

As for the 1000 ºC sample, a complete different behavior is observed when compared to the single implantations. In Figure 81b) it is observed that for the lower loads the wear rates seem to display a rather constant trend, almost independent of the applied normal load, which did not happen for the single implanted cases. The surface morphology of the dual implanted sample is quite identical to the Fe case, with the exception the large precipitates and lower content of the white phase, indentified as α – $FeSi_2$ in the surface. The single Fe implantation displayed a close-to-linear wear rate behavior, exhibiting slightly higher rates than Si at the lower loads, but inverting this tendency afterwards. It is rather difficult to point out the reasons why for the lower loads the wear rates exhibited a constant trend and were so high compared to the Si ones. After all, both XRD and XPS characterization detected the hard SiC phase. On one hand, it has been reported that the α – $FeSi_2$ phase has worse mechanical properties than Si [295], but since the top surface layer shows less content of the silicide phase, one should expect the dominance of the mechanical properties of Si, unless of course a higher content of α – $FeSi_2$ phase is buried underneath the actual surface, or the Si at the surface having worse mechanical properties. After all, wear is inversely proportional to hardness. There is also the possibilyof the α – $FeSi_2$ phase removal acting like a third body which might significantly increase the wear rates. The same idea could also be thought about SiO_2 present on the surface, since the sample was annealed at 1000 ºC. However the XPS results in Table 12 shows that the (Si-Ox/Si-Ototal) content in this sample is actually lower when compared to the other samples. The nanowear scans in Figure 80 show that scanned areas have features at the bottom, showing that there are different zones with different tribological properties within the same surface. The same was not observed for the 800 ºC or as-implanted samples. At the higher loads, 50 – 70 µN, one can see that the wear rates become significantly lower than the Si ones. This decrease is most likely associated with the presence of a higher content of SiC upon deeper layers, which significantly increase the nanowear resistance. Looking into Figure 81d) one can see that the FeCHT1000 sample presented the lowest specific wear coefficient value among the dual high fluences Fe and C samples, despite the terrible wear resistance at lower loads.

4.4 DUAL IMPLANTATION OF TI^+ AND C^+

4.4.1 STRUCTURAL STUDY

The microstructural evolution of the dual Ti and C implanted samples with temperature is shown in Figure 83. The micrographs of the as-implanted state are not present in Figure 83 since no microstructures could be observed, even at high magnification. For both studied fluences, it is possible to observe a precipitate-like microstructure after the annealings. The precipitates after 800 ºC annealing are in the range of 50 nm to 200 nm. At higher annealing temperature, precipitates in the range of microns can be observed. Note that the micrographs of the low and high fluence implantation after annealings at 1000 ºC do not have the same magnification. The precipitates of the higher fluence have a size in the order of ≈ 10 µm, around ten times the size of the precipitates observed for the lower fluence.

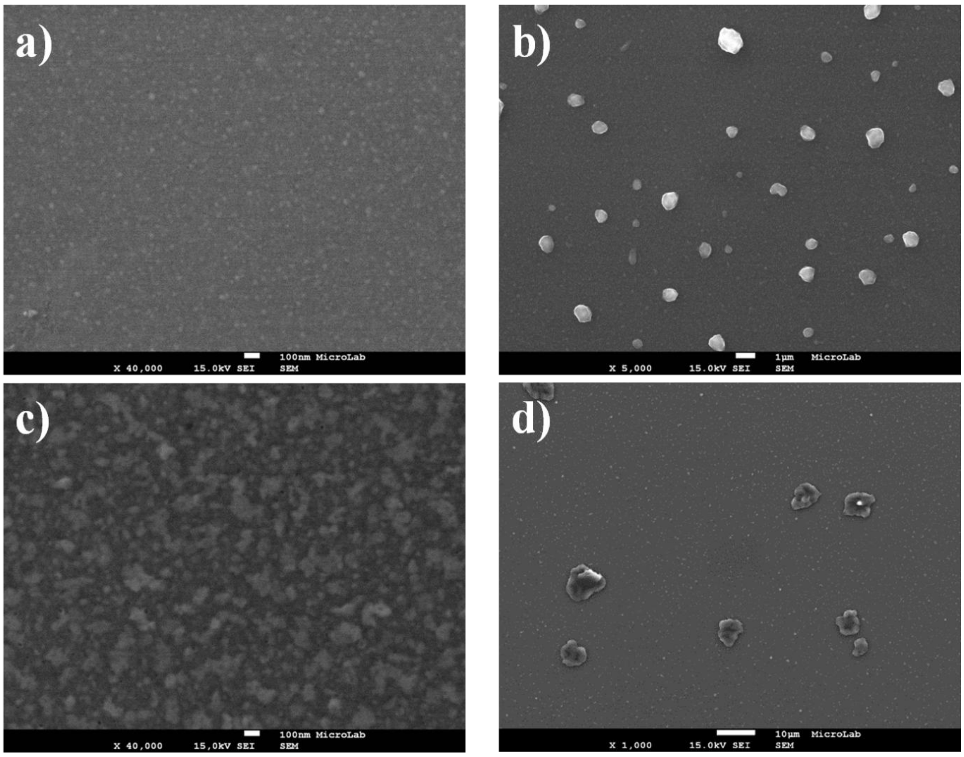

Figure 83. FEG-SEM micrographs corresponding to the microstrucutral evolution with temperature for the dual Ti and C ion-implanted samples, $(Ti^+ + C^+)$ $\Phi = 5x10^{16}$ cm^{-2} (a) annealed at 800 ºC, (b) annealed at 1000 ºC, $(Ti^+ + C^+)$ $\Phi = 2x10^{17}$ cm^{-2} (c) annealed at 800 ºC, (d) annealed at 1000 ºC

The phase evolution of dual Ti and C ion-implanted samples with the temperature is shown in Figure 84. Again, no peaks were observed for the as-implanted state for both fluences, just like all the previous studied implantations. One main difference can be observed when comparing the phase evolution of the different fluences. The presence of the SiC phase can be detected for the higher fluence for both annealings temperatures, while for the lower fluence it is not detected. Regarding the $TiSi_2$ evolution, initially looking to the 800 ºC annealing difractogram in Figure 84a) one essentially sees peaks corresponding to poly-Si phase, however carefully looking into the inset on the top right corner in Figure 84a), one also sees the presence of the silicide phases, in fact two different $TiSi_2$, the stable C54 - $TiSi_2$ phase and the metastable C49 - $TiSi_2$ one. These same phases can also be observed in Figure 84b) at 800 ºC. However, at the higher temperature annealing, the metastable phase is still present for the lower fluence case whereas for the higher fluence case is not. The metastable phase most likely fully transformed into C54 - $TiSi_2$.

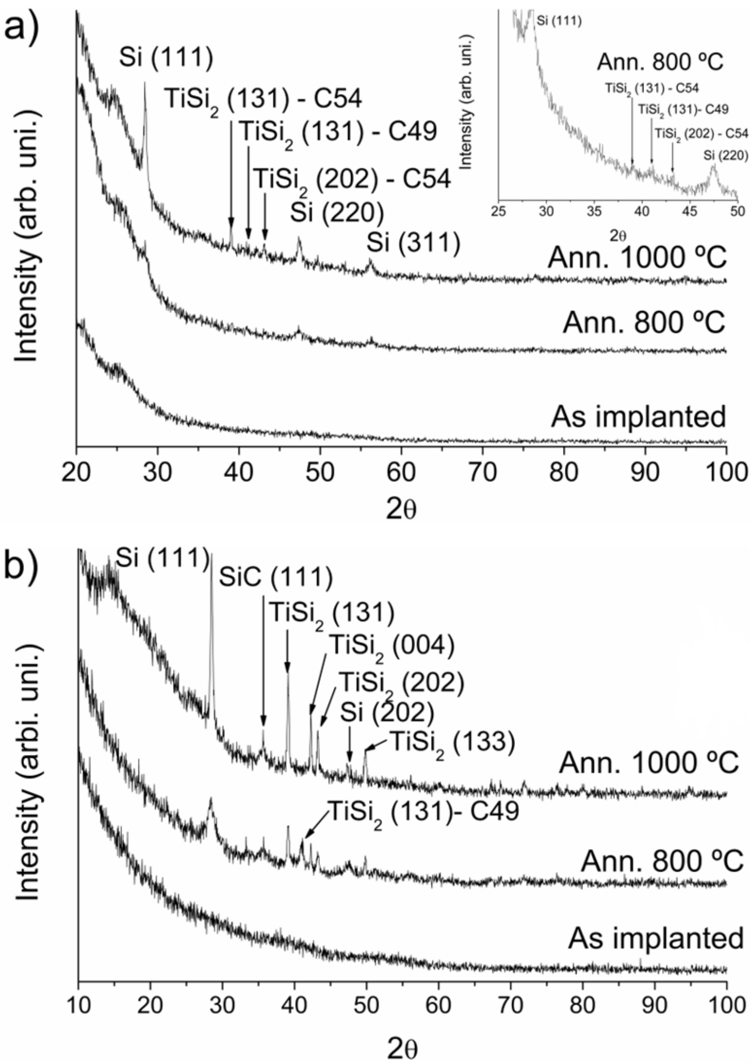

Figure 84. GIXRD evolution with temperature of the dual Ti and C ion-implanted and annealed samples (a) (Ti^++C^+) Φ =5x10^{16} cm^{-2}, (b) (Ti^++C^+) Φ =2x10^{17} cm^{-2}.

A RBS characterization was performed on the dual Ti-C ion implanted and annealed samples. The resulting aligned and random spectra were grouped and can be seen in Figure 85. For the sake of simplicity in Figure 85, for the Ti region, only the random spectra are represented and also in Figure 85a) the counts of Ti region were multiplied by a 3 factor in order to have a better perception of that same region. An amorphous layer induced by the implantation is easily detected in the aligned spectra in the Si region, with an extent larger than 250 nm according the represented scales. Upon the annealings, it is possible to observe a small advance of the amorphous/crystalline interface to some extent, which tells us that in the end, after the annealings, a polycrystalline surface is attained. Upon the annealings it also possible to observe that small shifts in the Ti barrier occur, being more significant in the in high fluence case, and that also, for this same fluence, a smaller content of Ti is detected after the annealings, being more visible for the 800 ºC annealed sample.

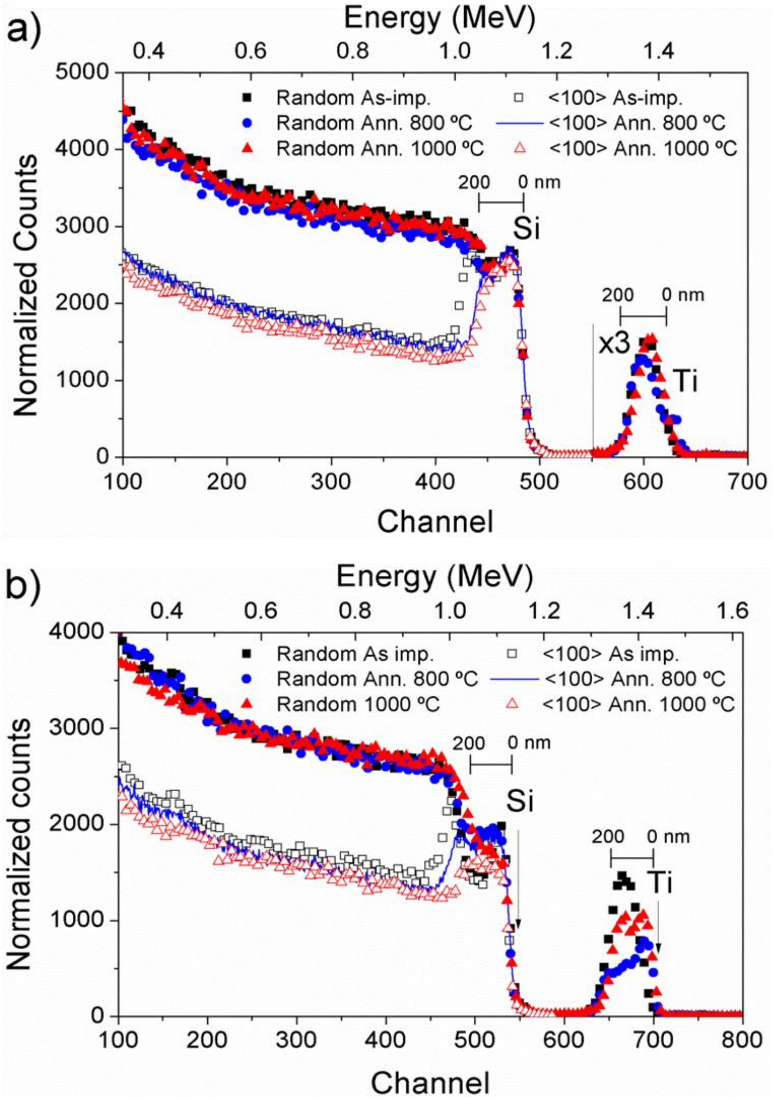

Figure 85.RBS random and aligned spectra of dual Ti and C implanted and annealed samples, at 800 ºC and 1000 ºC, acquired with alpha particles and with a total charge of 5 µC, (a) $\Phi = 5\text{x}10^{16}$ (Ti + C) cm^{-2}, at 160 keV and 50 keV, (b) $\Phi = 2\text{x}10^{17}$ (Ti + C) cm^{-2}, at 160 keV and 50 keV.

4.4.2 WETTABILITY STUDY

The water contact angle of the dual Ti and C ion implanted samples was determined, as well as the respective surface energies and surface components for all implanted and annealed samples. All these determined values were grouped in Figure 86. Directly comparing the different fluences water contact angles, Figure 86a) and c), one can see that one sample clearly stands out, the 800 ºC high dual fluence, that presents contact angles of 82 - 83 º, around more 20 º when compared with the same annealing temperature of the lower fluence. As for the other samples, more specifically the as-implanted and 1000 ºC annealed ones, the contact angles seem to be quite identical and higher than the Si <100> reference ones. Looking into Figure 86b) and d) one can observe the surface energy variation of both fluences. All samples present a energy lower that the Si <100>, being the lowest determined value the one corresponding to dual high fluence 800 ºC annealed sample, with a value of ≈ 30 mJ/m^2. Figure 86b) and d) also show that the dispersive component of the surface energy remains essentially constant for each fluence, being the polar component the main responsible for the contact angle variations.

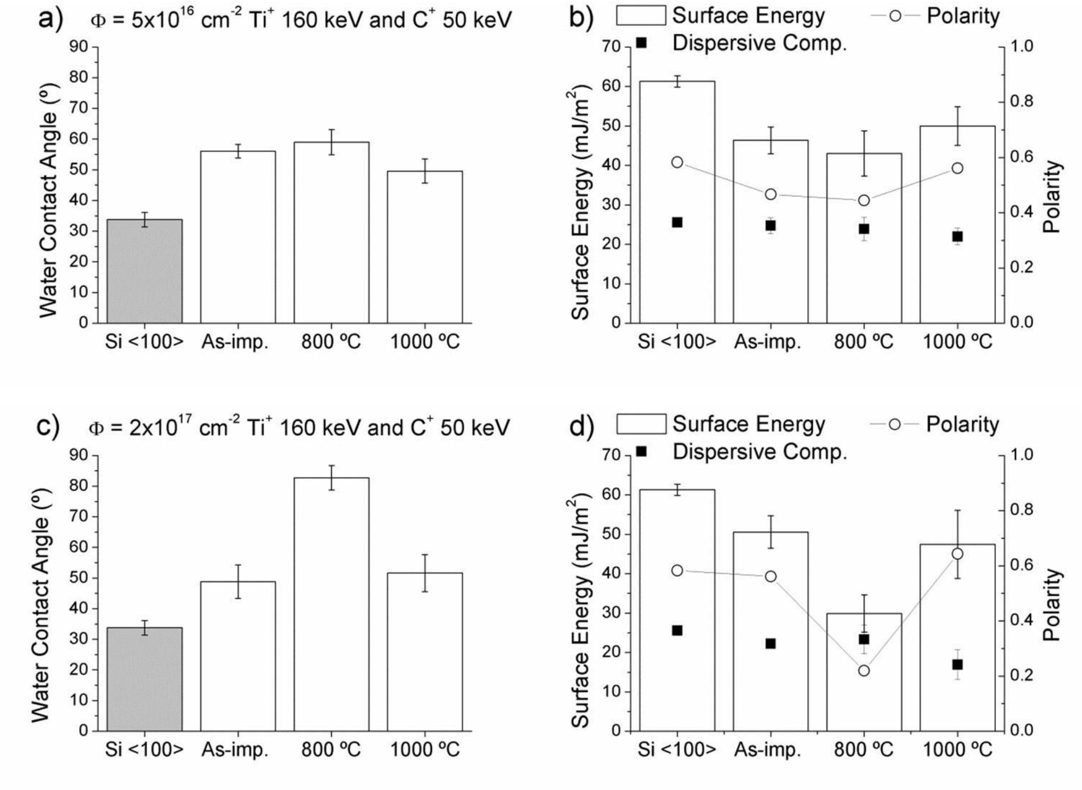

Figure 86. Water contact angle of the dual Φ = 5x10^{16} cm^{-2} Ti$^+$ and C$^+$ implanted and annealed samples, (b) Surface energy, dispersive component and polarity, (c) Water contact angle of the dual Φ = 2x10^{17} cm^{-2} Ti$^+$ and C$^+$ implanted and annealed samples, (d) Surface energy, dispersive component and polarity.

4.4.3 NANOTRIBOLOGICAL STUDY

The nanowear characterization was performed in the high fluence dual Ti and C implanted samples. The resulting nanowear scans for both as-implanted and annealed samples at 800 and 1000 ºC can be observed in Figure 87.

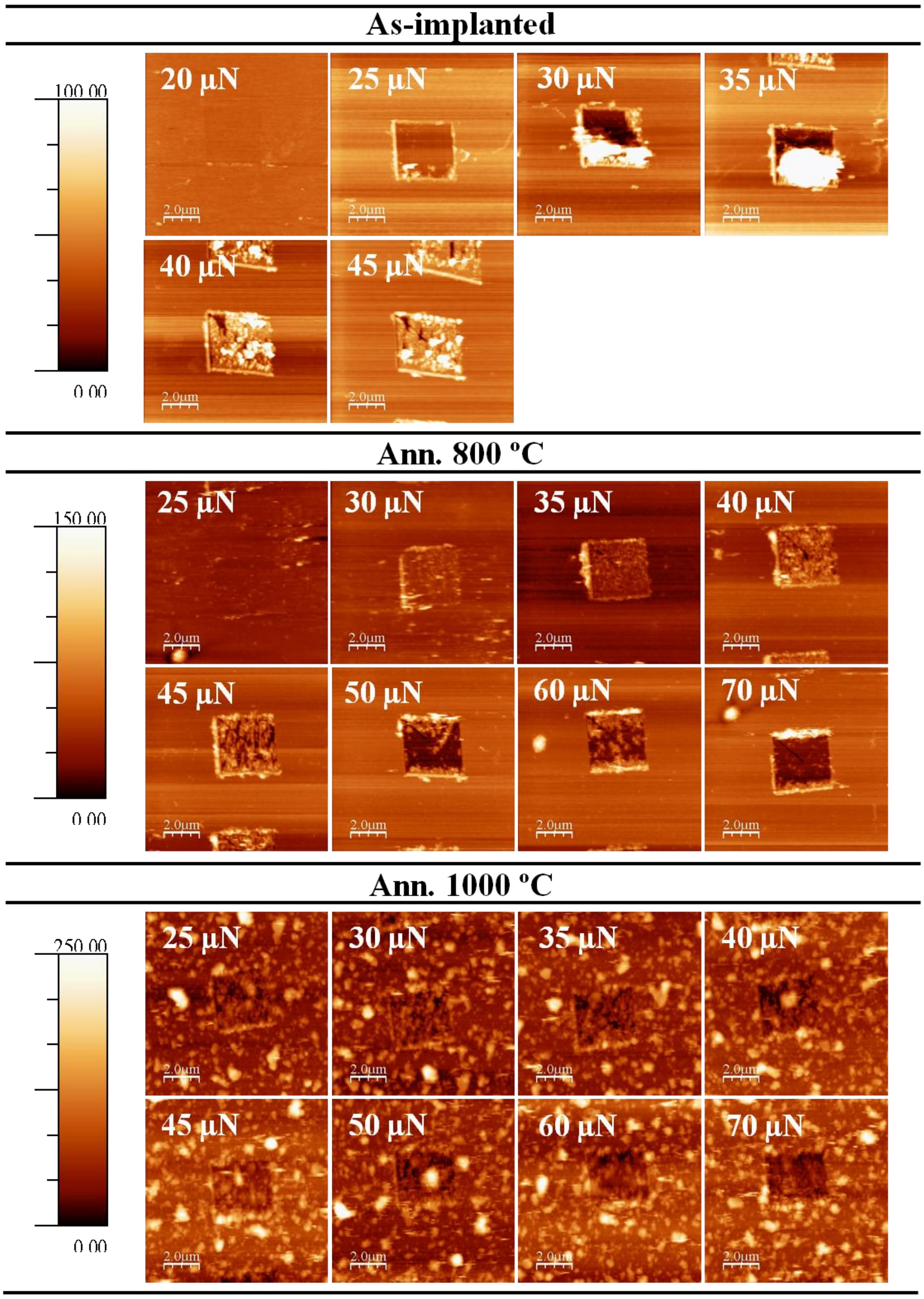

Figure 87. Nanowear scans of the $\Phi = 2\text{x}10^{17}$ cm^{-2} dual Ti (160 keV) and C (50 keV) implanted and annealed samples, at both 800 and 1000 ºC, for the different applied normal loads (height color scale in nm).

In the figure it is possible to observe that the as-implanted sample presents a different wear behavior when compared to the annealed ones. For the as-implanted sample wear initiates at a load of 20 µN, where a depth of 3 nm is measured. Upon the increasing of the load, within a range of 30 – 35 µN, deeper craters/depressions can be seen but at the same, a debris agglomeration phenomenon seems to be occurring at the edge of the scanned areas. When the load range reaches 40 to 50 µN values, craters/depressions are no longer visible but rather features at elevated heights, like the ones observed previously for the single C and dual Fe and C samples. The 800 and 1000 ºC annealed samples also exhibit the presence of similar features but for lower loads. For these samples the nanowear measurements were carried out until a sufficiently high normal load which enabled the determination of the hillocks-wear threshold. Looking to Figure 87 one can see that this transition occurs at ≈ 50 and 60 µN for the 800 and 1000 ºC annealed samples respectively. It is interesting to observe that before that same threshold is reached, the hillocks are no longer all above the surface, like in the as-implanted case, but most of them in a level inferior to the surface in terms of height, which leads one to believe that the hillock-wear transition may start slightly before the previously mentioned values.

From the AFM images, the wear rates were calculated in function of the applied normal load and the respective specific wear coefficients were determined. The results are shown in Figure 88. The wear rates were calculated even in the case when the features occurred, by using the lowest depth measured value (when found). As it was mentioned before, this constitutes a rough estimation. In Figure 88a) it is possible to observe that the as-implanted sample presents a linear relationship with the load while hole/craters are formed. As soon as the features begin to appear, the linear relationship no longer stands. All the calculated wear rates presented lower values when compared to the Si reference ones, being in fact the only studied as-implanted sample to present a higher wear resistance than the reference. As for the annealed samples, it is possible to see in Figure 88 that for the TiCHT800 sample the wear rates present a linear relationship from 25 µN to 50 µN, where the hillocks are formed, and also from 60 µN to 70 µN, where the hillocks are no longer observed but rather holes/craters. The linear regimes present a completely different slope, which is reflected in the specific wear coefficient presented in Figure 88b). The high temperature sample, 1000 ºC, exhibits also two different regimes, the first from 25 µN to 45 µN, where the scanned areas are full of features and a parabolic-like behavior is observed, in terms of wear rates in function of the load - Figure 88a), and the second regime, from 50 µN to 70 µN, where less features appear in the worn scans but where the wear rates show a linear behavior with the load. The specific wear coefficients for each regime were calculated and are presented in Figure 88b).

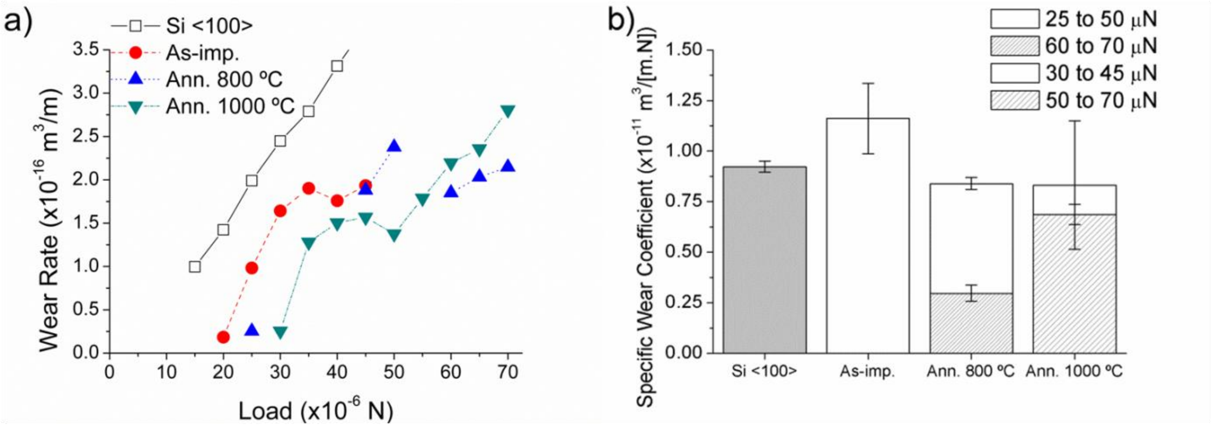

Figure 88. (a) Calculated wear rates for the dual high fluence Ti (160 keV) and C (50 keV) implanted and annealed samples, (b) calculated specific wear coefficients.

4.4.4 DISCUSSION

Also for the Ti+C implantation case there are no previous reports in the literature concerning Si which will bring an extra difficulty to compare and eventually discuss the attained results.

The microstructural characterization of the co-implanted Ti and C samples revealed a precipitate-like microstructure, where the precipitates ranged in size from the nanometers to microns range, depending essentially of the annealing temperature and fluence, as it can be seen in Figure 83. In the literature, the formation of Ti silicides microstructures has been observed mostly using deposition methods [337, 338], forming island-like microstructures which are significantly different from the precipitate-like structure attained in the present work.

The phase evolution of the co-implanted Ti and C samples observed in Figure 84 does not seem to change significantly with the fluence. The differences are essentially the presence of the SiC phase at the higher fluence, for all annealing temperatures, and the absence of the C49 metastable $TiSi_2$ phase at 1000 ºC. The author searched for the C-Si-Ti ternary phase diagrams in order to compare the phases formed with the expected ones. Unfortunately, the ternary phase diagrams found correspond only to isothermal sections starting from 1250 ºC [339], which is considerably different from the annealing temperatures used in the present thesis. One interesting aspect of the co-implantation of Ti and C in Si lies on the fact that the SiC formation/detection seems to be favored in this system since SiC is detected under GIXRD characterization staring from 800 ºC temperature. For the other C implanted systems, like the dual Fe and C one, the same only happens at 1000 ºC, and, for the single implantation, it is not even detected. For the dual Fe and C implantation at 800 ºC, SiC is only detected under XPS characterization, happening the same in the single C implantation case but only after a 1000 ºC annealing. Since the XPS characterization technique is considerably more sensitive to small concentrations when compared to the GIXRD, this confirms our initially assumption that SiC formation is more favorable in the Ti and C implantation case, when compared to the Fe and C or even the single C cases.

The identification of the C49-$TiSi_2$ metastable phase in Figure 84 was only possible by conjugating the database from the International Centre for Diffraction Data® (ICDD® PDF-2, 2006) with published results [340, 341], even though the $TiSi_2$ metastable phase was formed using different techniques. The polymorph transition between the metastable C49-$TiSi_2$ and stable C54-TiSi$_2$ has been studied in the past [338, 342]. The published results indicate that the temperature of this specific transition, C49 – C54, depends on the film thickness, being higher for the lower thicknesses [337, 342]. These results seem to correlate well with the attained results under the GIXRD characterization - Figure 84

The dual Ti and C implanted RBS spectra were simulated using the NDF code©, just like the previous samples. Both experimental and simulated spectra for the two implanted fluences and respective annealings are presented in Figure 89. In the top right corner of each individual figure of Figure 89 it is also presented the simulated result of the Ti signal in function of depth. The simulations allowed to confirm the implanted fluences for all samples, except for one, TiCHT800. The simulation of this specific sample presented a fluence value of ≈ 1.3x10^{17} cm^{-2}, instead of the expected value of 2x10^{17} cm^{-2}. The origin of such a difference may reside in the incorrect measurement of the current during the implantation. Also, it must be taken into consideration that the Ti implantations were carried out in ¼ of a 10 cm diameter wafer, and for a fluence of 2x10^{17} cm^{-2} under low current conditions, to avoid the sample´s heating, the implantation would take more than 20 hours in order to be achieved. So, to shorten the implantation time, the implantation beam was made to sweep the sample dimensions very close to the edges, which may have compromised the implanted fluence at some points. A less plausible explanation may be the possibility of some later segregation of Ti upon the annealing. However, the sample presented a homogenous microstructure thus making this explanation most likely not applicable to the situation. From the RBS spectra it is also possible to observe the Ti redistribution for the two different implanted fluences with the increase of temperature. The behaviour seems quite identical for both fluences until the 800 ºC annealing. Starting from a close-to-Gaussian profile, as expected for the respective as-implanted samples, the profiles for both fluences at 800 ºC temperature exhibit a shoulder for the higher energies. The shoulders most likely arise from a partial Ti diffusion to the surface as the amorphous/crystalline interface advances, as observed in Figure 85, which stops when the recrystallization takes place. For the higher temperature, the final profiles for the different fluences are quite distinct from each other. The lower implanted fluence shows a Gaussian-type profile, like the as-implanted sample. The elevated temperature allowed an even distribution of Ti upon the recrystallization in opposition to the 800 ºC. As for the higher fluence, upon the annealing, the Ti profile shows a bimodal distribution (inset in Figure 89), where the first peak is placed at the near surface and the second one ≈ 100 nm deeper buried into the surface, with a close concentration. The first peak arises from the diffusion of Ti towards the surface whereas the second one is most likely associated with Ti that was “dragged” or pulled as the amorphous/crystalline interface advanced.

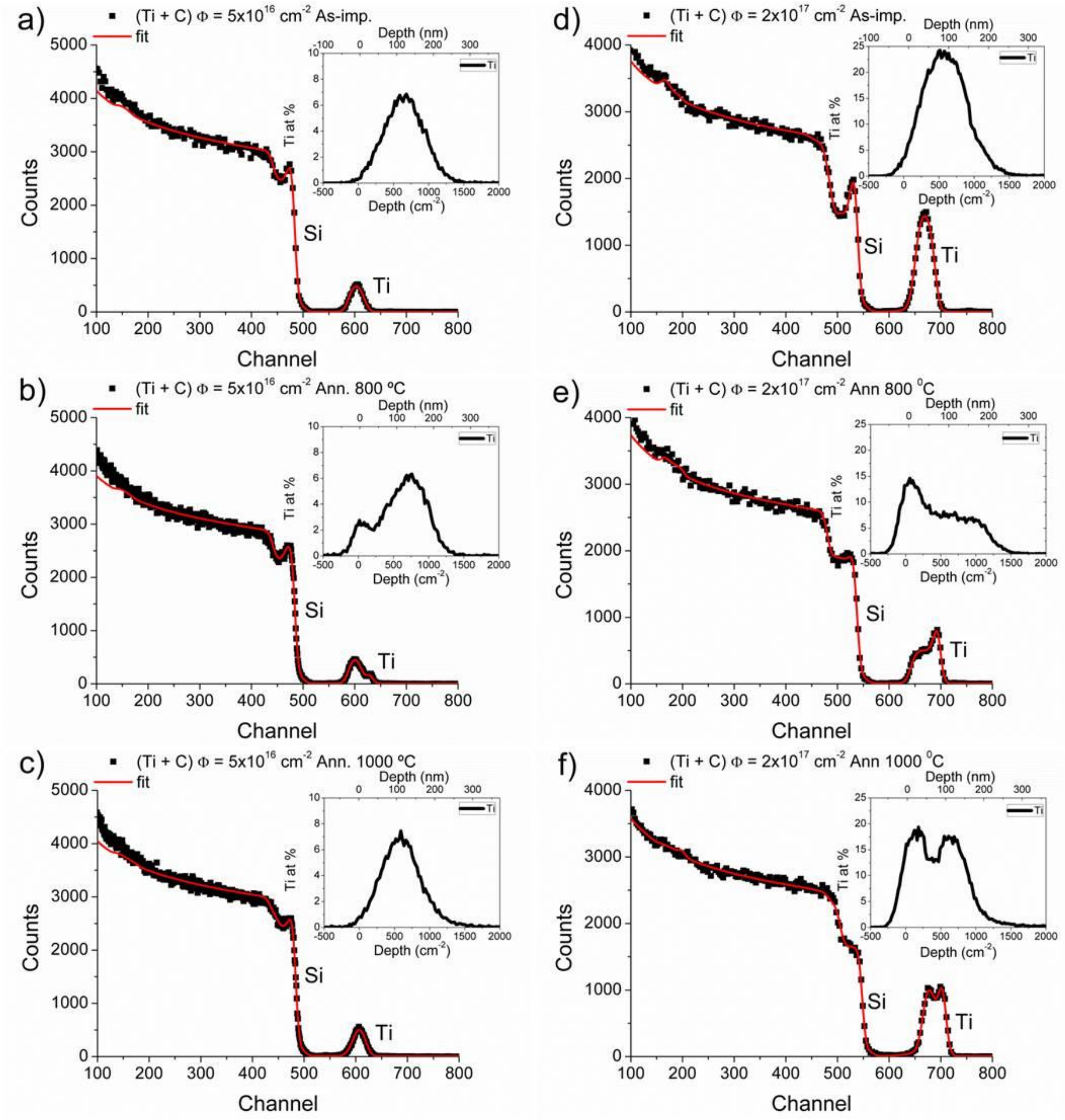

Figure 89. NDF© simulations of the dual ion implanted Ti$^+$ and C$^+$ spectra, low fluence (Φ = 5x10^{16} cm^{-2}) (a) as-implanted, (b) annealed at 800 ºC (C) annealed at 1000 ºC; high fluence (Φ = 2x10^{17} cm^{-2}) (d) as-implanted, (e) annealed at 800 ºC (f) annealed at 1000 ºC.

The wettability behavior of the dual ion implanted Ti and C samples is shown in Figure 86. Despite of being two completely different systems, the Fe-C and Ti-C systems seem to exhibit some similarities in terms of wettability behavior, more specifically in the high fluence samples of both systems ((Figure 78c), (Figure 86c)). The contact angles increase upon implantation and increase again even more after the 800 ºC annealing, where the maximum value of contact angle is reached. The following annealing at 1000 ºC lowers the contact to value close to the as-implanted one. Despite the same behavior, the values of the contact angles are slightly higher in Ti – C case. The corresponding surface energies values, and respective components, exhibit also the same trend having small differences between the two systems. The higher contact angle values, for each system considering the high fluences, were attained for the 800 ºC annealings, where the both surface energy and polar components reach their respective minima. As for the lower fluences, when comparing the results of Figure 78 and Figure 86, one can observe that the behavior between the systems does not exactly follow the exact same trend, as it happened for the high fluence case. In the Ti – C system no significant increase occurs at 800 ºC, as it happened in the higher fluence or even at the same fluence but for the Fe – C system.

The nanowear characterization of the high fluence dual Ti - C implantation shows that globally the nanowear resistance definitely improved by the addition of these two elements (Figure 88). From all studied implanted systems, the dual Ti - C case was the only one where the as-implanted sample actually presented lower wear rates than Si. In fact, if one compares the dual Ti - C implanted sample with the CHT1000 one, it is possible to observe that the wear threshold is quite identical (≈20 µN) and that the dual Ti - C sample actually presents a lower specific wear coefficient. A strange wear behavior is observed for the dual Ti -C as-implanted which seems to indicate that the sample is composed of different layers. For the lower tested loads wear occurs while for the higher tested loads elevated hillocks appear. Since the projected range of both Ti and C are similar, it is rather plausible to admit that the first few nanometers surface may be less damaged and less concentrated on the respective elements when compared to depths closer to the projected range. The first layers present already better nanowear resistance than Si, for a load of 35 µN a depth of ≈ 35 nm was reached. When higher loads are applied and deeper depths reached, the emergence of the hillocks is observed, from zones where probably the Ti and C respective concentrations are higher, and where probably a mixture of a – SiC, a – $TiSi_2$ and a – Si is present. As it was mentioned before, the hillocks represent a pre-stage of wear, which means that the buried layer has much higher wear threshold than the one at the surface. The simultaneous implantation of Ti and C has been tested in a different material than Si, Ni more specifically, and a significant improvement was observed in both hardness and Young´s modulus, from 1 GPa to 13.7 GPa, and 200 GPa to 420 GPa, respectively [343]. The mechanical properties of the dual implanted Ti -C samples (in Si) were not measured. Nonetheless, based on the nanowear results of the as-implanted sample, one may indirectly infer that the mechanical properties of Si were also increased by the addiction of Ti and C. According to Archard´s law, Equation 22 and Equation 25 in section § 2.3.3, the wear rate is inversely proportional to hardness, and lower nanowear rates were measured for the Ti and C as-implanted sample in comparison to Si. For all the other studied implanted systems that did not happen.

For the 800 ºC annealed sample the features start to emerge at lower loads – 30 µN. The GIXRD results show that at this temperature Si, SiC, C49 - $TiSi_2$ and C54 - $TiSi_2$ phases were detected (Figure 84), with a precipitate-like microstructure (Figure 83). At this temperature the surface is fully recrystallized. The estimation made by the author by calculating the wear rates based on depth shows no relation with the wear rates above the hillocks threshold. The same does not seem to happen for the 1000 ºC sample. Looking carefully into the nanowear scans in Figure 87 for that temperature one can see that 1000 ºC shows a slightly different wear behavior from when compared to the 800 ºC sample. Starting from a load of 40 µN, until 55 µN, features can be seen but mostly in a level lower than the surface and almost flat parts start to be recognizable at the bottom of the scans. This seems to indicate that the sample is composed of different layers, being the surface layer less wear resistant that the one buried beneath. The 1000 ºC sample is composed of Si, SiC and C54 - $TiSi_2$ phases according to the GIXRD results, having each respective phase different distinct mechanical properties. The global good wear resistance behavior of the dual Ti and C implanted samples is definitely associated with the presence of the SiC and C54 - $TiSi_2$ phases. The C54 - $TiSi_2$ silicide phase is known in the literature as a high melting point refractory/intermetallic phase with good oxidation and creep resistance that also possesses good mechanical properties, such as high hardness 870 HV (≈ 8.5 GPa) and Young´s modulus 255.6 GPa [28, 344]. These mechanical properties were measured for $TiSi_2$ made by HIP (Hot Isostatic Pressure) process, for pressures ≈ 200 MPa and temperatures of 1200 – 1300 ºC during 5 hours, and most likely correspond to bulk properties. These conditions are significantly different from the ones used in the present thesis, but in the end the same phase was reached thus being the author´s opinion that the attained silicide phase may possess at least similar mechanical properties. Regarding the mechanical properties of C49 - $TiSi_2$ only one work was found by the author, where a 149 GPa Young´s modulus was reported [345], being this value actually slightly lower than Si one ≈ 163 GPa. The best nanowear results were attained for the 800 ºC sample, which still contains some C49 phase that seems to possess inferior mechanical properties when compared to Si, SiC or C54 - $TiSi_2$. Since in the

GIRXD data -Figure 84 - only one peak was detected at this temperature and the annealing was performed at 800 ºC for 30 min, most of C49 - $TiSi_2$ has most likely been converted into C54 - $TiSi_2$, thus contributing less to the overall properties. The present thesis shows that the combined presence of SiC and $TiSi_2$, even in the form precipitates, significantly increases the nanowear resistance of Si.

4.5 FINAL DISCUSSION

Over the last chapters, results regarding the implantation of Si with different elements haven been shown and discussed and a fundamental question can be raised: from all studied implanted systems, which one benefited most simultaneously silicon´s wettability and nanotribological properties?

In order to answer the question the author summarized in Figure 90 both wettability and tribological results, more specifically, the average specific wear coefficient calculated by dividing each calculated wear rate by the respective load of the measurement. The criterion to find which implanted system, or specific sample, fulfils the intended requirements is relatively simple: the combination of the highest measured contact angle for the lowest calculated average specific wear coefficients. Looking into Figure 90b) and following the stated criteria, it immediately standouts that the single C implanted system must not be taken into consideration. In comparison with all the other systems, it presented the lowest contact angles, none above 60º, and all the calculated coefficients are actually higher than the Si reference.

The load range applied for the single C implanted system was actually lower when compared to the dual implanted samples, which may have influenced the calculated specific wear coefficients for this system. But still, the low contact angles would still make this system not appropriate for the intended applications. For the Fe single implanted system - Figure 90a) - higher contact angles were actually achieved, more precisely for the 1000 ºC annealed sample, around 72º. In addition, a decrease of the specific wear coefficient around ≈ 18 % is observed for the FeHT1000 relatively to the Si reference. In Figure 90c) and d) one can observe the effect of the dual Fe and C implantations for the two different studied fluences, low and high, respectively. The highest contact angle is observed for the 800 ºC annealed low fluence dual Fe and C implanted sample Figure 90c). This sample almost reached the hydrophobic state, in fact, in some measurements contact angles slightly above 90º were observed, but the final average value is around 85º. This is one remarkable achievement of the present thesis, according to Table 2 and as far as the author knows, this is one of the highest ever reported contact angle for implanted Si, without additional coatings, of the same magnitude of the value of 85º reported by Ueda *et al*. by N implantation [170], apparently resulting from the combination of β – $FeSi_2$ phase with C. Contact angles of this magnitude could drastically reduced the capillary adhesion of MEMS, improving their reliability.

Unfortunately the corresponding calculated average specific wear coefficient for this sample is actually higher than the Si reference one, which makes this sample fail the criteria. For the higher fluence Fe and C dual implantation, a similar contact angle variation is observed and the highest contact angle is also achieved for the 800 ºC annealed sample, but with a contact angle of 72º, around 15º less than for the lower fluence. However, looking to the specific wear coefficient, a smaller value than the Si reference is actually achieved, around 10 % less. It is interesting to observe that the single implanted Fe at 1000 ºC presents similar properties, that is, almost the same contact angle around 72º and a slightly smaller average specific wear coefficient, less 18 % than the reference. Globally, it stand outs that almost the same properties were achieved using either a single Fe or dual Fe and C implantation. However an important aspect must be taken into consideration: the temperature. Achieving almost the same properties but using a lower value of temperature annealing would make the high fluence dual Fe and C 800 ºC annealed samples more compatible with MEMS fabrication techniques.

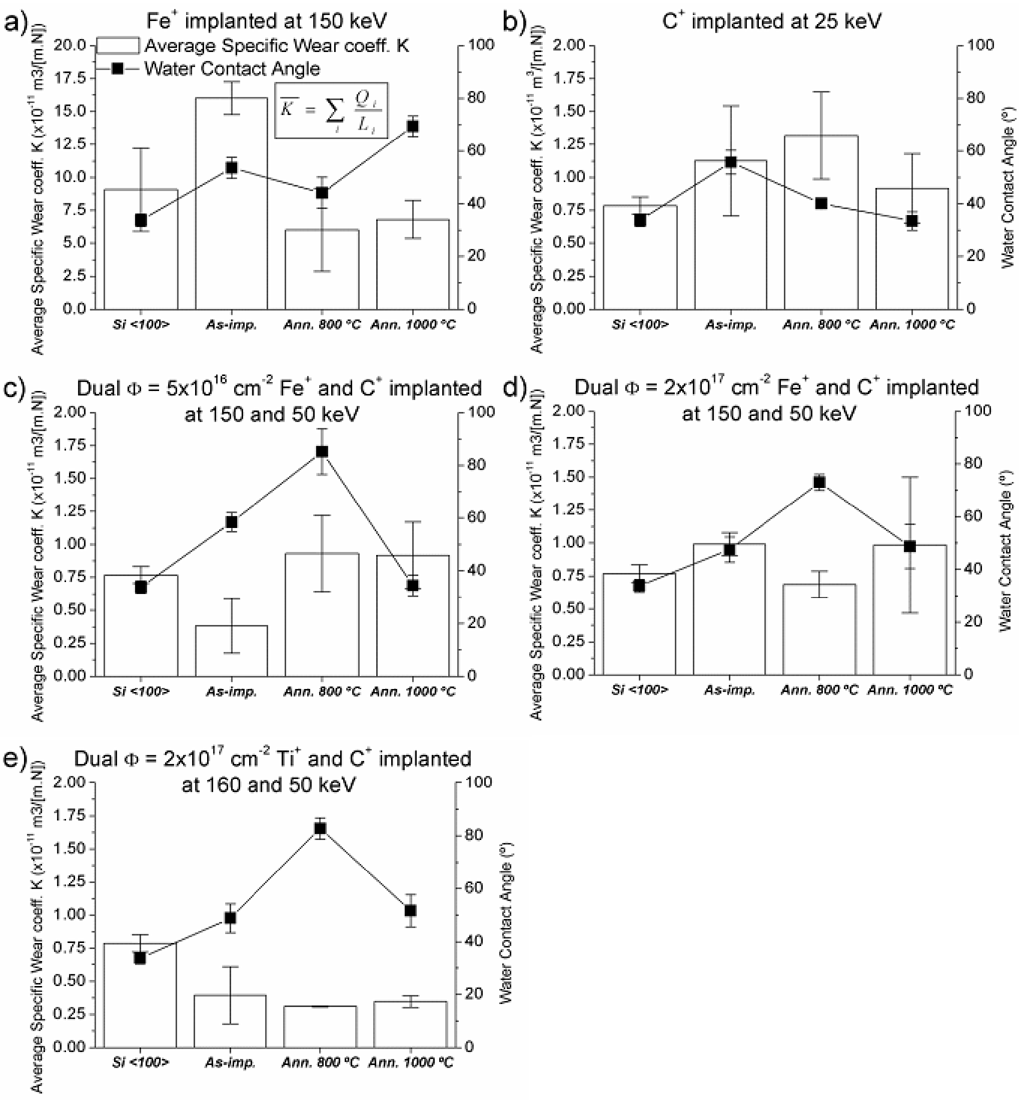

Figure 90. Calculated Average specific wear coefficient and Water contact angle for the different nanowear characterized implanted and annealed samples: (a) high fluence Fe^+ single implanted at 150 keV, (b) high fluence C^+ single implanted at 25 keV, (c) low fluence Fe^+ + C^+ dual implanted at 150 keV and 50 keV, (d) high fluence Fe^+ + C^+ dual implanted at 150 keV and 50 keV, (e) high fluence Ti^+ + C^+ dual implanted at 160 keV and 50 keV.

Finally, looking into Figure 90e) it becomes quite clear which sample better filled the intended requirements, that is, higher contact angle and lower average specific wear coefficient. The sample corresponds to the dual high fluence Ti and C 800 ºC annealed sample. This sample not only exhibited an almost hydrophobic contact angles, ≈ 82º ± 3º, but also presented the lowest calculated average specific wear coefficient, 3.09×10^{-12} $m^3/[N.m]$, around 60 % less than the Si reference. In fact, Figure 90 shows that the dual Ti and C system was the one that enabled the better nanotribological responses in terms of nanowear resistance, and also at the same time, the system on which higher wear thresholds were achieved. The better nanotribological properties of the dual Ti and C system were attributed to the simultaneous presence of both silicide and carbide phases: $TiSi_2$ (C-54) and SiC.

5 CONCLUSIONS

In the present thesis Si <100> surfaces have been implanted with C and Fe or co-implanted Ti:C and Fe:C. After implantation the samples were annealed at different temperatures, with the purpose of simultaneously remove the implantation damage and improve both wettability and nanowear resistance properties of Si for contact-based MEMS applications.

The characterization of the samples showed that globally the dual ion implanted systems tend to perform better when compared to the single implanted ones. Within all different implanted systems the poorer performance was achieved for the single C implantation case, where it were simultaneously observed the lower contact angles and also the higher wear rates, when compared to the remaining implanted systems.

The characterization of the dual Fe and C implanted system showed that an almost hydrophobic sample can be achieved by the simultaneous implantation of these two elements and an annealing at 800 ºC, for the lower implanted fluence. The average measured contact angle was 85º ± 8º, one of the highest, if not the highest, ever reported contact angle upon Si implantation without additional coatings or texturing. Some of the measurements actually reached hydrophobic values. The corresponding nanowear resistance did not however correlate with the conclusions from the contact angle measurements, exhibiting average specific wear coefficients higher than the reference. The higher fluence for the implanted elements, exhibited lower contact angles ≈ 72º, but still manages to conciliate good wear resistance properties at 800 ºC, exhibiting lower average specific wear coefficients than the Si ones.

From all studied implanted systems the one that was able to conciliate more significant improvements on Silicon´s wettability and nanowear resistance properties was the dual Ti and C one. The implantation of Ti and C on Si was able to produce a surface with much better wear resistance than Si, not only lowering both specific and average wear coefficients more than half, but also increasing the respective wear threshold values. This was observed for all Ti and C implanted and annealed samples. For all the other studied systems the corresponding as-implanted samples always presented lower nanowear resistance than Si. This shows how significantly the tribological properties were improved. The characterization of the Ti and C implanted samples revealed the presence of precipitate-like surface microstructures composed of SiC and C49 and C-54 - $TiSi_2$ depending on the temperature, which are most likely the main responsible for the good nanowear properties. The highest contact angle for this system was attained after a 800 ºC annealing, with a value around 82º ± 3º. Among all studied, this was the one that was able to most significantly increase simultaneously the contact angle and reduce the nanowear resistance, thus being the most suitable choice, within all studied samples, for contact-MEMS applications.

6 FUTURE WORK

The present thesis shows that Si properties, namely nanotribological and wettability ones can be significantly improved by single or co-implantation of elements, more specifically Fe and or co-implantation of Fe –C or Ti – C.. The present work was able to fill some gaps in the literature since, for instance, few or almost no works regarding dual implantations have been reported in Si, being the exception (as far as the author knows) the one published by Kodali *et al*. [167] where it was shown that C and N can significantly decrease the Si wear rates at the macroscale. It is the author's opinion that the good tribological/wettability results attained in the present thesis can be optimized and improved until some extent either using the ion-implantation technique, or slightly changing the course of action. The suggestions proposed by the author regarding the possible future work are the following:

- The optimization of tribological/mechanical/wettability properties of the single Ti or dual Ti – C systems, by adding some other elements close to Ti in the periodical table, that can also form silicides\carbides with good mechanical properties such as Mo, V, Zr, Nb or W [27].
- Explore the possibility of texturization using the ion-implantation technique by using the ions that give better tribological and wettability results, aiming to improve even more both properties. As it was shown in the introduction chapter of the present thesis, roughening a surface can simultaneously increase the contact angle and lower the value of friction coefficient. This combination goes exactly in the intended direction concerning the contact-MEMS requirements, making this approach worthy of exploration.
- Superhard Ti-Si-C-N coatings (~30 GPa) have been deposited on steel using plasma enhanced vapor deposition, being the films composed of several compounds such as: Ti(C,N), a-C and a-Si_3N_4 [346, 347]. An identical approach can be attempted using ion-implantation, by first implanting or depositing Ti in very high concentrations on the surface with a posterior implantation of C and N elements. Even harder coatings (H~80-100 GPa) [348] have been produced using also deposition techniques, containing a nanocomposite mixture of nc-TiN/a-Si_3N_4/a- and nc-$TiSi_2$ phases. The

combination of all intended phases is quite difficult using only ion-implantation. Nonetheless the promising results indicate that this possibility needs to be tested.

- A combination of hard phases, like the $TiSi_2$ for instance, with solid self-lubricant ones, such as MoS_2[349] or W-Si-C[350] would also be interesting to test in Si for contact-MEMS applications. The combination of both wear-resistance/low-friction phases would definitely improve Si tribological response.
- To perform the implantations and characterizations on deposited Si rather than Si <100> in order to have surfaces on similar conditions as the ones used in MEMS.

BIBLIOGRAPHY

1. Bhushan, B., *Springer handbook of nanotechnology*. 2nd rev. & extended ed. 2006, Berlin ; New York: Springer. xliv, 1916 p.

2. Kraft, M. and N. White, *MEMS for automotive and aerospace applications*. Woodhead Publishing series in electronic and optical materials. 2013, Oxford ; Philadelphia: Woodhead Pub. xv, 342 p.

3. Uttamchandani, D., *Handbook of MEMS for wireless and mobile applications*. Woodhead Publishing series in electronic and optical materials,. 2013, Cambridge: Woodhead Publishing Ltd. xxiv, 615 p.

4. Tanner, D.M., *MEMS reliability: Where are we now?* Microelectronics Reliability, 2009. **49**(9-11): p. 937-940.

5. Mounier, E. and L. Robin, *MEMS Markets Status of the MEMS Industry 2013 report (sample)*, Y. Développment, Editor. July, 2013.

6. Kim, S.H., D.B. Asay, and M.T. Dugger, *Nanotribology and MEMS.* Nano Today, 2007. **2**(5): p. 22-29.

7. Wautelet, M., *Scaling laws in the macro-, micro- and nanoworlds.* European Journal of Physics, 2001. **22**(6): p. 601-611.

8. Tas, N., *et al.*, *Stiction in surface micromachining.* Journal of Micromechanics and Microengineering, 1996. **6**(4): p. 385-397.

9. Bhushan, B., *Nanotribology and nanomechanics of MEMS/NEMS and BioMEMS/BioNEMS materials and devices.* Microelectronic Engineering, 2007. **84**(3): p. 387-412.

10. *Microelectromechanical Systems:Advanced Materials and Fabrication Methods*. 1997, Washington, DC: The National Academies Press.

11. Fleischman, A.J., *et al. Polycrystalline silicon carbide for surface micromachining*. in *Micro Electro Mechanical Systems, 1996, MEMS '96, Proceedings. An Investigation of Micro Structures, Sensors, Actuators, Machines and Systems. IEEE, The Ninth Annual International Workshop on*. 1996.

12. Smallwood, S.A., *et al.*, *Performance results of MEMS coated with a conformal DLC.* Wear, 2006. **260**(11-12): p. 1179-1189.

13. Bhushan, B., *et al.*, *Microtribological Characterization of Self-Assembled and Langmuir-Blodgett Monolayers by Atomic and Friction Force Microscopy.* Langmuir, 1995. **11**(8): p. 3189-3198.

14. Nainaparampil, J.J., *et al.*, *Ionic-liquid lubrication of sliding MEMS contacts: Comparison of AFM liquid cell and device-level tests.* Journal of Microelectromechanical Systems, 2007. **16**(4): p. 836-843.

15. Yee, Y., *et al.*, *Polysilicon surface-modification technique to reduce sticking of microstructures.* Sensors and Actuators a-Physical, 1996. **52**(1-3): p. 145-150.

16. Zou, M., *et al.*, *Adhesion and friction studies of a selectively micro/nano-textured surface produced by UV assisted crystallization of amorphous silicon.* Tribology Letters, 2005. **20**(1): p. 43-52.

17. Nunes, B., *et al.*, *Ageing effects on the wettability behavior of laser textured silicon.* Applied Surface Science, 2011. **257**(7): p. 2604-2609.

18. Song, Y., *et al.*, *Adhesion and friction properties of micro/nano-engineered superhydrophobic/hydrophobic surfaces.* Thin Solid Films, 2010. **518**(14): p. 3801-3807.

19. Jinno, T., *et al.*, *Effects of calcium ion implantation on osseointegration of surface-blasted titanium alloy femoral implants in a canine total hip arthroplasty model.* Journal of Arthroplasty, 2004. **19**(1): p. 102-109.

20. Zhang, Y.W., *et al.*, *High-fluence Co implantation in Si, SiO2/Si and Si3N4/Si Part III: heavy-fluence Co bombardment induced surface topography development.* Nuclear Instruments & Methods in Physics Research Section B-Beam Interactions with Materials and Atoms, 1999. **159**(3): p. 158-165.

21. Nakano, S. and H. Ogiso, *Functional fabrication of MEMS by ion implantation.* AIP Conference Proceedings, 2001. **576**(1): p. 939-942.

22. Nakano, S., H. Ogiso, and A. Yabe, *Advanced micromachine fabrication using ion-implanted layers.* Nuclear Instruments & Methods in Physics Research Section B-Beam Interactions with Materials and Atoms, 1999. **155**(1-2): p. 79-84.

23. Ayache, R., A. Bouabellou, and E. Richter, *Optical characterization of β-FeSi2 layers formed by ion beam synthesis.* Materials Science in Semiconductor Processing, 2004. **7**(4–6): p. 463-466.

24. Radermacher, K., *et al.*, *Ion-Beam Synthesis of Buried Alpha-Fesi2 and Beta-Fesi2 Layers.* Applied Physics Letters, 1991. **59**(17): p. 2145-2147.

25. Nunes, B., *et al.*, *Microstructure and nanomechanical properties of Fe+ implanted silicon.* Applied Surface Science, 2013. **284**: p. 533-539.

26. Sundararajan, S. and B. Bhushan, *Micro/nanotribological studies of polysilicon and SiC films for MEMS applications.* Wear, 1998. **217**(2): p. 251-261.

27. Gilman, J.J., *Chemistry and physics of mechanical hardness*. Wiley series on processing of engineering materials. 2009, Hoboken, N.J.: Wiley. xii, 214 p.

28. Rosenkranz, R., G. Frommeyer, and W. Smarsly, *Microstructures and properties of high melting point intermetallic Ti5Si3 and TiSi2 compounds.* Materials Science and Engineering: A, 1992. **152**(1–2): p. 288-294.

29. Li, M., H.X. Tang, and M.L. Roukes, *Ultra-sensitive NEMS-based cantilevers for sensing, scanned probe and very high-frequency applications.* Nature Nanotechnology, 2007. **2**(2): p. 114-120.

30. Kong, J., *et al.*, *Nanotube molecular wires as chemical sensors.* Science, 2000. **287**(5453): p. 622-625.

31. Walvaren, J.A. *Future challenges for MEMS failure analysis*. in *34th International Test Conference*. 2003. CHARLOTTE, North Carolina.

32. Nathanson, H.C., *et al.*, *The resonant gate transistor.* Electron Devices, IEEE Transactions on, 1967. **14**(3): p. 117-133.

33. Hartzell, A.L., M.G. Da Silva, and H.R. Shea, *MEMS reliability*. MEMS reference shelf. 2011, New York: Springer Science. xiii, 291 p.

34. Bhansali, S. and A. Vasudev, *Mems for Biomedical Applications*. 2012: Woodhead Publishing Limited.

35. van Spengen, W.M., *MEMS reliability from a failure mechanisms perspective.* Microelectronics Reliability, 2003. **43**(7): p. 1049-1060.

36. Achanta, S.C., J. P., *Nanotribology of MES/NEMS*, in *Fundamentals of friction and wear*. 2007, Springer. p. 521-547.

37. Maboudian, R. and C. Carraro, *Surface chemistry and tribology of MEMS.* Annual Review of Physical Chemistry, 2004. **55**: p. 35-54.

38. Van Spengen, W.M., R. Puers, and I. De Wolf, *On the physics of stiction and its impact on the reliability of microstructures.* Journal of Adhesion Science and Technology, 2003. **17**(4): p. 563-582.

39. Institute of Electrical and Electronics Engineers. and American Society of Mechanical Engineers., *Journal of microelectromechanical systems : a joint IEEE and ASME publication on microstructures, microactuators, microsensors, and microsystems*. 1992, Institute of Electrical and Electronics Engineers: New York, NY. p. v.

40. Mehregany, M., K.J. Gabriel, and W.S.N. Trimmer, *Micro Gears and Turbines Etched from Silicon.* Sensors and Actuators, 1987. **12**(4): p. 341-348.

41. Mehregany, M., K.J. Gabriel, and W.S.N. Trimmer, *Integrated Fabrication of Polysilicon Mechanisms.* Ieee Transactions on Electron Devices, 1988. **35**(6): p. 719-723.

42. Fan, L.S., Y.C. Tai, and R.S. Muller, *Integrated Movable Micromechanical Structures for Sensors and Actuators.* Ieee Transactions on Electron Devices, 1988. **35**(6): p. 724-730.

43. Fan, L.S., Y.C. Tai, and R.S. Muller, *Ic-Processed Electrostatic Micromotors.* Sensors and Actuators, 1989. **20**(1-2): p. 41-47.

44. Gabriel, K.J., *et al.*, *Insitu Friction and Wear Measurements in Integrated Polysilicon Mechanisms.* Sensors and Actuators a-Physical, 1990. **21**(1-3): p. 184-188.

45. Lim, M., Chang, J., Shultz, D., Howe, R., White, R. *Polysilicon microstructres to characterize static friction*. in *3RD WORKSHOP ON MICRO ELECTRO MECHANICAL SYSTEMS (MEMS 90)*. 1990. NAPA VALLEY, CA.

46. Mehregany, M., Senturia, S. D., Lang, J. H., *Friction and wear in microfabricated harmonic side-drive motors*, in *Solid-State Sensor and Actuator Workshop, 1990. 4th Technical Digest*, IEEE, Editor. 1990: Hilton Head Island, SC, USA. p. 17-22.

47. Tai, Y.C. and R.S. Muller, *Frictional Study of Ic-Processed Micromotors.* Sensors and Actuators a-Physical, 1990. **21**(1-3): p. 180-183.

48. Trimmer, W. and Institute of Electrical and Electronics Engineers., *Micromechanics and MEMS : classic and seminal papers to 1990*. 1997, New York: IEEE Press. xv, 701 p.

49. Garcia, E.J. and J.J. Sniegowski, *Surface Micromachined Microengine.* Sensors and Actuators a-Physical, 1995. **48**(3): p. 203-214.

50. Tang, W.C., *et al.*, *Electrostatic-comb drive of lateral polysilicon resonators.* Sensors and Actuators A: Physical, 1990. **21**(1–3): p. 328-331.

51. Tanner, D.M., *et al.*, *Frequency dependence of the lifetime of a surface micromachined microengine driving a load.* Microelectronics Reliability, 1999. **39**(3): p. 401-414.

52. Pharr, G.M., W.C. Oliver, and D.R. Clarke, *The Mechanical-Behavior of Silicon during Small-Scale Indentation.* Journal of Electronic Materials, 1990. **19**(9): p. 881-887.

53. Hopcroft, M.A., W.D. Nix, and T.W. Kenny, *What is the Young's Modulus of Silicon?* Journal of Microelectromechanical Systems, 2010. **19**(2): p. 229-238.

54. Simpson, T.R.E., *et al.*, *Influence of interfaces on the rates of crosslinking in poly(dimethyl siloxane) coatings.* Journal of Polymer Science Part a-Polymer Chemistry, 2004. **42**(6): p. 1421-1431.

55. Gad-el-Hak, M., *MEMS : introduction and fundamentals : the MEMS handbook*. 2nd ed. The MEMS handbook. 2006, Boca Raton: CRC Press/Taylor & Francis.

56. Tanner, D.M., *et al.*, *MEMS Reliability: Infrastructure, Test Structures, Experiments, and Failure Modes*. 2000, Sandia National Laboratories: Albuquerque.

57. Maboudian, R., *Surface processes in MEMS technology*. Surface Science Reports, 1998. **30**(6-8): p. 209-270.

58. Graf, D., *et al.*, *Oxidation of Hf-Treated Si Wafer Surfaces in Air.* Journal of Applied Physics, 1990. **68**(10): p. 5155-5161.

59. Mastrangelo, C.H., *Adhesion-related failure mechanisms in micromechanical devices.* Tribology Letters, 1997. **3**(3): p. 223-238.

60. Morita, M., *et al.*, *Control Factor of Native Oxide-Growth on Silicon in Air or in Ultrapure Water.* Applied Physics Letters, 1989. **55**(6): p. 562-567.

61. Jansen, H.V., *et al.*, *Applications of Fluorocarbon Polymers in Micromechanics and Micromachining.* Sensors and Actuators a-Physical, 1994. **41**(1-3): p. 136-140.

62. Matsumoto, Y. and M. Ishida, *The property of plasma-polymerized fluorocarbon film in relation to CH4/C4F8 ratio and substrate temperature.* Sensors and Actuators a-Physical, 2000. **83**(1-3): p. 179-185.

63. Zhuang, Y.X. and A. Menon, *Wettability and thermal stability of fluorocarbon films deposited by deep reactive ion etching.* Journal of Vacuum Science & Technology A, 2005. **23**(3): p. 434-439.

64. Man, P.F., B.P. Gogoi, and C.H. Mastrangelo, *Elimination of post-release adhesion in microstructures using conformal fluorocarbon coatings.* Journal of Microelectromechanical Systems, 1997. **6**(1): p. 25-34.

65. Smith, B.K., *et al.*, *Thin Teflon-like films for eliminating adhesion in released polysilicon micro structure.* Sensors and Actuators a-Physical, 1998. **70**(1-2): p. 159-163.

66. Imae, T., *Advanced chemistry of monolayers at interfaces : trends in methodology and technology*. Interface science and technology. 2007, Amsterdam ; London: Elsevier/Academic Press. xi, 365 p.

67. Ren, S., *et al.*, *Friction and wear studies of octadecyltrichlorosilane SAM on silicon.* Tribology Letters, 2002. **13**(4): p. 233-239.

68. Singh, R.A., *et al.*, *Friction behaviour of chemical vapor deposited self-assembled monolayers on silicon wafer.* Wear, 2007. **262**(1-2): p. 130-137.

69. Ashurst, W.R., *et al.*, *Alkene based monolayer films as anti-stiction coatings for polysilicon MEMS.* Sensors and Actuators a-Physical, 2001. **91**(3): p. 239-248.

70. Srinivasan, U., *et al.*, *Alkyltrichlorosilane-based self-assembled monolayer films for stiction reduction in silicon micromachines.* Journal of Microelectromechanical Systems, 1998. **7**(2): p. 252-260.

71. Patton, S.T., *et al.*, *Effect of surface chemistry on the tribological performance of a MEMS electrostatic lateral output motor.* Tribology Letters, 2000. **9**(3-4): p. 199-209.

72. Eapen, K.C., S.T. Patton, and J.S. Zabinski, *Lubrication of microelectromechanical systems (MEMS) using bound and mobile phases of Fomblin Zdol (R).* Tribology Letters, 2002. **12**(1): p. 35-41.

73. Bhushan, B., *Tribology and mechanics of magnetic storage devices*. 2nd ed. 1996, New York: Springer. xx, 1125 p.

74. Koinkar, V.N. and B. Bhushan, *Micro/nanoscale studies of boundary layers of liquid lubricants for magnetic disks.* Journal of Applied Physics, 1996. **79**(10): p. 8071-8075.

75. Liu, H.W. and B. Bhushan, *Nanotribological characterization of molecularly thick lubricant films for applications to MEMS/NEMS by AFM.* Ultramicroscopy, 2003. **97**(1-4): p. 321-340.

76. Eapen, K.C., *et al.*, *MEMS lubricants based on bound and mobile phases of hydrocarbon compounds: Film deposition and performance evaluation.* Journal of Microelectromechanical Systems, 2005. **14**(5): p. 954-960.

77. Satyanarayana, N. and S.K. Sinha, *Tribology of PFPE overcoated self-assembled monolayers deposited on Si surface.* Journal of Physics D-Applied Physics, 2005. **38**(18): p. 3512-3522.

78. Ma, J.Q., *et al.*, *Effect of multiply-alkylated cyclopentane (MAC) on durability and load-carrying capacity of self-assembled monolayers on silicon wafer.* Colloids and Surfaces a-Physicochemical and Engineering Aspects, 2007. **301**(1-3): p. 481-489.

79. Asay, D.B., *et al.*, *Macro- to nanoscale wear prevention via molecular adsorption.* Langmuir, 2008. **24**(1): p. 155-159.

80. Asay, D.B., M.T. Dugger, and S.H. Kim, *In-situ vapor-phase lubrication of MEMS.* Tribology Letters, 2008. **29**(1): p. 67-74.

81. Jimenez, A.E. and M.D. Bermudez, *Ionic liquids as lubricants for steel-aluminum contacts at low and elevated temperatures.* Tribology Letters, 2007. **26**(1): p. 53-60.

82. Mu, Z.G., *et al.*, *Effect of the functional groups in ionic liquid molecules on the friction and wear behavior of aluminum alloy in lubricated aluminum-on-steel contact.* Tribology International, 2005. **38**(8): p. 725-731.

83. Ye, C.F., *et al.*, *Room-temperature ionic liquids: a novel versatile lubricant.* Chemical Communications, 2001(21): p. 2244-2245.

84. Freemantle, M., *An Introduction to ionic liquids*. 2010, Cambridge: RSC Pub. xiv, 281 p.

85. Wasserscheid, P. and T. Welton, *Ionic liquids in synthesis*. Green chemistry. 2003, Weinheim: Wiley-VCH. xvi, 364 p.

86. Nainaparampil, J.J., *et al.*, *Micro-nano behaviour of DMBI-PF6 ionic liquid nanocrystals: large and small-scale interfaces.* Nanotechnology, 2005. **16**(11): p. 2474-2481.

87. Palacio, M. and B. Bhushan, *Ultrathin wear-resistant ionic liquid films for novel MEMS/NEMS applications.* Advanced Materials, 2008. **20**(6): p. 1194-+.

88. Bhushan, B., M. Palacio, and B. Kinzig, *AFM-based nanotribological and electrical characterization of ultrathin wear-resistant ionic liquid films.* Journal of Colloid and Interface Science, 2008. **317**(1): p. 275-287.

89. Mukhopadhyay, P. and R.K. Gupta, *Graphite, graphene, and their polymer nanocomposites*. 2013, CRC Press,: Boca Raton, FL. p. 1 online resource (xxii, 609 p.).

90. Savage, R.H., *Graphite Lubrication.* Journal of Applied Physics, 1948. **19**(1): p. 1-10.

91. Balandin, A.A., *et al.*, *Superior thermal conductivity of single-layer graphene.* Nano Letters, 2008. **8**(3): p. 902-907.

92. Lee, C., *et al.*, *Measurement of the elastic properties and intrinsic strength of monolayer graphene.* Science, 2008. **321**(5887): p. 385-388.

93. Wang, X., L.J. Zhi, and K. Mullen, *Transparent, conductive graphene electrodes for dye-sensitized solar cells.* Nano Letters, 2008. **8**(1): p. 323-327.

94. Lee, H., *et al.*, *Comparison of frictional forces on graphene and graphite.* Nanotechnology, 2009. **20**(32).

95. Lee, C., *et al.*, *Frictional Characteristics of Atomically Thin Sheets.* Science, 2010. **328**(5974): p. 76-80.

96. Lee, C., *et al.*, *Elastic and frictional properties of graphene.* Physica Status Solidi B-Basic Solid State Physics, 2009. **246**(11-12): p. 2562-2567.

97. Filleter, T. and R. Bennewitz, *Structural and frictional properties of graphene films on SiC(0001) studied by atomic force microscopy.* Physical Review B, 2010. **81**(15).

98. Li, Q.Y., *et al.*, *Substrate effect on thickness-dependent friction on graphene.* Physica Status Solidi B-Basic Solid State Physics, 2010. **247**(11-12): p. 2909-2914.

99. Lin, L.Y., *et al.*, *Friction and wear characteristics of multi-layer graphene films investigated by atomic force microscopy.* Surface & Coatings Technology, 2011. **205**(20): p. 4864-4869.

100. Somani, P.R., S.P. Somani, and M. Umeno, *Planer nano-graphenes from camphor by CVD.* Chemical Physics Letters, 2006. **430**(1-3): p. 56-59.

101. Pu, J.B., *et al.*, *Preparation and Tribological Study of Functionalized Graphene-IL Nanocomposite Ultrathin Lubrication Films on Si Substrates.* Journal of Physical Chemistry C, 2011. **115**(27): p. 13275-13284.

102. Ou, J.F., *et al.*, *Tribology Study of Reduced Graphene Oxide Sheets on Silicon Substrate Synthesized via Covalent Assembly.* Langmuir, 2010. **26**(20): p. 15830-15836.

103. Donnet, C., A. Erdemir, and J. Robertson, *Tribology of diamond-like carbon films : fundamentals and applications*. 2008, New York ; London: Springer. Xxvi, 664 p.

104. Grill, A., *Diamond-like carbon: state of the art.* Diamond and Related Materials, 1999. **8**(2-5): p. 428-434.

105. Colaco, R., *et al.*, *Micro-to-nano triboactivity of hydrogenated DLC films.* Journal of Physics D-Applied Physics, 2009. **42**(8).

106. Grill, A., *Tribology of diamondlike carbon and related materials: an updated review.* Surface & Coatings Technology, 1997. **94-5**(1-3): p. 507-513.

107. Kim, H.I., *et al.*, *Environmental effects on the friction of hydrogenated DLC films.* Tribology Letters, 2006. **21**(1): p. 53-58.

108. Eapen, K.C., *et al.*, *Aging of a fluorinated lubricant on bare and DLC-coated silicon-based MEMS.* Surface & Coatings Technology, 2005. **197**(2-3): p. 270-277.

109. Chua, D.H.C., *et al.*, *Fabrication of diamond-like amorphous carbon cantilever resonators.* Journal of Vacuum Science & Technology B, 2004. **22**(6): p. 2680-2684.

110. Krauss, A.R., *et al.*, *Ultrananocrystalline diamond thin films for MEMS and moving mechanical assembly devices.* Diamond and Related Materials, 2001. **10**(11): p. 1952-1961.

111. Fu, Y.Q., H.J. Du, and J.M. Miao, *Patterning of diamond microstructures on Si substrate by bulk and surface micromachining.* Journal of Materials Processing Technology, 2003. **132**(1-3): p. 73-81.

112. Sumant, A.V., *et al.*, *Toward the ultimate tribological interface: Surface chemistry and nanotribology of ultrananocrystalline diamond.* Advanced Materials, 2005. **17**(8): p. 1039-+.

113. Mehregany, M. and C.A. Zorman, *SiC MEMS: opportunities and challenges for applications in harsh environments.* Thin Solid Films, 1999. **355**: p. 518-524.

114. Flannery, A.F., *et al.*, *PECVD silicon carbide as a chemically resistant material for micromachined transducers.* Sensors and Actuators a-Physical, 1998. **70**(1-2): p. 48-55.

115. Rajan, N., *et al.*, *Performance of 3C-SiC thin films as protective coatings for silicon-micromachined atomizers.* Thin Solid Films, 1998. **315**(1-2): p. 170-178.

116. Yasseen, A.A., C.A. Zorman, and M. Mehregany, *Surface micromachining of polycrystalline SiC films using microfabricated molds of SiO2 and polysilicon.* Journal of Microelectromechanical Systems, 1999. **8**(3): p. 237-242.

117. Yasseen, A.A., *et al.*, *Fabrication and testing of surface micromachined polycrystalline SiC micromotors.* Ieee Electron Device Letters, 2000. **21**(4): p. 164-166.

118. Young, D.J., *et al.*, *High-temperature single-crystal 3C-SiC capacitive pressure sensor.* Ieee Sensors Journal, 2004. **4**(4): p. 464-470.

119. Mani, S.S., *et al. Effect of W coating on microengine performance*. in *Reliability Physics Symposium, 2000. Proceedings. 38th Annual 2000 IEEE International*. 2000.

120. George, S.M., A.W. Ott, and J.W. Klaus, *Surface chemistry for atomic layer growth.* Journal of Physical Chemistry, 1996. **100**(31): p. 13121-13131.

121. Leskela, M. and M. Ritala, *Atomic layer deposition (ALD): from precursors to thin film structures.* Thin Solid Films, 2002. **409**(1): p. 138-146.

122. Mayer, T.M., *et al.*, *Atomic-layer deposition of wear-resistant coatings for microelectromechanical devices.* Applied Physics Letters, 2003. **82**(17): p. 2883-2885.

123. Ashurst, W.R., *et al. Nanometer-thin titania films with SAM-level stiction and superior wear resistance for reliable MEMS performance*. in *Micro Electro Mechanical Systems, 2004. 17th IEEE International Conference on. (MEMS)*. 2004.

124. Achanta, S., D. Drees, and J.P. Celis, *Friction and nanowear of hard coatings in reciprocating sliding at milli-Newton loads.* Wear, 2005. **259**(1-6): p. 719-729.

125. Cao, X.K., *et al.*, *Micro/nanotribological and mechanical studies of TiN thin-film for MEMS applications.* Tribology Transactions, 2004. **47**(2): p. 227-232.

126. McDonald, J.C. and G.M. Whitesides, *Poly(dimethylsiloxane) as a material for fabricating microfluidic devices.* Accounts of Chemical Research, 2002. **35**(7): p. 491-499.

127. Quake, S.R. and A. Scherer, *From micro- to nanofabrication with soft materials.* Science, 2000. **290**(5496): p. 1536-1540.

128. Tambe, N.S. and B. Bhushan, *Scale dependence of micro/nano-friction and adhesion of MEMS/NEMS materials, coatings and lubricants.* Nanotechnology, 2004. **15**(11): p. 1561-1570.

129. Tambe, N.S. and B. Bhushan, *Micro/nanotribological characterization of PDMS and PMMA used for BioMEMS/NEMS applications.* Ultramicroscopy, 2005. **105**(1-4): p. 238-247.

130. Gelorme, J.D., R.J. Cox, and S.A.R. Gutierrez, *Photoresist composition and printed circuit boards and packages made therewith*. 1989, Google Patents.

131. Zhuang, Y.X. and A. Menon, *On the stiction of MEMS materials.* Tribology Letters, 2005. **19**(2): p. 111-117.

132. Saravanan, P., N. Satyanarayana, and S.K. Sinha, *Self-lubricating SU-8 Nanocomposites for Microelectromechanical Systems Applications.* Tribology Letters, 2013. **49**(1): p. 169-178.

133. Jiguet, S., *et al.*, *SU-8 nanocomposite coatings with improved tribological performance for MEMS.* Surface & Coatings Technology, 2006. **201**(6): p. 2289-2295.

134. Singh, R.A., N. Satyanarayana, and S.K. Sinha, *Surface chemical modification for exceptional wear life of MEMS materials.* Aip Advances, 2011. **1**(4).

135. Satyanarayana, N., S.K. Sinha, and B.H. Ong, *Tribology of a novel UHMWPE/PFPE dual-film coated onto Si surface.* Sensors and Actuators a-Physical, 2006. **128**(1): p. 98-108.

136. Tai, Z.X., *et al.*, *Tribological Behavior of UHMWPE Reinforced with Graphene Oxide Nanosheets.* Tribology Letters, 2012. **46**(1): p. 55-63.

137. Cheng, Y.T. and D.E. Rodak, *Is the lotus leaf superhydrophobic?* Applied Physics Letters, 2005. **86**(14).

138. Wenzel, R.N., *Resistance of solid surfaces to wetting by water.* Industrial and Engineering Chemistry, 1936. **28**: p. 988-994.

139. Cassie, A.B.D. and S. Baxter, *Wettability of porous surfaces.* Transactions of the Faraday Society, 1944. **40**: p. 0546-0550.

140. Baldacchini, T., *et al.*, *Superhydrophobic surfaces prepared by microstructuring of silicon using a femtosecond laser.* Langmuir, 2006. **22**(11): p. 4917-4919.

141. Israelachvili, J.N., *Intermolecular and surface forces*. 3rd ed. 2011, Burlington, Mass.: Academic Press. xxx, 674 p.

142. Sundararajan, S. and B. Bhushan, *Static friction and surface roughness studies of surface micromachined electrostatic micromotors using an atomic force/friction force microscope.* Journal of Vacuum Science & Technology a-Vacuum Surfaces and Films, 2001. **19**(4): p. 1777-1785.

143. Nair, R.P. and M. Zou, *Surface-nano-texturing by aluminum-induced crystallization of amorphous silicon.* Surface & Coatings Technology, 2008. **203**(5-7): p. 675-679.

144. Houston, M.R., R.T. Howe, and R. Maboudian, *Effect of hydrogen termination on the work of adhesion between rough polycrystalline silicon surfaces.* Journal of Applied Physics, 1997. **81**(8): p. 3474-3483.

145. Gomes, M.C., *et al.*, *Influence of the wettability of silicon substrates on the thickness of sol-gel silica films.* Journal of Materials Science, 1995. **30**(15): p. 3893-3896.

146. Cao, L.L., H.H. Hu, and D. Gao, *Design and fabrication of micro-textures for inducing a superhydrophobic behavior on hydrophilic materials.* Langmuir, 2007. **23**(8): p. 4310-4314.

147. Kumar, R.T.R., K.B. Mogensen, and P. Boggild, *Simple Approach to Superamphiphobic Overhanging Silicon Nanostructures.* Journal of Physical Chemistry C, 2010. **114**(7): p. 2936-2940.

148. Shafiei, M. and A.T. Alpas, *Nanocrystalline nickel films with lotus leaf texture for superhydrophobic and low friction surfaces.* Applied Surface Science, 2009. **256**(3): p. 710-719.

149. Pham, D., *et al.*, *Nanotribological properties of silicon nano-pillars coated by a Z-DOL lubricating film.* Journal of Mechanical Science and Technology, 2010. **24**(1): p. 59-65.

150. Singh, R.A., *et al.*, *Bio-inspired dual surface modification to improve tribological properties at small-scale.* Applied Surface Science, 2009. **255**(9): p. 4821-4828.

151. Singh, R.A. and E.-S. Yoon, *Friction of chemically and topographically modified Si (100) surfaces.* Wear, 2007. **263**(7): p. 912-919.

152. Singh, R.A., *et al.*, *Replication of surfaces of natural leaves for enhanced micro-scale tribological property.* Materials Science & Engineering C-Biomimetic and Supramolecular Systems, 2007. **27**(4): p. 875-879.

153. Burton, Z. and B. Bhushan, *Hydrophobicity, adhesion, and friction properties of nanopatterned polymers and scale dependence for micro- and nanoelectromechanical systems.* Nano Letters, 2005. **5**(8): p. 1607-1613.

154. Jung, Y.C. and B. Bhushan, *Contact angle, adhesion and friction properties of micro- and nanopatterned polymers for superhydrophobicity.* Nanotechnology, 2006. **17**(19): p. 4970-4980.

155. Myint, S.M., *et al.*, *Friction and wear durability studies on the 3D negative fingerprint and honeycomb textured SU-8 surfaces.* Tribology International, 2013. **60**: p. 187-197.

156. Singh, R.A., *et al.*, *Tribo-functionalizing Si and SU8 materials by surface modification for application in MEMS/NEMS actuator-based devices.* Journal of Physics D-Applied Physics, 2011. **44**(1).

157. Tay, N.B., M. Minn, and S.K. Sinha, *Polymer Jet Printing of SU-8 Micro-Dot Patterns on Si Surface: Optimization of Tribological Properties.* Tribology Letters, 2011. **42**(2): p. 215-222.

158. Burnett, P.J. and G.A.D. Briggs, *The Elastic Properties of Ion-Implanted Silicon.* Journal of Materials Science, 1986. **21**(5): p. 1828-1836.

159. Braun, M., *et al.*, *Formation and Characterization of Carbon Layers Deposited during Ion-Bombardment of Silicon.* Nuclear Instruments & Methods in Physics Research Section B-Beam Interactions with Materials and Atoms, 1989. **37-8**: p. 434-437.

160. Lekki, J., *et al.*, *Friction and Wear of Argon-Implanted Silicon-Crystals.* Journal of Materials Research, 1994. **9**(1): p. 91-95.

161. Miyamoto, T., S. Miyake, and R. Kaneko, *Wear-Resistance of C+-Implanted Silicon Investigated by Scanning Probe Microscopy.* Wear, 1993. **162**: p. 733-738.

162. Gupta, B.K., J. Chevallier, and B. Bhushan, *Tribology of Ion-Bombarded Silicon for Micromechanical Applications.* Journal of Tribology-Transactions of the Asme, 1993. **115**(3): p. 392-399.

163. Gupta, B.K., B. Bhushan, and J. Chevallier, *Modification of Tribological Properties of Silicon by Boron Ion-Implantation.* Tribology Transactions, 1994. **37**(3): p. 601-607.

164. Bhushan, B. and V.N. Koinkar, *Tribological Studies of Silicon for Magnetic Recording Applications.* Journal of Applied Physics, 1994. **75**(10): p. 5741-5746.

165. Gupta, B.K. and B. Bhushan, *Nanoindentation Studies of Ion-Implanted Silicon.* Surface & Coatings Technology, 1994. **68**: p. 564-570.

166. Miyamoto, T., *et al.*, *Wear resistance of N+-implanted silicon investigated by scanning probe microscopy.* Journal of Tribology-Transactions of the Asme, 1995. **117**(4): p. 612-616.

167. Kodali, P., *et al.*, *Tribological properties of carbon- and nitrogen-implanted Si(100).* Wear, 1997. **205**(1-2): p. 144-152.

168. Szabadi, M., *et al.*, *Elastic and mechanical properties of ion-implanted silicon determined by surface-acoustic-wave spectrometry.* Physical Review B, 1998. **58**(14): p. 8941-8948.

169. Chasse, M. and G.G. Ross, *Effect of aging on wettability of silicon surfaces modified by Ar implantation.* Journal of Applied Physics, 2002. **92**(10): p. 5872-5877.

170. Ueda, M., *et al.*, *Nanohardness and contact angle of Si wafers implanted with N and C and Al alloy with N by plasma ion implantation.* Surface & Coatings Technology, 2002. **156**(1-3): p. 190-194.

171. Williams, J., B. Haberl, and J. Bradby. *Nanoindentation of ion implanted and deposited amorphous silicon*. in *MRS Proceedings*. 2004. Cambridge Univ Press.

172. Follstaedt, D.M., J.A. Knapp, and S.M. Myers, *Mechanical properties of ion-implanted amorphous silicon.* Journal of Materials Research, 2004. **19**(1): p. 338-346.

173. Sun, R., T. Xu, and Q.J. Xue, *Effect of Ar+ ion implantation on the nano-mechanical properties and microstructure of single crystal silicon.* Applied Surface Science, 2005. **249**(1-4): p. 386-392.

174. Wan, G.J., *et al.*, *Surface wettabilly of nitrogen plasma-implanted silicon.* Nuclear Instruments & Methods in Physics Research Section B-Beam Interactions with Materials and Atoms, 2006. **242**(1-2): p. 296-299.

175. Mishra, P., S.R. Bhattacharyya, and D. Ghose, *Nanoindentation on single-crystal Si modified by 100 keV Cr+ implantation.* Nuclear Instruments & Methods in Physics Research Section B-Beam Interactions with Materials and Atoms, 2008. **266**(8): p. 1629-1634.

176. Fang, T.H., *et al.*, *Effect of nitrogen doping on nanomechanical and surface properties of silicon film.* Current Applied Physics, 2009. **9**(6): p. 1241-1245.

177. Xu, Z.H., Y.B. Park, and X.D. Li, *Nano/micro-mechanical and tribological characterization of Ar, C, N, and Ne ion-implanted Si.* Journal of Materials Research, 2010. **25**(5): p. 880-889.

178. Bhushan, B., *Introduction to tribology*. Second edition. ed. Tribology series. 2013. xix, 732 p.

179. Liang, H. and D.R. Craven, *Tribology in chemical-mechanical planarization*. 2005, Boca Raton: CRC Press. 185 p.

180. Bhushan, B., *Principles and applications of tribology*. Second edition. ed. Tribology Series. 2013, New York: John Wiley. xix, 1020 p.

181. Graça, S., *Tribo-mechanical Behaviourof the Ni-Co System: From Micro to nanoscale*, in *Departamento de Materiais*. 2008, Universidade Técnica de Lisboa: Instituto Superior Técnico.

182. Hertz, H., *Miscellaneous papers, translated from first German edition (1895) by DE Jones and JA Schott*. 1896, London: MacMillan.

183. Mate, C.M., *Tribology on the small scale : a bottom up approach to friction, lubrication, and wear*. Mesoscopic physics and nanotechnology. 2008, Oxford ; New York: Oxford University Press. xiii, 333 p.

184. Hutchings, I.M., *Tribology : friction and wear of engineering materials*. 1st ed. 1992, Boca Raton: CRC Press. viii, 273 p.

185. Dieter, G.E. and D. Bacon, *Mechanical metallurgy*. SI metric ed. McGraw-Hill series in materials science and engineering. 1988, London: McGraw-Hill. xxiii,751p.

186. Popov, V.L. and SpringerLink (Online service), *Contact mechanics and friction physical principles and applications*. 2010, Springer,: Heidelberg ; New York. p. xv, 362 p.

187. Graça, S., *Tribo-Mechanical Behaviour of the Ni-Co System: From Micro to Nanoscale*, in *Department of Materials*. 2008, Technical Unisersity of Lisbon (University of Lisbon): Instituto Superior Téncnico - Lisboa.

188. Greenwood, J.A. and J.B. Williams, *Contact of Nominally Flat Surfaces.* Proceedings of the Royal Society of London Series a-Mathematical and Physical Sciences, 1966. **295**(1442): p. 300-&.

189. Rabinowicz, E., *Friction and wear of materials*. 1st ed. Wiley series on the science and technology of materials. 1965, New York,: Wiley. x, 244 p.

190. Colaço, R., *Comportamento ao Desgaste Abrasivo de Ligas Fe-Cr-C Processadas e Desenvolvidas por Laser*, in *Departamento de Materiais*. 2001, Universidade Técnica de Lisboa: Instituto Superior Téncnico.

191. Mayer, J.W. and L. Eriksson, *Ion implantation in semiconductors, silicon and germanium*. 1970, New York,: Academic Press. xiii, 280 p.

192. Hnatek, E.R., *Integrated circuit quality and reliability*. 2nd ed. Electrical engineering and electronics. 1995, New York: M. Dekker. xiii, 786 p.

193. Rubin, L. and J. Poate, *Ion implantation in silicon technology.* Industrial Physicist, 2003. **9**(3): p. 12-15.

194. Mazzoldi, P., *Ion Implantation for Surface Engineering*, in *Advanced Techniques for Surface Engineering*, W. Gissler and H. Jehn, Editors. 1992, Springer Netherlands. p. 83-104.

195. Davis, J.R. and ASM International. Handbook Committee., *Tool materials*. ASM specialty handbook. 1995, Materials Park, OH: ASM International. v, 501 p.

196. McCafferty, E. and SpringerLink (Online service), *Introduction to corrosion science*. 2010, Springer,: New York. p. xvi, 575 p.

197. Gispert, M.P., *et al.*, *Tribological behaviour of Cl-implanted TiN coatings for biomedical applications.* Wear, 2007. **262**(11-12): p. 1337-1345.

198. Gonsalves, K.E., *Biomedical nanostructures*. 2008, Hoboken, N.J.: Wiley-Interscience. xxiii, 507 p., 8 p. of plates.

199. Nastasi, M.A., J.W. Mayer, and J.K. Hirvonen, *Ion-solid interactions : fundamentals and applications*. Cambridge solid state science series. 1996, Cambridge ; New York: Cambridge University Press. xxvi, 540 p.

200. Lindhard, J., M. Scharff, and H.E. Schiøtt, *Range concepts and heavy ion ranges (Notes on atomic collisions, II)*. Det Kgl Danske videnskabernes selskab, Copenhagen Matematiskfysiske meddelelser,. 1963, København,: Munksgaard. 42 p.

201. Mohr, P.J., B.N. Taylor, and D.B. Newell, *CODATA recommended values of the fundamental physical constants: 2010.* Reviews of Modern Physics, 2012. **84**(4): p. 1527-1605.

202. da Silva, R.M.C., *Estudo por RBS e Canalização Iónica de Ligas de Mg, Al e Fe Formadas por Implantação Iónica.*, in *Departamento de Física*. 1992, Universidade de Lisboa: Faculdade de Ciências.

203. Nastasi, M.A. and J.W. Mayer, *Ion implantation and synthesis of materials*. 2006, Berlin: Springer-Verlag. xiii, 263 p.

204. Ziegler, J.F., *Ion implantation : science and technology*. 2nd ed. 1988, Boston: Academic Press. ix, 498 p.

205. Ryssel, H. and K. Hoffmann, *Ion Implantation*, in *Process and Device Simulation for MOS-VLSI Circuits*, P. Antognetti, et al., Editors. 1983, Springer Netherlands. p. 125-179.

206. Ziegler, J.F. [cited 2014 22th of June]; Available from: http://srim.org/.

207. Christel, L.A., J.F. Gibbons, and T.W. Sigmon, *Displacement Criterion for Amorphization of Silicon during Ion-Implantation.* Journal of Applied Physics, 1981. **52**(12): p. 7143-7146.

208. Pelaz, L., L.A. Marques, and J. Barbolla, *Ion-beam-induced amorphization and recrystallization in silicon.* Journal of Applied Physics, 2004. **96**(11): p. 5947-5976.

209. Priolo, F. and E. Rimini, *Ion-beam-induced epitaxial crystallization and amorphization in silicon.* Materials Science Reports, 1990. **5**(7): p. 321-379.

210. Olson, G.L. and J.A. Roth, *Kinetics of solid phase crystallization in amorphous silicon.* Materials Science Reports, 1988. **3**(1): p. 1-77.

211. Csepregi, L., *et al.*, *Reordering of amorphous layers of Si implanted with 31P, 75As, and 11B ions.* Journal of Applied Physics, 1977. **48**(10): p. 4234-4240.

212. Kennedy, E.F., *et al.*, *Influence of 16O, 12C, 14N, and noble gases on the crystallization of amorphous Si layers.* Journal of Applied Physics, 1977. **48**(10): p. 4241-4246.

213. Nygren, E., *et al.*, *Impurity-Stimulated Crystallization and Diffusion in Amorphous-Silicon.* Applied Physics Letters, 1988. **52**(6): p. 439-441.

214. Thornton, R.P., R.G. Elliman, and J.S. Williams, *Amorphous-to-Polycrystalline Phase-Transformations in Sn-Implanted Silicon.* Journal of Materials Research, 1990. **5**(5): p. 1003-1012.

215. Williams, D.B. and C.B. Carter, *Transmission electron microscopy : a textbook for materials science*. 2nd ed. 2008, New York ; London: Springer. lxii, 760 p., I-15.

216. Goldstein, J., *Scanning electron microscopy and x-ray microanalysis*. 3rd ed. 2003, New York: Kluwer Academic/Plenum Publishers. xix, 689 p.

217. Cioffi, N. and M. Rai, *Nano-antimicrobials progress and prospects*. 2012, Springer,: Berlin ; New York. p. 1 online resource (xvi, 556 p.).

218. Reimer, L., *Scanning electron microscopy : physics of image formation and microanalysis*. 2nd completely rev. and updated ed. Springer series in optical sciences. 1998, Berlin ; New York: Springer. xiv, 527 p.

219. Cahn, R.W. and P. Haasen, *Physical metallurgy*. 4th, rev. and enhanced ed. 1996, Amsterdam ; New York: North-Holland.

220. Zhou, W. and Z.L. Wang, *Scanning microscopy for nanotechnology : techniques and applications*. 2007, New York: Springer. xiv, 522 p., 12 p. of plates.

221. Binnig, G., C.F. Quate, and C. Gerber, *Atomic Force Microscope.* Physical Review Letters, 1986. **56**(9): p. 930-933.

222. Eaton, P.J. and P. West, *Atomic force microscopy*. 2010, Oxford ; New York: Oxford University Press. viii, 248 p.

223. Bowen, W.R. and N. Hilal, *Atomic force microscopy in process engineering : introduction to AFM for improved processes and products*. 1st ed. 2009, Oxford ; Burlington, MA: Butterworth-Heinemann. xvi, 283 p.

224. *Nanoworld innovative technologies*. [cited 2014 25th of July]; Available from: http://www.nanoworld.com/tapping-mode-afm-tip-arrow-nc.

225. Braga, P.C. and D. Ricci, *Atomic force microscopy biomedical methods and applications*, in *Methods in molecular biology 242*. 2004, Humana Press,: Totowa, N.J. p. xiv, 394 p.

226. Kempf, M., M. Goken, and H. Vehoff, *Nanohardness measurements for studying local mechanical properties of metals.* Applied Physics a-Materials Science & Processing, 1998. **66**: p. S843-S846.

227. Marshall, G.W., *et al.*, *Mechanical properties of the dentinoenamel junction: AFM studies of nanohardness, elastic modulus, and fracture.* Journal of Biomedical Materials Research, 2001. **54**(1): p. 87-95.

228. Degiampietro, K. and R. Colaco, *Nanoabrasive wear induced by an AFM diamond tip on stainless steel.* Wear, 2007. **263**: p. 1579-1584.

229. Graca, S., R. Vilar, and R. Colaco, *The role of indentation size effect on the abrasive wear behaviour of ductile metallic materials: A nanotribological study.* Wear, 2010. **268**(7-8): p. 931-938.

230. Yoon, E.S., *et al.*, *An experimental study on the adhesion at a nano-contact.* Wear, 2003. **254**(10): p. 974-980.

231. Brundle, C.R., C.A. Evans, and S. Wilson, *Encyclopedia of materials characterization : surfaces, interfaces, thin films*. Materials characterization series. 1992, Boston Greenwich, CT: Butterworth-Heinemann; Manning. xix, 751 p.

232. Birkholz, M., P.F. Fewster, and C. Genzel, *Thin film analysis by X-ray scattering*. 2006, Weinheim: Wiley-VCH. xxii, 356 p.

233. Cullity, B.D., *Elements of X-ray diffraction*. Addison-Wesley metallurgy series. 1956, Reading, Mass.,: Addison-Wesley Pub. Co. 514 p.

234. Cullity, B.D., *Elements of x-ray diffraction*. 2d ed. Addison-Wesley series in metallurgy and materials. 1978, Reading, Mass.: Addison-Wesley Pub. Co. xii, 555 p.

235. Callister, W.D. and D.G. Rethwisch, *Fundamentals of materials science and engineering : an integrated approach*. 3rd ed. 2008, Hoboken, NJ: John Wiley & Sons. xxv, 882 p.

236. Rau, U., D. Abou-Ras, and T. Kirchartz, *Advanced characterization techniques for thin film solar cells*. 2011, Weinheim, Germany: Wiley-VCH. xxxvi, 547 p.

237. *Pearson's Crystal Data Crystal Structure Database for Inorganic Compounds*. [cited 2014 25th of July]; Available from: http://www.crystalimpact.com/pcd/].

238. Walls, J.M., *Methods of surface analysis*. 1989, Cambridge Cambridgeshire ; New York: Cambridge University Press. x, 342 p.

239. Chu, W.-K., J.W. Mayer, and M.-A. Nicolet, *Backscattering spectrometry*. 1978, New York: Academic Press. xv, 384 p.

240. Tesmer, J.R. and M.A. Nastasi, *Handbook of modern ion beam materials analysis*. 1995, Pittsburgh, Pa.: Materials Research Society. vii, 704 p.

241. Bird, J.R. and J.S. Williams, *Ion beams for materials analysis*. 1989, Sydney ; San Diego: Academic Press. xviii, 719 p.

242. Marques, C.P.G., *Modification of Aluminium oxides Trough Ion Implantation of Transition and Noble Metals*. 2009, Universidade Nova de Lisboa - faculdade de Ciências e Tencnologias Lisboa.

243. Magalhães, S.N.C., *Caracterização e Modificação de Heteroestruturas de Nitretos do Grupo III*, in *Departamento de Física*. 2013, Universidade de Aveiro.

244. Barradas, N.P., C. Jeynes, and R.P. Webb, *Simulated annealing analysis of Rutherford backscattering data.* Applied Physics Letters, 1997. **71**(2): p. 291-293.

245. Adamson, A.W., *Physical chemistry of surfaces*. 6th ed. 1997, New York: J. Wiley. xviii, 664 p.

246. Butt, H.-J., K. Graf, and M. Kappl, *Physics and chemistry of interfaces*. 2003, Weinheim: Wiley-VCH. xii, 361 p.

247. Ebnesajjad, S., C.F. Ebnesajjad, and Books24x7 Inc., *Surface treatment of materials for adhesion bonding, second edition*. 2014, William Andrew,: Kidlington, Oxford ; Waltham, Mass.

248. Barnes, G. and I. Gentle, *Interfacial science : an introduction*. 2nd ed. 2011, Oxford ; New York: Oxford University Press. xxii, 325 p.

249. Von Recum, A. and J.E. Jacobi, *Handbook of biomaterials evaluation : scientific, technical, and clinical testing of implant materials*. 2nd ed. 1999, Philadelphia, PA: Taylor & Francis. xix, 915 p.

250. Serro, A.P.V., *Biomineralização de Materiais de Implante: Estudo de Molhabilidade*, in *Department of Chemistry*. 2001, Technical Unisersity of Lisbon (University of Lisbon): Instituto Superior Téncnico - Lisboa.

251. Packham, D.E., *Work of adhesion: contact angles and contact mechanics.* International Journal of Adhesion and Adhesives, 1996. **16**(2): p. 121-128.

252. Schrader, M.E. and G.I. Loeb, *Modern approaches to wettability : theory and applications*. 1992, New York: Plenum Press. xxiii, 451 p.

253. Fowkes, F.M., *Attractive Forces at Interfaces.* Industrial and Engineering Chemistry, 1964. **56**(12): p. 40-&.

254. Fowkes, F.M., *Calculation of Work of Adhesion by Pair Potential Summation.* Journal of Colloid and Interface Science, 1968. **28**(3-4): p. 493-&.

255. Correia, N.T., *et al.*, *Estimation of the surface tension of a solid: Application to a liquid crystalline polymer.* Journal of Colloid and Interface Science, 1997. **189**(2): p. 361-369.

256. Żenkiewicz, M., *Methods for the calculation of surface free energy of solids.* Journal of Achievements in Materials and Manufacturing Engineering, 2007. **24**(1): p. 137-145.

257. Owens, D.K. and R.C. Wendt, *Estimation of Surface Free Energy of Polymers.* Journal of Applied Polymer Science, 1969. **13**(8): p. 1741-&.

258. Michalski, M.C., J. Hardy, and B.J.V. Saramago, *On the surface free energy of PVC/EVA polymer blends: Comparison of different calculation methods.* Journal of Colloid and Interface Science, 1998. **208**(1): p. 319-328.

259. Adao, M.H.V.C., B.J.V. Saramago, and A.C. Fernandes, *Estimation of the surface properties of styrene-acrylonitrile random copolymers from contact angle measurements.* Journal of Colloid and Interface Science, 1999. **217**(1): p. 94-106.

260. Kerkeb, M.L., F. Gonzalezcaballero, and E. Chibowski, *Changes in Cholesterol Surface Free-Energy Components Due to Its Phase-Transition.* Journal of Colloid and Interface Science, 1993. **159**(2): p. 439-443.

261. Rotenberg, Y., L. Boruvka, and A.W. Neumann, *Determination of Surface Tensions and Contact Angles from the Shape of Axisymmetric Interfaces.* Journal of the American Oil Chemists Society, 1982. **59**(4): p. A297-A297.

262. Cheng, P., *et al.*, *Automation of Axisymmetric Drop Shape-Analysis for Measurement of Interfacial-Tensions and Contact Angles.* Colloids and Surfaces, 1990. **43**(2-4): p. 151-167.

263. Moulder, J.F. and J. Chastain, *Handbook of x-ray photoelectron spectroscopy : a reference book of standard spectra for identification and interpretation of XPS data*. 1992, Eden Prairie, Minn.: Physical Electronics Division, Perkin-Elmer Corp. 261 p.

264. Botelho do Rego, A.M., *et al.*, *X-Ray Photoelectron Spectroscopy: A Tool for Studying Biopolymers*, in *Handbook of Biopolymer-Based Materials*. 2013, Wiley-VCH Verlag GmbH & Co. KGaA. p. 473-531.

265. Wagner, J.M., *X-ray photoelectron spectroscopy*. Chemical engineering methods and technology. 2011, New York: Nova Science Publishers. xi, 277 p.

266. Oliver, W.C. and G.M. Pharr, *Measurement of hardness and elastic modulus by instrumented indentation: Advances in understanding and refinements to methodology.* Journal of Materials Research, 2004. **19**(1): p. 3-20.

267. Doerner, M.F. and W.D. Nix, *A method for interpreting the data from depth-sensing indentation instruments.* Journal of Materials Research, 1986. **1**(04): p. 601--609.

268. Chong, Y.T., *et al.*, *The effect of ion implantation energy and dosage on the microstructure of the ion beam synthesized FeSi2 in Si.* Materials Science and Engineering: B, 2005. **124–125**(0): p. 444-448.

269. Marinova, M., G. Zlateva, and M. Baleva, *Influence of the implantation dose and of the annealing duration on the Raman spectra of ion-beam synthesized beta-FeSi2 layers.* Plasma Processes and Polymers, 2006. **3**(2): p. 229-232.

270. Naito, M. and M. Ishimaru, *Early stage of the crystallization in amorphous Fe–Si layers: Formation and growth of metastable α-FeSi2.* Nuclear Instruments and

Methods in Physics Research Section B: Beam Interactions with Materials and Atoms, 2009. **267**(8–9): p. 1290-1293.

271. Sugiyama, M. and Y. Maeda, *Microstructure characterization of ion-beam synthesized beta-FeSi2 phase by transmission electron microscopy.* Thin Solid Films, 2001. **381**(2): p. 225-230.

272. Schaaf, P., *et al.*, *Mossbauer optimization of the direct synthesis of beta-FeSi2 by ion beam mixing of Fe/Si bilayers.* Hyperfine Interactions, 2002. **139**(1-4): p. 615-621.

273. Galkin, N.G., *et al.*, *Morphological, structural and luminescence properties of Si/beta-FeSi2/Si heterostructures fabricated by Fe ion implantation and Si MBE.* Journal of Physics D-Applied Physics, 2007. **40**(17): p. 5319-5326.

274. Xu, S.C., *et al.*, *High quality beta-FeSi2 thin films prepared on silicon (100) by using pulsed laser ablation of Fe target.* Materials Chemistry and Physics, 2012. **135**(2-3): p. 991-997.

275. Armelao, L., *et al.*, *X-Ray Photoelectron-Spectroscopy and Scanning Electron-Microscopy of Beta-Fesi2 Films Grown by Ion-Beam-Assisted Deposition.* Surface and Interface Analysis, 1994. **22**(1-12): p. 36-40.

276. Reuther, H. and M. Dobler, *Implantation and growth of large beta-FeSi2 precipitates and alpha-FeSi2 network structures in silicon.* Applied Physics Letters, 1996. **69**(21): p. 3176-3178.

277. Shao, G., *et al.*, *Fine structure of beta-FeSi2 formed out of alpha-FeSi2 decomposition: metastable phase transformations.* Journal of Materials Science Letters, 1998. **17**(14): p. 1243-1245.

278. Katsumata, H., *et al.*, *Synthesis of beta-FeSi2 for optical applications by Fe triple-energy ion implantation into Si(100) and Si(111) substrates.* Thin Solid Films, 1996. **282**(1-2): p. 252-255.

279. Gao, Y., *et al.*, *Post-annealing effect on the microstructure and photoluminescence properties of the ion beam synthesized FeSi2 precipitates in Si.* Nuclear Instruments & Methods in Physics Research Section B-Beam Interactions with Materials and Atoms, 2007. **259**(2): p. 871-874.

280. Ayache, R., *et al.*, *Structural and optical properties of beta-FeSi2 phase prepared by ion beam synthesis.* Reviews on Advanced Materials Science, 2004. **8**(1): p. 97-100.

281. Panknin, D., *et al.*, *Investigation of Ion-Beam Synthesized Fesi2 and the Alpha-]Beta-Phase Transformation.* Vacuum, 1993. **44**(3-4): p. 171-174.

282. *ASM Handbook Volume 3: Alloy Phase Diagrams*, ed. H. Baker. 1992: ASM International.

283. Wang, P.W., *et al.*, *Studies of Implanted Iron in Silicon by Channeling and Rutherford Backscattering.* Journal of Applied Physics, 1986. **60**(4): p. 1336-1341.

284. Williams, J.S., B. Haberl, and J.E. Bradby, *Nanoindentation of Ion Implanted and Deposited Amorphous Silicon.* MRS Online Proceedings Library, 2004. **843**: p. null-null.

285. Warren, O.L., *et al.*, *Investigation of machine compliance uniformity for nanoindentation screening of wafer-supported libraries.* Review of Scientific Instruments, 2005. **76**(6).

286. Grillo, S.E., *et al.*, *Nanoindentation of Si, GaP, GaAs and ZnSe single crystals.* Journal of Physics D-Applied Physics, 2003. **36**(1): p. L5-L9.

287. Kulikovsky, V., *et al.*, *Mechanical properties of amorphous and microcrystalline silicon films.* Thin Solid Films, 2008. **516**(16): p. 5368-5375.

288. Hu, J.Z., *et al.*, *Crystal Data for High-Pressure Phases of Silicon.* Physical Review B, 1986. **34**(7): p. 4679-4684.

289. Kailer, A., Y.G. Gogotsi, and K.G. Nickel, *Phase transformations of silicon caused by contact loading.* Journal of Applied Physics, 1997. **81**(7): p. 3057-3063.

290. Domnich, V., Y. Gogotsi, and S. Dub, *Effect of phase transformations on the shape of the unloading curve in the nanoindentation of silicon.* Applied Physics Letters, 2000. **76**(16): p. 2214-2216.

291. Bradby, J.E., J.S. Williams, and M.V. Swain, *In situ electrical characterization of phase transformations in Si during indentation.* Physical Review B, 2003. **67**(8).

292. Haberl, B., *et al.*, *Phase transformations induced in relaxed amorphous silicon by indentation at room temperature.* Applied Physics Letters, 2004. **85**(23): p. 5559-5561.

293. Tani, J.-i., M. Takahashi, and H. Kido, *First-principles calculations of the structural and elastic properties of β-FeSi2 at high-pressure.* Intermetallics, 2010. **18**(6): p. 1222-1227.

294. Nakamura, S., *et al.*, *Facing target sputtered iron-silicide thin film.* Thin Solid Films, 2007. **515**(22): p. 8205-8209.

295. Milekhine, V., *et al.*, *Mechanical properties of FeSi (epsilon), FeSi2 (zeta(alpha)) and Mg2Si.* Intermetallics, 2002. **10**(8): p. 743-750.

296. Johnson, K.L., *Contact mechanics*. 1985, Cambridge Cambridgeshire ; New York: Cambridge University Press. xi, 452 p.

297. Graça, S., *et al.*, *A displacement sensing nanoindentation study of tribo-mechanical properties of the Ni–Co system.* Applied Surface Science, 2008. **254**(22): p. 7306-7313.

298. Acar, C. and A. Shkel, *MEMS vibratory gyroscopes : structural approaches to improve robustness*. MEMS reference shelf. 2008, New York ; London: Springer. xii, 256 p.

299. Kim, H.J., S.S. Yoo, and D.E. Kim, *Nano-scale Wear: A Review.* International Journal of Precision Engineering and Manufacturing, 2012. **13**(9): p. 1709-1718.

300. Khurshudov, A.G., K. Kato, and H. Koide, *Nano-wear of the diamond AFM probing tip under scratching of silicon, studied by AFM.* Tribology Letters, 1996. **2**(4): p. 345-354.

301. Wang, D.F. and K. Kato, *Tribological evaluation of carbon coatings with and without nitrogen incorporation applicable to MicroElectroMechanical systems.* Sensors and Actuators a-Physical, 2001. **93**(3): p. 251-257.

302. Stachowiak, G.W. and A.W. Batchelor, *Engineering tribology*. 2013, Butterworth-Heinemann,: Oxford. p. 1 online resource.

303. Chyan, O.M.R., J.J. Wu, and J.J. Chen, *Comparative studies of hydrogen termination on single-crystal silicon surfaces by FT-IR and contact-angle measurements.* Applied Spectroscopy, 1997. **51**(12): p. 1905-1909.

304. Collins, S., I.W. Hamley, and T. Mykhaylyk, *An atomic force microscopy study of ozone etching of a polystyrene/polyisoprene block copolymer.* Polymer, 2003. **44**(8): p. 2403-2410.

305. Levitin, G., C. Timmons, and D.W. Hess, *Photoresist and etch residue removal effect of surface energy and interfacial tension.* Journal of the Electrochemical Society, 2006. **153**(7): p. G712-G720.

306. Custer, J.S., *et al.*, *Epitaxial-Growth Versus Nucleation in Amorphous Si Doped with Cu and Ag.* Journal of Materials Research, 1993. **8**(4): p. 820-829.

307. Chayahara, A., *et al.*, *High-Dose Implantation of Mev Carbon Ion into Silicon.* Japanese Journal of Applied Physics Part 1-Regular Papers Short Notes & Review Papers, 1992. **31**(1): p. 139-140.

308. Chayahara, A., *et al.*, *Formation of Crystalline Sic Buried Layer by High-Dose Implantation of Mev Carbon-Ions at High-Temperature.* Japanese Journal of Applied Physics Part 2-Letters, 1993. **32**(9A): p. L1286-L1288.

309. Poudel, P.R., *et al.*, *An XPS study to investigate the dependence of carbon ion fluences in the formation of buried SiC.* Nuclear Instruments & Methods in Physics Research Section B-Beam Interactions with Materials and Atoms, 2012. **283**: p. 93-96.

310. Poudel, P.R., *et al.*, *Synthesis of buried layers of beta-SiC in Si by multiple energy carbon ion implantations and post thermal annealing.* Thin Solid Films, 2012. **524**: p. 35-38.

311. Lindner, J.K.N., *et al.*, *keV- and MeV- Ion Beam Synthesis of Buried SiC Layers in Silicon.* MRS Online Proceedings Library, 1994. **354**: p. null-null.

312. Hopf, T., *et al.*, *Ion-beam synthesis of 3C-SiC surface layers on silicon.* Surface and Interface Analysis, 2012. **44**(4): p. 399-404.

313. Markwitz, A., *et al.*, *Formation of SiC-surface nanocrystals by ion implantation and electron beam rapid thermal annealing.* Applied Physics Letters, 2005. **86**(1).

314. Seng, W.F. and P.A. Barnes, *Calculations of tungsten silicide and carbide formation on SiC using the Gibbs free energy.* Materials Science and Engineering B-Solid State Materials for Advanced Technology, 2000. **72**(1): p. 13-18.

315. Durand, F. and J.C. Duby, *Carbon solubility in solid and liquid silicon—A review with reference to eutectic equilibrium.* Journal of Phase Equilibria, 1999. **20**(1): p. 61-63.

316. Frieser, R.G., *Characterization of Thermally Grown Sio2 Surfaces by Contact Angle Measurements.* Journal of the Electrochemical Society, 1974. **121**(5): p. 669-672.

317. Morita, M., *et al.*, *Growth of Native Oxide on a Silicon Surface.* Journal of Applied Physics, 1990. **68**(3): p. 1272-1281.

318. Schoell, S.J., *et al.*, *Functionalization of 6H-SiC surfaces with organosilanes.* Applied Physics Letters, 2008. **92**(15).

319. Shin, Y.J., *et al.*, *Surface-Energy Engineering of Graphene.* Langmuir, 2010. **26**(6): p. 3798-3802.

320. Cicero, G., G. Galli, and A. Catellani, *Interaction of water molecules with SiC(001) surfaces.* Journal of Physical Chemistry B, 2004. **108**(42): p. 16518-16524.

321. Onneby, C. and C.G. Pantano, *Silicon oxycarbide formation on SiC surfaces and at the SiC/SiO2 interface.* Journal of Vacuum Science & Technology a-Vacuum Surfaces and Films, 1997. **15**(3): p. 1597-1602.

322. Petoral, R.M., *et al.*, *Organosilane-functionalized wide band gap semiconductor surfaces.* Applied Physics Letters, 2007. **90**(22).

323. Kaneko, R., *et al.*, *Microwear.* Thin Solid Films, 1996. **273**(1-2): p. 105-111.

324. Kaneko, R., *et al.*, *Recent progress in microtribology.* Wear, 1996. **200**(1-2): p. 296-304.

325. Song, C.F., *et al.*, *Friction-induced nanofabrication method to produce protrusive nanostructures on quartz.* Nanoscale Research Letters, 2011. **6**.

326. Yu, B.J., *et al.*, *Friction-induced hillocks on monocrystalline silicon in atmosphere and in vacuum.* Wear, 2010. **268**(9-10): p. 1095-1102.

327. Yu, B.J., *et al.*, *Towards a deeper understanding of the formation of friction-induced hillocks on monocrystalline silicon.* Journal of Physics D-Applied Physics, 2012. **45**(14).

328. Yu, J.X., *et al.*, *Nanofretting behaviors of monocrystalline silicon (1 0 0) against diamond tips in atmosphere and vacuum.* Wear, 2009. **267**(1–4): p. 322-329.

329. Villarrubia, J.S., *Algorithms for scanned probe microscope image simulation, surface reconstruction, and tip estimation.* Journal of Research of the National Institute of Standards and Technology, 1997. **102**(4): p. 425-454.

330. Ovsyannikov, S.V., *et al.*, *Raman characterization of hydrogen ion implanted silicon: "High-dose effect"?* Physica B-Condensed Matter, 2008. **403**(19-20): p. 3424-3428.

331. Shimada, T., *et al.*, *Raman-Scattering in Low Wavenumber Region as a New Probe to Structural-Properties of Microcrystalline Silicon.* Journal of Non-Crystalline Solids, 1983. **59-6**(Dec): p. 783-786.

332. Intarasiri, S., *et al.*, *Characterization of the crystalline quality of β-SiC formed by ion beam synthesis.* Nuclear Instruments and Methods in Physics Research Section B: Beam Interactions with Materials and Atoms, 2006. **249**(1–2): p. 851-855.

333. Intarasiri, S., *et al.*, *Crystalline quality of 3C-SiC formed by high-fluence C+-implanted Si.* Applied Surface Science, 2007. **253**(11): p. 4836-4842.

334. Naumkin, A.V., *et al.*, *X-ray Photoelectron Spectroscopy Database, NIST Standard Reference Database 20, Version 4.1, Accessed in September 2014*.

335. Vogel, F.L., *Implantation of Carbon into Thin Iron Films.* Thin Solid Films, 1975. **27**(2): p. 369-376.

336. Horton, L.L., *et al.*, *Microstructural Characterization of Iron-Ion Implantation of Silicon-Carbide.* Nuclear Instruments & Methods in Physics Research Section B-Beam Interactions with Materials and Atoms, 1992. **65**(1-4): p. 345-351.

337. Jeon, H., *et al.*, *Morphology and Phase-Stability of Tisi2 on Si.* Journal of Applied Physics, 1992. **71**(9): p. 4269-4276.

338. Motakef, S., *et al.*, *Stability of C49 and C54 Phases of Tisi2 under Ion-Bombardment.* Journal of Applied Physics, 1991. **70**(5): p. 2660-2666.

339. Bandyopadhyay, D., *The Ti-Si-C system (Titanium-silicon-carbon).* Journal of Phase Equilibria and Diffusion, 2004. **25**(5): p. 415-420.

340. Kittl, J.A., M.A. Gribelyuk, and S.B. Samavedam, *Mechanism of low temperature C54 TiSi2 formation bypassing C49 TiSi2: Effect of Si microstructure and Mo impurities on the Ti-Si reaction path.* Applied Physics Letters, 1998. **73**(7): p. 900-902.

341. Wang, S., H. Liang, and P. Zhu, *Preferential growth of C54 TiSi2 by metal vapor vacuum arc ion source implantation and post-annealing.* Surface and Coatings Technology, 2000. **131**(1–3): p. 84-87.

342. Ma, Z. and L.H. Allen, *Kinetic mechanisms of the \textit{C} 49-to- \textit{C} 54 polymorphic transformation in titanium disilicide thin films: A microstructure-scaled nucleation-mode transition.* Physical Review B, 1994. **49**(19): p. 13501-13511.

343. Myers, S.M., *et al.*, *Strength and tribology of bulk and electroformed nickel amorphized by implantation of titanium and carbon.* Surface & Coatings Technology, 1998. **104**: p. 287-292.

344. Senkov, O.N., *et al.*, *Metallic materials with high structural efficiency*. NATO science series Series II, Mathematics, physics, and chemistry. 2004, Dordrecht ; Boston: Kluwer Academic Publishers. xvi, 440 p.

345. Jongste, J.F., *et al.*, *Elastic-Constants and Thermal-Expansion Coefficient of Metastable C49 Tisi2.* Journal of Applied Physics, 1993. **73**(6): p. 2816-2820.

346. Ma, D., *et al.*, *Microstructure and tribological behaviour of super-hard Ti–Si–C–N nanocomposite coatings deposited by plasma enhanced chemical vapour deposition.* Thin Solid Films, 2006. **496**(2): p. 438-444.

347. Ma, S.L., *et al.*, *Synthesis and characterization of super hard, self-lubricating Ti–Si–C–N nanocomposite coatings.* Acta Materialia, 2007. **55**(18): p. 6350-6355.

348. Veprek, S., *et al.*, *Composition, nanostructure and origin of the ultrahardness in nc-TiN/a-Si3N4/a- and nc-TiSi2 nanocomposites with HV=80 to ≥105 GPa.* Surface and Coatings Technology, 2000. **133–134**(0): p. 152-159.

349. Polcar, T., M. Evaristo, and A. Cavaleiro, *Self-Lubricating W–S–C Nanocomposite Coatings.* Plasma Processes and Polymers, 2009. **6**(6-7): p. 417-424.

350. Clauss, F.J., *Solid lubricants and self-lubricating solids*. 1972, New York,: Academic Press. xii, 260 p.